7-2015

Design Guidelines for Offset Journal Bearings in Two-Stroke Engines

David P. Anderson

Recommended Citation

Anderson, David P., "Design Guidelines for Offset Journal Bearings in Two-Stroke Engines" (2015). Thesis. Rochester Institute of Technology. Accessed from

Design Guidelines for Offset Journal Bearings in Two-Stroke Engines

by

David P. Anderson

A Thesis Submitted in Partial Fulfillment of the
Requirements for the Degree of Master of Science
in Mechanical Engineering

Supervised by

Dr. Stephen Boedo
Department of Mechanical Engineering
Kate Gleason College of Engineering
Rochester Institute of Technology
Rochester, New York
July 2015

Approved by:

Dr. Stephen Boedo, Professor
Thesis Advisor, Department of Mechanical Engineering

Dr. Hany Ghoneim, Professor
Committee Member, Department of Mechanical Engineering

Dr. Jason Kolodziej, Associate Professor
Committee Member, Department of Mechanical Engineering

Dr. Alex Liberson, Associate Professor
Department Representative, Mechanical Engineering

Abstract

Design Guidelines for Offset Journal Bearings in Two-Stroke Engines

David P. Anderson

Supervising Professor: Dr. Stephen Boedo

Offset journal bearings are an attractive design option for cross-head and piston bearings for two-stroke engines. Two-stroke engine design has seen a resurgence in the last few years due to potential gains in engine efficiency over their four-stroke counterparts. The cross-head and piston bearings comprising such engines, however, are characterized by non-reversing loads with limited oscillating journal motion, the combination of which provides poor bearing performance for conventional cylindrical bearings. The division of bearing journal and sleeve into offset segments allows for periodic load relaxation in the segments and development of squeeze-film action which substantially improves bearing performance. Offset bearings have been in production for the past 60 years, but there are no general design guidelines available to the engine analyst. This thesis provides predictions of the primary bearing performance factors, cyclic-minimum film thickness and cyclic-maximum film pressure, over a wide range of design parameters found in production-level, two-stroke engines.

Acknowledgments

I owe many people thanks for their continuous support and guidance through this whole experience. To all of my friends and family, thank you for always supporting me. To my committee and the engineering staff and faculty, particularly advisors Karen Hirst and Diane Selleck, thank you for your continuing guidance and accountability. To my friend Colin, thank you for making me explain concepts, constantly offering bits of wisdom and advice, and for always being there for me to vent to when things were tough. To my parents, thank you for always supporting and loving me in my endeavors and encouraging me to challenge myself. Finally, to my advisor Dr. Stephen Boedo, thank you for providing an excellent and challenging thesis experience: you have taught me to be critical and to follow things through. It is thanks to all of these people that I can finally say,

…and that's the story.

Table of Contents

List of Tables

List of Figures

Nomenclature

a_i	Sleeve Segment Offset Vector
b_i	Journal Segment Offset Vector
e_0	Journal Reference Eccentricity
e_i	Journal Segment Eccentricity
$f(\theta)$	Normalized Cylinder Pressure Profile
h	Film Thickness
i	Segment Index
n	Number of Segments
p_{cyl}^*	Peak Cylinder Gas Pressure
p_{cyl}	Cylinder Gas Pressure
p_{max}	Peak Film Pressure
r	Crank Radius
s	Piston Position
t	Simulation Time
t_{scale}	Simulation to Real Time Scale
t_{step}	Simulation Time Step
x', y'	Journal Reference Frame
x, y	Sleeve Reference Frame
A_{cyl}	Cylinder Area
B	Bearing Segment Length
C	Bearing Radial Clearance
D	Journal Segment Diameter
$\bar{F}$	Engine Load Number
F	Load from Piston Pin Journal to Sleeve
F_b	Connecting Rod Big End Inertial Load
F_c	Load from Crank Pin Journal to Sleeve
F_p	Piston Inertial Load
F_s	Connecting Rod Small End Inertial Load

F_{gas}	Cylinder Gas Load
L	Connecting Rod Length
M_b	Connecting Rod Big End Mass
M_p	Piston Mass
M_s	Connecting Rod Small End Mass
N	Piston Sidewall Load
O	Offset Bearing Sleeve Reference
O'	Offset Bearing Journal Reference
O''_i	Offset Bearing Sleeve Segment Center
O'''_i	Offset Bearing Journal Segment Center
P	Bearing Film Load
R	Journal Segment Radius
V	Squeeze Velocity
W	Impedance
X_1, Y_1	Engine Block Reference Frame
X_2, Y_2	Crankshaft Reference Frame
X_3, Y_3	Connecting Rod Reference Frame
α	Segment Length Factor
β	Journal Inclination Angle
δ	Offset Magnitude
ϵ	Eccentricity Ratio
μ	Lubricant Viscosity
ω	Crankshaft Angular Velocity
ω_j	Journal Angular Speed
ω_s	Sleeve Angular Speed
ϕ	Connecting Rod Angle relative to X_1, Y_1
τ	Nondimensional Time
θ	Crankshaft Angle

Chapter 1

Introduction

1.1 Background

Hydrodynamically lubricated journal bearings are a type of bearing in which two cylindrically-shaped surfaces are separated by a thin fluid film (usually on the scale of micrometers), and the oil film pressure required to separate the surfaces is maintained by the motion of the journal relative to the bearing sleeve. Due to their geometric simplicity, low cost, and their ability to handle dynamic loads and kinematics, such journal bearings are a common feature in internal combustion engines. Figure 1.1 shows an engine schematic consisting of a piston, connecting rod, crankshaft, and a crosshead. Journal bearings are commonly employed in the crankshaft and the connecting rod.

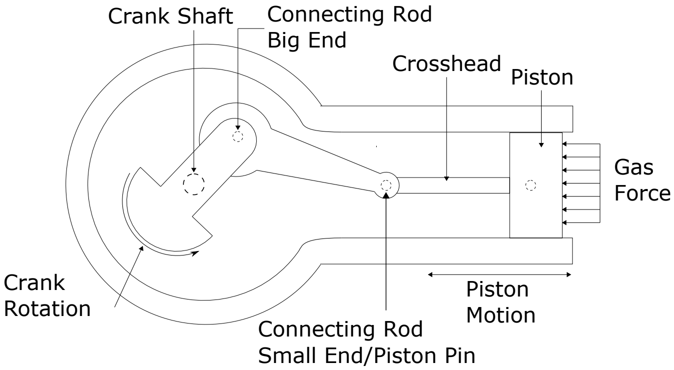

Figure 1.1: Basic Engine Cylinder Components

Film loads in journal bearings are supported by two primary actions: wedge film and squeeze film. In a wedge film, two surfaces move tangentially toward each other at an angle (a wedge). In a squeeze film, surfaces undergo normal approach.

In a two-stroke diesel engine, the loading on the small end bearing (typically the piston pin) varies in magnitude but is unidirectional (non-reversing), and the journal undergoes a very limited oscillating motion. The combination of non-reversing load and limited oscillation result in limited wedge film action which in turn results in high film pressures and very small film thicknesses.

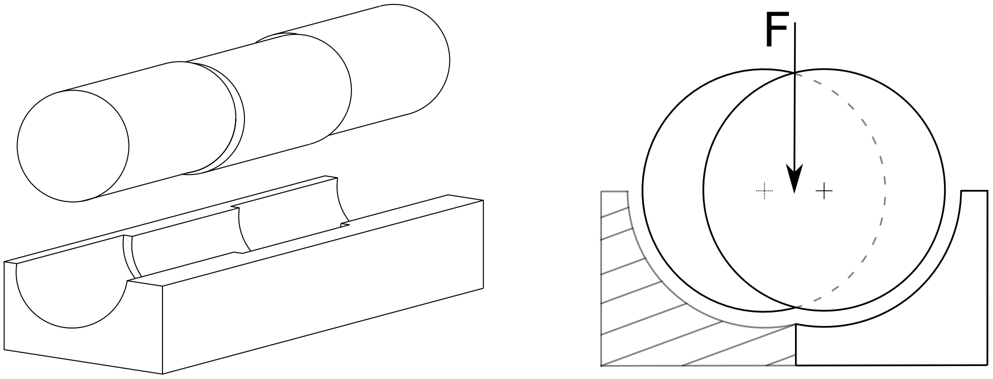

(a) Isometric View (b) 2D End View

Figure 1.2: Isometric and End View Sketch of a 3-Segment Full Offset Bearing

A variety of geometric configurations have been employed to attempt to increase the film thickness and to reduce the film pressure in piston pin bearings. Figure 1.2 shows an isometric and end view of one such design, known as an "offset bearing". The bearing geometry is such that it has multiple parallel, cylindrical segments arranged on different axes that have an offset between them[1]. The offset is very small, often being on the order of the clearance in the bearing. The offsets shown in Figure 1.2 are thus exaggerated for illustrative purposes. This bearing has been most commonly designed with dual axes, and thus has also been referred to as a bi-axial journal bearing. Offset journal bearings have

---

[1] The term "offset bearing" is also used to refer to a lobed bearing such as that in Figure 3b in [1]. This type of bearing consists of a single segment in which the sleeve is composed of two offset semi-circular components, and not multiple segments with offset axes.

been implemented in two-stroke engine connecting rod bearings at least since the 1950s [2].

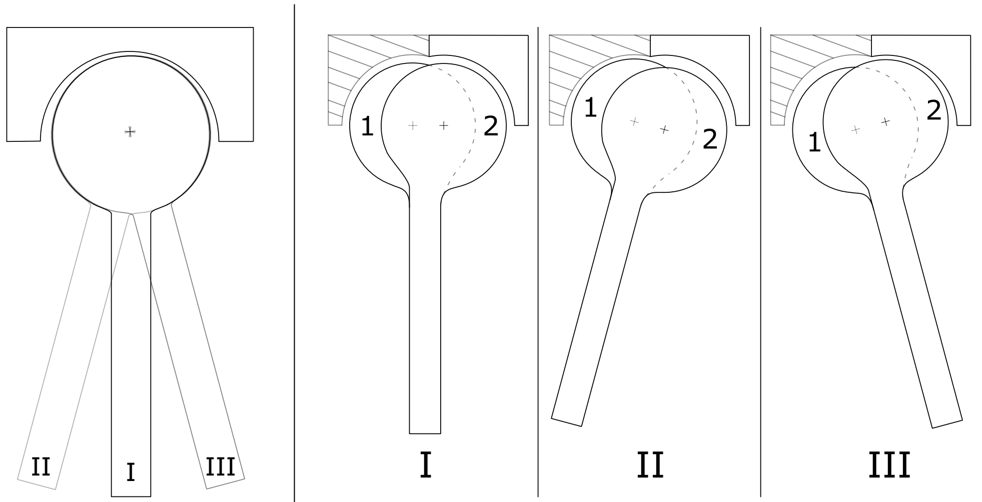

(a) Conventional Bearing

(b) Full Offset Bearing

Figure 1.3: Kinematics of Conventional and Offset Journal Bearings

The offset bearing provides a significant improvement in bearing performance at very little additional cost. The effort required to implement this design is far less than, for example, increasing the oil feed pressure to the bearing, or investigating the use of wear-resistant surface coatings.

Figure 1.3 shows a comparison of the motion between a conventional and an offset journal bearing. Position I shows the connecting rod aligned vertically. Positions II, and III illustrate the angular extent of the journal arising from oscillatory motion. As the journal rotates from position I to II, load in the offset bearing is carried by segment 1 primarily from squeeze film action. As the journal rotates from position II to III, segment 1 changes from a load-bearing stage to a lubricant-filling stage, and vice versa for segment 2. In an application with periodic, oscillatory motion the segments will continually alternate between the two stages. The conventional bearing exhibits only wedge film action over the entire periodic duty cycle.

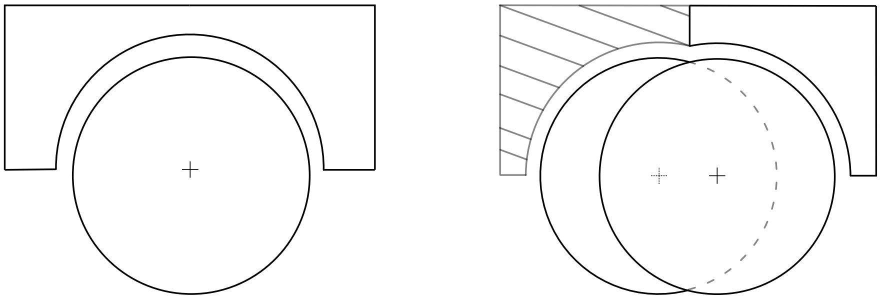

(a) Conventional Bearing (b) Full Offset Bearing

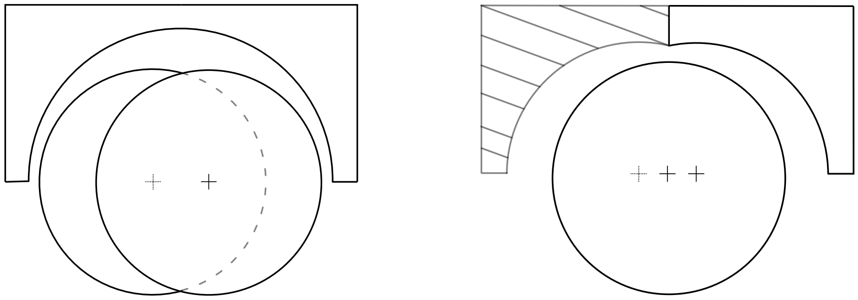

(c) Wakuri Journal-Offset Bearing (d) Camella Sleeve-Offset Bearing

Figure 1.4: Comparison of Offset Bearing Configurations

The offset bearing has been implemented over the years in three different configurations which are shown in Figure 1.4. The preferred "full offset" configuration breaks both journal and sleeve into offset segments. Configurations which provide offsets to only the sleeve or journal have also been used and studied. A journal-offset bearing with an aligned sleeve and segmented journal was studied by Wakuri [3]. A "Camella" bearing is designed with an aligned journal and segmented sleeve [4].

In the 1977 issue of the German journal MTZ, various improved features of two-stroke engines fabricated by Grandi Motori Trieste (GMT) were represented. One particular improvement of relevance to this thesis is the introduction of the "eccentric crosshead bearing" [5]. This bearing is presented as an alternative to the conventional single-axis cylindrical journal bearing used in two-stroke engine applications. One of the major concerns of GMT with their new B600 engine was inadequate hydrodynamic lubrication. The B600 engine makes use of a crosshead, which is a rod that links the bottom of the piston to the connecting rod small end. A crosshead is used when the engine stroke is large and the connecting rod is kinematically limited in the cylinder. In the GMT design, the journals are fixed to the crosshead and do not rotate while the bearing sleeves are fixed to and rotate with the small end of the connecting rod bearing. This configuration is essentially equivalent to a configuration where the journal(s) are attached to and rotate with the connecting rod and the bearing sleeve(s) are built into the piston as bores and remain angularly fixed.

Also in 1977, a paper by Ciliberto (who was associated with GMT) was published describing the crosshead bearing of two-cycle engines in more detail [6]. It is noted that the offset pad design was implemented as early as 1975 in the GMT A1060 and GMT A900 engines [7] [8].

1.2 Literature Review

While the advantage and increased performance of a limited set of offset bearings has been discussed repeatedly in the literature, this has only been done so for specific cases [3, 9, 10]. The availability of general guidelines to design offset bearings is nearly non-existent. Some general design guidelines for offset journal bearings comes from Wakuri [3]. Wakuri's generalizations in his 1982 publication apply to the Wakuri journal-offset bearing, shown in Figure 1.4(c), in which only the journal is offset and the sleeve segments are aligned. In 1985, Wakuri also published an analysis of a full offset bearing in which both journal and sleeve contained offsets [10]. Both of these publications study a paired, two-segment design. In the 1982 publication, Wakuri provides the (few) very general recommendations based on a limited nondimensional study [3]:

> "In order to make the max. oil-film pressure on the bearing surface as small as possible and to realized an effective change of oil-film, it is necessary to satisfy the following items:

> i The distance between journal centers should be larger than 0.75 times and less than 1.25 times the radial clearance.
>
> ii The width of main journal is to be adjusted to 70~80% of the whole bearing width.
>
> iii The eccentric journal center should be set slightly lower than the main journal center or horizontally.
>
> iv The effective circumferential angle of bearing should be taken larger than 120°."

Wakuri's results for the 2-segment journal-offset bearing included charts for journal motion, pressure ratio distributions, and variation of maximum film pressure ratio. These charts were created for a single engine duty configuration and for limited ranges of the following nondimensional bearing parameters:

- bearing load capacity
- offset ratio
- segment length ratio
- offset inclination
- bearing wrap angle
- aspect ratio
- material deflection ratio

The majority of charts created were done for a single bearing load capacity and offset ratio. While the bearing parameter study was well-structured, the nomenclature used by Wakuri differs from the majority of the literature on offset bearings.

Wakuri's conclusions in 1985 for the full offset bearing provided additional information concluded from a limited dimensional study [10]:

> "Concerning the offset typed crosshead-pin bearing, the following conclusions are made clear from the theoretical analysis on the lubrication characteristics and the experimental investigations on the load carrying capacity.

1. According to the change of revolving direction the split bearing surfaces into main and eccentric segments alternately carry the load with the oil-film squeeze action which facilitates the exchange of oil-film in the unloaded segment.
2. In order to utilize this character the design criteria are pointed out as below.
   - i The radial clearance should be less than two-thousandths of the journal radius.
   - ii The offset should be as large as possible but less than about one-hundredth of the journal radius.
3. The allowable load pressure can be expected to become larger than twice the conventional bearing with axial oil-grooves."

The types of designs considered by Wakuri, along with the articulation used to describe these designs, is particularly useful in providing ideas and suggestions for how to expand and describe the design space that is to be developed in this thesis.

The work done by Wakuri on the full offset bearing includes theoretical work and experimental results. The bearing appears to be the same as that presented by MTZ [5] and Ciliberto [6]. Minimum film thickness and maximum pressure were found with respect to a varied offset ratio. The experimental results include data for the cyclic oil film thickness and a bearing load limit test. In the load limit test the load and temperature were gradually increased until the metal surfaces seized. A comparison was made between a conventional cylindrical bearing and the offset geometry design. The offset geometry design proved a seizure load carrying capacity of over twice that of the conventional bearing.

The Camella sleeve-offset bearing shown in Figure 1.4(d) can be considered the geometric inverse of the Wakuri journal-offset bearing. The application for the Camella bearing was for naval vessels with very large loads and low engine speeds. The bearing design provided a solution to problems of oil flow and shaft stability. Given the available machining technology in 1963, this design is attractive as it requires only that eccentric bores be made.

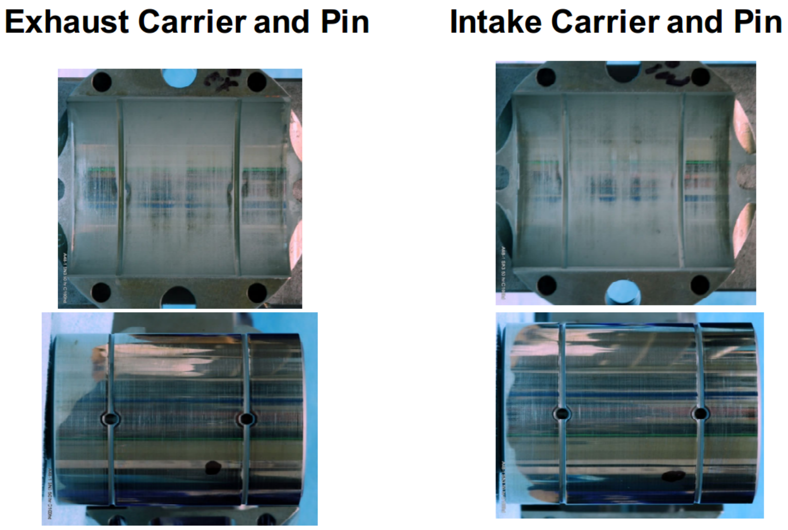

Figure 1.5: Achates A48 1.6L Single Cylinder Engine: Wrist Pins after 50 Hrs. Full Load Durability

The design by Wakuri [3] requires the manufacture of eccentric segments on the shaft, a relatively more challenging task.

While the offset bearing has been applied historically in naval and locomotive engines, it is also providing solutions to the problem of bearing capacity in recently developed opposed-piston two-stroke engines. California-based company Achates Power is in the process of developing an opposed piston two-stroke engine to compete with four-stroke engines that are common in medium and heavy duty trucks. Despite increased fuel efficiency, the two-stroke engine has been barred from consumer and commercial use in vehicles due to a variety of challenges. One challenge internal to the engine is the durability of the wrist pin. For peak cylinder pressures in excess of 150 bar, the wrist pin in a two-stroke engine suffers in durability; however, use of an offset bearing (bi-axial wrist pin) in the Achates Power single-cylinder A48-1 engine permitted peak pressures of 220 bar [11]. Figure 1.5 shows offset bearings that underwent "50 hours of full load operation at rated power" in an A48 engine.[2] "The pictures show no sign of scuffing or cavitation, which demonstrates the potential of the [offset bearing] for heavy-duty durability requirements" [12].

---

[2] Figure 1.5 is Figure 14 in [12], and is used with permission from the authors.

Within the past 3 years both Electro-Motive Diesel and Achates Power have filed patents for offset bearings. In 2012 Electro-Motive Diesel filed a patent for an offset bearing and dual connecting rod assembly for “a two-cycle diesel engine of a locomotive” [8]. The locomotive application is most likely the EMD 710 two-stroke engine series [13]. In 2014 Achates power patented a design for a “rocking journal bearing” for two-stroke opposed piston engines [7]. The offset bearing was also patented in a non-engine application, a reciprocating compressor, by Carrier Corporation in 1999 [14].

With the current machining and manufacturing technology available, manufacture of an offset bearing design with combined segmented sleeve and journal is much more feasible. Such geometries could be manufactured by computer numerical control (CNC) machines or perhaps even by rapid prototyping. Rapid prototyping in particular is becoming a much more robust technology, and as tolerances are improved, it could become an ideal method for creating offset bearings with micrometer scale clearances and offsets.

The studies presented by Booker, Goenka, and van Leeuwen in 1982 [9]; Booker, and Olikara in 1984 [15], and Olikara [16] present some of the most consistent, straightforward nomenclature and methods of solution for offset journal bearings. Consequently, this thesis will use primarily the nomenclature from [9] and the solution methods presented in all three papers. The thesis by Olikara [16] provides a more comprehensive narrative which aided in developing and understanding the iterative solution process necessary for the offset bearing. The nomenclature and solution process will be presented in the following chapters.

While this thesis focuses on the application of offset journal bearings to two-stroke engines, the offset journal bearing can provide performance improvements in any application that has non-reversing loading and limited oscillation. Olikara and Booker studied the general case of a bearing subjected to a steady, non-reversing load and limited oscillation [15, 16]. This general case was studied further by Boedo and Anderson, in part as a consequence of this thesis. The technical note, accepted for publication in ASME Journal of

Tribology, shows the limitations of conventional bearings and the improvements possible with offset bearings subjected to the same loads and kinematics [17].

1.3 Thesis Goals

The goal of this thesis is to provide design guidelines that cover a broader range of parameters than those currently available in the literature. The first step to achieve this goal is to recreate prior work to test that the developed program functions properly based on results in the literature. A range of engine and bearing parameters are collected and used to calculate a general range of non-dimensional parameters to cover a large engine-bearing design space. Using these nondimensional parameters, results such as minimum film thickness ratio and maximum film pressure ratio are calculated using an iterative impedance method to be described in the following chapters. The end result is a collection of figures and data that may be used to provide previously unavailable insight into the performance of offset bearings. This insight may be used to guide future studies of the offset bearing or to enable a bearing designer to more easily determine the specifications of a two-axis offset journal bearing.

Chapter 2

Problem Formulation

The solution process for the offset journal bearing involves two general steps: determination of loads applied to the bearing, and determination of the journal motion in the clearance space. This chapter will first look at the determination of loads in an engine, then look at the process for finding the journal motion. The determination of journal motion involves bearing kinematics, fluid film model, and the applied load. The method of determining bearing performance factors such as film thickness and pressure are then introduced, followed by a discussion for implementing the full solution in a computer program.

2.1 Analysis Assumptions

The following assumptions are used in the development of both the load and bearing analyses:

- The crankshaft is rotating at a steady angular velocity $\omega \equiv \dot{\theta}$, $\ddot{\theta} = 0$.
- All components in the engine are considered rigid bodies.
- The effect of gravity is negligible.
- Residual inertia from the connecting rod can be neglected.
- The main bearing is in line with the axis of the engine cylinder.
- The piston is aligned with the piston chamber.
- Bearings are idealized as pin joints.
- All bearings/segments are aligned within their respective sleeves.

- Lubricant viscosity and density are constant.

Additional assumptions will be introduced in the proceeding sections as necessary.

2.2 Engine Duty: Calculation of Bearing Loads and Dynamics

The following analysis of the bearing loading and dynamics is drawn primarily from Appendix C in [9] and analyses in [18] and [19]. In Figure 2.1, $\vec{r}$, $\vec{L}$, and $\vec{s}$ are position vectors corresponding to different components in the engine cylinder. Vector $\vec{r}$ extends radially from the center of the crankshaft to the center of the crank pin; $\vec{L}$ extends from the center of the connecting rod big end to the center of the connecting rod small end, and $\vec{s}$ extends from the crankshaft axis to the piston. Reference frame X_1, Y_1 is attached to the (static) engine block with its origin at the crankshaft axis; frame X_2, Y_2 is attached to the (moving) crankshaft; and frame X_3, Y_3 is attached to the (moving) connecting rod.

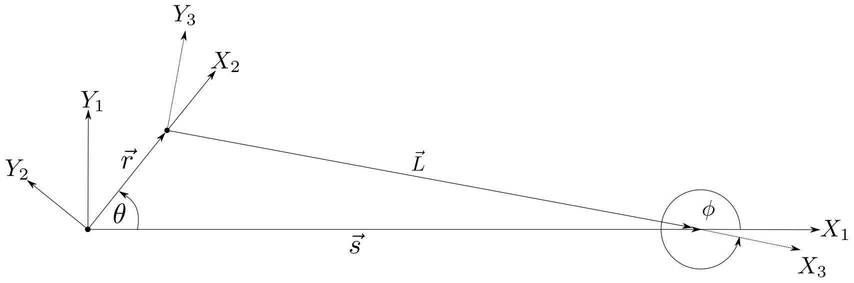

Figure 2.1: Connecting Rod Geometry

The independent angle θ is the crank angle, and dependent angle ϕ is the angle of the connecting rod with respect to the block (computation) frame. The angular velocity of the crankshaft, $\dot{\theta}$, is referred to as ω. It is assumed that an external, time-variable torque acts on the crankshaft, a necessary system constraint in order for the crankshaft to rotate at a steady speed [20].

2.2.1 Kinematics

The individual positions of each vector can be expressed as follows, where $\hat{i}_1$ and $\hat{j}_1$ are the unit vectors corresponding to the X_1, Y_1 block frame:

$$\vec{r} = rcos\theta\hat{i}_1 + rsin\theta\hat{j}_1 \tag{2.1}$$

$$\vec{L} = Lcos\phi\hat{i}_1 + Lsin\phi\hat{j}_1 \tag{2.2}$$

$$\vec{s} = (rcos\theta + Lcos\phi)\hat{i}_1 + 0\hat{j}_1 \tag{2.3}$$

These vectors are related by the kinematic loop

$$\vec{r} + \vec{L} = \vec{s} \tag{2.4}$$

from which it follows that

$$sin\phi = -\frac{r}{L}sin\theta \tag{2.5}$$

$$cos\phi = (1 - sin^2\phi)^{\frac{1}{2}} \tag{2.6}$$

$$\dot{\phi} = -\omega\frac{r}{L}\frac{cos\theta}{cos\phi} \tag{2.7}$$

$$\ddot{\phi} = \frac{\omega^2\frac{r}{L}sin\theta + \dot{\phi}^2 sin\phi}{cos\phi} \tag{2.8}$$

In order to determine the inertial loads of the big and small ends of the connecting rod the second time derivatives of $\vec{r}$ and $\vec{s}$ are necessary:

$$\ddot{\vec{r}} = -r\omega^2 cos\theta\hat{i}_1 - r\omega^2 sin\theta\hat{j}_1 \tag{2.9}$$

$$\ddot{\vec{s}} = \ddot{s}\hat{i}_1 + 0\hat{j}_1 = -(r\omega^2 cos\theta + L\dot{\phi}^2 cos\phi + L\ddot{\phi}sin\phi)\hat{i}_1 + 0\hat{j}_1 \tag{2.10}$$

2.2.2 Loads

As noted, the particular point of interest is the bearing at the small end of the connecting rod. This bearing serves as the connection between the connecting rod small end and either the crosshead or the piston. The piston pin, which serves as the bearing journal, is affixed to the small end of the connecting rod. The bearing sleeve is attached to either the crosshead or the piston. Should a crosshead be present, it is assumed that the crosshead is rigidly attached to the piston.

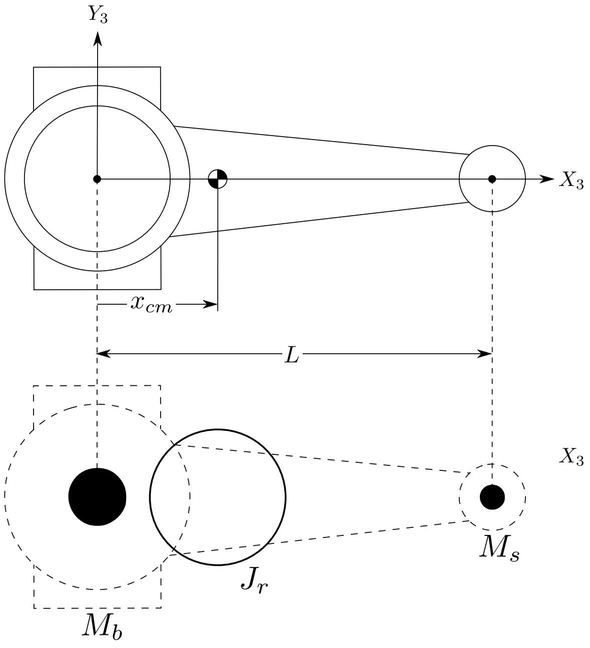

Figure 2.2: Dynamically Equivalent Connecting Rod Model

To simplify the load analysis, it is convenient to replace the connecting rod-piston pin assembly with a dynamically equivalent model as shown in Figure 2.2. The connecting rod-piston pin assembly with mass, M, length, L, and center of mass, x_{cm}, is replaced by point masses, M_b and M_s, a distance L apart, and residual polar moment of inertia, J_r[1].

---

[1] This inertia correction term, J_r is usually small and can be neglected.

The free body diagrams of the piston[2] and the connecting rod-piston pin assembly are found in Figures 2.3, and 2.4, respectively. In Figure 2.3, $\vec{F}$ is the load from the journal (piston pin) to the sleeve (piston bore); $\vec{N}$ is the reaction normal force from the cylinder wall to the piston cylinder; $\vec{F}_p$ is the inertial load of the piston; and $\vec{F}_{gas}$ is the external load from gas combustion. In Figure 2.4, $\vec{F}_s$ is the inertial load of the small end mass; $\vec{F}_b$ is the inertial load of the big end mass; and $\vec{F}_c$ is the load from the crank pin journal to the big end sleeve.

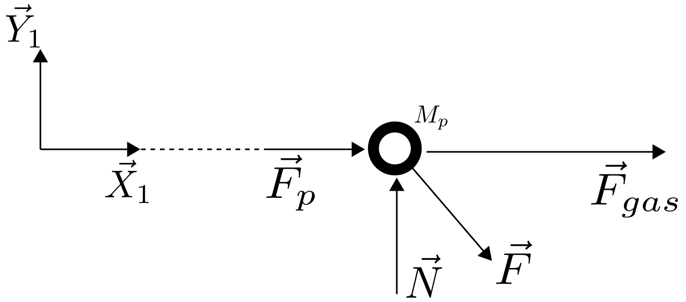

Figure 2.3: Piston/Crosshead Free Body Diagram

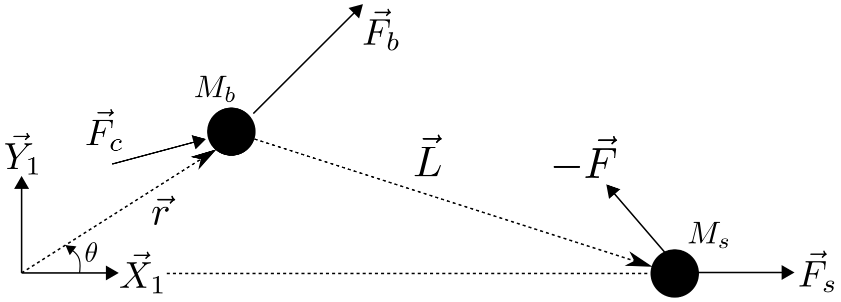

Figure 2.4: Connecting Rod-Piston Pin Free Body Diagram

Summing the forces on the piston in terms of components in the X_1, Y_1 frame gives

$$F^{X_1} = -F_p - F_{gas} \tag{2.11}$$

$$F^{Y_1} = -N \tag{2.12}$$

---

[2] In Figure 2.3 the piston/crosshead point mass is represented as an annulus as a reminder that the bearing sleeve is built into the piston/crosshead.

where piston inertial load and gas loads are defined along the X_1 axis as

$$F_p = -M_p\ddot{s} \tag{2.13}$$

$$F_{gas} = -p_{cyl}(\theta)A_{cyl} \tag{2.14}$$

Summing the moments about the big end mass gives

$$\vec{L} \times (\vec{F}_s - \vec{F}) = \vec{0} \tag{2.15}$$

or

$$\left(Lcos\phi\,\hat{i}_1 + Lsin\phi\,\hat{j}_1\right) \times \left((F_s - F^{X_1})\hat{i}_1 - F^{Y_1}\hat{j}_1\right) = 0\hat{k}_1 \tag{2.16}$$

which in terms of the $\hat{k}_1$-component gives

$$-F^{Y_1}Lcos\phi - (F_s - F^{X_1})Lsin\phi = 0 \tag{2.17}$$

where the small end inertial load is defined by

$$F_s = -M_s\ddot{s} \tag{2.18}$$

Therefore, the load from the journal to sleeve $\vec{F}$ has the following components:

$$\begin{aligned} F^{X1}(\theta) &= p_{cyl}(\theta)A_{cyl} \\ &- M_p r\omega^2 cos\theta \\ &- M_p L\dot{\phi}^2 cos\phi \\ &- M_p L\ddot{\phi} sin\phi \end{aligned} \tag{2.19a}$$

$$\begin{aligned} F^{Y1}(\theta) = {} & F^{X1} tan(\phi) \\ & - M_s tan(\phi) r\omega^2 cos\theta \\ & - M_s tan(\phi) L\dot{\phi}^2 cos\phi \\ & - M_s tan(\phi) L\ddot{\phi} sin\phi \end{aligned} \tag{2.19b}$$

Note that only the y-component of the piston-pin load depends on the small end connecting rod mass.

2.3 Bearing Analysis

2.3.1 Offset Bearing Geometry and Dynamics

The offset bearing requires some special consideration in regard to its dynamics. The conventions and nomenclature used in this subsection follow Booker *et al.* [9] and Olikara [16]. This section describes the offset bearing's dynamic dependence on the reference eccentricity and illustrates the relationship between segment[3] offsets and eccentricities.

The coordinate frame origins used to describe the offset bearing are

O	Sleeve reference
O'	Journal reference
O''_i	Sleeve segment center
O'''_i	Journal segment senter

The vectors describing segment and reference positions, and segment offsets are defined as

$\vec{e}_0$	Journal reference eccentricity
$\vec{e}_i$	Journal segment eccentricity
$\vec{a}_i$	Sleeve segment center offset
$\vec{b}_i$	Journal segment center offset

---

[3] The offset bearing has multiple "segments", or rather, multiple connected journal bearings with offset center axes like shown in the sketch of Figure 1.2(a). Circumferential grooves between segments is a common feature.

where i is the i^{th} segment in the offset bearing. The parameter, δ in Figure 2.5 designates the total center-to-center distance of the bearing segments. In this thesis, the offset vector magnitudes are defined to be equal such that

$$|\vec{a}_i| = |\vec{b}_i| = \delta/2 \tag{2.20}$$

This constraint is common in practice and simplifies the span of the design space.

Figure 2.5 shows a two-segment offset bearing journal and sleeve with its respective reference frames and offsets. Figure 2.6(a) shows the journal in the sleeve with a reference position $\vec{e}_0$ from the journal to the sleeve references, and Figure 2.6(b) shows the full vector geometry for the two-segment offset bearing. Coordinate frame x, y is attached to the sleeve reference frame, aligned with the piston cylinder axis, and is thus aligned with the load block frame X_1, Y_1. Frame x', y' is the reference frame attached to the journal and aligned with the rod frame X_3, Y_3. Figure 2.7 generalizes the offset bearing geometry by showing the vector relationships for the i^{th} segment in an offset bearing with a fixed sleeve and rotating journal.

The eccentricity and offset vectors are related as follows:

$$\vec{e_i} = \vec{e_0} + \vec{b_i} - \vec{a_i} \tag{2.21}$$

Sleeve and journal offset vectors $\vec{a}_i$ and $\vec{b}_i$ are fixed in reference frames x, y and x', y', respectively. While reference eccentricity $\vec{e}_0$ is common to all segments, each $\vec{a}_i, \vec{b}_i$, and $\vec{e}_i$ are specific to the ith segment. Using angle ϕ between the sleeve and journal reference frames, the journal offset vector $\vec{b}$ with fixed components $b_i^{x'}, b_i^{y'}$ in the journal frame can be expressed in the sleeve frame as

$$\begin{Bmatrix} b_i^x \\ b_i^y \end{Bmatrix} = \begin{bmatrix} cos\phi & -sin\phi \\ sin\phi & cos\phi \end{bmatrix} \begin{Bmatrix} b_i^{x'} \\ b_i^{y'} \end{Bmatrix} \tag{2.22}$$

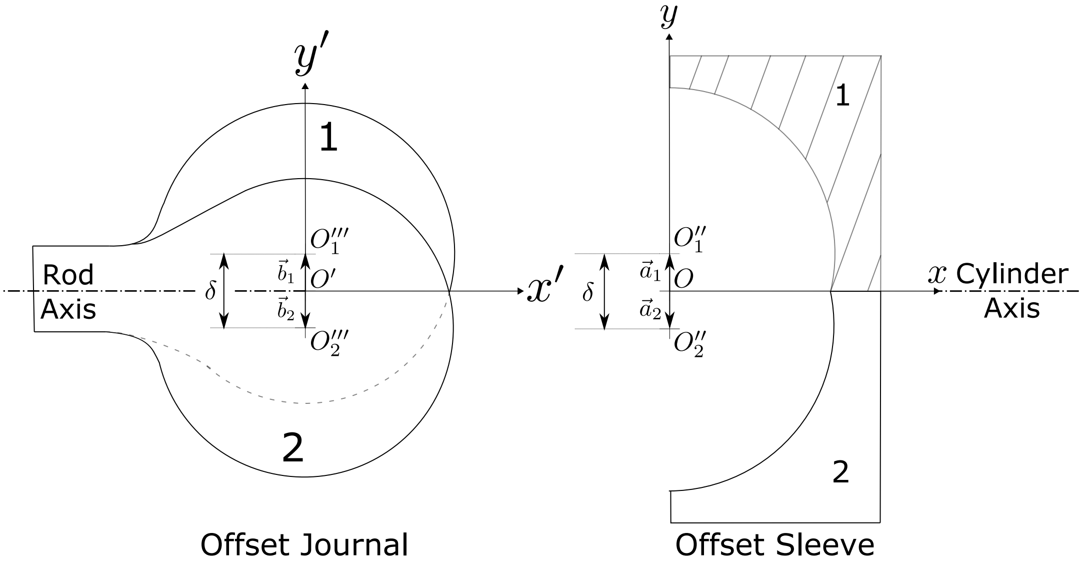

Offset Journal

Offset Sleeve

Figure 2.5: Offset Journal and Sleeve Split View

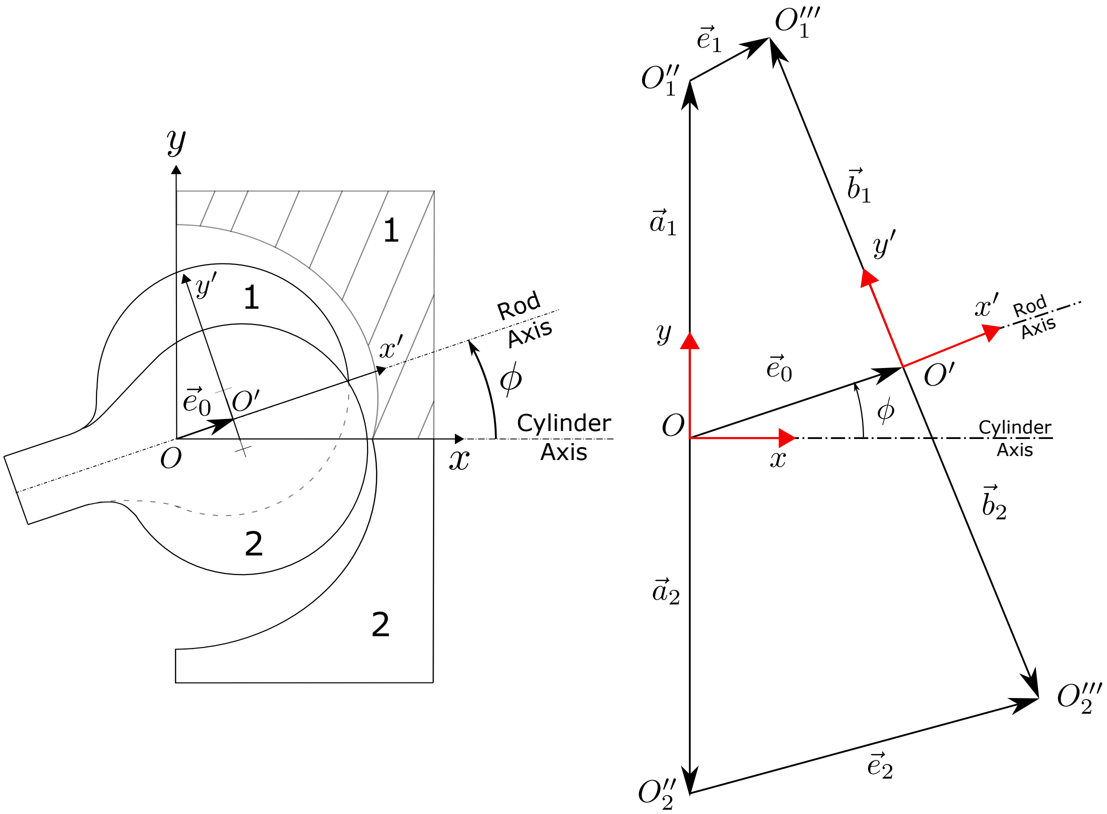

(a)

(b)

Figure 2.6: 2-Axis Offset Bearing Coordinates

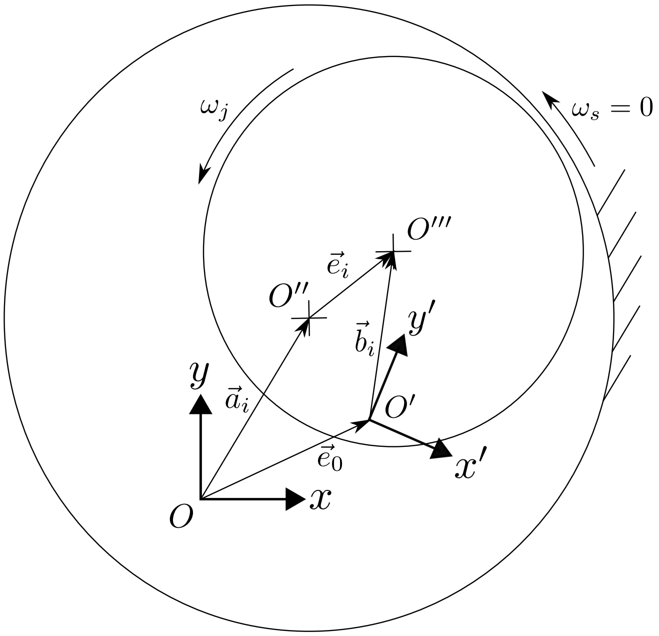

Figure 2.7: Geometry of Arbitrary Segment

which can be used to write equation (2.21) in sleeve frame component form

$$\begin{Bmatrix} e_i^x \\ e_i^y \end{Bmatrix} = \begin{Bmatrix} e_0^x \\ e_0^y \end{Bmatrix} + \begin{bmatrix} cos\phi & -sin\phi \\ sin\phi & cos\phi \end{bmatrix} \begin{Bmatrix} b_i^{x'} \\ b_i^{y'} \end{Bmatrix} - \begin{Bmatrix} a_i^x \\ a_i^y \end{Bmatrix} \tag{2.23}$$

Given reference eccentricity, offset information, and crank angle θ, equations (2.23), (2.5), and (2.6) are used to determine the individual segment eccentricities. Segment velocities, which are necessary for finding the segment loads, are found through the time derivative of equation (2.23):

$$\begin{Bmatrix} \dot{e}_i^x \\ \dot{e}_i^y \end{Bmatrix} = \begin{Bmatrix} \dot{e}_0^x \\ \dot{e}_0^y \end{Bmatrix} + \omega_j \begin{bmatrix} -sin\phi & -cos\phi \\ cos\phi & -sin\phi \end{bmatrix} \begin{Bmatrix} b_i^{x'} \\ b_i^{y'} \end{Bmatrix} \tag{2.24}$$

where $\omega_j = \dot{\phi}$ is the journal angular velocity from equation (2.7).

2.3.2 Determining Segment Loads

Given a conventional, single-center, ungrooved journal bearing[4] in an engine application, the film load is equal to the applied load directly; consequently, mobility methods developed by Booker [21] can be used to determine the journal center translational velocity. In the case of the offset journal bearing in an engine application, neither the segment velocities nor film loads are predetermined. The only load that is known is the **total** applied load. However, given some initial reference eccentricity and velocity the segment film loads can be determined using the following process:

1. "Guess" the journal initial reference velocity, $\dot{\vec{e}}_0$
2. Find individual segment eccentricities per equation (2.23)
3. Find individual segment velocities per equation (2.24)
4. Determine segment film loads via the impedance method [22]
5. Compare the applied load with the calculated total film load
6. Reiterate the above steps, modifying the reference velocity until the applied and film loads are balanced

The load balance is expressed with the system of nonlinear equations

$$F^x - \sum_{i=1}^{n} P_i^x(\dot{e}_0^x, \dot{e}_0^y) = 0 \tag{2.25a}$$

$$F^y - \sum_{i=1}^{n} P_i^y(\dot{e}_0^x, \dot{e}_0^y) = 0 \tag{2.25b}$$

---

[4] An "ungrooved" journal can be thought of as a smooth cylinder. A "grooved" journal is a cylinder with circumferential grooves that allow for oil flow and split the cylinder into multiple sections. Figure 1.5 shows a "grooved" bearing with the grooves between offset segments.

where n is the number of segments, $\vec{F}$ is the applied load[5], and $\vec{P_i}$ is the film load for the i-th segment. Applied load components F^x and F^y are determined from equation (2.19). Segment film loads are found using segment velocities with impedance methods described by [22]. A review of mobility and impedance methods along with a guide for their application has been recently published by Booker [23].

2.3.3 Bearing Performance Factors

Bearing performance factors, such as minimum film thickness and maximum film pressure, can be determined from segment eccentricities and film loads. The minimum film thickness in each segment given by

$$(h_{min})_i = 1 - |\vec{e_i}| \tag{2.26}$$

The maximum film pressure, p_{max} at any instant is found either analytically or through curve fits of maximum film pressure data, such as those found in [24] and [25]. Film pressure is determined through solution of the Reynolds Equation. “A ‘finite bearing’ (complete) solution satisfies the full Reynolds PDE.” As a result, finite bearing solutions are often complex and require curve fits for general solutions. “A ‘short bearing’ (approximate) solution satisfies a Reynolds PDE modified so as to neglect all circumferential flow in a nonrotating bearing” [23]. An analytical model for the pressure results from the approximate short bearing solution. Both short and finite bearing solutions are considered in this thesis.

2.4 Complete Solution Implementation

As discussed in subsection 2.3.2, an iterative process is required to determine the reference journal center velocity. A nonlinear solver can be used to modify the reference velocity until the roots of the nonlinear system in equation (2.25) are found. The program described below was written in MATLAB, and the nonlinear solver used was the function *fsolve* from

---

[5] Recall that reference frames X_1, Y_1 and x, y are aligned. Because of this, the applied engine load in the engine block frame is equal to the applied engine load in the bearing reference frame, $\vec{F}^{X_1,Y_1} = \vec{F}^{x,y}$.

MATLAB's optimization toolbox. All that is required for this program to be implemented is the engine duty (kinematics and loads), bearing geometry and properties, and initial reference eccentricity and velocity. Kinematics ϕ, ω_j, ω_s, and applied loads F^x, F^y are usually specified in tabulated form as functions of the crankshaft angle θ. The program process is summarized using the following loop:

Loop:

At crankshaft angle θ, proceed with the following steps:

Step 1: Determine segment eccentricities from $\vec{e}_0$

Step 2: Determine segment squeeze velocities from $\dot{\vec{e}}_0$

Step 3: Using the segment velocities and eccentricities from steps 1 and 2, the individual segment loads can be calculated from

$$\vec{P}_i = 2\mu L_i (R/C)^3 |V_i| \vec{W}_i \left(\vec{\epsilon}_i, \frac{B}{D}\right) \tag{2.27}$$

$$P^x = \sum_{i=1}^{n} P_i^x \tag{2.28}$$

$$P^y = \sum_{i=1}^{n} P_i^y \tag{2.29}$$

where

$$\vec{\epsilon}_i = \vec{e}_i / C \tag{2.30}$$

is the journal eccentricity ratio, and $\vec{W}_i$ is the impedance vector calculated using Childs [22] and Booker [23].

Step 4: Compare applied and film loads

$$Let\, x_1 = \frac{de_0^x}{dt} \tag{2.31}$$

$$Let\, x_2 = \frac{de_0^y}{dt} \tag{2.32}$$

$$f_1(x_1, x_2) = P^x(x_1, x_2) - F^x \tag{2.33}$$

$$f_2(x_1, x_2) = P^y(x_1, x_2) - F^y \tag{2.34}$$

and modify the reference velocity until a velocity $\dot{\vec{e}}_{0_{new}}$ is found such that $f_1 = f_2 = 0$. This is the instantaneous translational velocity of the journal bearing center resulting from the applied load.

Step 5: Update the Journal Motion

The reference eccentricity and velocity are then updated appropriately and simulation time advances by the specified time step. A time scale factor is used to convert from simulation time (ie: deg) to real time (sec). The updated reference eccentricity is found via Euler integration

$$\vec{e}_{0_{new}} = \vec{e}_0 + \frac{d\vec{e}_{0_{new}}}{dt} t_{step} t_{scale} \tag{2.35}$$

where t_{step} is the simulation time interval (deg), and the time scaling factor t_{scale} (specified in s/deg) is found from

$$t_{scale} = \frac{\pi}{180\omega} \tag{2.36}$$

where ω is crankshaft angular velocity in rad/s. The updated reference velocity becomes the initial "guess" for the *fsolve* function at the next time step.

End Loop

The loop described above is continued until some user specified time, t_{final}, or until periodicity over the engine duty cycle is achieved. Single-center, conventional bearings often take a long time to achieve periodic solutions (hundreds of engine cycles), while offset bearings often show converged journal motion relatively quickly (less than twenty engine cycles). Figure 2.8 uses a flow chart to describe the program structure. The "bearing model" subprogram block in Figure 2.8 is detailed in another flow chart in Figure 2.9.

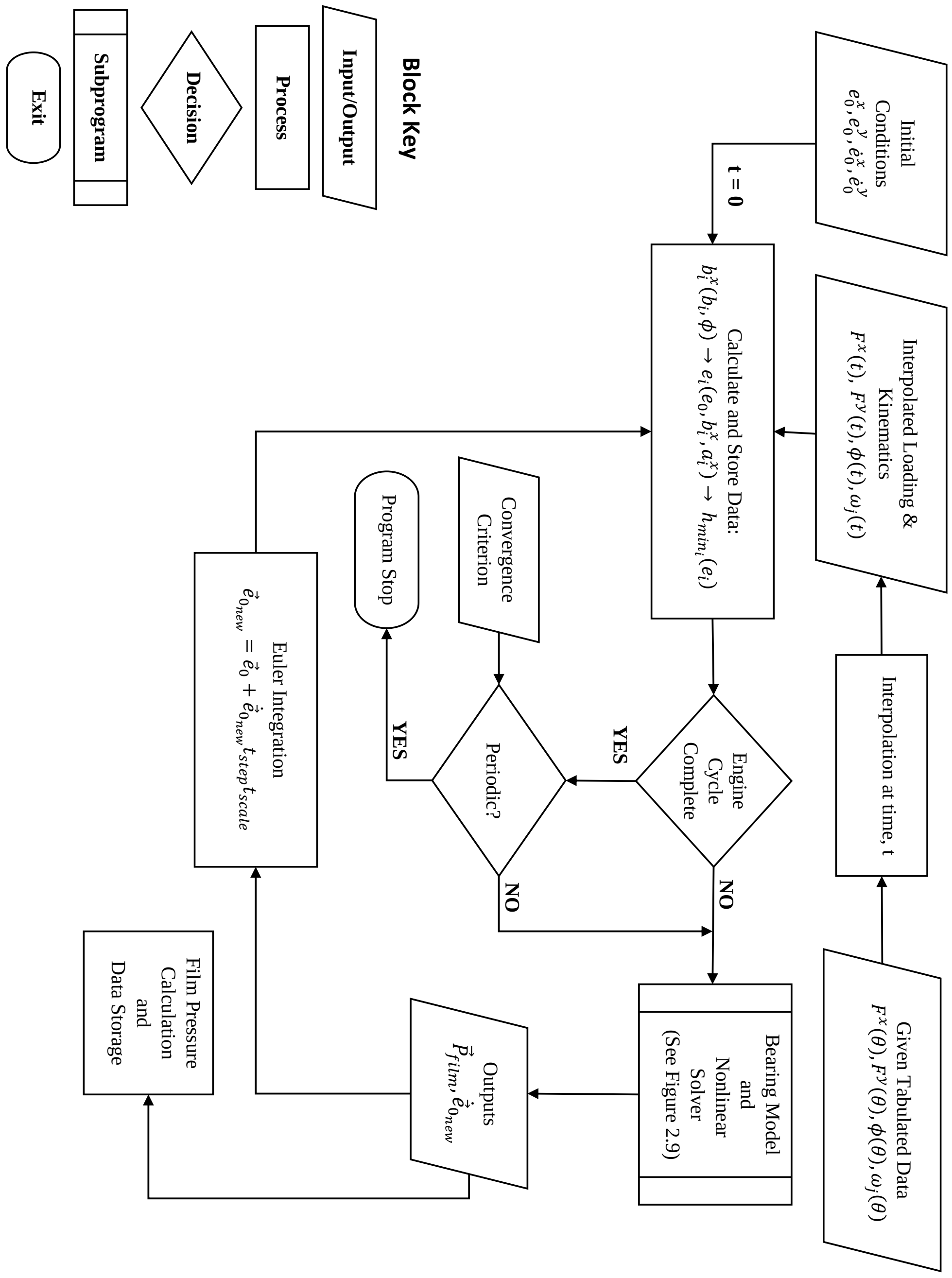

Figure 2.8: Top Level Program Structure

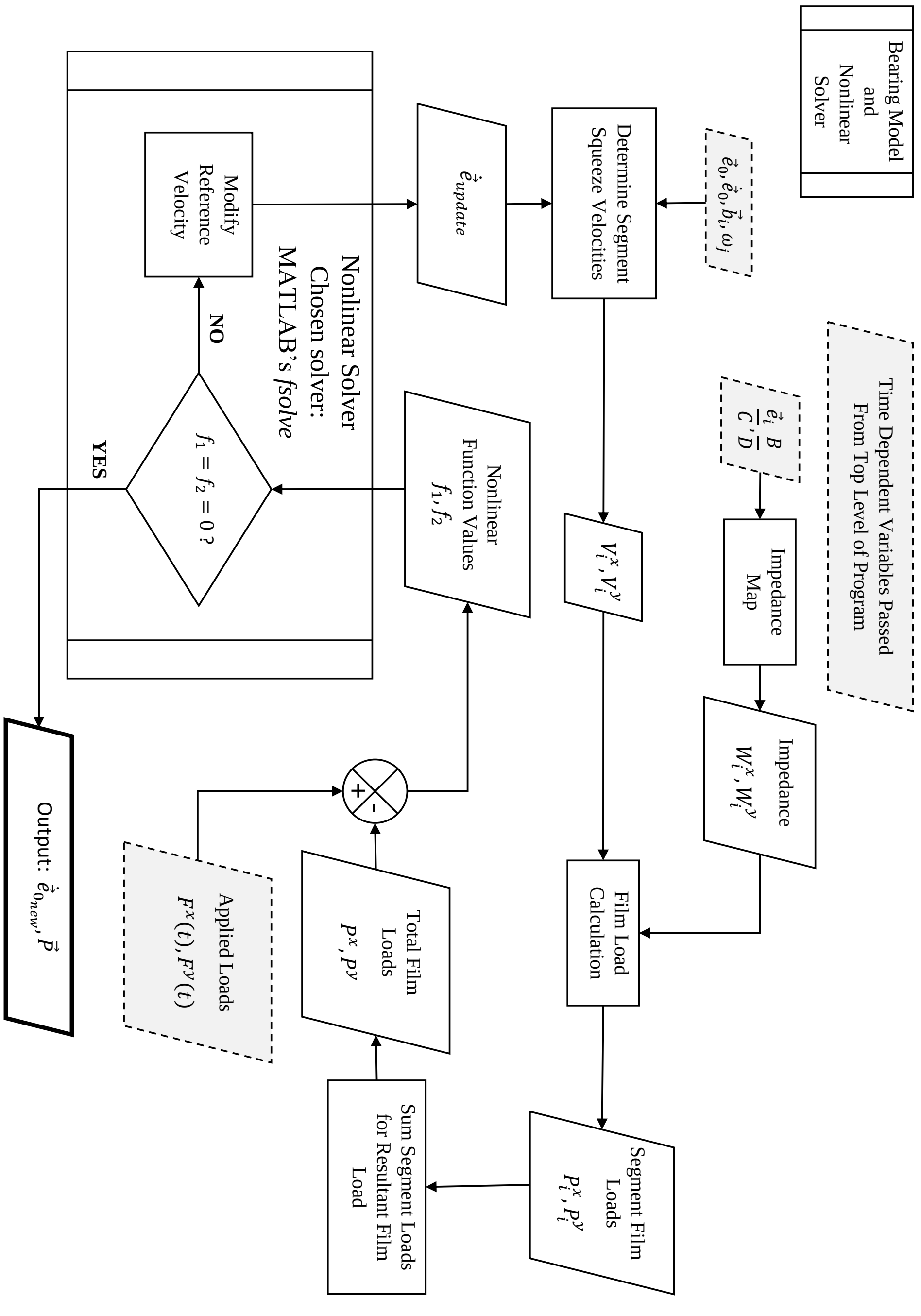

Figure 2.9: Iterative Solver

Chapter 3

Dimensional Example

3.1 Two-Stroke Engine Example

The following example is taken from Booker *et al.* [9]. Table 3.1 contains engine specifications which have been taken from Table C1 in [9]. As indicated in the source paper, the data is representative of a GM Detroit Diesel Allison division turbocharged series 149 two-stroke engine. Figure 3.1 shows a plot of typical cylinder gage pressure vs crank rotation for the DD149 engine as taken from [9][1].

Table 3.1: GM Detroit Diesel Series 149 Engine Data

Parameter		Units	Value
Piston Mass	M_p	(kg)	4.68
Connrod Small End Mass	M_s	(kg)	6.16
Crank Radius	r	(m)	0.073
Connrod Length	L	(m)	0.305
Cylinder x-section Area	A_{cyl}	(m^2)	0.0167
Peak Cylinder Pressure	p^*_{cyl}	(Pa)	12.1×10^6
Crank Angular Speed	ω	(rpm)	1900

Using the pressure profile and the data from Table 3.1, the engine duty (rod angle ϕ, and piston pin loads F^{X_1} and F^{Y_1}) was determined per section 2.2.2 and plotted in Figure 3.2. It is worth noting that the (sidewall) loading in the Y_1-direction is very small relative to the

---

[1] The cylinder pressure plot as provided in [9] contains an error in the y-axis label, but it has been corrected and redrawn in Figure 3.1.

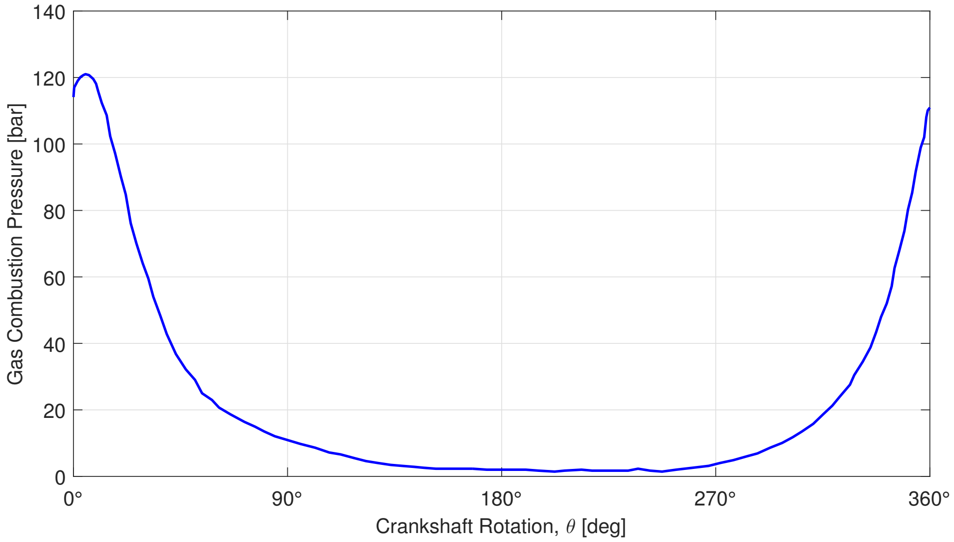

Figure 3.1: Two-Stroke Engine (DD149) Cylinder Gas Pressure

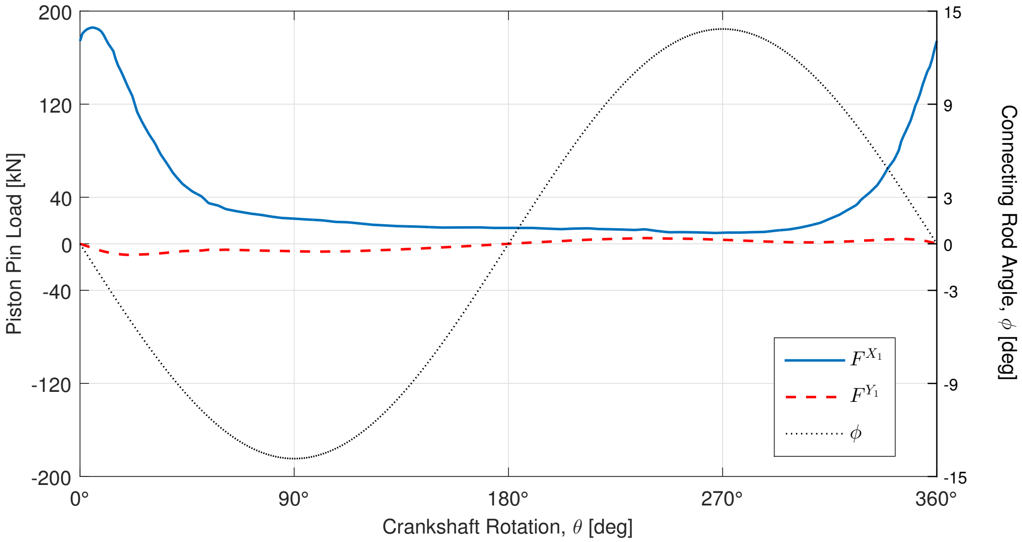

Figure 3.2: Connecting Rod Small End Loads and Kinematics

loading in the X_1-direction. This observation is revisited later in this chapter to determine the significance of the sidewall loading on the piston with respect to bearing performance.

Multiple configurations of the piston pin bearing are analyzed to determine their impact on performance. These configurations include both grooved and ungrooved conventional (aligned, single-center) bearings[2], and a dual-center, 3-segment offset bearing. The grooved conventional bearing consists of three axially-aligned segments with circumferential grooves separating them. The bearing specifications are summarized in Table 3.2. A short bearing solution is used for the conventional bearing. The offset bearing is represented by both short and finite bearing lubrication models[3]. The finite bearing solution for the conventional bearing has been excluded due to potential model invalidity resulting from very high eccentricity ratios.

All bearings are studied with a full sleeve as opposed to the partial-arc bearings employed in the example calculation by Booker *et al.* The results of Booker *et al.* are included in each figure for comparison. The results of Booker *et al.* were also calculated using a short bearing theory, but simulations were done using finite difference methods to account for the partial arc of the sleeve. Table 3.3 provides a summary of bearing performance results.

Table 3.2: Bearing Design Data

Parameter		Units	Ungrooved Single-Axis Bearing	Grooved Single-Axis Bearing	Two-Axis Offset Bearing
Viscosity	μ	$[Pa \cdot s]$	0.00965	0.00965	0.00965
Radial Clearance	C	$[\mu m]$	30	30	30
Segment Diameter	D	$[m]$	0.0610	0.0610	0.0610
Number of Segments	n	$[-]$	1	3	3
Segment Length	B	$[m]$	0.0915	0.0305	0.0305
Total Offset	δ	$[\mu m]$	0	0	120

---

[2] See foonote 4 in Section 2.3.2 for “grooved” and “ungrooved” definitions

[3] See Section 2.3.3 for explanations of “short” and “finite” bearing models

Figures 3.3 and 3.4 show periodic time histories of minimum film thickness and maximum pressure, respectively, for a conventional bearing with and without grooves. The minimum film thickness is relatively very thin and does not fluctuate very much over the engine cycle. Even the cyclic maximum value of the minimum film thickness for the grooved bearing is, at most, 1.86% of the radial clearance in the bearing. Peak film pressures are over 33 times the peak cylinder pressure of 12.1 MPa.

Two parameters in Table 3.2 are critical for the offset bearing. Parameter δ is representative of the center-to-center distance between the sleeve and journal segments, and n specifies the number of segments. The offset vectors for bearing and sleeve introduced in section 2.3.1 are defined using δ as follows:

$$a^x = \begin{bmatrix} 0 & 0 & 0 \end{bmatrix} \tag{3.1}$$

$$a^y = \begin{bmatrix} \frac{\delta}{2} & -\frac{\delta}{2} & \frac{\delta}{2} \end{bmatrix} \tag{3.2}$$

$$b^{x'} = \begin{bmatrix} 0 & 0 & 0 \end{bmatrix} \tag{3.3}$$

$$b^{y'} = \begin{bmatrix} \frac{\delta}{2} & -\frac{\delta}{2} & \frac{\delta}{2} \end{bmatrix} \tag{3.4}$$

where each array element represents the offset components for each segment. See Figures 2.5, 2.6, and 2.7 for diagrams showing how these offset components are defined in the offset bearing.

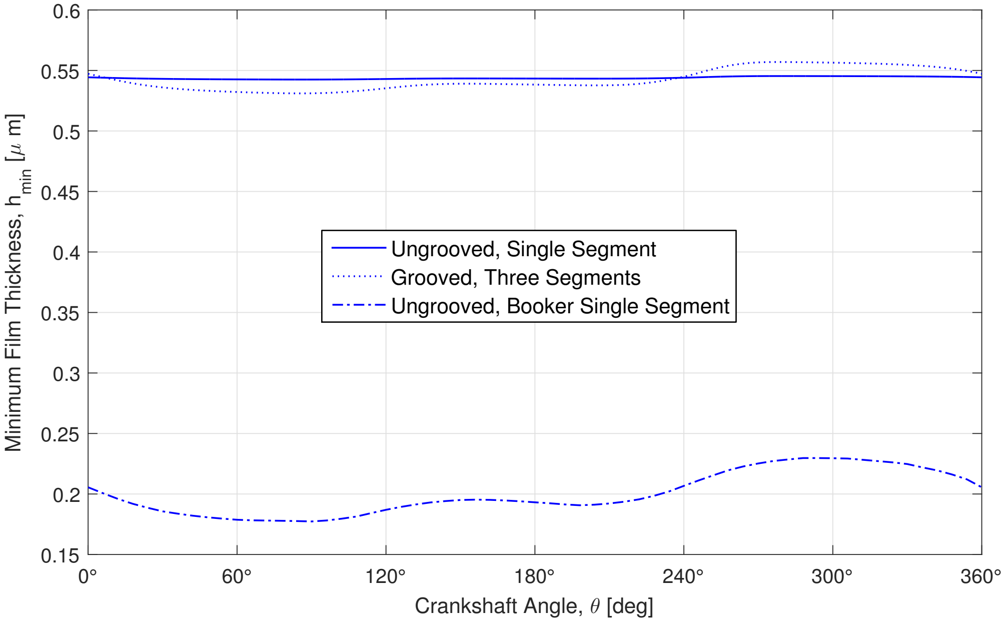

Figure 3.3: Minimum Film Thickness: Conventional Bearing

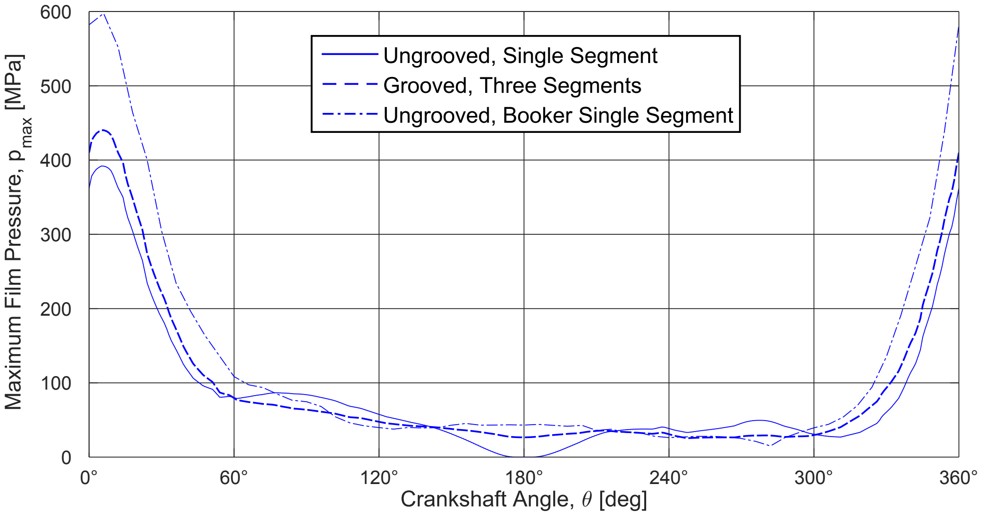

Figure 3.4: Maximum Film Pressure: Conventional Bearing

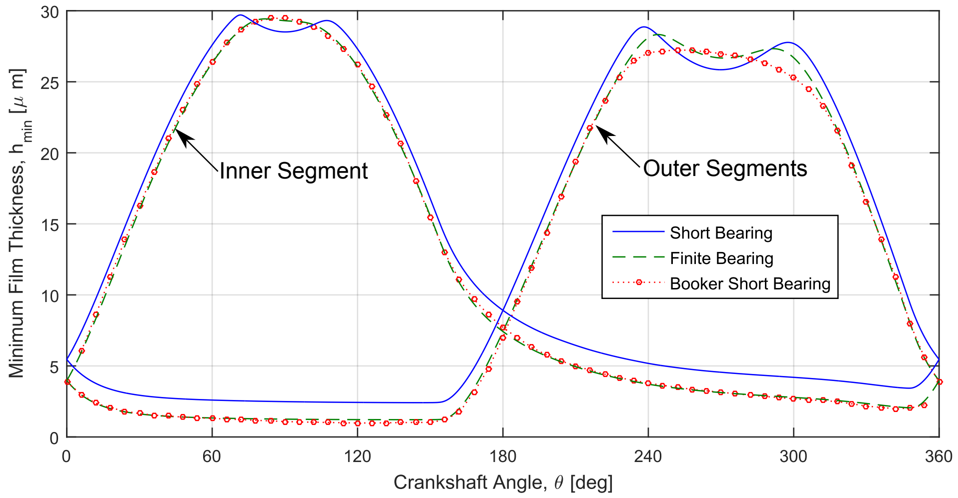

Figure 3.5: Minimum Film Thickness: Offset Bearing

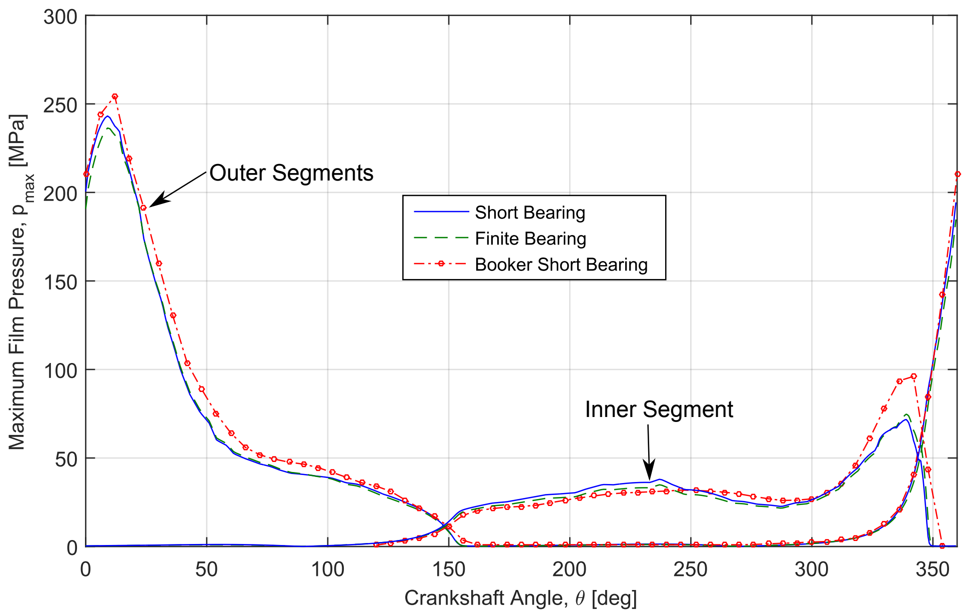

Figure 3.6: Maximum Film Pressure: Offset Bearing

Figures 3.5 and 3.6 show periodic time histories of minimum film thickness and maximum pressure, respectively, for inner and outer segments of the offset bearing. Although it is not an extreme difference, the outer segments tend to bear more of the load in this equal length segment configuration. In regard to the models, the finite bearing model predicts slightly thinner films and slightly lower pressures as compared to the short bearing model. For both film models and for all segments, the cyclic maximum value of minimum film thickness is very thick, approaching the radial clearance in the bearing. The thinnest film predicted by the finite bearing model on the outer segments is 4.06% of the radial clearance in the bearing. This, while still a relatively thin film, is over twice the cyclic minimum film thickness predicted for the conventional bearing.

Table 3.3: Summary of Bearing Performance Results

Bearing Geometry	Film Model	Segments	h_{min} [µm]	p_{max}, $[MPa]$
Conventional, Ungrooved, Full	Short	-	0.5424	392.0
Conventional, Grooved, Full	Short	-	0.5311	440.3
Booker *et al.*[9], Conventional, Ungrooved, Partial Arc	Short	-	0.1770	606.0
Offset, 2 Axes, 3 Segments, Full	Short	Outer	2.4147	243.2
		Inner	3.4338	71.7
Offset, 2 Axes, 3 Segments, Full	Finite	Outer	1.2166	236.4
		Inner	2.0538	74.7
Booker *et al.*[9], Offset, 2 Axes, 3 Segments, Partial Arc	Short	Outer	0.9844	254.4
		Inner	1.9890	96.1

One of the biggest improvements, however, is not in the development of the thicker film, but the fact that the films are only thin on any segment for less than 180°of crankshaft rotation. Slightly before the piston is at bottom dead center (180°) the load is transferred from the outer segments to the inner segment. This explicitly shows the advantage of the offset bearing: the load alternates between segments, providing the opportunity for the film lubricant to be replenished periodically.

The cyclic maximum film pressures also show significant improvement. The higher of the two film pressures, corresponding to the short bearing model, is only approximately 20 times the peak cylinder gas pressure. Compared to the conventional bearing, this is nearly a 50% improvement in peak film pressure.

Another advantage to the offset bearing problems is simply computation time. The conventional bearing was simulated for hundreds of cycles before periodicity was achieved, while the offset bearing produced periodic results in less than 20 cycles.

One clear difference between the results of Booker *et al.* and the present study is that the film thickness predicted by Booker *et al.* are even smaller and the film pressures are slightly higher. This is expected due to increased side leakage associated with the partial arc bearing. The partial bearing used for both the conventional and offset configurations used all of the same parameters found in Table 3.2, but the sleeve had a total wrap angle of only 150°.

The loading in the X_1-direction[4]: is, as shown in Figure 3.2, always positive and is the dominant load component. The load in the Y_1-direction[5] does reverse direction, but the load magnitude is always relatively small. Because the resultant load does not reverse direction, a partial bearing is a reasonable design option for this engine configuration. This observation will be revisited in evaluating parametric design trends in the following chapter.

---

[4] Recall from Section 2.3.1 that the engine coordinate frame X_1, Y_1 is aligned along the x-axis with the bearing coordinate frame x, y.

[5] See footnote 4 above

3.2 Effect of Neglecting Sidewall Loading on the Piston

It was noted in the prior section that the sidewall loading on the piston was significantly lower than the loading along the axis of engine cylinder. This introduces the question of whether the sidewall loading has any significant impact on the performance of the connecting rod small-end bearing. If the sidewall loading can be neglected, the design study can be simplified in foregoing sections. This is tested for the engine in the previous section by setting $F^{Y_1} = 0$ in the engine duty. Simulations for the offset bearing were re-run for both finite and short bearing film models. Figures 3.7, 3.8, 3.9, and 3.10 show how performance factors h_{min} and p_{max} vary when $F^{Y_1} = 0$.

For both short and finite bearings there is no significant change in the results. Deviations between the two sets of data do not occur at performance-limiting points. When the sidewall loading is neglected the peak film thickness on the inner segment increases, but the minimum film thickness does not appear to change at all. This observation is also revisited in a parametric study in the following chapter.

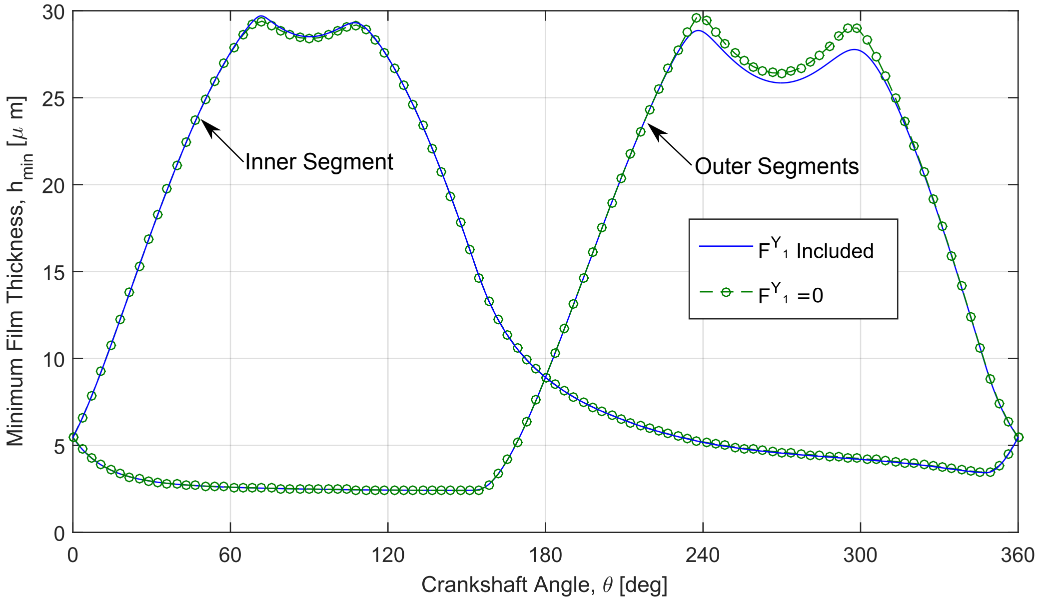

Figure 3.7: Short Bearing Film Thickness Comparison With and Without F^{Y_1}

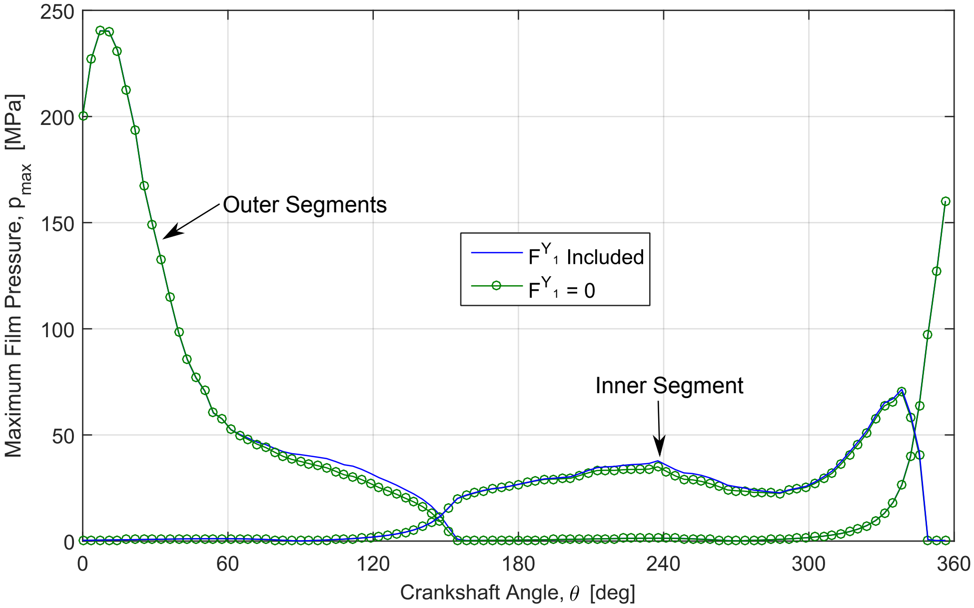

Figure 3.8: Short Bearing Pressure Comparison With and Without F^{Y_1}

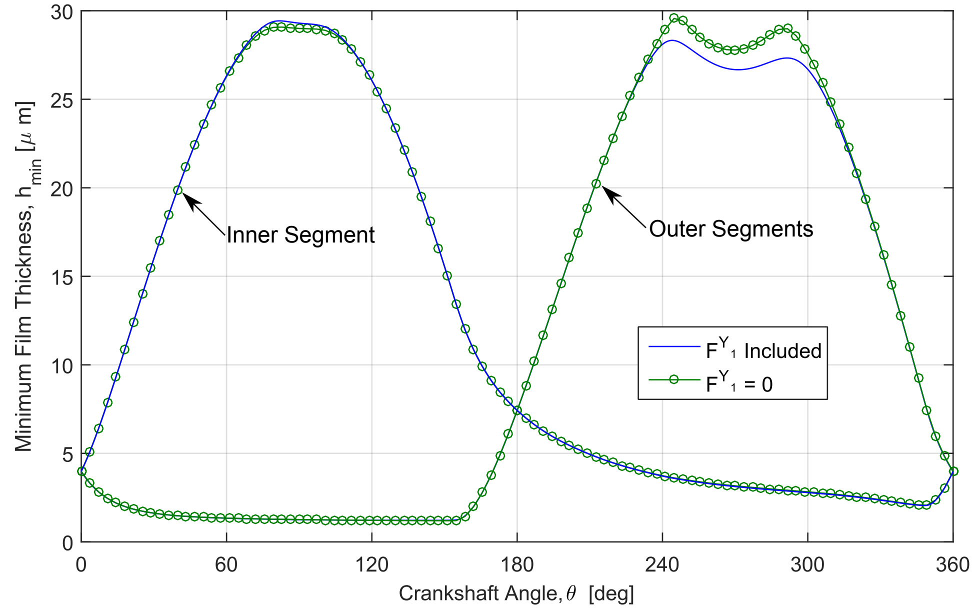

Figure 3.9: Finite Bearing Film Thickness Comparison With and Without F^{Y_1}

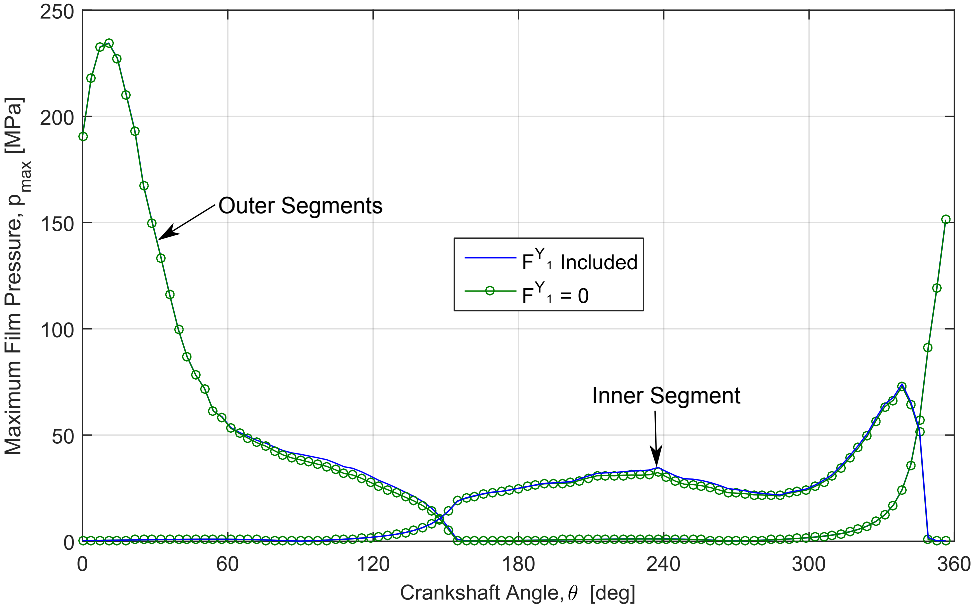

Figure 3.10: Finite Bearing Pressure Comparison With and Without F^{Y_1}

Chapter 4

Nondimensional Formulation

In order to develop generic design charts for this thesis, a design space needs to be determined. First, this chapter looks at both engine and bearing loads to determine appropriate nondimensional parameters. Second, engine data is presented to determine practical ranges of the nondimensional parameters. Third, assumptions regarding the problem solution are revisited using the practical limits of the design space. Finally some additional design parameters are introduced and discussed.

4.1 Load Nondimensionalization

To nondimensionalize bearing loads it is appropriate to use a scale that is explicitly defined throughout the engine cycle. One such scale is the peak cylinder gas force, $p^*_{cyl}A_{cyl}$. Piston pin loads, as shown by equation (2.19), depend on the cylinder gas force as a function of crankshaft angle, θ. This load can be expressed as

$$p_{cyl}(\theta)A_{cyl} = \left[p^*_{cyl}f(\theta)\right]A_{cyl} \tag{4.1}$$

where $f(\theta)$ is the normalized cylinder pressure profile which varies from 0 to 1. To the extent of the literature review it seems that the normalized cylinder pressure profile is quite similar for two-stroke diesel engines[1]. Based on this assumption, the cylinder pressure

---

[1] See pressure data provided by ERPI [26], Wakuri [10] and Booker *et al.* [9]

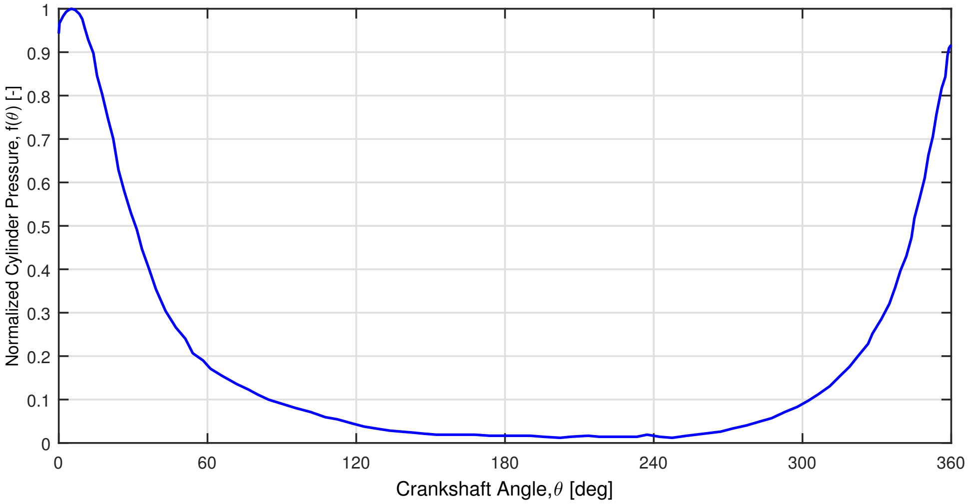

Figure 4.1: Normalized Pressure Curve for a Two-Stroke Diesel Engine

data from Booker *et al.* [9] has been scaled by the peak cylinder pressure in the paper to provide the normalized profile, $f(\theta)$, for use in this thesis. Figure 4.1 shows this normalized cylinder pressure profile.

In addition to cylinder pressure history, the piston pin loads are dependent on the following engine parameters: $M_s,\ M_p,\ r,\ L,\ \omega$. Division of equation (2.19) by $p^*_{cyl}A_{cyl}$ and rearrangement/grouping of terms results in the following expressions for nondimensional piston pin load components:

$$\begin{aligned}\frac{F^{X1}(\theta)}{p^*_{cyl}A_{cyl}} &= f(\theta)\\ &\quad-\left(\frac{M_pr\omega^2}{p^*_{cyl}A_{cyl}}\right)cos\theta\\ &\quad-\left(\frac{M_pr\omega^2}{p^*_{cyl}A_{cyl}}\right)\sin\theta tan\phi\\ &\quad-\left(\frac{M_pr\omega^2}{p^*_{cyl}A_{cyl}}\right)\left(\frac{r}{L}\right)\frac{cos^2\theta}{cos\phi}\\ &\quad-\left(\frac{M_pr\omega^2}{p^*_{cyl}A_{cyl}}\right)\left(\frac{r}{L}\right)\frac{tan^2\phi cos^2\theta}{cos\phi}\end{aligned} \tag{4.2a}$$

$$\begin{aligned}\frac{F^{Y1}}{p^*_{cyl}A_{cyl}} = \frac{F^{X1}}{p^*_{cyl}A_{cyl}}&tan\phi \\ &- \left(\frac{M_s}{M_p}\right)\left(\frac{M_p r\omega^2}{p^*_{cyl}A_{cyl}}\right)cos\theta tan\phi \\ &+ \left(\frac{M_s}{M_p}\right)\left(\frac{M_p r\omega^2}{p^*_{cyl}A_{cyl}}\right)sin\theta tan^2\phi \\ &+ \left(\frac{M_s}{M_p}\right)\left(\frac{M_p r\omega^2}{p^*_{cyl}A_{cyl}}\right)\left(\frac{r}{L}\right)\left(\frac{cos^2\theta}{cos\phi}\right)tan\phi \\ &+ \left(\frac{M_s}{M_p}\right)\left(\frac{M_p r\omega^2}{p^*_{cyl}A_{cyl}}\right)\left(\frac{r}{L}\right)\left(\frac{cos^2\theta}{cos\phi}\right)tan^3\phi\end{aligned} \tag{4.2b}$$

Observation of equations (4.2) makes it clear that the nondimensional pin loads are dependent on three different nondimensional terms, defined by the engine parameters and normalized cylinder pressure profile. These nondimensional terms are labeled and summarized in Table 4.1.

Table 4.1: Nondimensional Engine Load Factors

	$\frac{F^{X1}(\theta)}{p^*_{cyl}A_{cyl}}$	$\frac{F^{Y1}(\theta)}{p^*_{cyl}A_{cyl}}$
Normalized Pressure Curve	$f(\theta)$	$f(\theta)$
Ratio of Crank Radius to Conn. Rod Length	$\frac{r}{L}$	$\frac{r}{L}$
Ratio of Piston Inertial Load term to Peak Gas Load	$\frac{M_p r\omega^2}{p^*_{cyl}A_{cyl}}$	$\frac{M_p r\omega^2}{p^*_{cyl}A_{cyl}}$
Conn. Rod Small End to Piston Mass Ratio	-	$\frac{M_s}{M_p}$

The film load is also nondimensionalized using the peak cylinder force. At any instant in the engine cycle, the total film load $\vec{P}$ is a sum of the segment loads

$$\vec{P} = \sum_{i=1}^{N} \vec{P}_i \tag{4.3}$$

where the segment loads are defined by

$$\vec{P}_i = 2\mu B(R/C)^3|\vec{V}_i|\vec{W}_i(\vec{\epsilon}_i, B/D) \tag{4.4}$$

with $\vec{V}_i$ as the instantaneous squeeze velocity, and $\vec{W}_i$ as the dimensionless impedance.

Scaling the segment film load by the peak cylinder load gives

$$\frac{\vec{P}_i}{p^*_{cyl}A_{cyl}} = \frac{2\mu B(R/C)^3|\vec{V}_i|}{p^*_{cyl}A_{cyl}}\vec{W}_i(\vec{\epsilon}_i, B/D) \tag{4.5}$$

where all but the squeeze velocity magnitude and impedance are constants.

Assuming the bearing sleeve has zero angular velocity ($\omega_s = 0$), the magnitude of the squeeze velocity is defined as

$$|\vec{V}_i| = \left|\dot{\vec{e}}_i - \frac{1}{2}\omega_j\hat{k} \times \vec{e}_i\right| \tag{4.6}$$

where eccentricity position and velocity are given by equations (2.23) and (2.24), and ω_j is the journal angular velocity. Segment eccentricity is conventionally scaled by the radial clearance, resulting in an eccentricity ratio, $\vec{\epsilon}_i = \vec{e}_i/C$. Dividing equation (2.23) by the radial clearance results in the dimensionless relationship

$$\begin{Bmatrix} \epsilon^x_i \\ \epsilon^y_i \end{Bmatrix} = \begin{Bmatrix} \epsilon^x_0 \\ \epsilon^y_0 \end{Bmatrix} + \begin{bmatrix} cos\phi & -sin\phi \\ sin\phi & cos\phi \end{bmatrix} \begin{Bmatrix} \frac{b^{x'}_i}{C} \\ \frac{b^{y'}_i}{C} \end{Bmatrix} - \begin{Bmatrix} \frac{a^x_i}{C} \\ \frac{a^y_i}{C} \end{Bmatrix} \tag{4.7}$$

If journal and sleeve offset magnitudes $|\vec{b}|$ and $|\vec{a}|$, respectively, are equal for each segment in a two-axis system, then they can be related by a single offset factor

$$\delta = 2|\vec{b}| = 2|\vec{a}| \tag{4.8}$$

which represents the total center-to-center distance for both journal and sleeve segments. It follows that the segment eccentricity ratio components depend on the offset ratio $\frac{\delta}{C}$ as given by

$$\begin{Bmatrix} \epsilon^x_i \\ \epsilon^y_i \end{Bmatrix} = \begin{Bmatrix} \epsilon^x_0 \\ \epsilon^y_0 \end{Bmatrix} + \begin{bmatrix} cos\phi & -sin\phi \\ sin\phi & cos\phi \end{bmatrix} \begin{Bmatrix} \frac{\delta}{2C} \\ \frac{\delta}{2C} \end{Bmatrix} - \begin{Bmatrix} \frac{\delta}{2C} \\ \frac{\delta}{2C} \end{Bmatrix} \tag{4.9}$$

Taking the time derivative of eccentricity ratio equation (4.7) gives the eccentricity rate equation

$$\begin{Bmatrix} \dot{\epsilon}_i^x \\ \dot{\epsilon}_i^y \end{Bmatrix} = \begin{Bmatrix} \dot{\epsilon}_0^x \\ \dot{\epsilon}_0^y \end{Bmatrix} + \omega_j \begin{bmatrix} -sin\phi & -cos\phi \\ cos\phi & -sin\phi \end{bmatrix} \begin{Bmatrix} \frac{\delta}{2C} \\ \frac{\delta}{2C} \end{Bmatrix} \tag{4.10}$$

The only dimensional parameter left between equations (4.9) and (4.10) is the journal angular velocity, $\omega_j = \frac{d\phi}{dt}$. Introducing nondimensional time,

$$\tau \equiv \theta = \omega t \tag{4.11}$$

where θ is the crankshaft angle, equation (4.10) is rewritten as

$$\begin{Bmatrix} \frac{d\epsilon_i^x}{d\tau} \\ \frac{d\epsilon_i^y}{d\tau} \end{Bmatrix} = \begin{Bmatrix} \frac{d\epsilon_0^x}{d\tau} \\ \frac{d\epsilon_0^y}{d\tau} \end{Bmatrix} + \frac{d\phi}{d\tau} \begin{bmatrix} -sin\phi & -cos\phi \\ cos\phi & -sin\phi \end{bmatrix} \begin{Bmatrix} \frac{\delta}{2C} \\ \frac{\delta}{2C} \end{Bmatrix} \tag{4.12}$$

Equations (4.9) and (4.12) can be substituted into equation (4.6), which gives

$$|\vec{V}_i| = \omega C \left(\frac{d\vec{\epsilon}_0}{d\tau} - \frac{1}{2}\frac{d\phi}{d\tau}\hat{k} \times \vec{\epsilon}_i \right) \tag{4.13}$$

which in turn is substituted into the nondimensional segment load equation (4.5), resulting in

$$\frac{\vec{P}_i}{p^*_{cyl}A_{cyl}} = \frac{\mu\omega BD(R/C)^2}{p^*_{cyl}A_{cyl}} \left(\frac{d\vec{\epsilon}_0}{d\tau} - \frac{1}{2}\frac{d\phi}{d\tau}\hat{k} \times \vec{\epsilon}_i \right) \vec{W}_i(\vec{\epsilon}_i, B/D) \tag{4.14}$$

Through the above study of the film load and squeeze velocity, the film load, and consequently the bearing motion $\epsilon_0(\tau)$, is shown to be dependent on four dimensionless parameters. These parameters are defined and summarized in Table 4.2. The segment load number in Table 4.2 is directly applicable to a bearing modeled with a finite bearing film model. This segment load number is modified in the case of a short bearing film. The Ocvirk short bearing impedance can be calculated for any B/D aspect ratio based on the short bearing

Table 4.2: Nondimensional Bearing Load Parameters

Number of Segments	n
Offset Ratio	$\frac{\delta}{C}$
Segment Load Number	$\frac{\left(p^*_{cyl}A_{cyl}\right)(C/R)^2}{\mu\omega BD}$
Segment Aspect Ratio	$\frac{B}{D}$

impedance map for $B/D = 1$ with the following relationship [21][23]:

$$\vec{W}\left(\vec{\epsilon}, \frac{B}{D}\right) = \vec{W}(\vec{\epsilon}, B/D = 1)\left(\frac{B}{D}\right)^2 \tag{4.15}$$

Substituting equation (4.15) into (4.14) gives

$$\text{Segment Load Number (Short Bearing)} = \frac{\left(p^*_{cyl}A_{cyl}\right)(C/R)^2}{\mu\omega BD}\left(\frac{D}{B}\right)^2 \tag{4.16}$$

and thus the set of non-dimensional parameters in Table 4.2 does not explicitly depend on the bearing aspect ratio B/D. Using the form of the load number in equation (4.16), short bearing data need only be generated for $B/D = 1$ in order to be applied generally to any aspect ratio.

It is only appropriate that the bearing performance factors for film thickness and film pressure also be presented in some nondimensional form. Like the eccentricity, the minimum film thickness can be scaled by the radial clearance. For consistency, the nondimensionalization of peak film pressure is done using the peak cylinder pressure and the projected journal segment area BD. These nondimensional performance factors are summarized in Table 4.3.

Table 4.3: Nondimensional Bearing Related Performance Factors

Minimum Film Ratio	$\frac{h_{min}}{C}$
Maximum Pressure Ratio	$\frac{p_{max}BD}{p^*_{cyl}A_{cyl}}$

4.2 The Design Space

Production engine data was acquired from several sources so that practical ranges of the nondimensional parameters can be chosen. The sources used include Booker *et al.* [9], ERPI [26], Government of India Ministry of Railways [27], and Magazinoviȁ [28]. The data acquired encompasses small, medium, and heavy duty diesel engines. The data for different engines are shown in Table 4.4.

Table 4.4: Nondimensional Load Factors Based on Production Engine Data

Engine	$\frac{M_p r\omega^2}{p^*_{cyl} A_{cyl}}$	$\frac{r}{L}$	$\frac{M_s}{M_p}$
Undisclosed	N.A.	0.2626	N.A.
Undisclosed	N.A.	0.2093	N.A.
Detroit Diesel 149 Series	0.0668	0.2393	1.3162
Undisclosed	0.0736	0.2500	1.2859
Undisclosed	0.0753	0.2471	1.2282
Electromotive Diesel 645	0.0919	0.2174	0.2919
Electromotive Diesel 710	0.1156	0.2391	0.2545

All engine data appear to have similar r/L ratios, with mass and load ratios split into two primary groups. The following ranges of nondimensional engine parameters were selected based on Table 4.4:

$$0.05 \leq \frac{M_p r\omega^2}{p^*_{cyl} A_{cyl}} \leq 0.15 \tag{4.17}$$

$$0.20 \leq \frac{r}{L} \leq 0.30 \tag{4.18}$$

$$0.25 \leq \frac{M_s}{M_p} \leq 1.5 \tag{4.19}$$

Ranges such as above must also be found for the offset bearing nondimensional parameters in Table 4.2. For the full offset bearing the best case scenario of kinematic limit can be found by setting the reference eccentricity, $\vec{e}_0 = \vec{0}$. The limit, derived from equation

(2.21), is expressed by the following relationship:

$$\frac{\delta}{C} < \frac{1}{sin(\phi/2)} \; for \; \vec{e}_0 = 0 \tag{4.20}$$

The rod angle, ϕ, is limited by the ratio r/L. Using equation (2.5) and equation (4.20) with $0 < r/L < 1$, an upper limit on δ/C can be found for any value of r/L.

Figure 4.2 provides a convenient way for a designer to determine the kinematic limit for δ/C at $\vec{e}_0 = 0$ based on the ratio r/L or maximum rod angle, ϕ_{max}. Using this figure with the limits on r/L in equation (4.18) results in the following upper limits for the full offset bearing:

$$\left(\frac{\delta}{C}\right)_{max} = 9.5 \; at \; \frac{r}{L} = 0.2 \tag{4.21a}$$

$$\left(\frac{\delta}{C}\right)_{max} = 6.6 \; at \; \frac{r}{L} = 0.3 \tag{4.21b}$$

Based on equation (4.21) a peak design value of $(\delta/C)_{max} = 6.5$ was chosen.

As in the literature, only 2 and 3 segment designs are considered. The combination of multiple segments in an offset bearing generally means that, for realistic engine applications, each individual segment will have a relatively small aspect ratio (B/D). Because of this, aspect ratios are chosen[2] so that $B/D \leq 1$.

Little data was found regarding the range of the segment load number. The segment load number calculated for the DD149 engine piston pin bearing described in Booker *et al.* (see Chapter 3) was 54.73 for a finite bearing model and 218.91 for a short bearing model. The range for the segment load number was chosen to be rather large to be as inclusive as possible given the lack of additional data.

---

[2] This is useful also because both short and finite bearing models used are generally applicable for $B/D \leq 1$

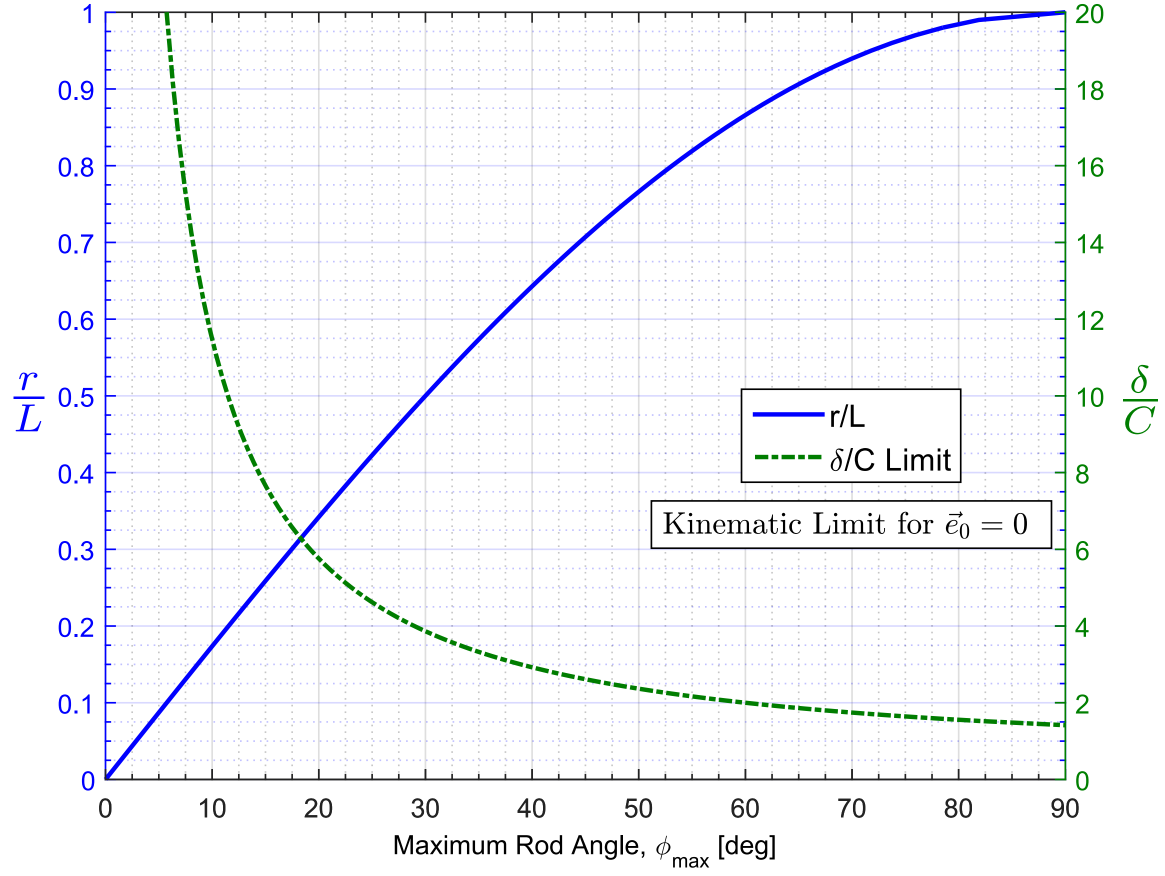

Figure 4.2: Kinematic Limit: Full Offset Bearing

Ranges for offset bearing nondimensional parameters are summarized in the equations below.

$$n = 2, 3 \tag{4.22}$$

$$0 \leq \frac{\delta}{C} \leq 6 \tag{4.23}$$

$$10 \leq \frac{\left(p^*_{cyl} A_{cyl}\right)(C/R)^2}{\mu \omega B D} \leq 90 \qquad [FiniteBearing] \tag{4.24}$$

$$5 \leq \frac{\left(p^*_{cyl} A_{cyl}\right)(C/R)^2}{\mu \omega B D} \left(\frac{D}{B}\right)^2 \leq 500 \qquad [ShortBearing] \tag{4.25}$$

$$0.25 \leq B/D \leq 1 \tag{4.26}$$

The above ranges apply to two-axis full offset bearings. The Wakuri and Camella bearings discussed in the introduction (see Figure 1.4) differ only in the limit on the offset ratio. Like the full offset bearing, the Wakuri journal-offset bearing is limited kinematically. Using equation (2.21) with both $\vec{e}_0$ and $\vec{b}_i$ set to zero, it is found that the offset ratio is required to be $\delta/C < 2$, independent of ϕ.

In the case of the Camella bearing, the limiting factor is not kinematic (due to the circumferential symmetry of the single-center journal), but rather geometric as shown in Figure 4.3 and expressed as

$$R \leq \Delta \tag{4.27}$$

where Δ is the distance from the sleeve reference to the sleeve vertex (intersection of sleeve arcs). The limit on the offset ratio is determined to be a function of the journal radius to clearance ratio as follows:

$$\frac{\delta}{C} < \left(8\left(\frac{R}{C}\right) + 4\right)^{\frac{1}{2}} \tag{4.28}$$

In the example of Chapter 3, $R/C = 1016.7$ which results in $(\delta/C)_{max} = 90.2$ using equation (4.28). Based on this example, it is assumed that the Camella bearing has high limits on offset ratio.

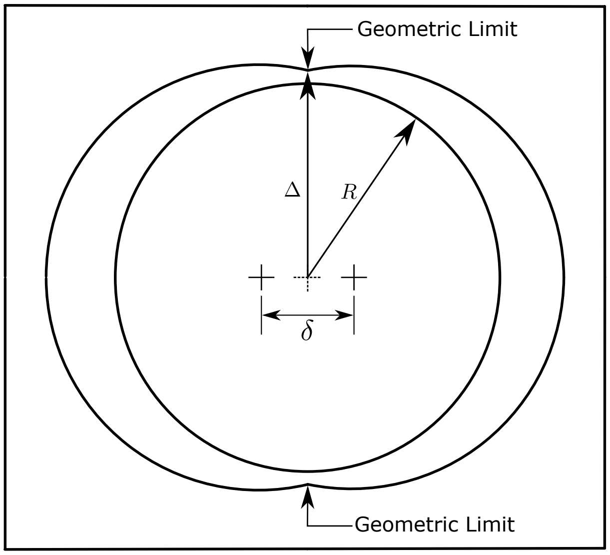

Figure 4.3: Camella Bearing Geometric Limit

4.3 Nondimensional Example

In this section, a case study using the full offset bearing is done to ensure dynamic similarity for the nondimensional parameters established in the prior section. Table 4.5 shows two different sets of dimensional data. Data set 1 is the data from the example in Chapter 3. Data set 2 contains different parameters that result in the same nondimensional parameters as data set 1. Table 4.6 shows the calculated nondimensional parameters. The case study was run using short and finite bearing lubrication models.

Figures 4.4-4.7 are plots of cyclic minimum film thickness ratio and cyclic maximum film pressure ratio for short and finite bearing models. Results from both data sets 1 and 2 are clearly equal for each lubrication model. This is a good indicator that the nondimensional parameters and performance factors shown in this chapter form a complete representation of the dimensional problem.

Table 4.5: Dimensional Data for Nondimensional Comparison

	Parameter		Units	Data Set 1	Data Set 2
Engine	Piston Mass	M_p	(kg)	4.68	3.80
	Connrod Small End Mass	M_s	(kg)	6.16	5.00
	Crank Radius	r	(m)	0.073	0.048
	Connrod Length	L	(m)	0.305	0.200
	Cylinder X-section Area	A_{cyl}	(m^2)	0.0167	0.0167
	Peak Cylinder Pressure	p^*_{cyl}	(Pa)	$12.1 \cdot 10^6$	$4.46 \cdot 10^6$
	Crank Angular Speed	ω	(rpm)	1900	500
Offset Bearing	Viscosity	μ	$[Pa \cdot s]$	0.00965	0.12995
	Radial Clearance	C	$[\mu m]$	30	40
	Segment Diameter	D	$[m]$	0.0610	0.0400
	Segment Length	B	$[m]$	0.0305	0.0200
	Number of Segments	n	$[-]$	3	3
	Total Offset	δ	$[\mu m]$	120	160
	Offset Components	$\vec{a}^x$	$[\mu m]$	[0 0 0]	[0 0 0]
		$\vec{a}^y$	$[\mu m]$	[60 -60 60]	[80 -80 80]
		$\vec{b}^x$	$[\mu m]$	[0 0 0]	[0 0 0]
		$\vec{b}^y$	$[\mu m]$	[60 -60 60]	[80 -80 80]

Table 4.6: Nondimensional Case Study Parameters

	Nondimensional Parameter		Value
Engine	Crank/Rod Ratio	$\frac{r}{L}$	0.2393
	Mass Ratio	$\frac{M_s}{M_p}$	1.3162
	Engine Load #	$\frac{M_p r \omega^2}{p^*_{cyl} A_{cyl}}$	0.0668
Offset Bearing	Number of Segments	n	3
	Offset Ratio	$\frac{\delta}{C}$	4
	Segment Load # (short)	$\frac{\left(p^*_{cyl} A_{cyl}\right)(C/R)^2}{\mu \omega B D} \left(\frac{D}{B}\right)^2$	218.9
	Segment Load # (finite)	$\frac{\left(p^*_{cyl} A_{cyl}\right)(C/R)^2}{\mu \omega B D}$	54.7
	Segment Aspect Ratio (finite)	$\frac{B}{D}$	0.5

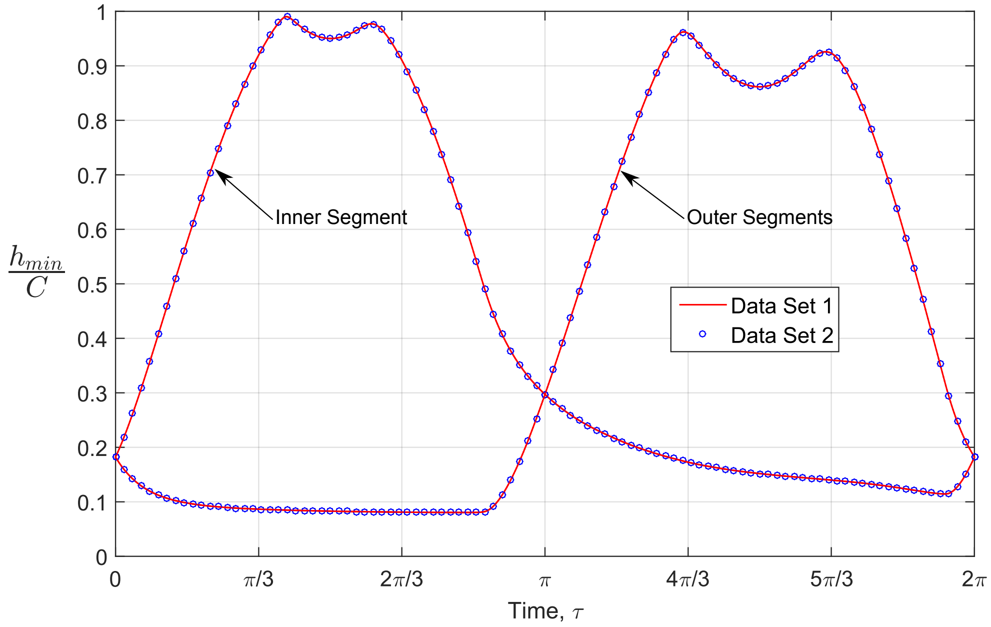

Figure 4.4: Periodic Time History of Minimum Film Thickness Ratio (short): Table 4.5 Data

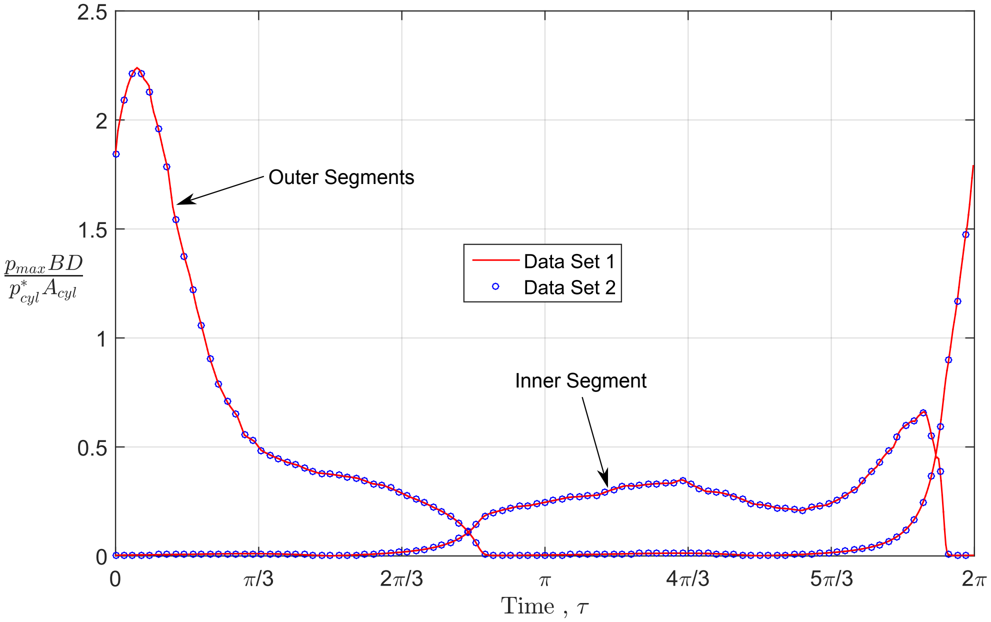

Figure 4.5: Periodic Time History of Maximum Film Pressure Ratio (short): Table 4.5 Data

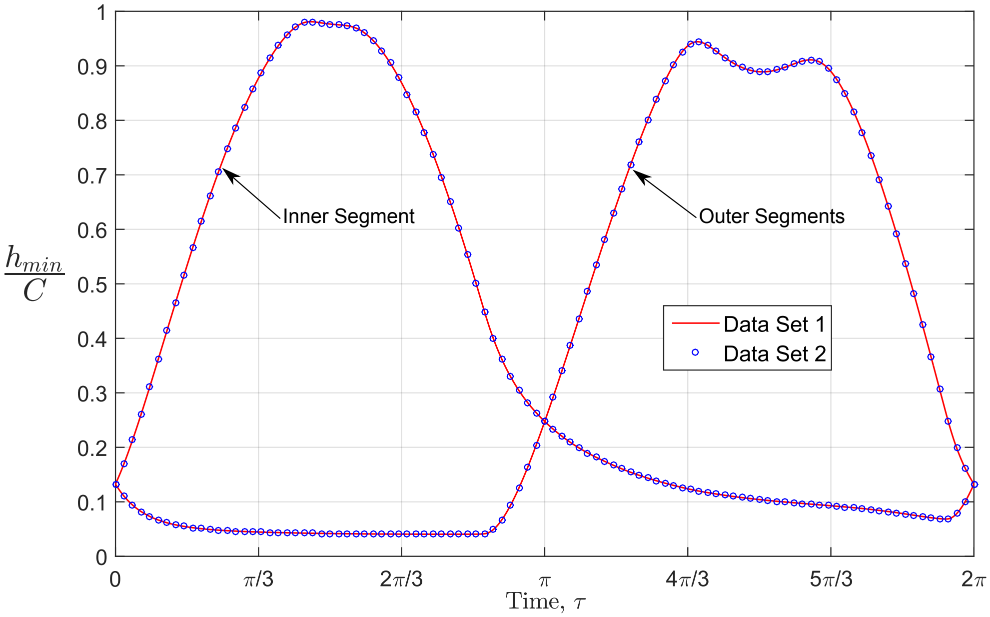

Figure 4.6: Periodic Time History of Minimum Film Thickness Ratio (finite): Table 4.5 Data

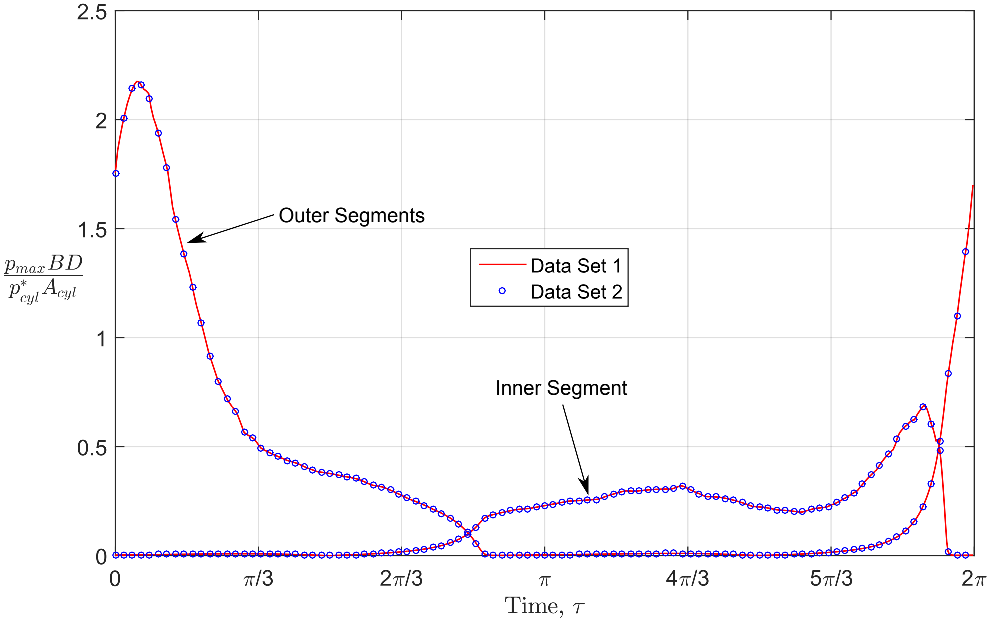

Figure 4.7: Periodic Time History of Maximum Film Pressure Ratio (finite): Table 4.5 Data

4.4 Assumption Validation

4.4.1 Criteria for Load Reversal

In Chapter 3 the partial arc bearing of Booker *et al.* [9] was compared to a full bearing. In a two-stroke diesel engine the load is not usually expected to reverse direction - making a partial arc bearing a practical design option. In this section, the nondimensional load parameters required for the load to reverse direction are determined. Defining engine nondimensional load number

$$\bar{F} = \frac{M_p r \omega^2}{p^*_{cyl} A_{cyl}} \tag{4.29}$$

and combining similar terms, equation (4.2a) can be rewritten as follows:

$$\frac{F^{X_1}(\theta)}{p^*_{cyl} A_{cyl}} = f(\theta) - \bar{F}(cos\theta + sin\theta tan\phi) - \bar{F}\left(\frac{r}{L}\right)\left(\frac{cos^2\theta}{cos\phi}\right)(1 - tan^2\theta) \tag{4.30}$$

The load will reverse direction when

$$\frac{F^{X_1}(\theta)}{p^*_{cyl} A_{cyl}} < 0 \tag{4.31}$$

or when

$$f(\theta) - \bar{F}(cos\theta + sin\theta tan\phi) - \bar{F}\left(\frac{r}{L}\right)\left(\frac{cos^2\theta}{cos\phi}\right)(1 - tan^2\phi) < 0 \tag{4.32}$$

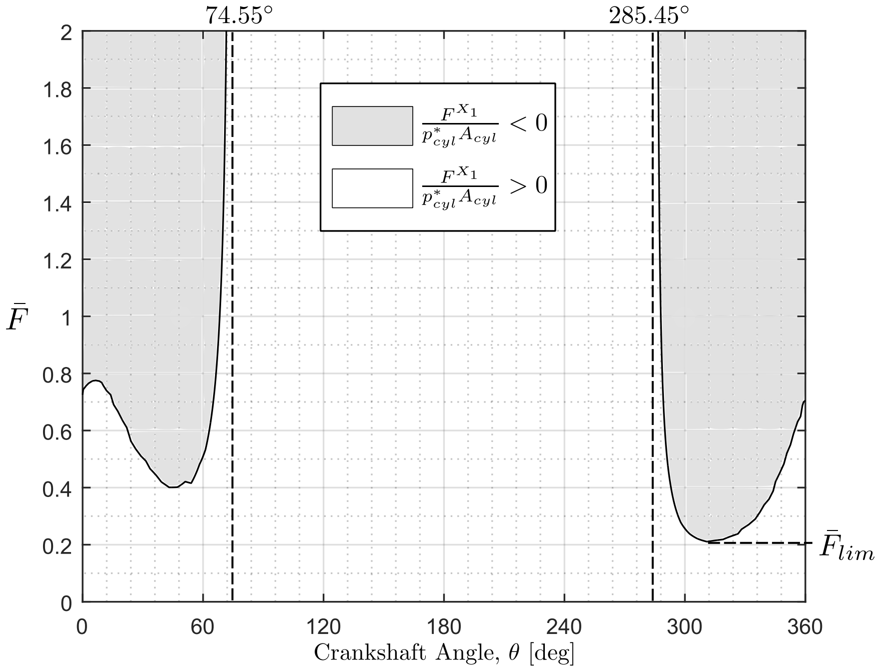

Figure 4.8: Load Reversal Study with $\frac{r}{L} = 0.3$

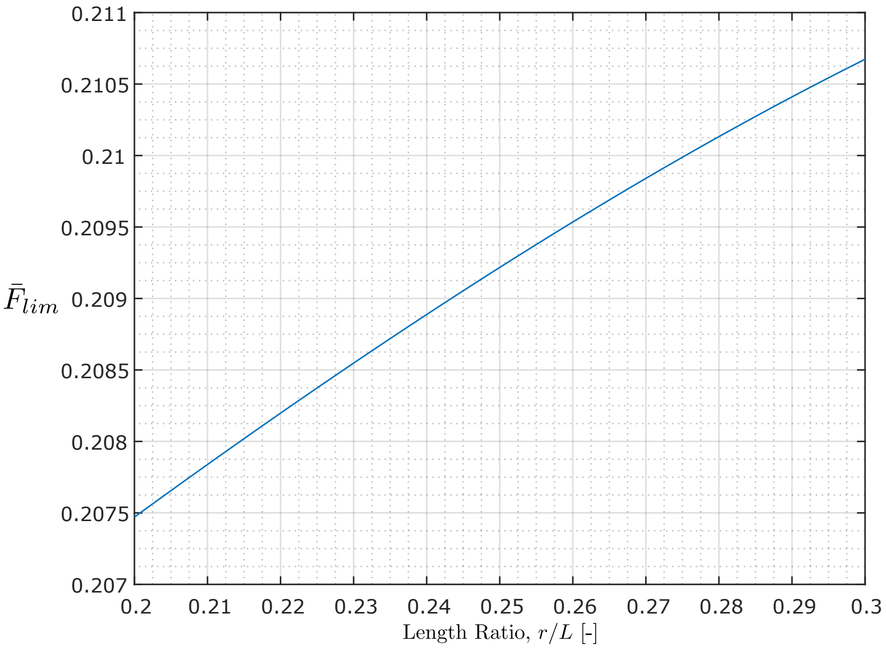

Figure 4.9: Engine Load Number Threshold

Figure 4.8 shows such a load reversal study for $r/L = 0.3$, where r/L is chosen from the upper limit in Table 4.4. Conclusions from this study are listed below:

- In the region $0° \leq \theta \leq 74.55°$ the load reverses for $\bar{F} > 0.4$
- In the region $74.55° \leq \theta \leq 285.4°$ the load never reverses as long as $p^*_{cyl} > 0$
- In the region $285.45° \leq \theta \leq 360°$ the load reverses for $\bar{F} > 0.2107$

In summary, for $r/L = 0.3$, the load on the piston will never reverse direction over the duty cycle when $\bar{F} \leq \bar{F}_{lim}$ where $\bar{F}_{lim} = 0.2107$.

The above study was repeated for the full design range of r/L. Figure 4.9 shows the load number threshold $\bar{F}_{lim}$ for various r/L values. The load numbers provided in Table 4.4 are below $\bar{F}_{lim}$ for all r/L values, meaning that the load is not expected to reverse direction within the design space used in this thesis. While this thesis primarily studies the performance of full bearings, this study shows that partial arc bearings could be used in practice.

4.4.2 Effect of Sidewall Loading

In the dimensional study of Chapter 3, the sidewall loading was shown to have little effect on the bearing performance factors. The nondimensional sidewall load component, $\frac{F^{Y_1}}{p^*_{cyl}A_{cyl}}$, is uniquely dependent upon the mass ratio M_s/M_p. If the effects of sidewall loading on bearing performance can be shown to be practically negligible then the mass ratio can be ignored, and the design space can be made smaller. Simulations were run with multiple engine duty configurations and a single offset bearing configuration. These configurations are described in Table 4.7. Each configuration has a different length ratio and engine load number, and is run with varying options for the mass ratio.

Time histories for film thickness for configuration A are plotted in Figure 4.10. The inner segment minimum film thickness ratio differs only near the end of the duty cycle for $M_s/M_p = 1.5$. For the outer segments, the curve with $M_s/M_p = 0.25$ essentially overlaps

Table 4.7: Engine Configurations for Sidewall Load Study

	Nondimensional Parameter		Configuration			
			A	B	C	D
Engine	Crank/Rod Ratio	$\frac{r}{L}$	0.2	0.2	0.3	0.3
	Engine Load Number	$\frac{M_p r \omega^2}{p^*_{cyl} A_{cyl}}$	0.15	0.05	0.15	0.05
	Mass Ratio	$\frac{M_s}{M_p}$	0.25 1.5 -†			
Offset Bearing	Number of Segments	n	3			
	Offset Ratio	$\frac{\delta}{C}$	4			
	Segment Load Number (short)	$\frac{(p^*_{cyl} A_{cyl})(C/R)^2}{\mu \omega B D} \left(\frac{D}{B}\right)^2$	220			

†The “-” indicates $F^{Y_1} = 0$; thus M_s/M_p is not applicable.

the curve with $F^{Y_1} = 0$, but the curve corresponding to $M_s/M_p = 1.5$ has a slightly lower peak minimum film thickness ratio. Most importantly, the cyclic minimum film thickness ratio is essentially unaffected by the sidewall force.

Time histories of maximum film pressure ratio are plotted in Figure 4.11. The $M_s/M_p = 0.25$ and $F^{Y_1} = 0$ curves lie very close to each other, having very similar peak pressure ratios and locations. The $M_s/M_p = 1.5$ curve has a nearly identical maximum pressure ratio value and location on the outer segments, but is slightly higher than the other two curves at the inner segment. Generally all three curves are very similar, and extreme values across all segments are essentially the same.

For this configuration, across all mass ratio variations, the cyclic minimum film thickness ratio is about 0.087 at $\tau \approx 2.74\,rad$ on the outer segments, and the cyclic maximum film pressure ratio is about 1.9 at $\tau \approx 3.8\,rad$ on the inner segment.

This study was repeated for configurations B, C, and D and data for the cyclic minimum film thickness ratios, cyclic maximum film pressure ratios, and their locations was

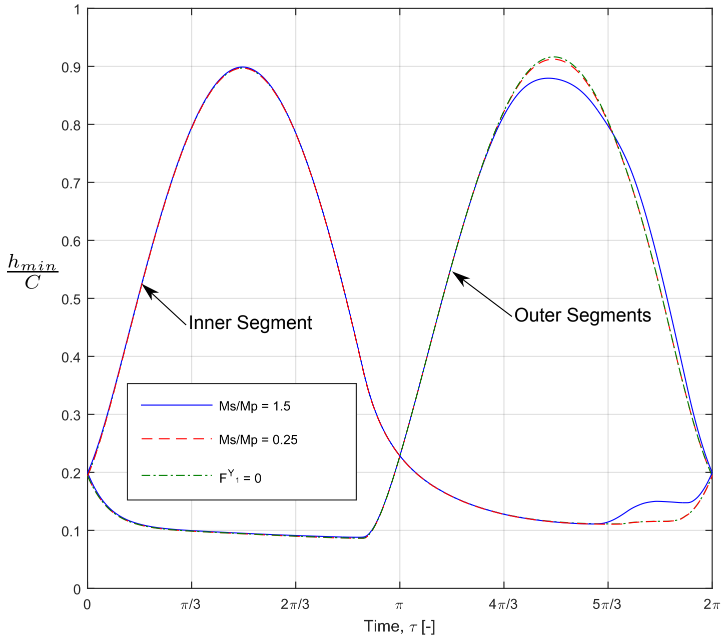

Figure 4.10: Minimum Film Thickness Ratio Time History: Configuration A

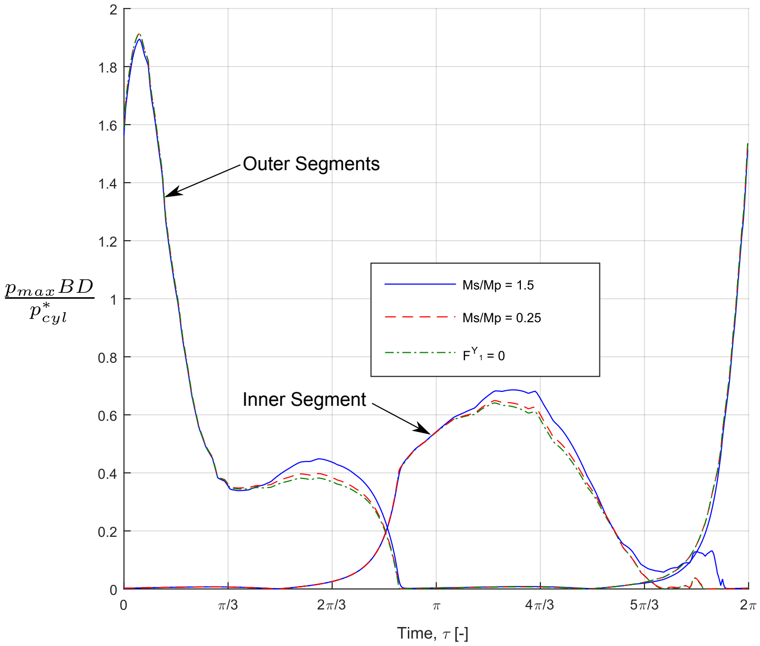

Figure 4.11: Maximum Film Pressure Ratio: Configuration A

compared. The data in scatter plot Figures 4.12, 4.13, 4.14, and 4.15 was grouped according to configuration, and the legend corresponds to the various mass ratio options, including neglecting the sidewall load. The cyclic minimum film thickness ratio varies the most in configuration C on the outer segments, and its location varies the most in configuration C on the inner segments. The pressure ratio magnitude varies the most in configuration C on the inner segment, and the pressure ratio location varies the most in configuration A on the inner segment.

Table 4.8 shows the greatest differences in the data for both cyclic minimum film thickness ratio and cyclic maximum film pressure ratio. The largest difference in cyclic film thickness ratio values, located on the outer segments in configuration C, is 0.0046 - a difference that is less than 5.3% of the corresponding ratio for $F_1^Y = 0$ at the same configuration/segment. The largest difference in the cyclic maximum film pressure ratio values, located on the inner segments in configuration C, is 0.0284 - a difference that is less than 4% of the corresponding ratio for $F^{Y_1} = 0$ at the same configuration/segment. Such small relative differences lend support to the assumption that the sidewall loading F^{Y_1} can be neglected in the design study.

Table 4.8: Sidewall Load Study: Greatest Absolute Differences

	Magnitude	Location (τ)
Minimum Film Ratio	0.0046	0.864
Configuration, Segment	C, Outer	C, Inner
Between Curves	$\frac{M_s}{M_p} = 1.5$, $\frac{M_s}{M_p} = 0.25$	$\frac{M_s}{M_p} = 1.5$, $F^{Y_1} = 0$
Maximum Pressure Ratio	0.0284	0.175
Configuration, Segment	C, Inner	A, Inner
Between Curves	$\frac{M_s}{M_p} = 1.5$, $F^{Y_1} = 0$	$\frac{M_s}{M_p} = 1.5$, $F^{Y_1} = 0$

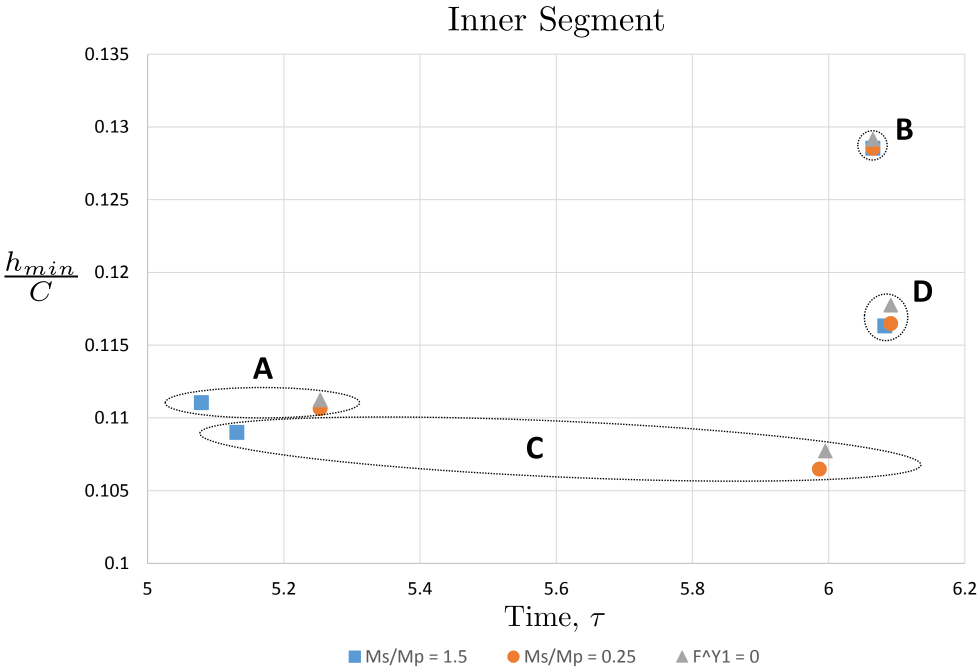

Figure 4.12: Cyclic Minimum Film Thickness Ratio Scatter Plot: Inner Segments

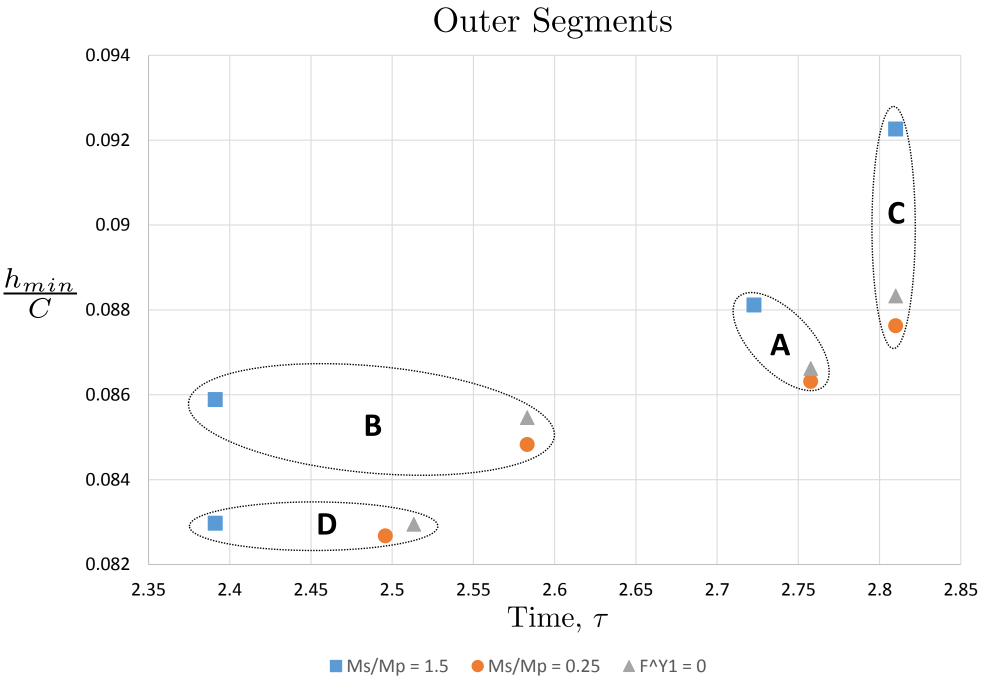

Figure 4.13: Cyclic Minimum Film Thickness Ratio Scatter Plot: Outer Segments

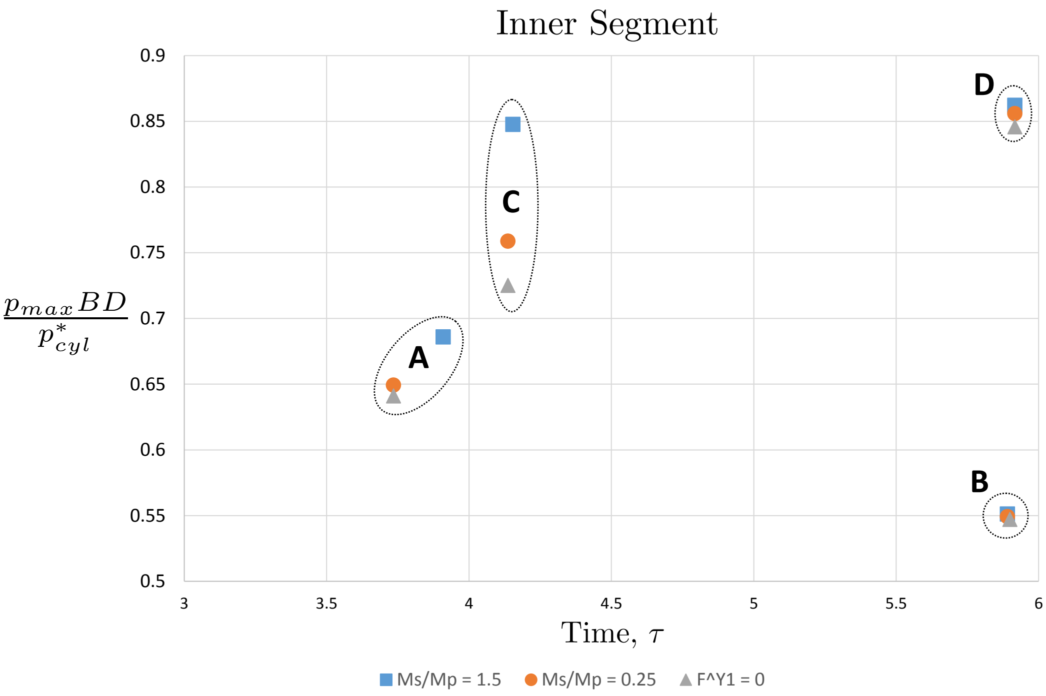

Figure 4.14: Cyclic Maximum Film Pressure Ratio Scatter Plot: Inner Segments

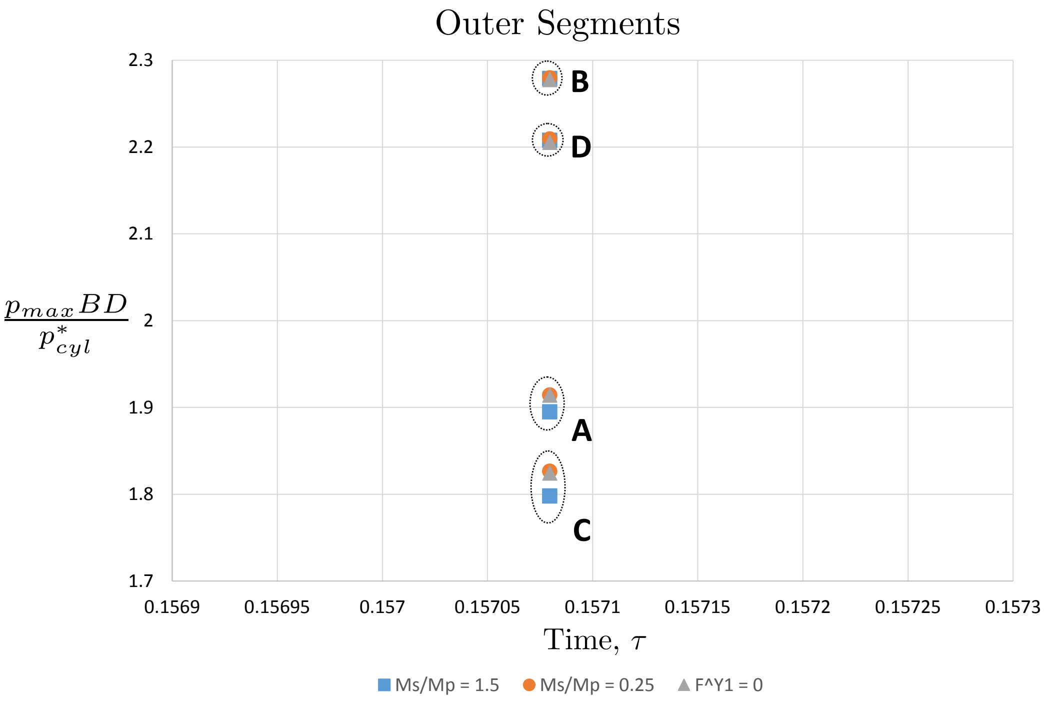

Figure 4.15: Cyclic Maximum Film Pressure Ratio Scatter Plot: Outer Segments

4.5 Alternative Three Segment Full Offset Bearing Designs

The example in Section 4.3 was done for a three equal segments full offset bearing. The time histories (see Figures 4.4-4.7) for this bearing show that the outer segments had slightly thinner films and significantly higher pressures than the inner segment. The design charts in Appendix A (specifically Figures A.19-A.36) discussed in section 5.2 confirm the following observation in an even more general sense: the outer segments are a performance-limiting factor in three equal segment full offset bearings.

There are a variety of approaches that could be taken to attempt to balance the performance of the inner and outer segments. Two approaches are briefly discussed and analyzed in the following sections. These approaches include a) varying the lengths of the segments, and b) inclining the journal so that its offset components are not entirely perpendicular to the axis of the connecting rod.

The first approach mentioned has been used in at least three cases. The image provided of an EMD 710 offset bearing journal by Achates [13] appears to have unequal length segments. The outer segments appear to be equal, and the inner segment is larger than either one of the outer segments. The offset bearing journal in the A48 1.6L single cylinder engine has this same design (See Figure 1.5)[12]. Wakuri also does a study on the variation of segment lengths in his paper on the two segment Wakuri journal-offset bearing[3]. In this thesis two cases of length variation are considered. The first case looks at making the inner segment larger than either of the outer segments, and the second case looks at making the outer segments larger than the inner segment.

The second approach was only found in the literature once in Wakuri's studies of the two segment Wakuri journal-offset bearing[3]. In this study the journal was inclined at angles of -10°, 0°, and 10° from "horizontal". The most improvement in film thickness and balancing of pressures across the two segments occurred in the 10° inclination case. In this thesis, the journal inclination is varied similarly for a three equal segment full offset bearing design, and the respective design charts have been created for an inclination angle of 2°.

4.5.1 Segment Length Variation

In order to vary the segment lengths, a method was desired such that the variable length design would be comparable to the equal length three segment design. This is done through the introduction of the length modification factor, α, as shown in Figure 4.16. For a bearing with total length $3B$, parameter α directly changes the length of the inner segment. If $\alpha = 1$, the bearing simply has three equal segments. For $\alpha > 1$ the inner segment becomes larger than the outer segments, and for $\alpha < 1$, the inner segment becomes smaller than the outer segments.

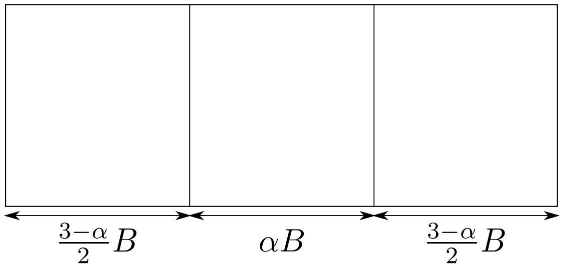

Figure 4.16: Usage of Length Modification Factor, α

In order to provide a consistent means of comparison, the nondimensional parameters in Table 4.6 from Section 4.3 have been used to generate time histories of the maximum film pressure ratio and minimum film thickness ratio. Parameter α was varied as follows:

$$\alpha = 0.5,\ 0.75,\ 1,\ 1.5 \tag{4.33}$$

Using short bearing theory, Figures 4.17 and 4.18 shows time histories for the minimum film thickness ratio and maximum film pressure ratio, respectively, for various values of α. The case where $\alpha = 1$ represents the equal length segment case from section 4.3. Observations below are made in comparison to the (equal segment length) $\alpha = 1$ case.

For $\alpha = 0.5$, a shorter inner segment, the minimum film ratio increased for the outer segments, but decreased rather notably for the inner segment. The pressure ratio for this case remained highest on the outer segments, however, the maximum pressure in the duty cycle dropped for the outer segments and increased slightly for the inner segment.

For $\alpha = 1.5$, a longer inner segment, the minimum film ratio decreased for the outer segments, and increased significantly for the inner segment. The pressure ratio for this case also remained highest on the outer segments, increasing the pressure ratio above the $\alpha = 1$ case. The pressure ratio on the inner segment, however, dropped slightly.

In order to find some sort of middle ground, the case of $\alpha = 0.75$ was also considered. In this case the minimum film ratio was generally increased for both inner and outer segments. The absolute minimum film ratio in the whole cycle appears to be the same, but occurs on the inner segment late in the engine cycle rather than on the outer segments during the first half of the cycle. The maximum pressure ratio also improved slightly for the outer segments, and increased very little for the inner segment.

Based on these studies, it would appear that $\alpha < 1$ provides improved performance for this specific set of data. Nonetheless, design charts are presented in Appendix A for both $\alpha = 0.5$ (Figures A.49-A.54) and $\alpha = 1.5$ (Figures A.55-A.60) in order to have a more complete study for this design option.

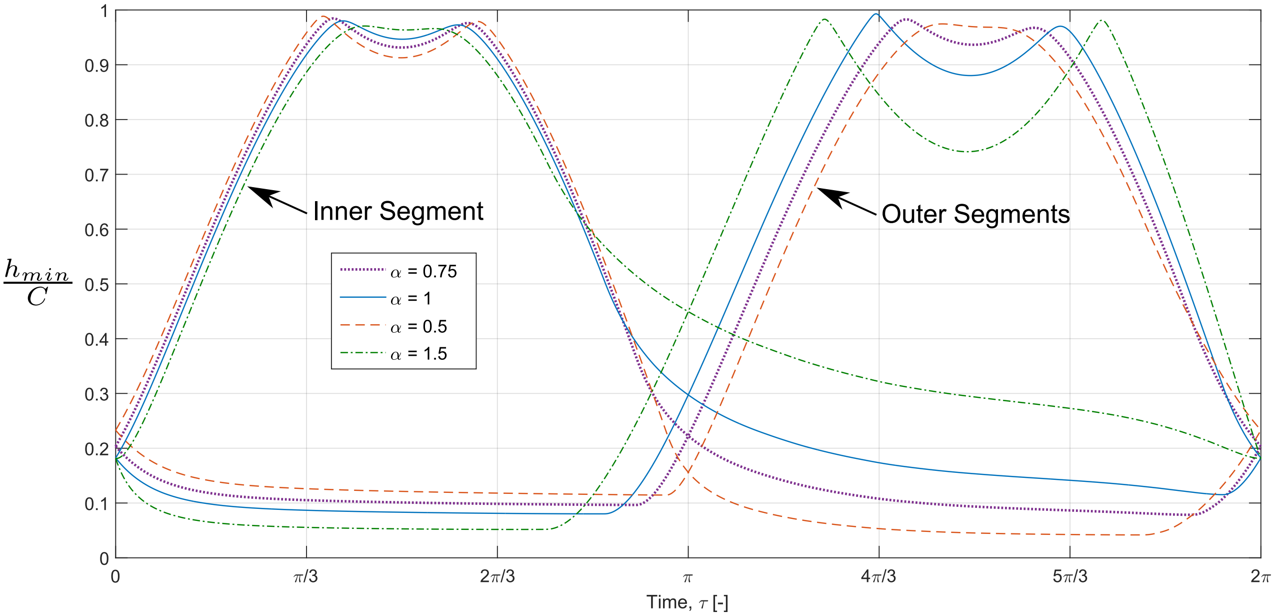

Figure 4.17: Effect of α on Minimum Film Thickness Ratio

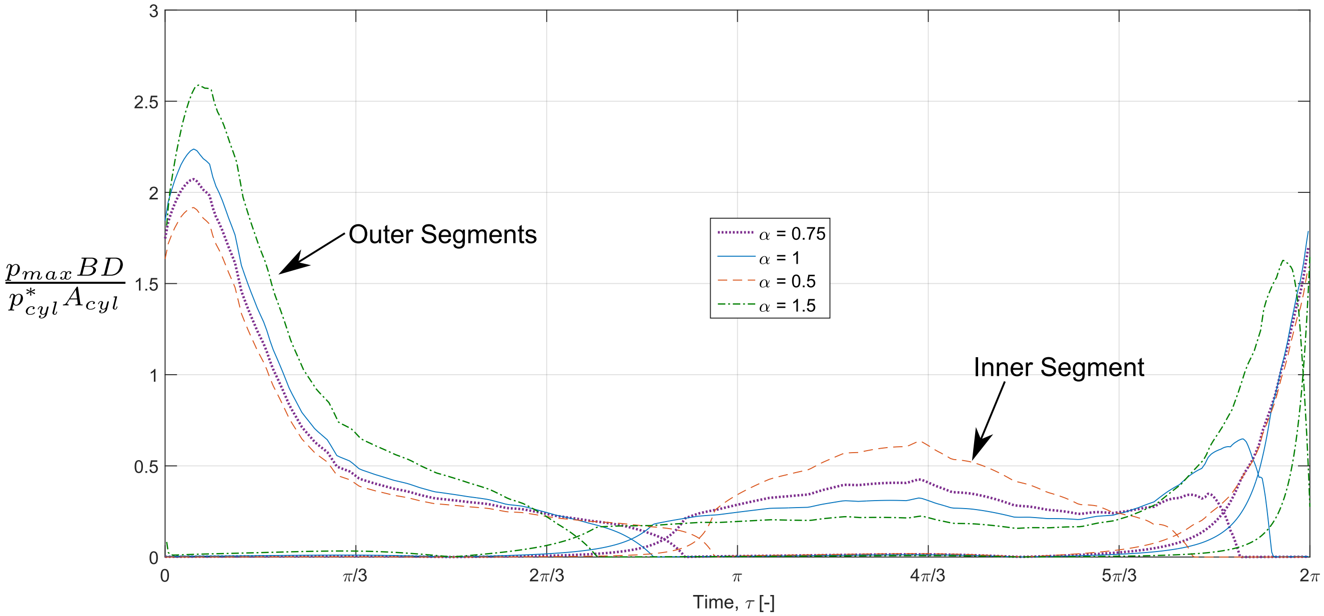

Figure 4.18: Effect of α on Maximum Film Pressure Ratio

4.5.2 Journal Inclination

As discussed earlier in this section, for the previous three equal segment full offset bearing designs the outer segments are a performance-limiting factor. Section 4.5.1 attempted to balance the performance of segments by modifying segment lengths. This length modification method did not look at the possible reasons that the outer segments limit the bearing performance. This section looks at how inclination of the journal may improve the overall bearing performance.

In the engine cycle, based on the pressure profile in Figure 4.1, the peak cylinder pressure, p^*_{cyl} occurs around the crankshaft angle $\theta^* = 5°$. Using equation (2.5) with $0.2 < \frac{r}{L} < 0.3$, the rod angle at peak pressure is determined to be in the following range:

$$-1.5° \leq \phi(\theta^*) \leq -1.0° \tag{4.34}$$

When the nondimensional offset components are defined perpendicular to the rod axis, the outer journal segments are oriented towards the top of the cylinder when the peak pressure occurs. If the journal segments were oriented such that, near the time of peak pressure, both inner and outer segments were perpendicular to the cylinder axis then it is suspected that the segments would share the loading more equally.

This is done here by introducing an inclination angle, β. Angle β defines the angle of the journal offset vectors away from the y' axis (the connecting rod axis). Figure 4.19 illustrates this angle, and may be compared to Figure 2.6(a) in which the offset vector is coincident ($\beta = 0$) with the y' axis of the journal reference frame.

The nondimensional journal offset components can be written in cartesian form for a 3 segment full offset bearing as follows:

$$\frac{b^{x'}}{C} = \begin{bmatrix} -\frac{\delta}{2C} sin\beta & \frac{\delta}{2C} sin\beta & -\frac{\delta}{2C} sin\beta \end{bmatrix} \tag{4.35}$$

$$\frac{b^{y'}}{C} = \begin{bmatrix} \frac{\delta}{2C} cos\beta & -\frac{\delta}{2C} cos\beta & \frac{\delta}{2C} cos\beta \end{bmatrix} \tag{4.36}$$

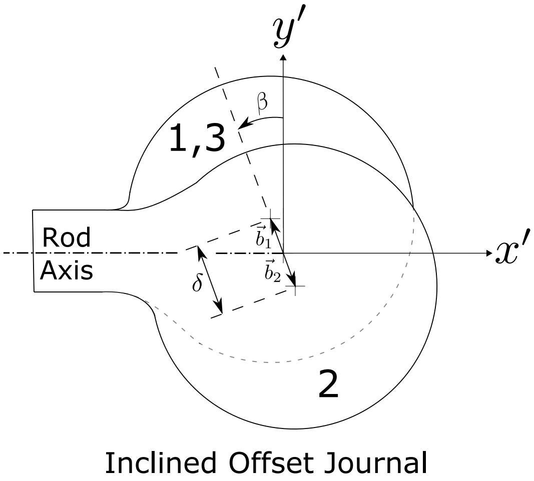

Figure 4.19: Diagram of Journal Inclination Angle

As with the introduction of the length modification factor, α, the parameters in Table 4.6 from Section 4.3 have been used to generate time histories of the maximum pressure ratio and minimum film ratio using various values of the inclination angle β. The inclination angle was varied as follows:

$$\beta = -5^\circ,\ 0^\circ,\ 2^\circ,\ 5^\circ \tag{4.37}$$

Figures 4.20 and 4.21 shows time histories for the minimum film thickness ratio and maximum film pressure ratio, respectively, for various values of β. The case where $\beta = 0^\circ$ represents the equal length segment case from section 4.3. Observations below are made in comparison to the $\beta = 0^\circ$ case.

Inclining the journal by $\beta = -5^\circ$ orients the outer segments even more towards the top of the cylinder at the time of peak cylinder pressure. For this case, the cylic minimum film thickness ratio for the outer segments remains essentially the same. The minimum film ratio is lower for a longer period of time, and has a peak minimum film ratio less than the zero-inclination case. The inner segments actually show a generally improved minimum film ratio. The maximum film pressure does not seem to differ significantly for the outer segments except that they bear the pressure during more of the cycle than with the zero inclination case.

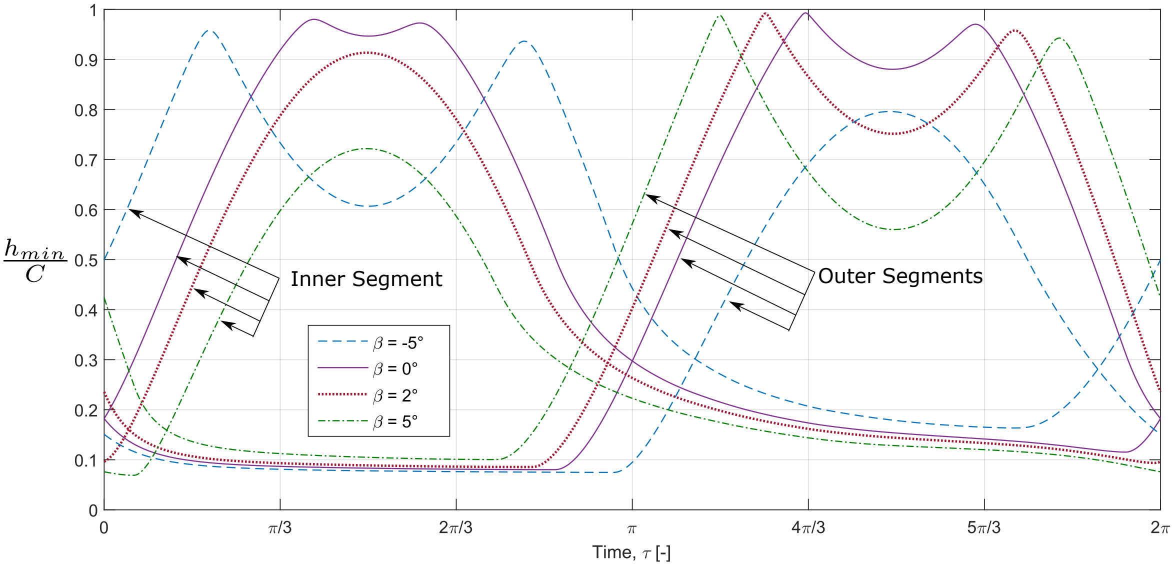

Figure 4.20: Effect of Inclination Angle on Minimum Film Thickness Ratio

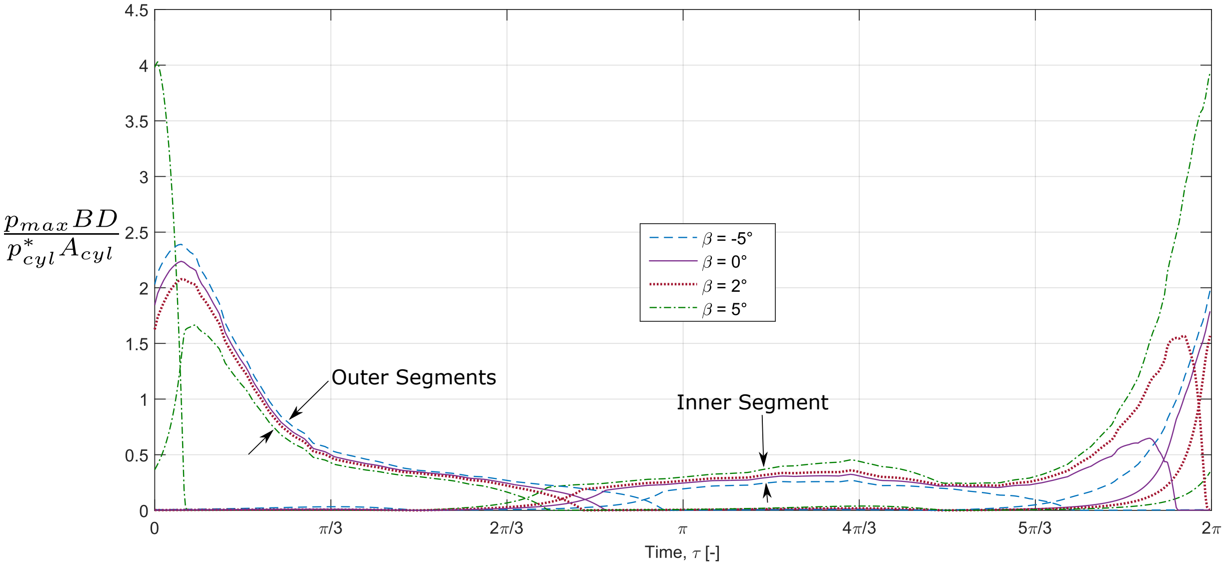

Figure 4.21: Effect of Inclination Angle on Maximum Film Pressure Ratio

When the journal is inclined at $\beta = 5^\circ$ the inner segment will be slightly oriented towards the top of the cylinder at the time of peak cylinder pressure. In this case, the absolute minimum film thickness occurs on the inner segments and is actually lower than the zero-inclination case. However, the minimum film ratio on the outer segments is slightly increased, and the minimum film ratio increases in value earlier in the cycle than the zero-inclination case. The maximum film pressure is reduced for the outer segments, but for the inner segment it is nearly eight times the pressure of the zero-inclination case. The maximum pressure ratio value also occurs around top-dead-center (TDC, $\tau = 0$) in the cylinder as opposed to slightly after TDC where it usually is seen.

As with the length modification study, some sort of middle ground is desired. Consequently the case where $\beta = 2^\circ$ was chosen. In this case the film ratio for both inner and outer segments is very similar to the zero-inclination case, but appears to have a very slightly increased absolute minimum film ratio. The largest pressure ratios for both inner and outer segments are much closer in magnitude. The largest pressure ratio on the outer segments occurs around the same location and is less than the zero-inclination case. The largest pressure ratio on the inner segment occurs slightly later in the engine cycle (just before TDC) and is greater than the zero-inclination case. The absolute maximum film ratio is lower, but at the cost of increased pressure on the inner segment.

Because $\beta = 2^\circ$ produced the most desirable results in the above study, design charts in Figures A.61-A.66 have been developed for $\beta = 2^\circ$.

Chapter 5

Results

This chapter presents general conclusions for the design charts presented in Appendix A. As was discussed in Section 4.4.1 all data was obtained with the sidewall loading, F^{Y_1}, neglected. The charts show the variation of cyclic minimum film thickness ratio and cyclic maximum film pressure ratio as the offset ratio (the x-axis of the design charts) and segment load number (the curves on each design chart) are varied. The data sets include both inner and outer segments, and each chart is done for a specific nondimensional engine duty configuration.

Table 5.1 shows the configuration details along with the appropriate figure ranges. The sections corresponding to the discussion for each design are in the first column of Table 5.1. It is intended that Table 5.1 would act as a navigation guide of sorts for Appendix A.

Note that all discussion of the design charts will refer to the “cyclic minimum film thickness ratio” as just the “film ratio”, and the “cyclic maximum film pressure ratio” as the “pressure ratio”. Discussion pertaining to the “largest pressure ratio” or “smallest film ratio” will thus refer to the largest or smallest value of the pressure ratio or film ratio, respectively, in any one, or set of, plot(s).

Table 5.1: Results Configurations

Section	Offset Bearing Type	Number of Segments	Lubrication Model	Aspect Ratio	Figure Range
5.1	Full	2	Short	-	A.1-A.6
5.1	Full	2	Finite	1	A.7 - A.12
5.1	Full	2	Finite	1/4	A.13-A.18
5.2	Full	3	Short	-	A.19-A.24
5.2	Full	3	Finite	1	A.25-A.30
5.2	Full	3	Finite	1/4	A.31-A.36
5.3	Wakuri	3	Short	-	A.37-A.42
5.3	Camella	3	Short	-	A.43-A.48
5.4.1	Full, $\alpha = 1.5$	3	Short	-	A.49-A.54
5.4.1	Full, $\alpha = 0.5$	3	Short	-	A.55-A.60
5.4.2	Full, $\beta = 2°$	3	Short	-	A.61-A.66

5.1 Full Offset Bearing, Two Segments

The two equal segment designs in Figures A.1-A.18 all have the following nondimensional offset components:

$$\frac{a^x}{C} = \begin{bmatrix} 0 & 0 \end{bmatrix} \tag{5.1}$$

$$\frac{a^y}{C} = \begin{bmatrix} \frac{\delta}{2C} & -\frac{\delta}{2C} \end{bmatrix} \tag{5.2}$$

$$\frac{b^{x'}}{C} = \begin{bmatrix} 0 & 0 \end{bmatrix} \tag{5.3}$$

$$\frac{b^{y'}}{C} = \begin{bmatrix} \frac{\delta}{2C} & -\frac{\delta}{2C} \end{bmatrix} \tag{5.4}$$

Below are some general observations regarding this design. Unless otherwise specified, observations are applicable to both finite and short bearing models. Design charts for the short bearing model are Figures A.1-A.6. Design charts for the finite bearing model, $B/D = 1$, are Figures A.7 - A.12. Design charts for finite bearing model, $B/D = 1/4$, are Figures A.13-A.18.

- The outer segments are a performance limiting factor for both film ratio and pressure ratio.
- Optimal performance values (largest film ratio and smallest pressure ratio across both segments) typically occur in the offset ratio range $1 \leq \frac{\delta}{C} \leq 3.5$ for all of the data.
- For the outer segments, as the segment load number increases, the pressure ratio increases.
- For the short bearing model with $\frac{r}{L} = 0.3$ the pressure ratio begins to drastically increase for $\frac{\delta}{C} > 3.5$ for both inner and outer segments.
- For the short bearing model in the segment load number range $90 \leq \frac{\left(p^*_{cyl}A_{cyl}\right)(C/R)^2}{\mu\omega BD}\left(\frac{D}{B}\right)^2 \leq 500$, and $\frac{\delta}{C} \leq 3.5$ the pressure ratio on the outer segments generally has little variation.

- For the short bearing the pressure ratio for the inner segments decreases in the segment load number range

$$5 \leq \frac{\left(p^*_{cyl} A_{cyl}\right)(C/R)^2}{\mu\omega BD} \left(\frac{D}{B}\right)^2 \leq 50$$

  and increases in the range

$$90 \leq \frac{\left(p^*_{cyl} A_{cyl}\right)(C/R)^2}{\mu\omega BD} \left(\frac{D}{B}\right)^2 \leq 500$$

- For short bearing the pressure slightly increases as the engine load number decreases.
- For the finite bearing there is very little variation in the film ratio and pressure curves for any given segment load number in the offset ratio range $1 \leq \frac{\delta}{C} \leq 5$.
- For the finite bearing, data for aspect ratio $B/D = 1/4$, indicates a much poorer performance than does the data for aspect ratio $B/D = 1$.
- For finite bearing, $B/D = 1$ the film ratio upper limit is 0.45 for all data - a comparable upper limit to 0.5 of the short bearing data. The finite bearing, $B/D = 1/4$ data, however, has a much lower upper limit of 0.12.
- For finite bearing, $B/D = 1$ the pressure ratio upper limit is 6, for the short bearing it is 9, and for the finite bearing, $B/D = 1/4$ it is 10.

5.2 Full Offset Bearing, Three Segments

The three equal segment designs in Figures A.19-A.36 all have the following nondimensional offset components

$$\frac{a^x}{C} = \begin{bmatrix} 0 & 0 & 0 \end{bmatrix} \tag{5.5}$$

$$\frac{a^y}{C} = \begin{bmatrix} \frac{\delta}{2C} & -\frac{\delta}{2C} & \frac{\delta}{2C} \end{bmatrix} \tag{5.6}$$

$$\frac{b^{x'}}{C} = \begin{bmatrix} 0 & 0 & 0 \end{bmatrix} \tag{5.7}$$

$$\frac{b^{y'}}{C} = \begin{bmatrix} \frac{\delta}{2C} & -\frac{\delta}{2C} & \frac{\delta}{2C} \end{bmatrix} \tag{5.8}$$

For the short bearing model and three segments (Figures A.19-A.24), the following observations can be made:

- The outer segments are generally a performance limiting factor for both film ratio and pressure ratio. The difference in performance extrema between inner and outer segments is, however, not as large as it generally was with the two equal segments design.
- Optimal performance values (largest film ratio and smallest pressure ratio across all segments) typically occur in the offset ratio range $1.5 \leq \frac{\delta}{C} \leq 3.5$ for all of the data.
- For the outer segments, as the segment load number increases, the pressure ratio increases.
- For $\frac{\delta}{C} \leq 3.5$, for any given bearing load number, the outer and inner segments have very little variation in the pressure ratio values
- For the short bearing model, while film ratio values are generally in the same range as the two-segment designs, the pressure is significantly lower, having an upper limit of 4 as opposed to the upper limit of 9 for the two-segment designs

- For the short bearing model with $\frac{r}{L} = 0.3$ the pressure ratio begins to drastically increase for $\frac{\delta}{C} > 3.5$ for both inner and outer segments.
- For the short bearing model in the segment load number range $90 \leq \frac{\left(p^*_{cyl}A_{cyl}\right)(C/R)^2}{\mu\omega BD}\left(\frac{D}{B}\right)^2 \leq 500$, and $\frac{\delta}{C} \leq 3.5$ the pressure ratio on the outer segments generally has little variation.
- For the short bearing the pressure ratio for the inner segment decreases for

  $$5 \leq \frac{\left(p^*_{cyl}A_{cyl}\right)(C/R)^2}{\mu\omega BD}\left(\frac{D}{B}\right)^2 \leq 50$$

  and increases for

  $$90 \leq \frac{\left(p^*_{cyl}A_{cyl}\right)(C/R)^2}{\mu\omega BD}\left(\frac{D}{B}\right)^2 \leq 500$$

For the finite bearing model and three segments (Figures A.25-A.36) the following observations can be made:

- The finite bearing data generally indicate lower film ratios and lower pressure ratios than the short bearing data.
- The finite bearing $B/D = 1/4$ (Figures A.31-A.36) data indicates a markedly improved performance over the two segment, finite bearing, $B/D = 1/4$ data.
- For the finite bearing there is very little variation in the film ratio and pressure curves for any given segment load number in the offset ratio range $1 \leq \frac{\delta}{C} \leq 5$.
- For the finite bearing, data for aspect ratio $B/D = 1/4$, indicates a much poorer performance than does the data for aspect ratio $B/D = 1$.
- For finite bearing, $B/D = 1$ Figures (A.25-A.30) the film ratio upper limit is 0.4 for all data - a slightly lower upper limit than 0.55 for the short bearing data. The finite bearing, $B/D = 1/4$ data, however, has a much lower upper limit of 0.15.
- For finite bearing, $B/D = 1$ the pressure ratio upper limit is 3.5, for the short bearing it is 4, and for the finite bearing, $B/D = 1/4$ it is 4.5.

5.3 Partially Segmented Designs

In Appendix A design charts for the Wakuri bearing correspond to Figures A.37-A.42, and design charts for the Camella bearing correspond to Figures A.43-A.48. For these studies the offset ratio was restricted $0.25 \leq \frac{\delta}{C} \leq 1.75$. The offset components for the Wakuri journal offset bearing are

$$\frac{a^x}{C} = \begin{bmatrix} 0 & 0 & 0 \end{bmatrix} \tag{5.9}$$

$$\frac{a^y}{C} = \begin{bmatrix} 0 & 0 & 0 \end{bmatrix} \tag{5.10}$$

$$\frac{b^{x'}}{C} = \begin{bmatrix} 0 & 0 & 0 \end{bmatrix} \tag{5.11}$$

$$\frac{b^{y'}}{C} = \begin{bmatrix} \frac{\delta}{2C} & -\frac{\delta}{2C} & \frac{\delta}{2C} \end{bmatrix} \tag{5.12}$$

The offset components for the Camella sleeve offset bearing are

$$\frac{a^x}{C} = \begin{bmatrix} 0 & 0 & 0 \end{bmatrix} \tag{5.13}$$

$$\frac{a^y}{C} = \begin{bmatrix} \frac{\delta}{2C} & -\frac{\delta}{2C} & \frac{\delta}{2C} \end{bmatrix} \tag{5.14}$$

$$\frac{b^{x'}}{C} = \begin{bmatrix} 0 & 0 & 0 \end{bmatrix} \tag{5.15}$$

$$\frac{b^{y'}}{C} = \begin{bmatrix} 0 & 0 & 0 \end{bmatrix} \tag{5.16}$$

The follow observations can be made regarding both the Camella and Wakuri designs:

- Comparison of data for both Camella and Wakuri designs for any given engine parameters reveals that these designs have nearly identical results. Careful comparison of the data shows that the Camella bearing has slightly improved performance factors (larger film ratio and smaller pressure ratio) as compared to the Wakuri bearing. The difference, however is so small that the remaining observations may apply equally to both designs.

- While it is not by a significant amount, the inner segment is a performance limiting factor particularly for offset ratio values $\frac{\delta}{C} > 0.5$.
- As the segment load number increases the film ratio decreases and the pressure ratio increases.
- The optimal range for the offset ratio appears to be $0.5 \leq \frac{\delta}{C} \leq 1$.
- The film ratio upper limit is 0.35 for all data, and the pressure ratio upper limit is 7.
- The pressure ratio does not exceed 5 for offset ratio $\frac{\delta}{C} \leq 1.25$
- The partially segmented designs have similar pressure ratios and slightly lower film ratios than the three segment full bearing design, in their respective optimal offset ratio ranges.

5.4 Alternative Designs: Full Offset Bearing, Three Segments

5.4.1 Segment Length Variation

The following observations can be made regarding the variable length offset bearing design charts (Figures A.49-A.60):

- Optimal performance values (largest film ratio and smallest pressure ratio across all segments) typically occurs in the offset ratio range $1 \leq \frac{\delta}{C} \leq 3.5$ for all of the data.
- For any given segment load number, and for offset ratio $\frac{\delta}{C} \leq 3.5$ the pressure ratio on the outer segments generally has little variation.
- The outer segments pressure ratio increases as the segment load number increases.
- The inner segment pressure ratio decreases for

  $$5 \leq \frac{\left(p^*_{cyl} A_{cyl}\right) (C/R)^2}{\mu \omega B D} \left(\frac{D}{B}\right)^2 \leq 50$$

  and increases for

  $$90 \leq \frac{\left(p^*_{cyl} A_{cyl}\right) (C/R)^2}{\mu \omega B D} \left(\frac{D}{B}\right)^2 \leq 500$$

- For $\alpha = 1.5$ (Figures A.49-A.54) the outer segments are a performance limiting factor for both film ratio and pressure ratio.
- In the optimal offset ratio range the data for $\alpha = 1.5$ generally indicates the following in comparison to the three equal segments design
  - Improved film ratio on the inner segments.
  - Slightly lower film ratio on the outer segments.
  - Generally higher or equivalent pressure ratio for all segments.
- For $\alpha = 0.5$ (Figures A.55-A.60) the inner segment is a performance limiting factor for the film ratio, but the outer segment is a performance limiting factor for the pressure ratio.

- For $\alpha = 0.5$ and $\frac{r}{L} = 0.3$ the pressure ratio on the inner segment drastically increases for $\frac{\delta}{C} > 2$.
- In the optimal offset ratio range the data for $\alpha = 0.5$ generally indicates the following in comparison to the three equal segments design
    - Improved film ratio on the outer segments.
    - Slightly lower film ratio on the inner segments.
    - Generally improved pressure ratio for all segments.

5.4.2 Journal Inclination

The following observations can be made regarding the inclined journal design charts (Figures A.61-A.66):

- While the pressure ratio on the outer segments generally is slightly higher than for the inner segments, the film ratio data seems to indicate generally equal minimum film ratios for all segments. Neither the inner nor outer segments clearly limit the bearing performance more than the other - unlike all previous designs.
- Optimal performance values (largest film ratio and smallest pressure ratio across all segments) typically occurs in the offset ratio range $1 \leq \frac{\delta}{C} \leq 3.5$ for all of the data.
- For any given segment load number, and for offset ratio $\frac{\delta}{C} \leq 3.5$ the film and pressure ratios on the outer segments generally have little variation.
- The outer segments pressure ratio increases as the segment load number increases.
- The inner segment pressure ratio decreases for

  $$5 \leq \frac{\left(p_{cyl}^{*} A_{cyl}\right)(C/R)^2}{\mu\omega BD}\left(\frac{D}{B}\right)^2 \leq 50$$

  and increases for

  $$90 \leq \frac{\left(p_{cyl}^{*} A_{cyl}\right)(C/R)^2}{\mu\omega BD}\left(\frac{D}{B}\right)^2 \leq 500$$

- While the performance seems more balanced between inner and outer segments, except for low segment load numbers, the inclined journal data here does not seem to show significantly improved performance as compared to the $\beta = 0°$ case (three equal segments).

Chapter 6

Conclusions

The work done in this thesis provides an encompassing study of offset journal bearings. Chapter 4 provided a way, not previously shown in the literature, to fully nondimensionalize the offset bearing problem for two stroke engines. A broad design space was developed using production engine data. It was determined that across the design space of this thesis the sidewall loading on the piston has a very negligible effect on bearing performance. It was also determined that the load in a two stroke engine is not expected to reverse direction in the design space - indicating that a partial arc offset bearing is a generally viable option in the piston pin bearing.

Using the above formulation and assumptions, design trends not previously found in the literature for two stroke engine piston pin bearings were determined. For the equal length un-inclined two and three segment designs, the design trends are all very similar. Peak performance values are all found in the offset ratio range $1 \leq \frac{\delta}{C} \leq 3.5$. The limiting part of the offset bearing is almost always the outer segment(s).

As the offset ratio is increased the cyclic film thickness ratio reaches some peak value on the inner and outer segments and then decreases, or in the case of the outer segments it may plateau after it peaks. For short bearing segment load numbers above 90 and for finite bearing load numbers above 40, the film ratio often appears insensitive to offset ratio specification. In ranges where the bearing performance is insensitive to the offset ratio specification, the manufacturing tolerances for the offset may not have to be as severe.

The cyclic maximum pressure ratio on the inner segments appears to be generally more dependent on offset ratio, but in the optimal offset ratio range, the outer segments often show little variation in the pressure ratio.

The Wakuri and Camella bearings have essentially identical design trends. The optimal offset ratio range is $0.5 \leq \frac{\delta}{C} \leq 1$. Although the inner and outer segments do not differ much in the optimal offset ratio range, the inner segment is typically where the extreme performance values occur. In their optimal offset ratio range, Wakuri and Camella designs do seem to offer comparable performance to their full offset bearing counterparts. This is a promising realization as it means only the sleeve or the journal needs to be offset - potentially reducing manufacturing cost.

Compared to the full offset bearing, the film ratio on the outer segments for the Camella and Wakuri designs more distinctly decreases after the peak film ratio occurs. The pressure ratio on both the inner outer segments is quite variable. On the outer segments the pressure ratio is typically in the range 1-3 for lower offset ratios. In the middle of the offset ratio range a minimum occurs, and at the maximum offset ratio of 1.75 the pressure ratio is generally in the range 3.5 to 5.5. On the inner segments, for the lowest offset ratio the pressure ratio is generally in the range 0.5 to 1.5, and the the pressure ratio rises to above 7 for all segment load numbers at the highest offset ratio.

Two other design options were tested for the three segment full offset bearing. These options involved modifying the segment lengths and inclining the offset bearing journal. These were done with the hopes of balancing the loads more evenly between inner and outer segments.

The length variation study generally did not seem to provide overall better performance. While the loads may be more balanced, the extreme performance values did not change significantly. In most cases, the inner segment, rather than the outer segment, simply became the performance limiting component of the bearing.

The journal inclination study did seem to generally provide good performance and balance the extrema between the inner and outer segments. The improvement seen over the three equal segment un-inclined offset bearing is fairly dependent, however, on the segment load number. The inclined journal seemed to perform better for lower segment load numbers. If the cost to manufacture the incline was greater than the cost to make the standard three segment offset bearing, it is hard to say that it would be worthwhile based on the study presented in this thesis.

The numerous design charts here are a small sample of the extensive number of ways that the offset bearing could be configured. For example, bearing inclination and variable segment lengths could be combined to find some configuration which has an overall improved performance without any caveats over a three equal segments full offset bearing. Designs with more than two axes, or with offset components that do not have equal magnitude could also be considered in additional studies.

The design charts could also guide finite element and experimental studies of the offset bearing. Future work could confirm or expand upon the design space used in this thesis as well. Overall, the design charts in Appendix A, with their respective observations, provide some insight into the performance of the offset bearing over a large design space. This insight may be used not only for those who wish to utilize offset bearings more knowledgeably, but may also be used to guide and direct future studies of offset bearings. The work and knowledge resulting from this thesis will hopefully encourage the use and study of offset bearings, helping to remove the worry of inadequate hydrodynamic lubrication from the list of obstacles in applications such as two stroke engines.

References

[1] Allaire, P. E., and Flack, R. D., 1981, "Design of Journal Bearings for Rotating Machinery," In Proceedings of the 10th Turbomachinery Symposium., Tex A&M Univ, Turbomach Lab, pp. 25–45.

[2] Sammons, H., and Chatterton, E., 1954, "Napier Nomad Aircraft Diesel Engine," In SAE Meeting Jun 6-11, Society of Automotive Engineers (SAE).

[3] Wakuri, Y., Ono, S., and Soejima, M., 1982, "On The Lubrication of Crosshead-Pin Bearing with Eccentric Journal," *Bulletin of the JSME,* ***25***(206), pp. 1312–1320.

[4] Anonymous, 1964, "Camella Restricted-Clearance Bearings," *Naval Engineers Journal,* ***76***(2), pp. 219–222.

[5] Maciotta, R., 1977, "Uber Den Gegenwartigen Entwicklungsstand Der Gmt-dieselmotoren - 5 Jahre Nach Beginn Ihrer Produktion (Present Development of Gmt Engines - 5 Years After The Beginning of Their Production)," *Motortechnische Zeitschrift: MTZ,* ***38***, pp. 61–66.

[6] Ciliberto, G., and Mariani, L., 1977, "Évolution du Coussinet de Tête à Crosse Dans les Moteurs à 2 Temps (Evolution of the Crosshead Bearing in 2-Cycle Engines)," In CIMAC 12th International Congress on Combustion Engines, Tokyo, Japan Paper A21.

[7] Dion, E. P., Klyza, C. A., MacKenzie, R. G., and Wahl, M. H., 2014, "Rocking Journal Bearings for Two-Stroke Cycle Engines,", US20140238360 A1.

[8] Foege, A. G., 2014, "Piston Assembly Having Offset Bearing,", US8763584 B2.

[9] Booker, J. F., Goenka, P. K., and Van Leeuwen, H. J., 1982, "Dynamic Analysis of Rocking Journal Bearings with Multiple Offset Segments," *ASME J. Tribol.,* ***104***(4), pp. 478–490.

[10] Wakuri, Y., and Soejima, M., 1985, "Studies On Load Carrying Capacity of An Offset-typed Crosshead-pin Bearing," *Proceedings of the JSLE International Trib. Conf., Tokyo, Japan, July 8-10,* ***2***, pp. 319–324.

[11] Fromm, L., 2014, "Achieving the Most Stringent CO2 Commercial Truck Standards with Opposed Piston Engine," In Heavy-Duty, On- and Off-Highway Engines 9th International MTZ Conference, Achates Power, Inc.

[12] Fromm, L., Herold, R., Koszewnik, J., and Regner, G., 2012, "Modernizing the Oppose-Piston, Two-Stroke Engine for More Eficient Commercial Vehicle Applicatinos," In 7th MTZ Conference Heavy-Duty, On- and Off-Highway Engines, Achates Power, Inc.

[13] Fromm, L., Herold, R., Koszewnik, J., and Regner, G., 2014, "Modernizing the Opposed-Piston Engine for More Efficient Military Ground Vehicle Applications," In NDIA Ground Vehicle Systems Engineering and TEchnology Symposium, Achates Power, Inc.

[14] Beagle, W. P., and Booker, J. F., 2000, "Multiple Offset Journal Bearing With Stepped Diameters for Ease of Assembly,", US6120189 A.

[15] Booker, J. F., and Olikara, P., 1984, "Dynamics of offset Bearings: Parametric Studies," *ASME J. Tribol.,* ***106***(3), pp. 352–359.

[16] Olikara, P., 1981, "Dynamics of Offset Bearings," Thesis, Cornell University.

[17] Boedo, S., and Anderson, D., 2015, "Oscillating Journal Bearings under Steady Load: A Numerical Study of Limiting Cases," *ASME J. Tribol.*

[18] Boedo, S., and Booker, J. F., 1988, "Transient Dynamics of Engine Bearing Systems," In Proc. 15th Leeds-Lyon Symposium on Tribology In Tribological Design of Machine Elements eds. D. Dowson, C.M. Taylor, D. Berthe Elsevier, 1989, pp.323-332.

[19] Boedo, S., 2010, "Practical Tribological Issues in Big End Bearings," In *Tribology and Dynamics of Engine and Powertrain*, H. Rahnejat, ed., 1st ed. Woodhead Publishing, Cambridge, ch. 19, pp. 615–635.

[20] Blais, T., 2013, "Analysis of Connecting Rod Bearing Design Trends Using a Mode-Based Elastohydrodynamic Lubrication Model," Master's thesis, Rochester Institute of Technology.

[21] Booker, J. F., 1965, "Dynamically Loaded Journal Bearings – Mobility Method of Solution," *ASME J. Basic Eng.,* ***87***(3), pp. 537–546.

[22] Childs, D., Moes, H., and van Leeuwen, H., 1977, "Journal Bearing Impedance Descriptions for Rotordynamic Applications," *ASME J. Tribol.,* ***99***(2), pp. 198–210.

[23] Booker, J. F., 2013, "Mobility/Impedance Methods: A Guide for Application," *ASME J. Tribol.,* ***136***(2), pp. 024501–024501.

[24] Goenka, P. K., 1984, “Analytical Curve Fits for Solution Parameters of Dynamically Loaded Journal Bearings,” *ASME J. Tribol.,* ***106***(4), pp. 421–427.

[25] Booker, J. F., 1969, “Dynamically Loaded Journal Bearings: Maximum Film Pressure,” *ASME J. Tribol.,* ***91***(3), pp. 534–537.

[26] Anonymous, 1997, Diesel Engine Analysis Guide Technical Results TR-107135, Electric Power Research Institute.

[27] Designs, E. D. D. R., and Organisation, S., 2013, Development of Electronic Unit Injector (EUI) Fuel System for DLW Built 16-Cylinder 4500 HP EMD 710 G3B Locomotives Technical Specification TS/ED/2012/65, Government of India Ministry of Railways, Manak Nagar, Lucknow-226011.

[28] Magazinoviȅ, 1998, “Shaftline Design Considerations of Five-Cylinder Low-Speed Propulsion Plants,” In 13th Symposium on Theory and Practice of Shipbuilding.

Appendix A

Design Charts

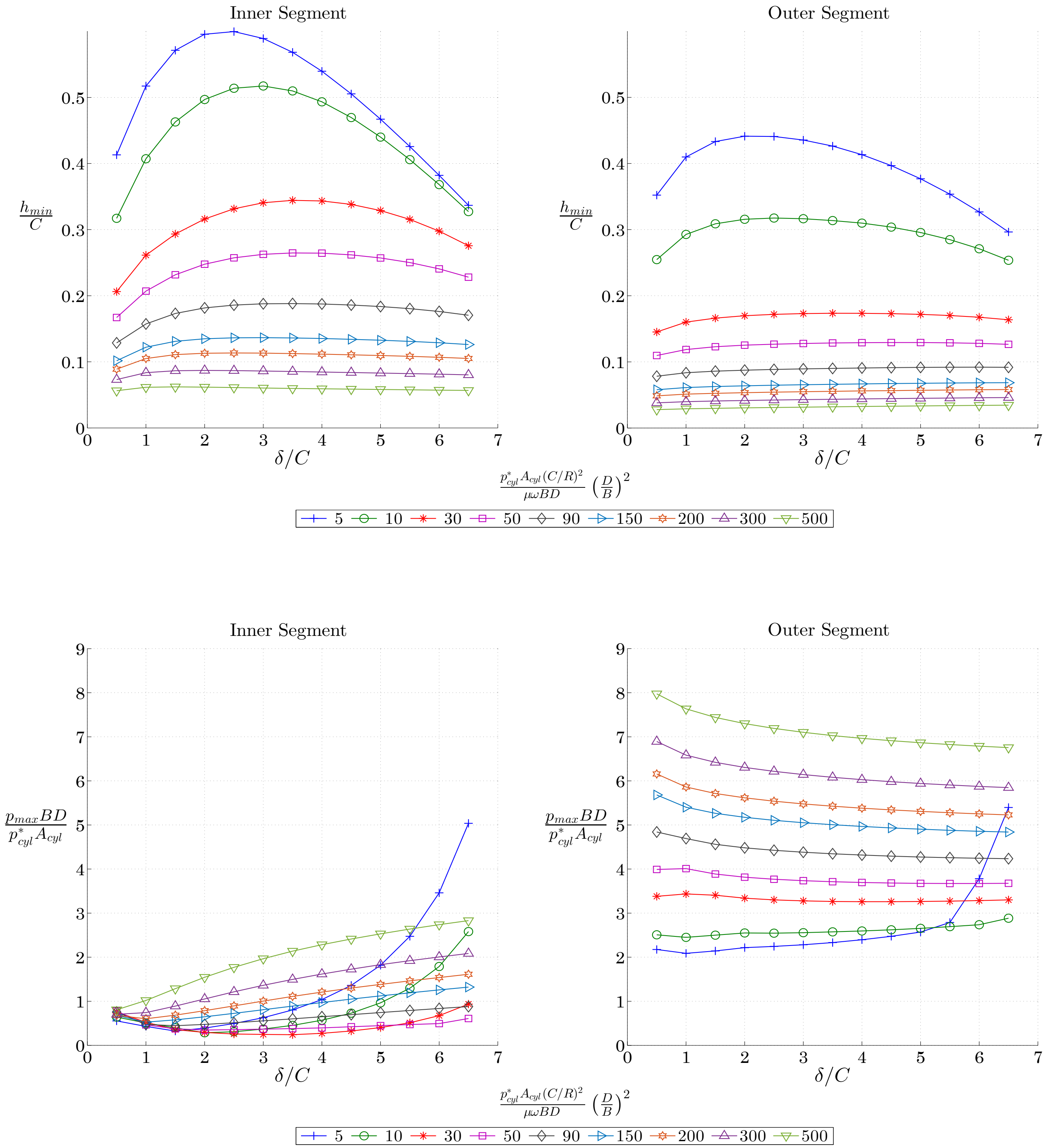

Figure A.1: Full Offset, n=2, $\frac{M_p r\omega^2}{p^*_{cyl}A_{cyl}} = 0.05$; $\frac{r}{L} = 0.2$ (Short)

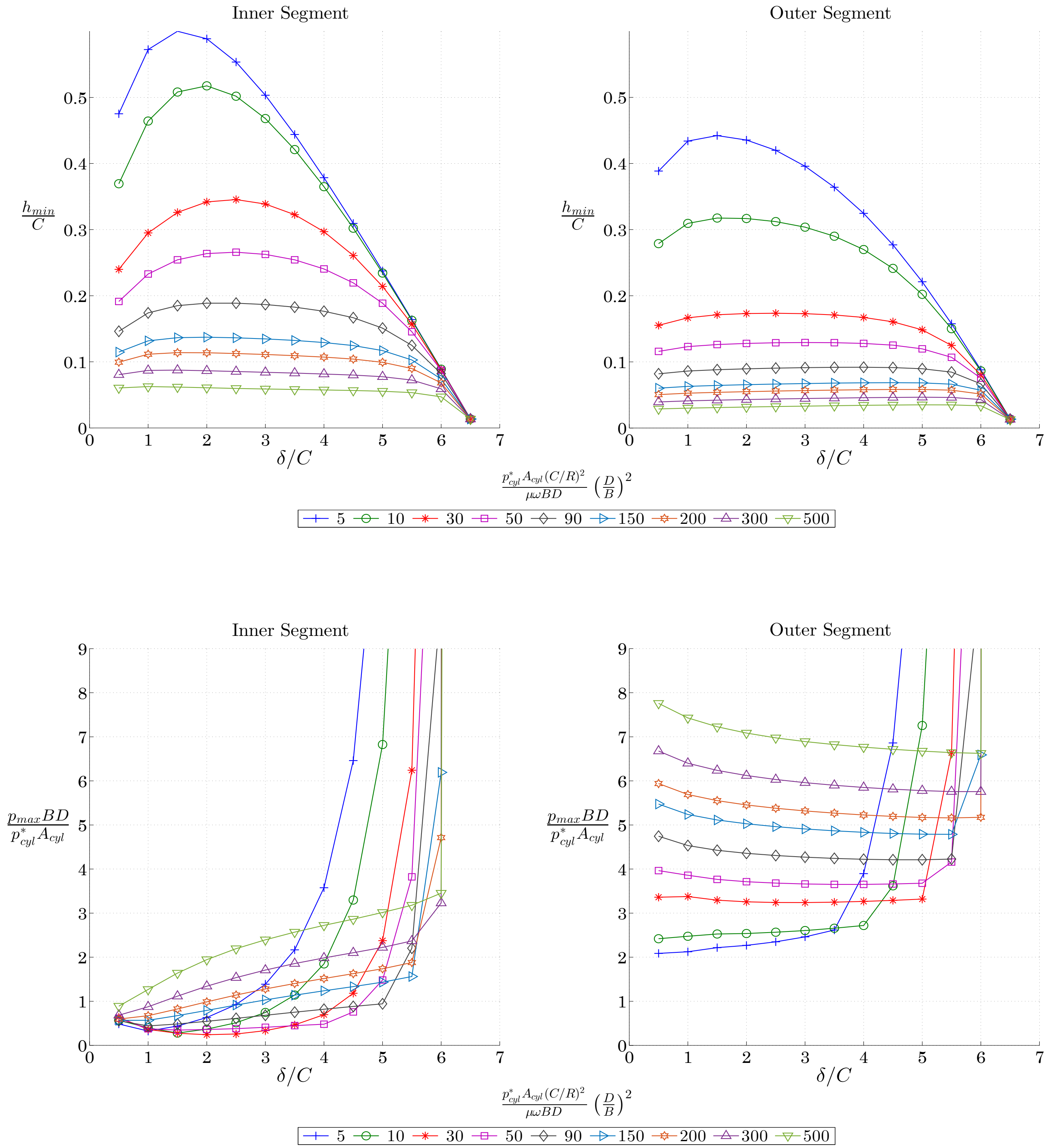
Inner Segment

Outer Segment

Inner Segment

Outer Segment

Figure A.2: Full Offset, n=2, $\frac{M_p r\omega^2}{p^*_{cyl}A_{cyl}} = 0.05$; $\frac{r}{L} = 0.3$ (Short)

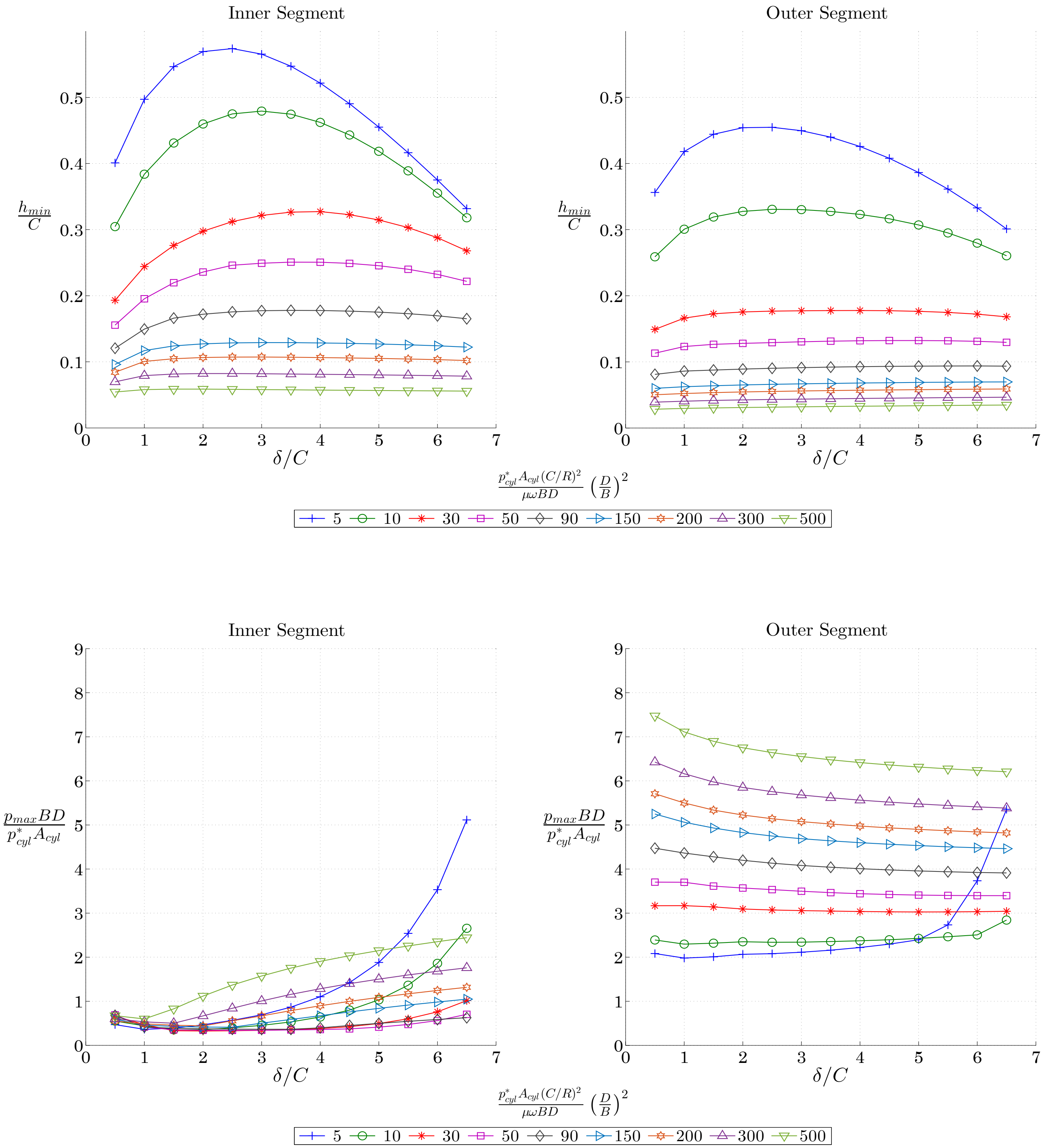

Figure A.3: Full Offset, n=2, $\frac{M_p r\omega^2}{p^*_{cyl}A_{cyl}} = 0.1$; $\frac{r}{L} = 0.2$ (Short)

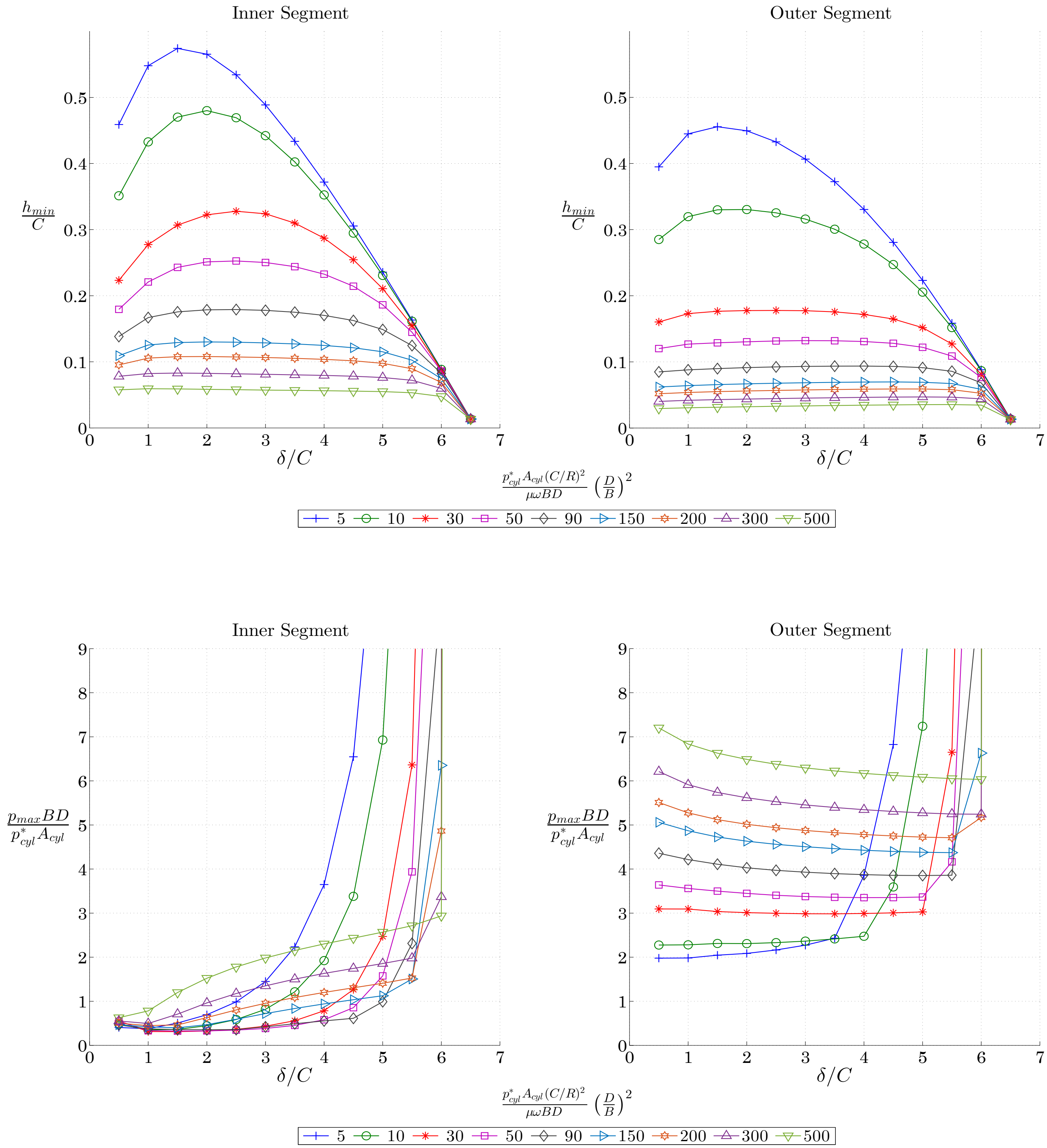

Figure A.4: Full Offset, n=2, $\frac{M_p r\omega^2}{p^*_{cyl}A_{cyl}} = 0.1$; $\frac{r}{L} = 0.3$ (Short)

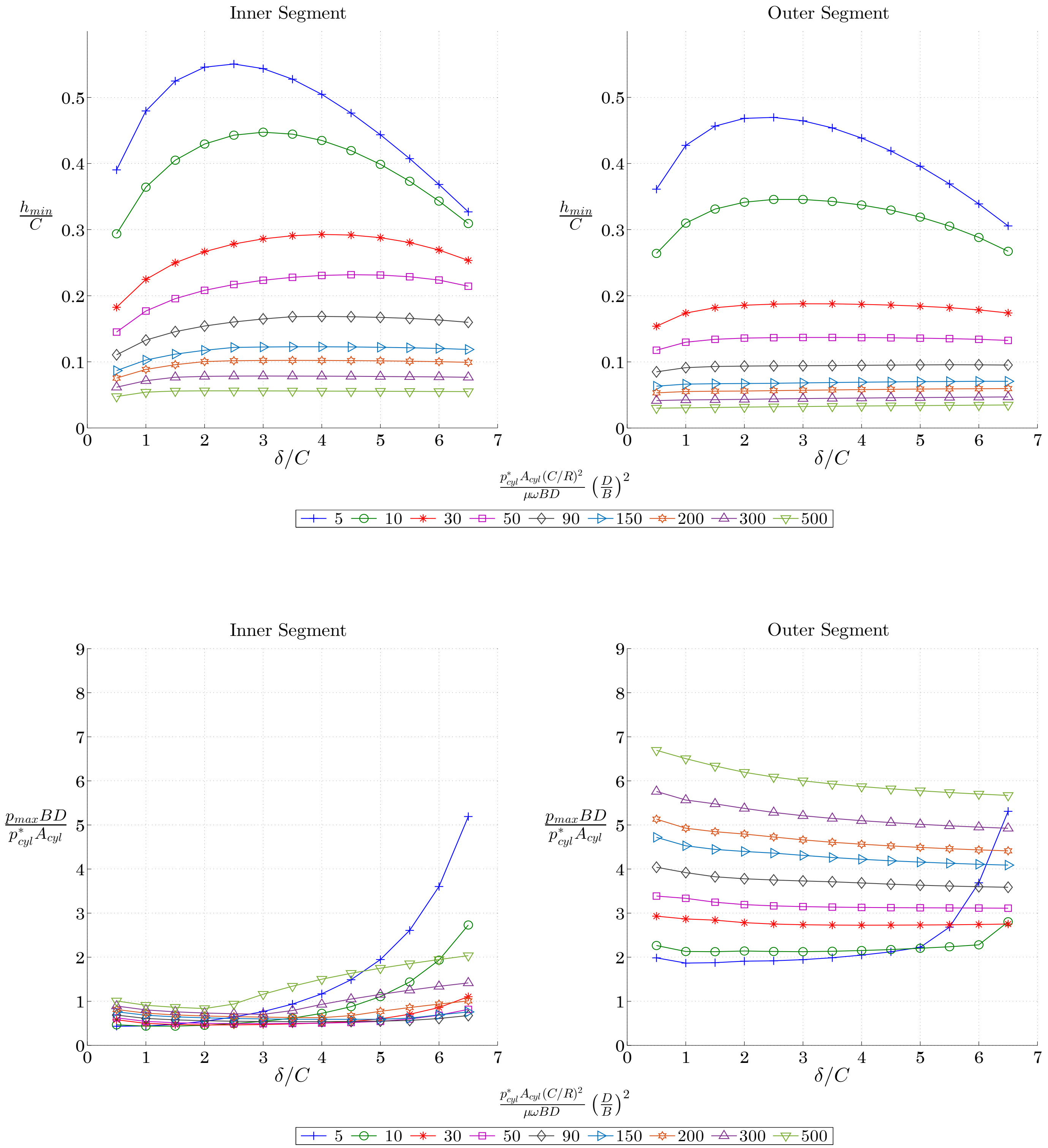

Figure A.5: Full Offset, n=2, $\frac{M_p r\omega^2}{p^*_{cyl}A_{cyl}} = 0.15$; $\frac{r}{L} = 0.2$ (Short)

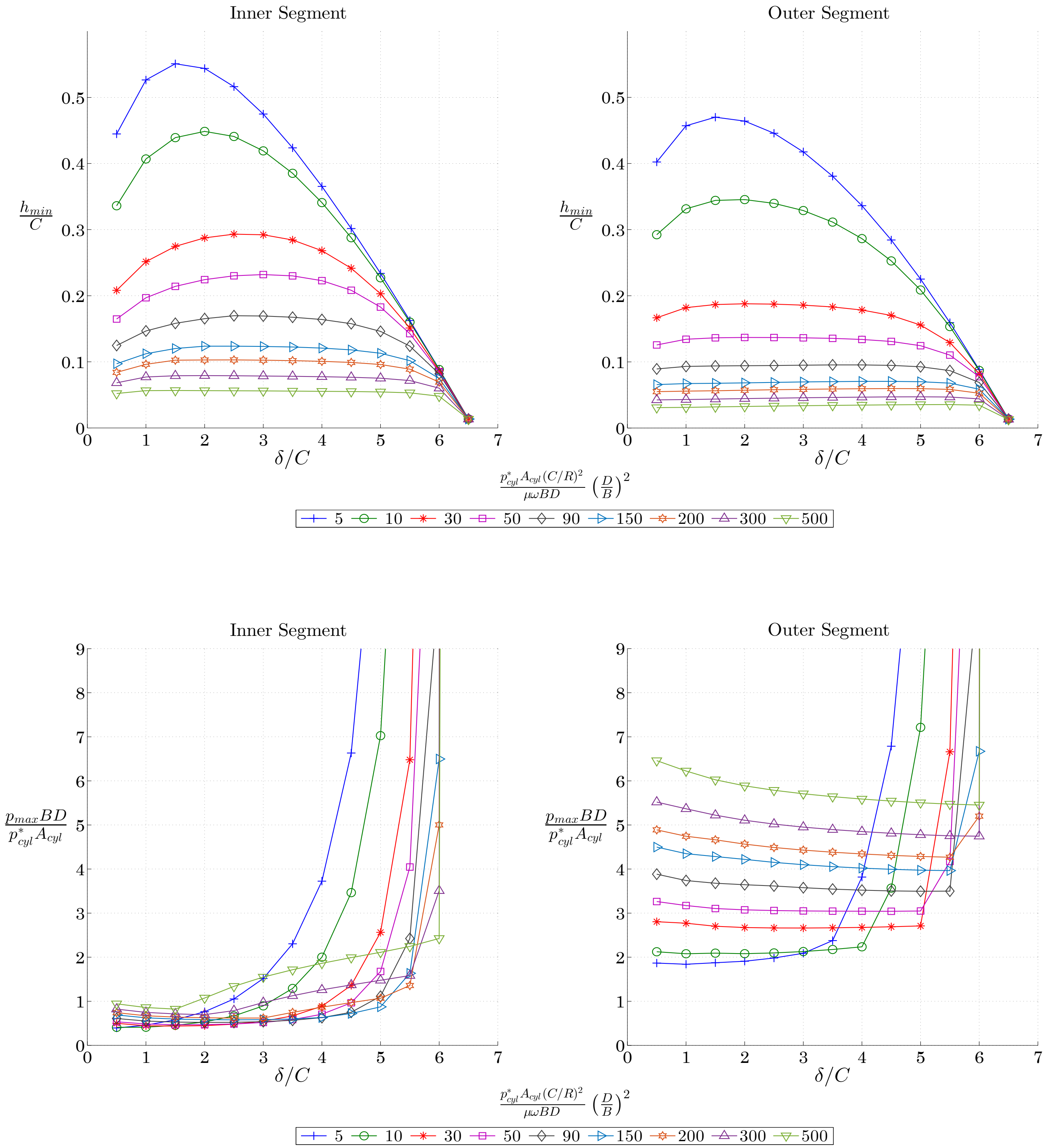

Figure A.6: Full Offset, n=2, $\frac{M_p r\omega^2}{p^*_{cyl}A_{cyl}} = 0.15$; $\frac{r}{L} = 0.3$ (Short)

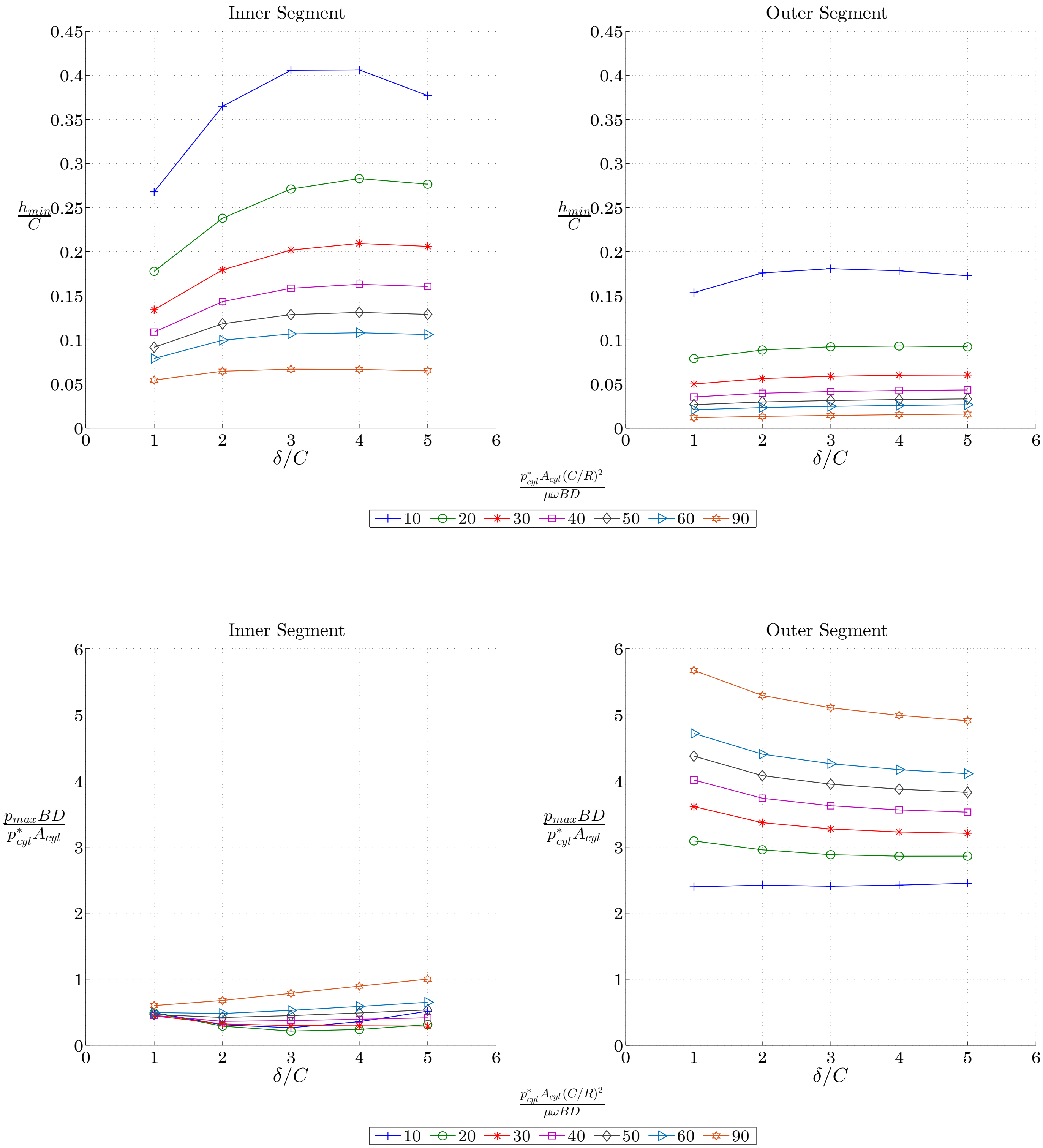

Figure A.7: Full Offset, n=2, $\frac{M_p r\omega^2}{p^*_{cyl}A_{cyl}}$ = 0.05; $\frac{r}{L}$ = 0.2 (Finite, B/D = 1)

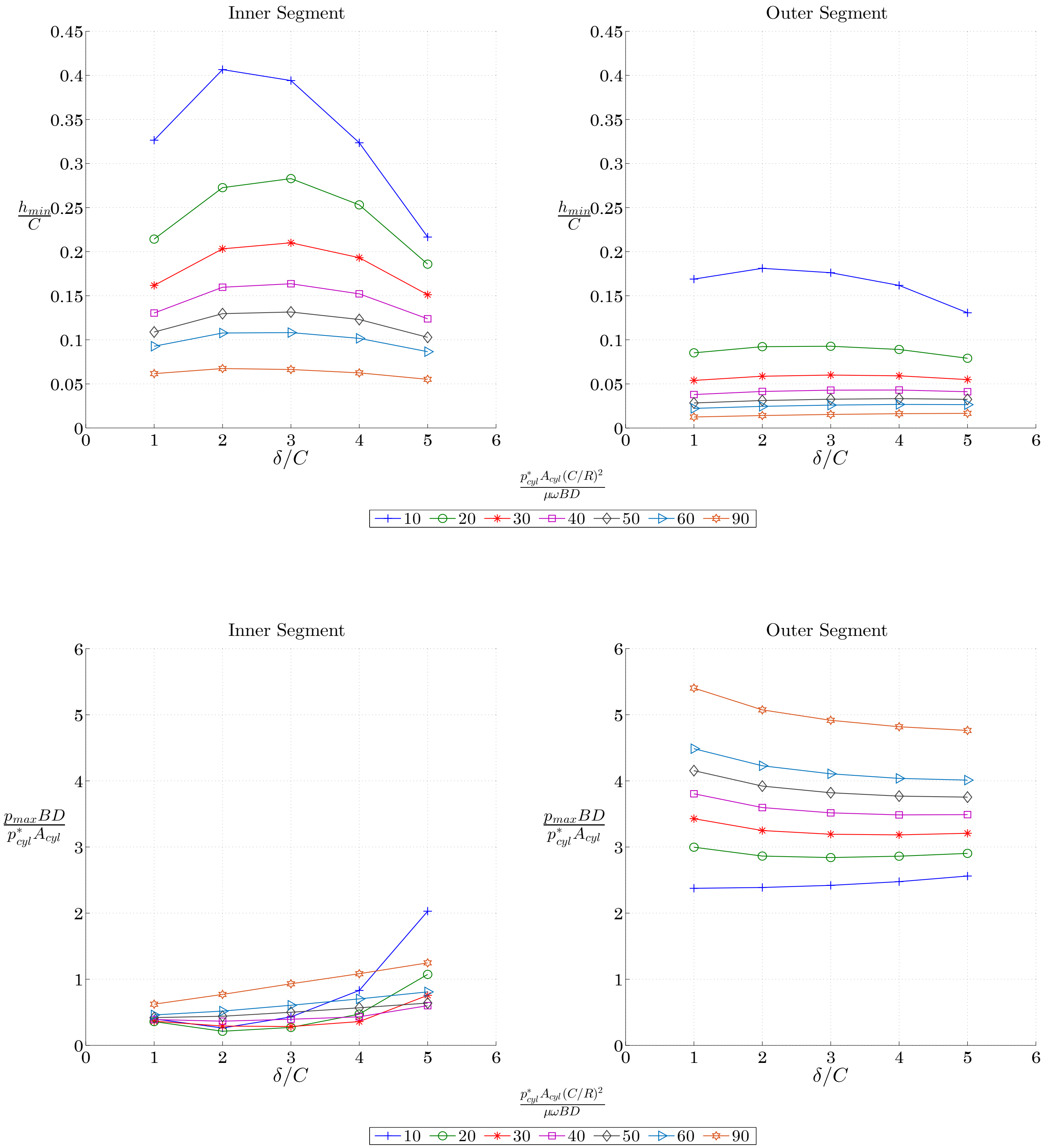

Figure A.8: Full Offset, n=2, $\frac{M_p r\omega^2}{p^*_{cyl}A_{cyl}}$ = 0.05; $\frac{r}{L}$ = 0.3 (Finite, B/D = 1)

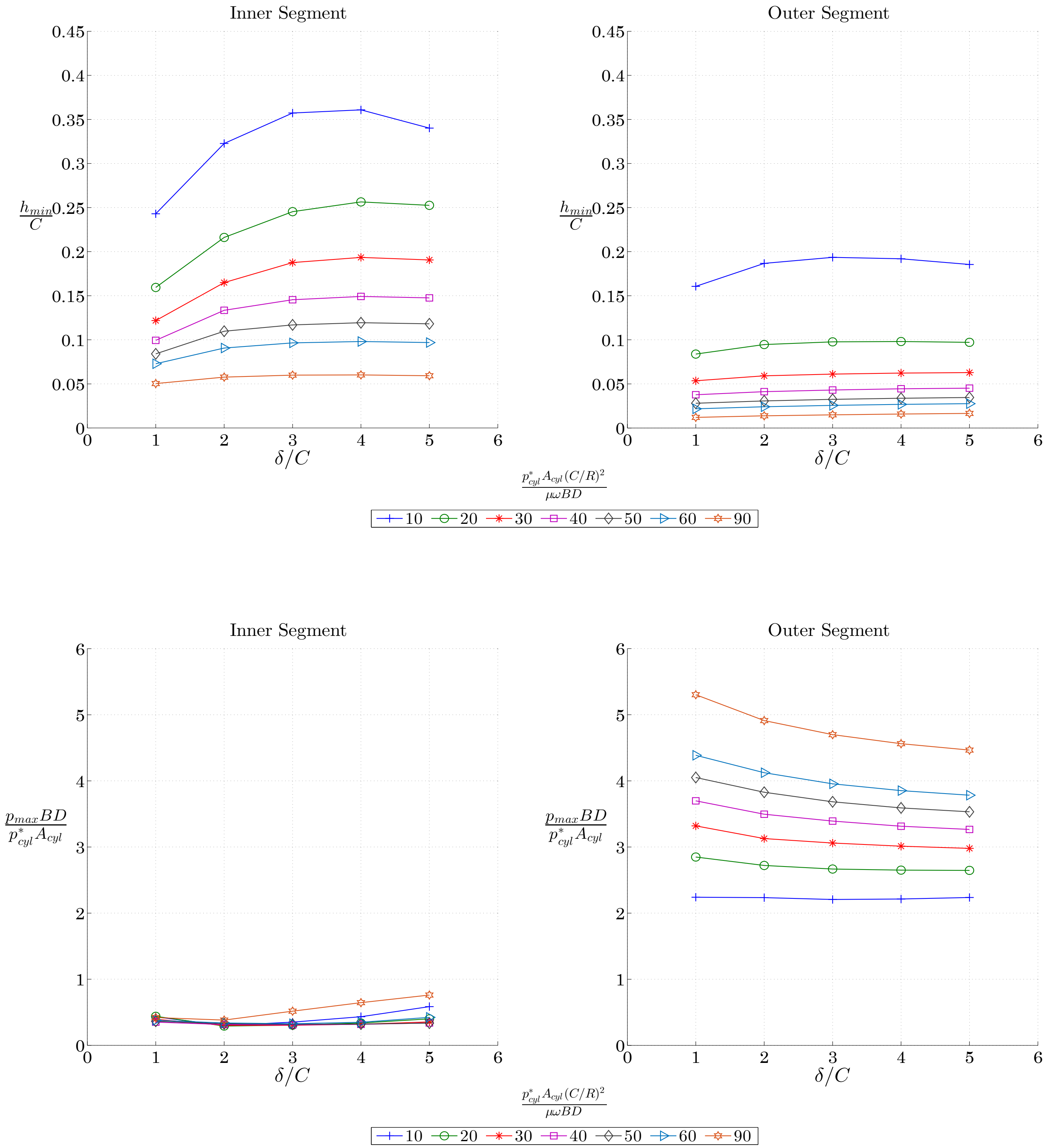

Figure A.9: Full Offset, n=2, $\frac{M_p r\omega^2}{p^*_{cyl}A_{cyl}}$ = 0.1; $\frac{r}{L}$ = 0.2 (Finite, B/D = 1)

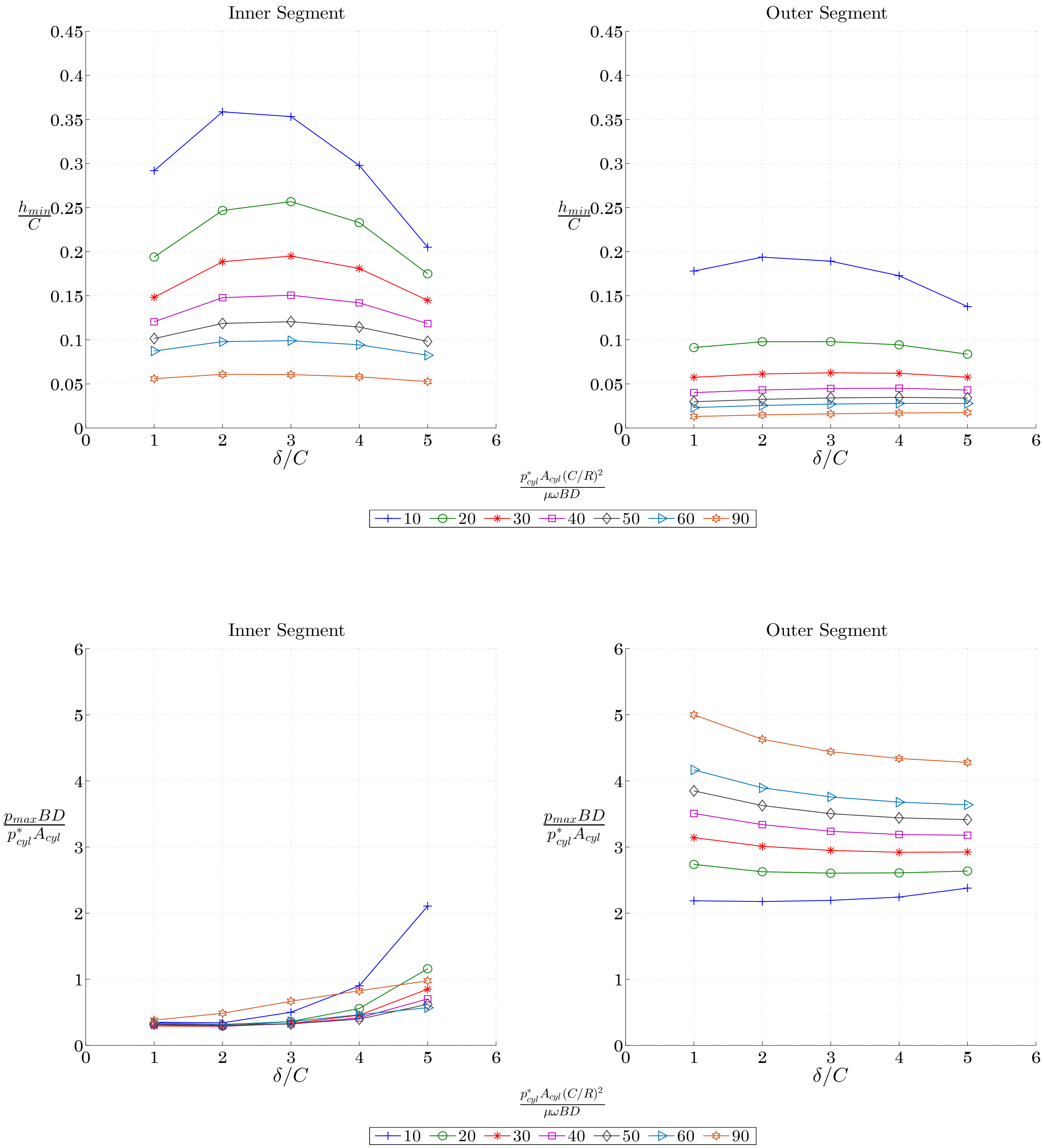

Figure A.10: Full Offset, n=2, $\frac{M_p r\omega^2}{p^*_{cyl}A_{cyl}}$ = 0.1; $\frac{r}{L}$ = 0.3 (Finite, B/D = 1)

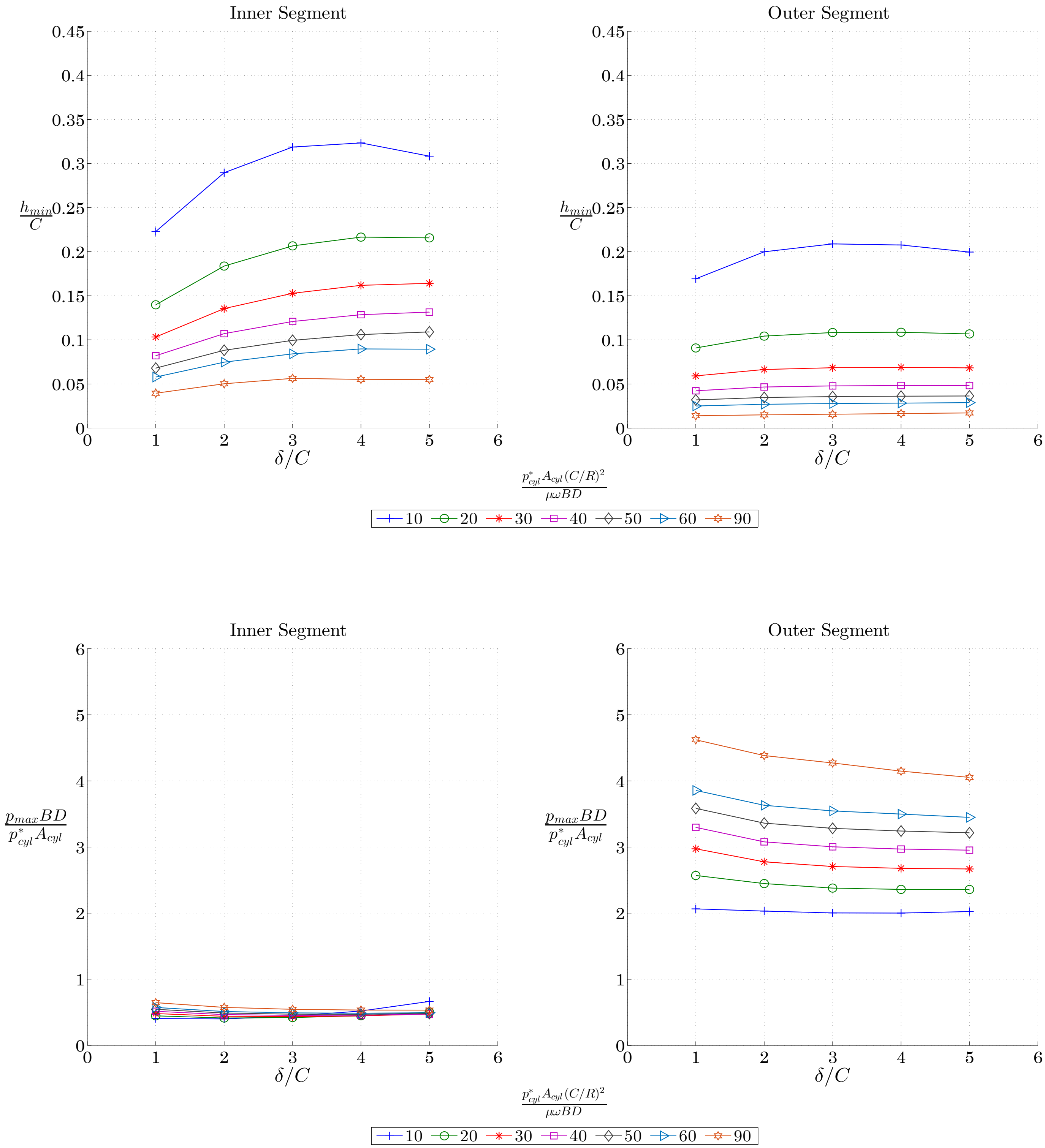

Figure A.11: Full Offset, n=2, $\frac{M_p r\omega^2}{p^*_{cyl}A_{cyl}} = 0.15$; $\frac{r}{L} = 0.2$ (Finite, B/D = 1)

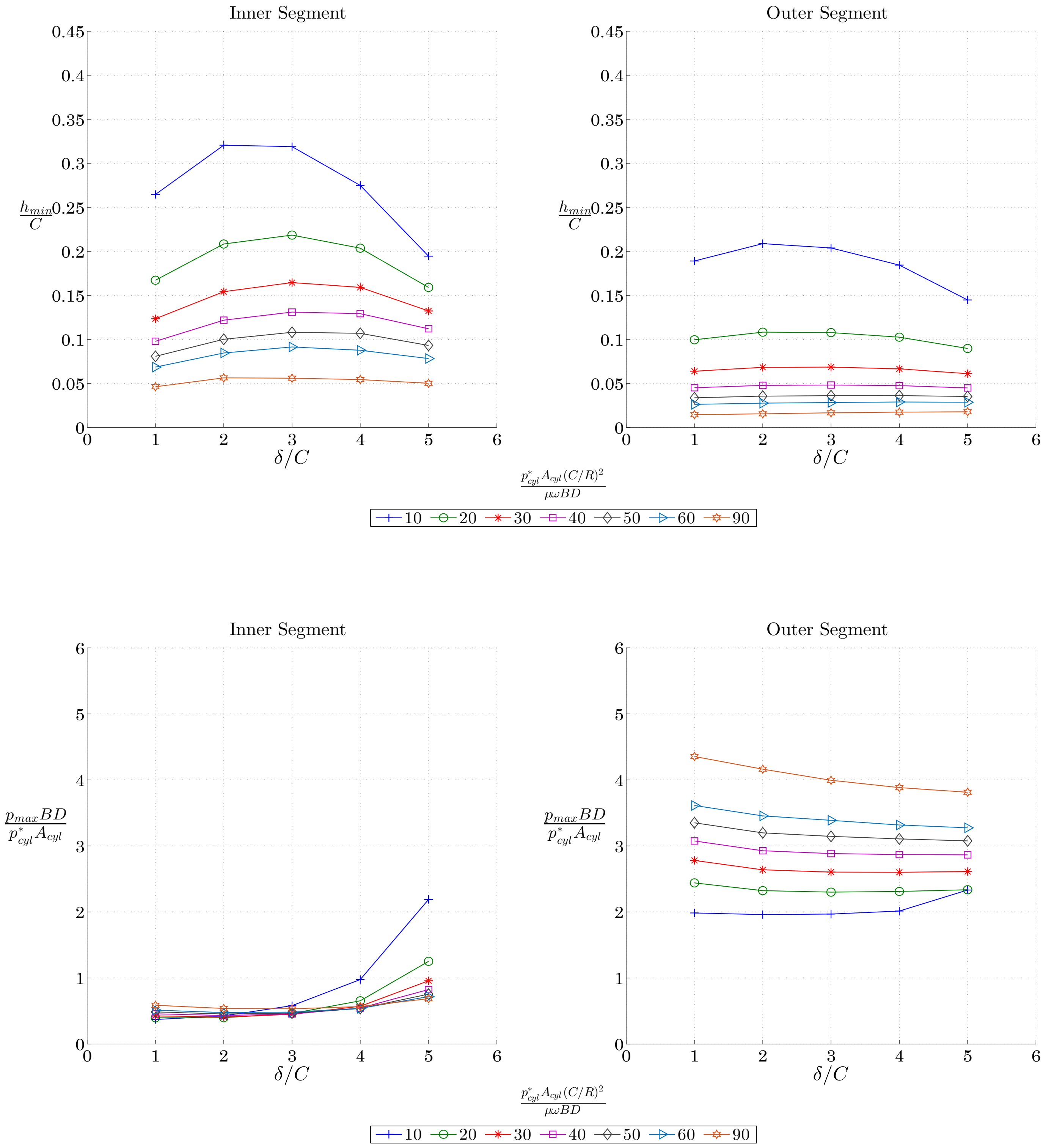

Figure A.12: Full Offset, n=2, $\frac{M_p r\omega^2}{p^*_{cyl}A_{cyl}} = 0.15$; $\frac{r}{L} = 0.3$ (Finite, B/D = 1)

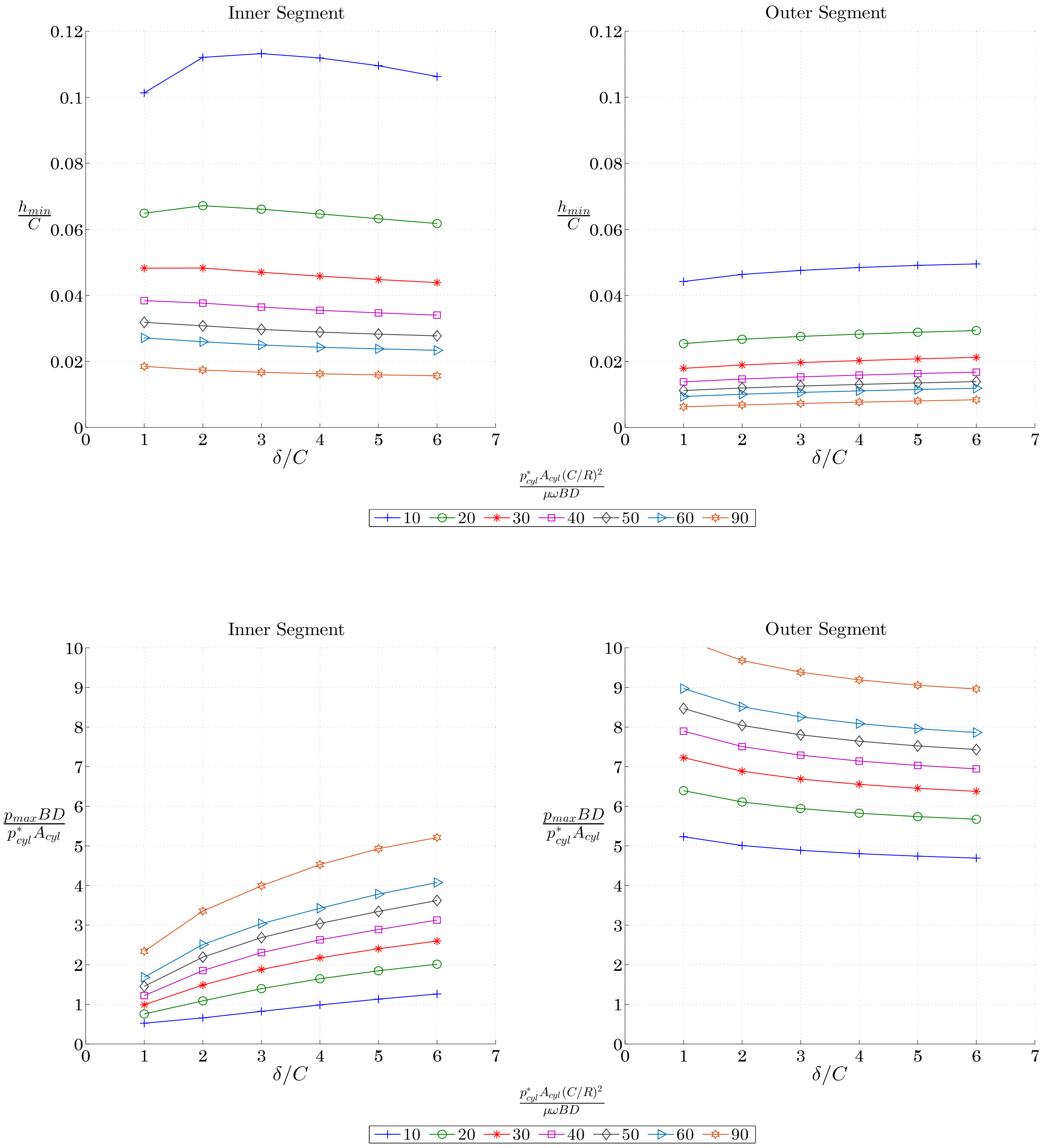

Figure A.13: Full Offset, n=2, $\frac{M_p r\omega^2}{p^*_{cyl}A_{cyl}}$ = 0.05; $\frac{r}{L}$ = 0.2 (Finite, B/D = 1/4)

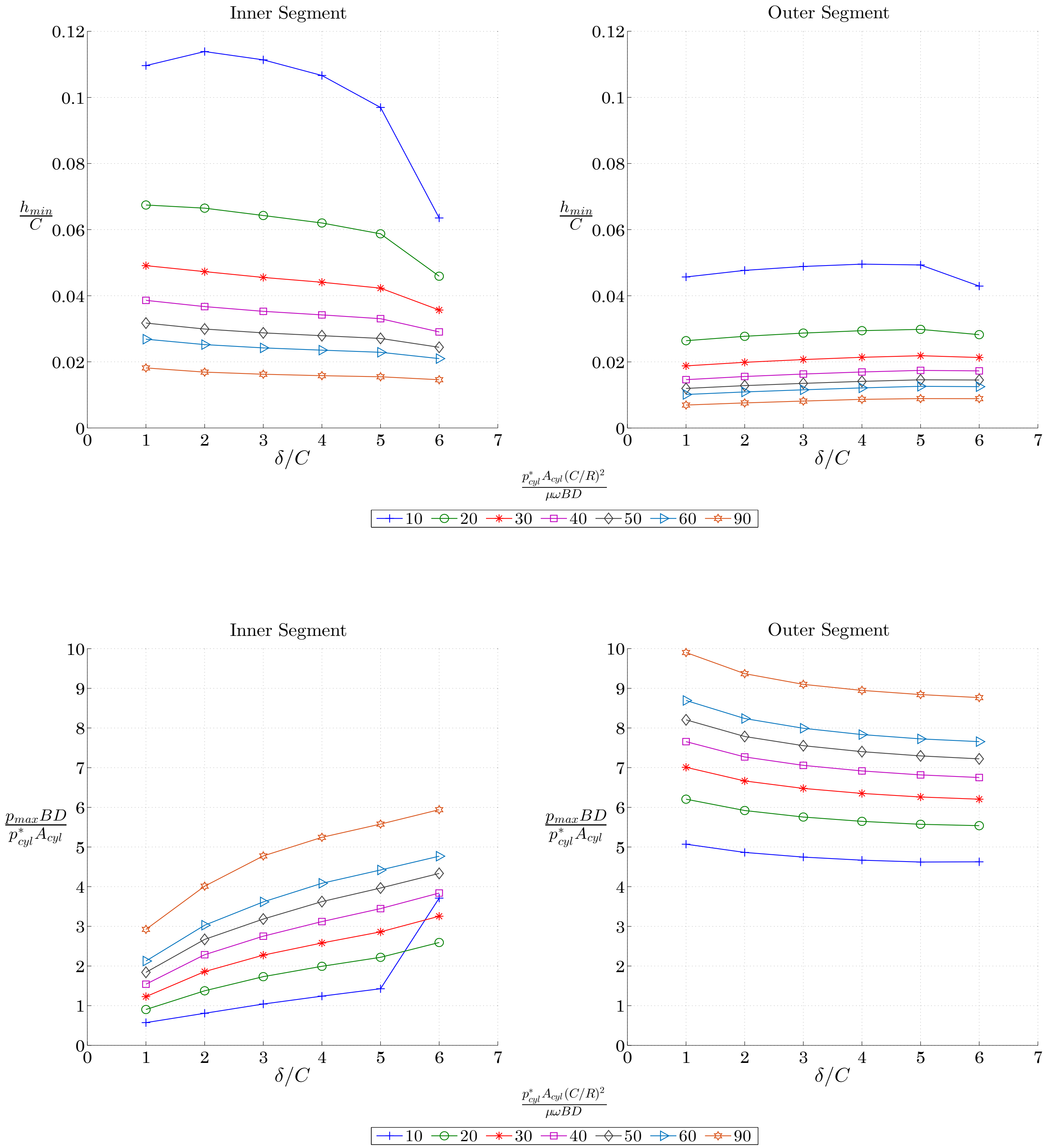

Figure A.14: Full Offset, n=2, $\frac{M_p r\omega^2}{p^*_{cyl}A_{cyl}}$ = 0.05; $\frac{r}{L}$ = 0.3 (Finite, B/D = 1/4)

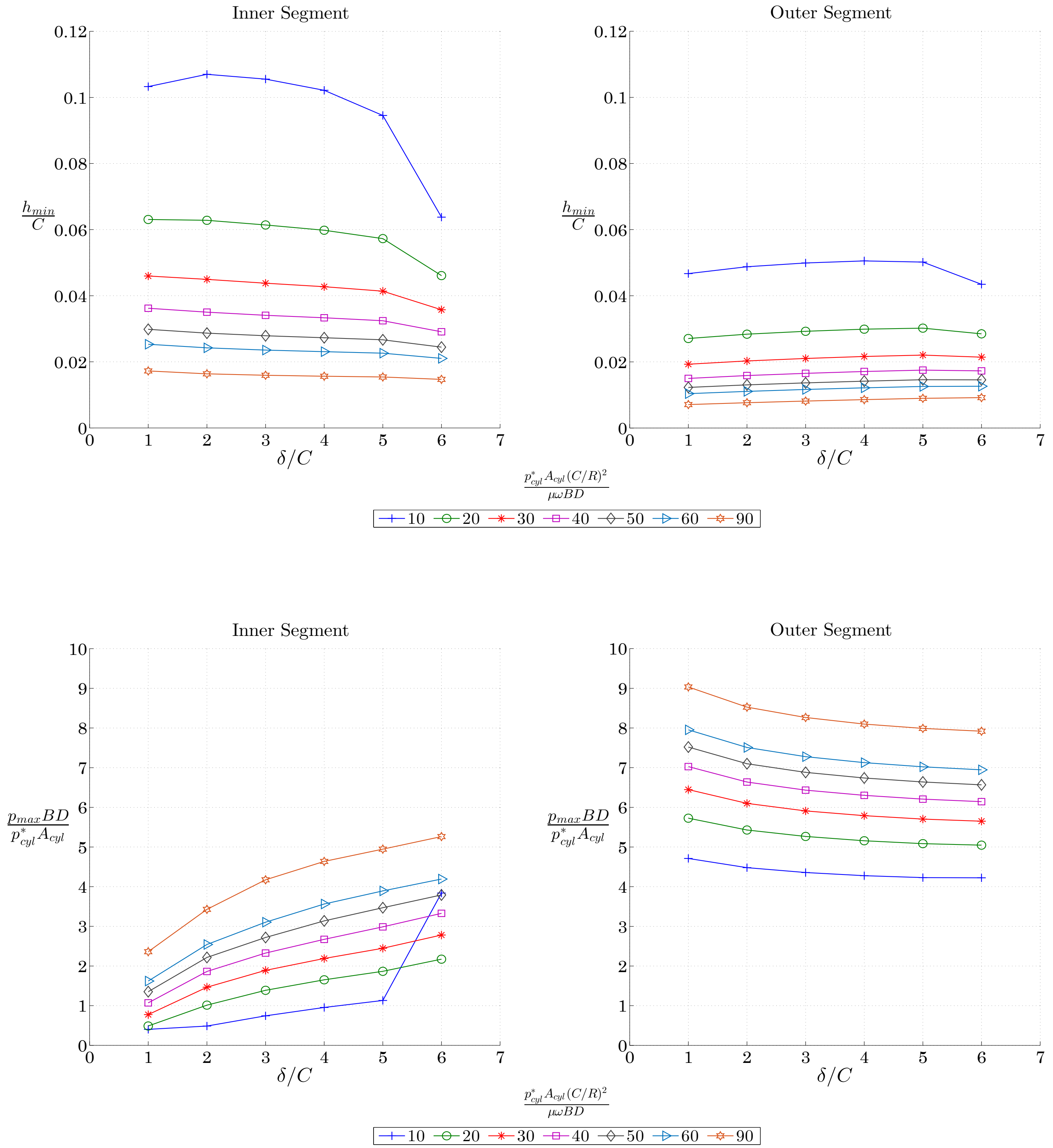

Figure A.15: Full Offset, n=2, $\frac{M_p r\omega^2}{p^*_{cyl}A_{cyl}}$ = 0.1; $\frac{r}{L}$ = 0.3 (Finite, B/D = 1/4)

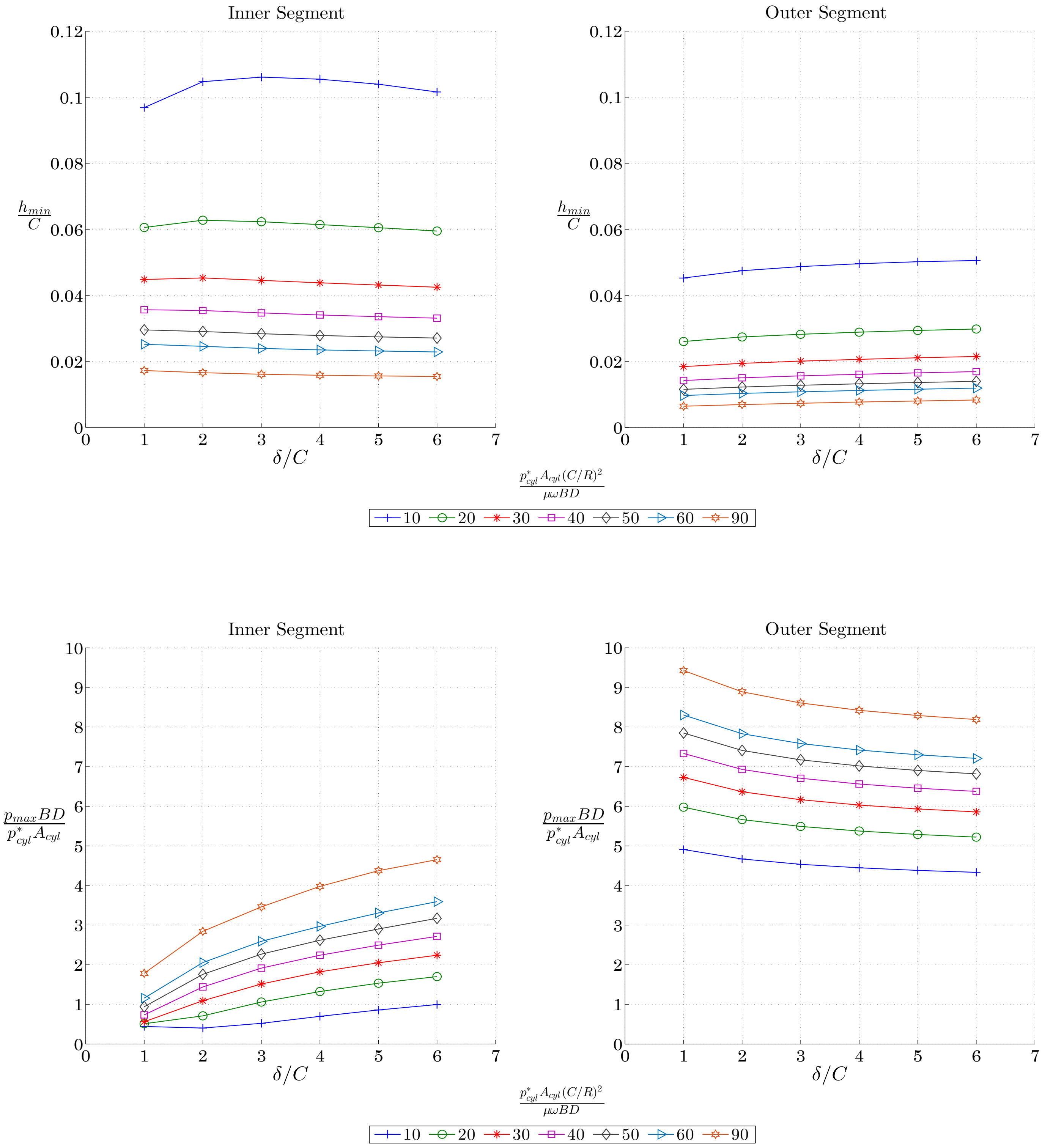

Figure A.16: Full Offset, n=2, $\frac{M_p r\omega^2}{p^*_{cyl}A_{cyl}}$ = 0.1; $\frac{r}{L}$ = 0.2 (Finite, B/D = 1/4)

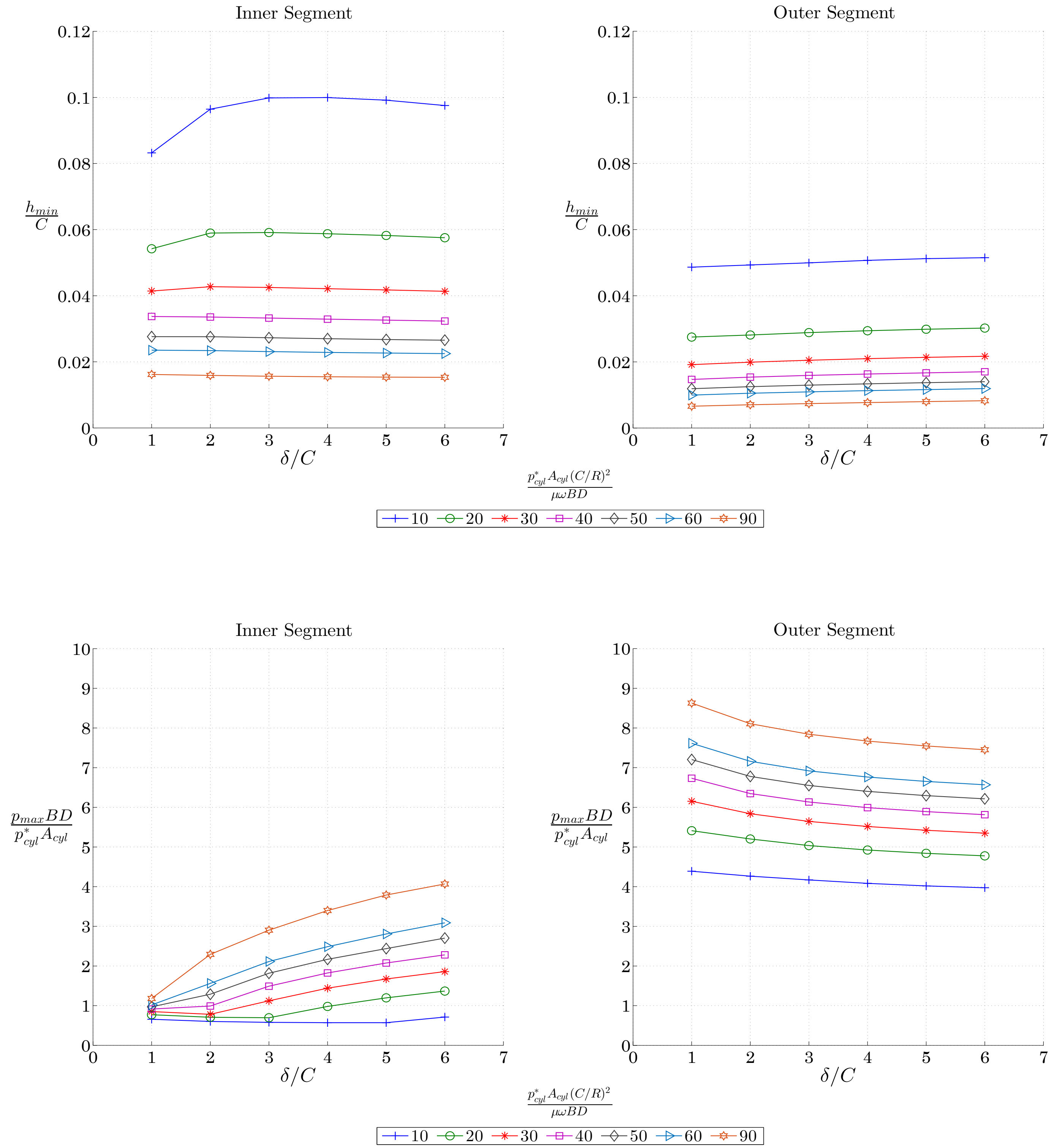

Figure A.17: Full Offset, n=2, $\frac{M_p r\omega^2}{p^*_{cyl}A_{cyl}}$ = 0.15; $\frac{r}{L}$ = 0.2 (Finite, B/D = 1/4)

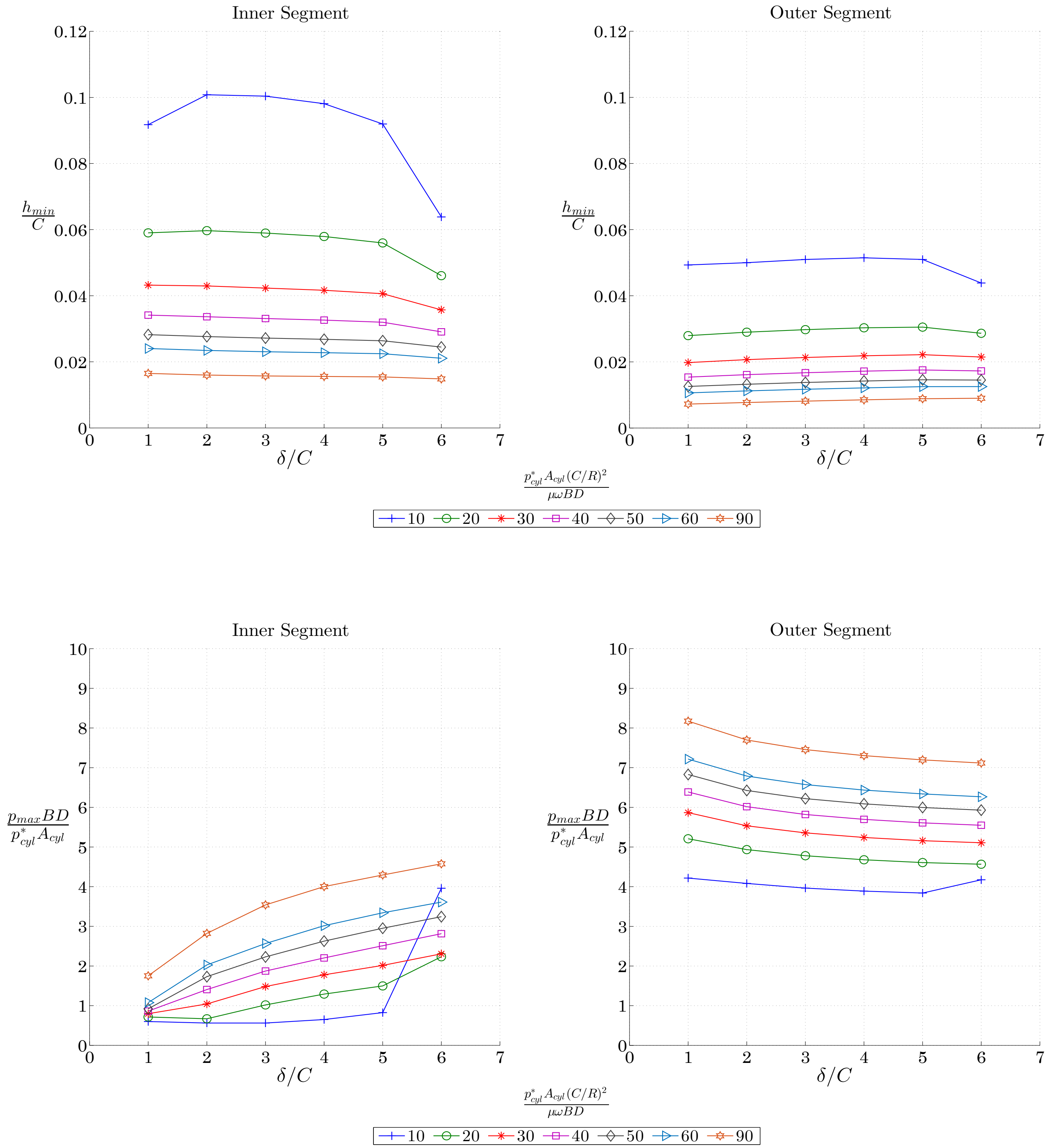

Figure A.18: Full Offset, n=2, $\frac{M_p r\omega^2}{p^*_{cyl}A_{cyl}}$ = 0.15; $\frac{r}{L}$ = 0.3 (Finite, B/D = 1/4)

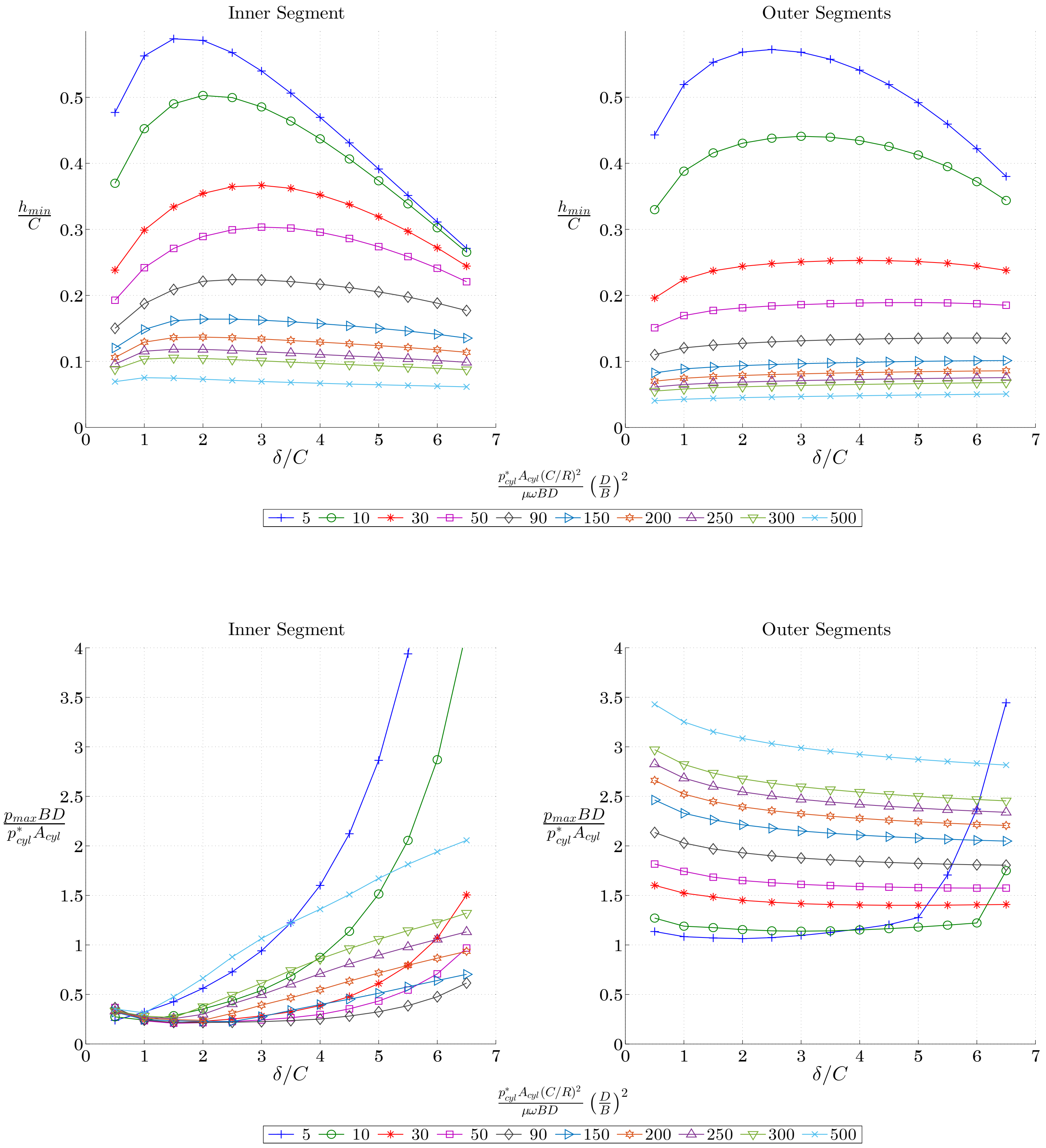

Figure A.19: Full Offset, n=3, $\frac{M_p r\omega^2}{p^*_{cyl}A_{cyl}} = 0.05$; $\frac{r}{L} = 0.2$ (Short)

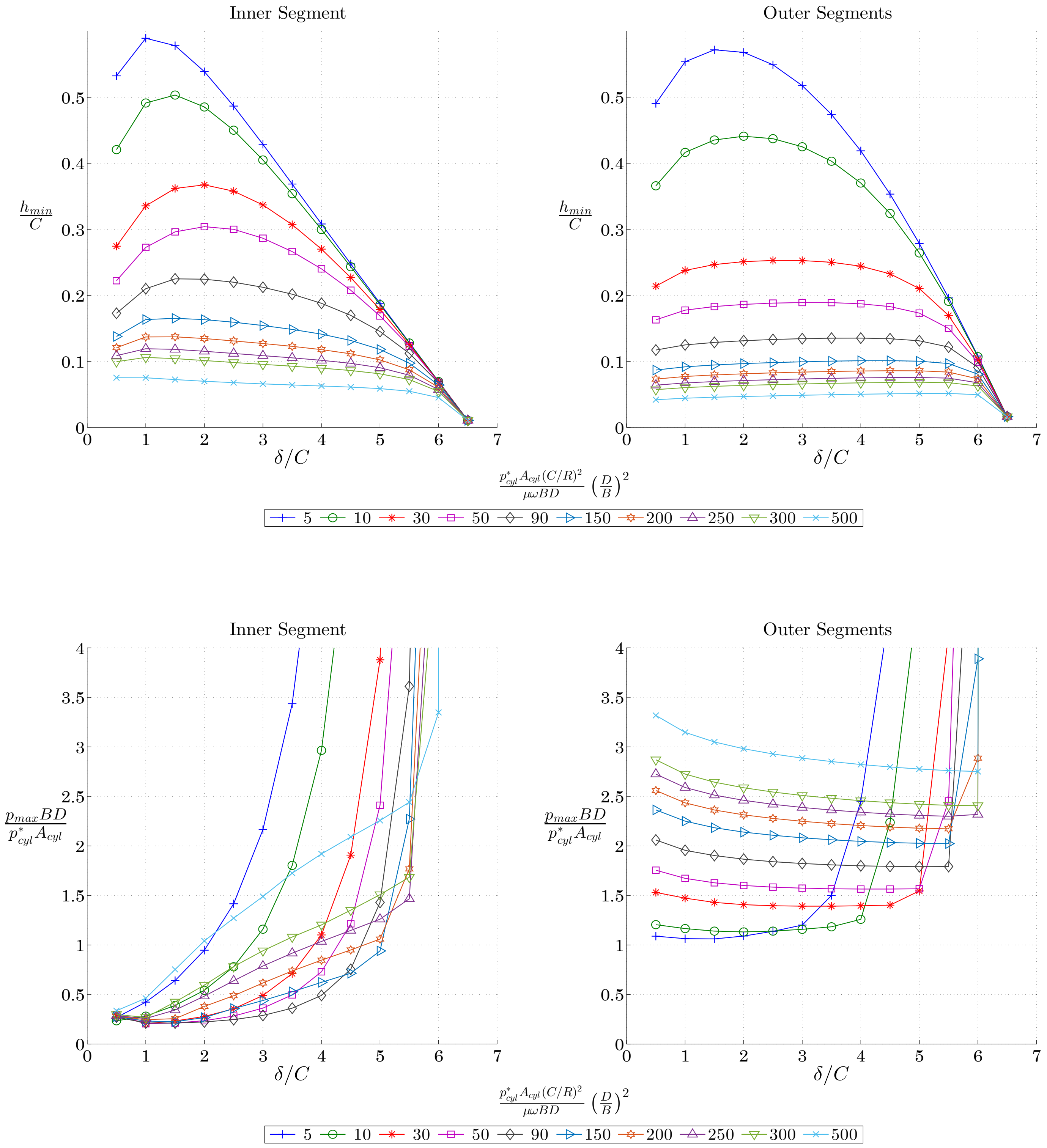

Figure A.20: Full Offset, n=3, $\frac{M_p r\omega^2}{p^*_{cyl}A_{cyl}}$ = 0.05; $\frac{r}{L}$ = 0.3 (Short)

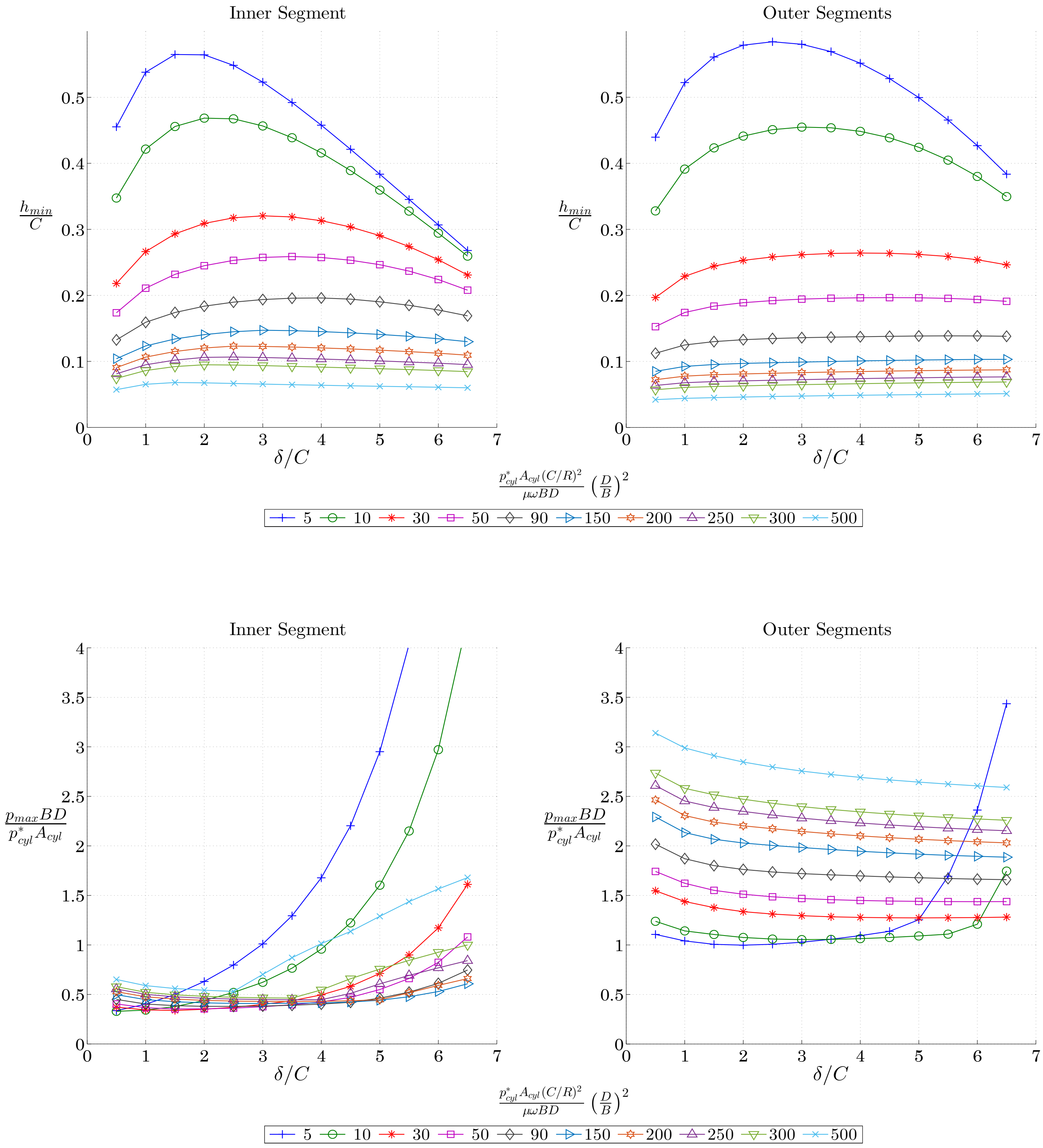

Figure A.21: Full Offset, n=3, $\frac{M_p r\omega^2}{p^*_{cyl}A_{cyl}} = 0.1$; $\frac{r}{L} = 0.2$ (Short)

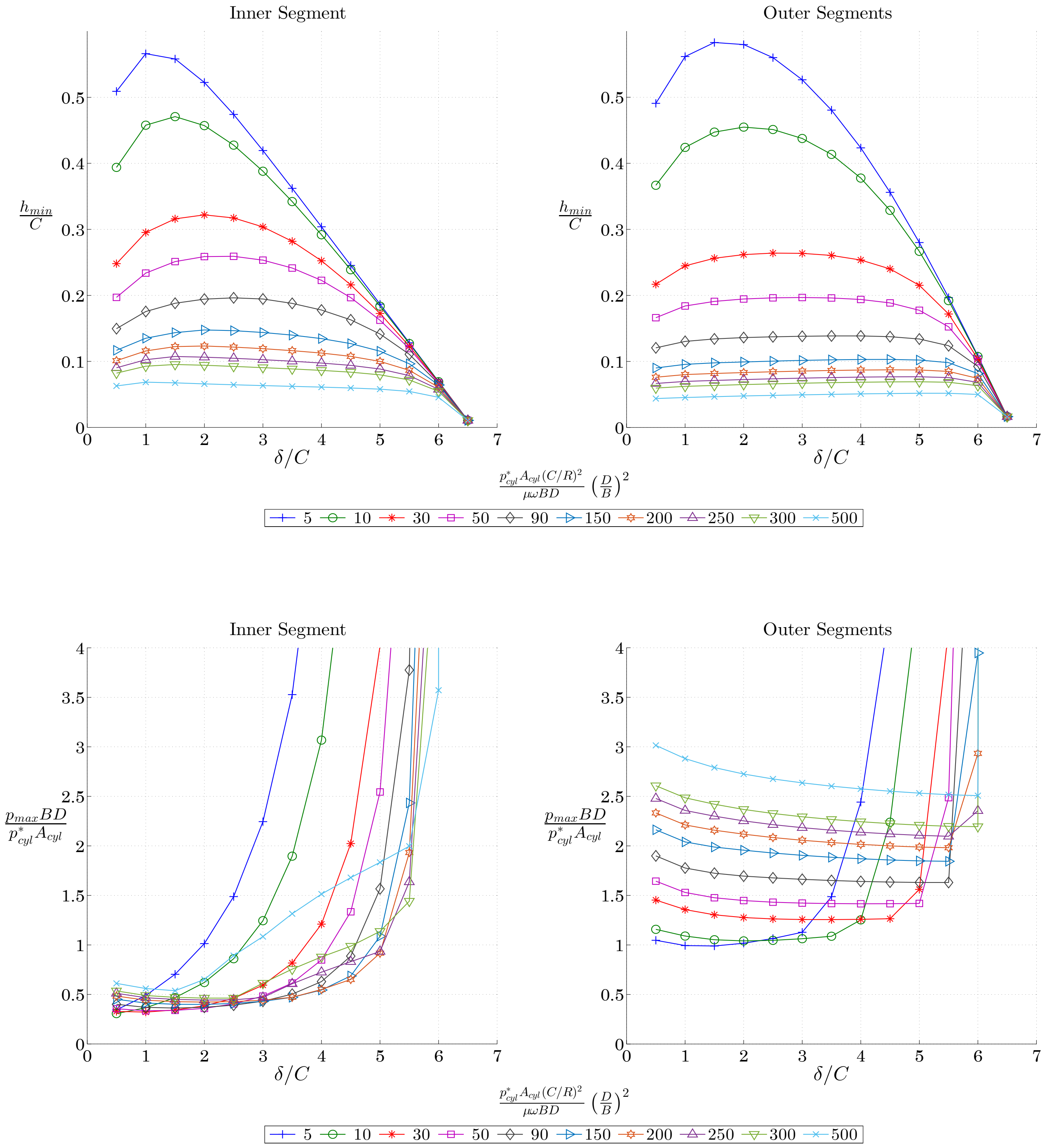

Figure A.22: Full Offset, n=3, $\frac{M_p r\omega^2}{p^*_{cyl}A_{cyl}} = 0.1$; $\frac{r}{L} = 0.3$ (Short)

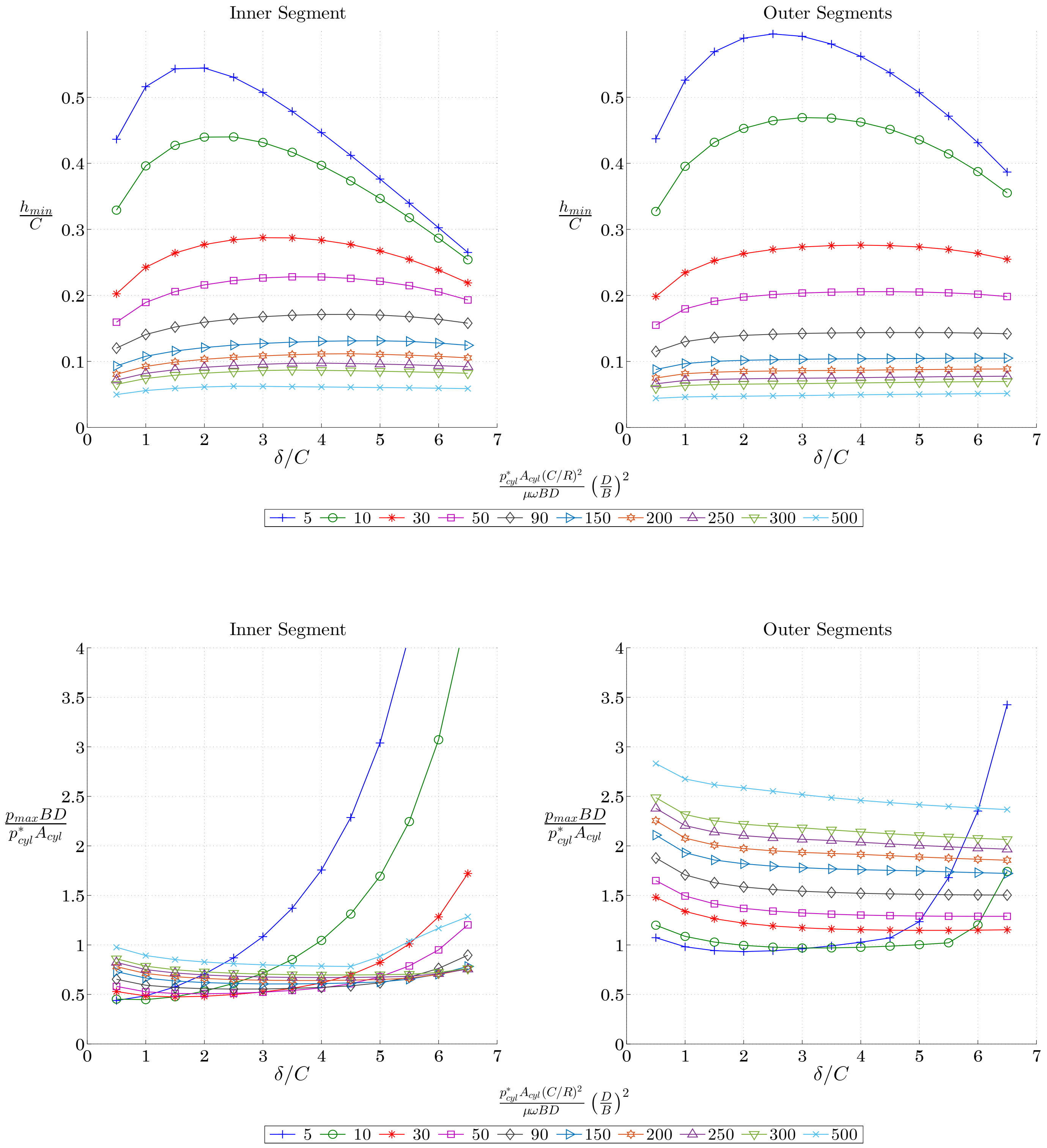

Figure A.23: Full Offset, n=3, $\frac{M_p r\omega^2}{p^*_{cyl}A_{cyl}} = 0.15$; $\frac{r}{L} = 0.2$ (Short)

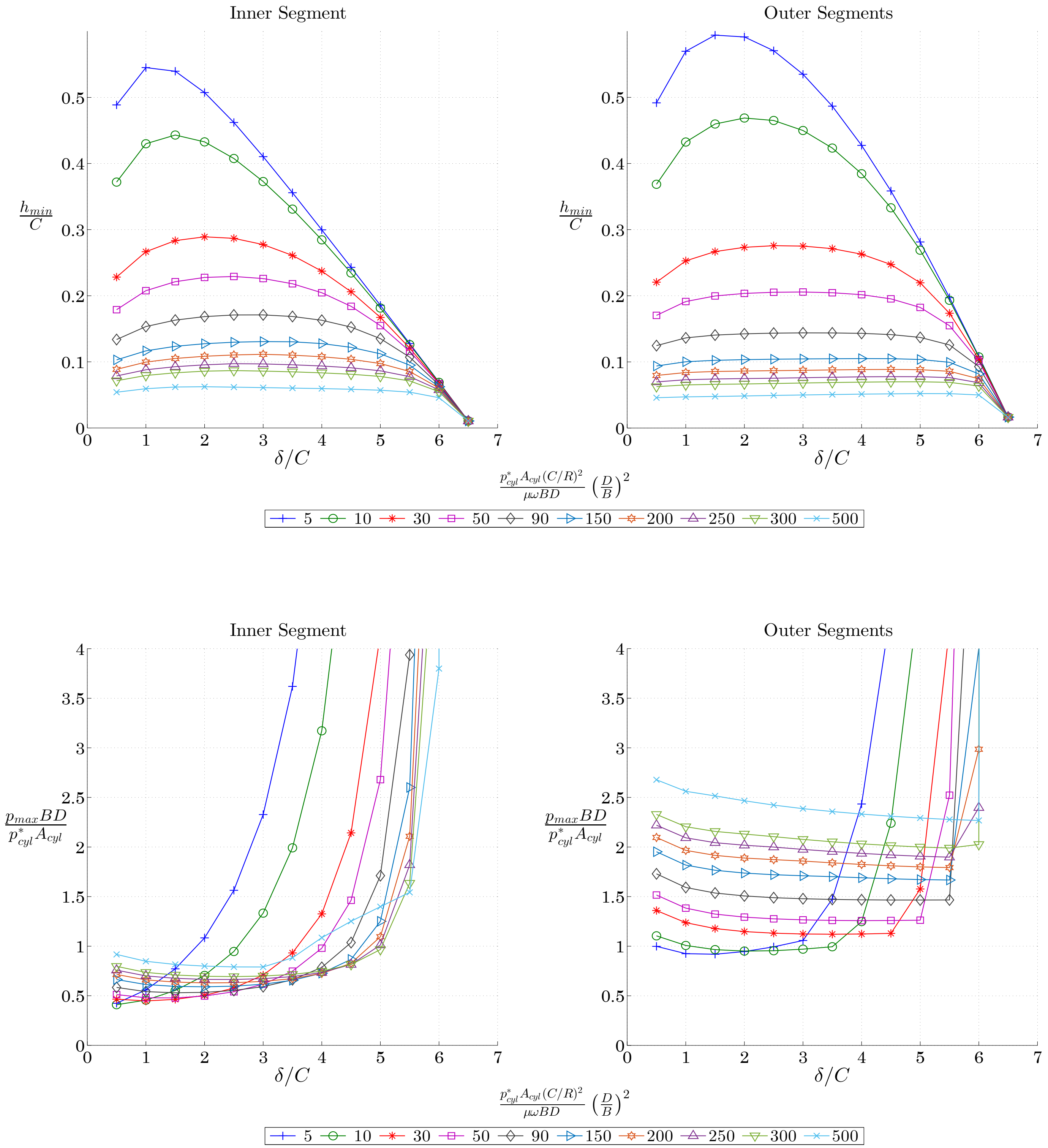

Figure A.24: Full Offset, n=3, $\frac{M_p r\omega^2}{p^*_{cyl}A_{cyl}} = 0.15$; $\frac{r}{L} = 0.3$ (Short)

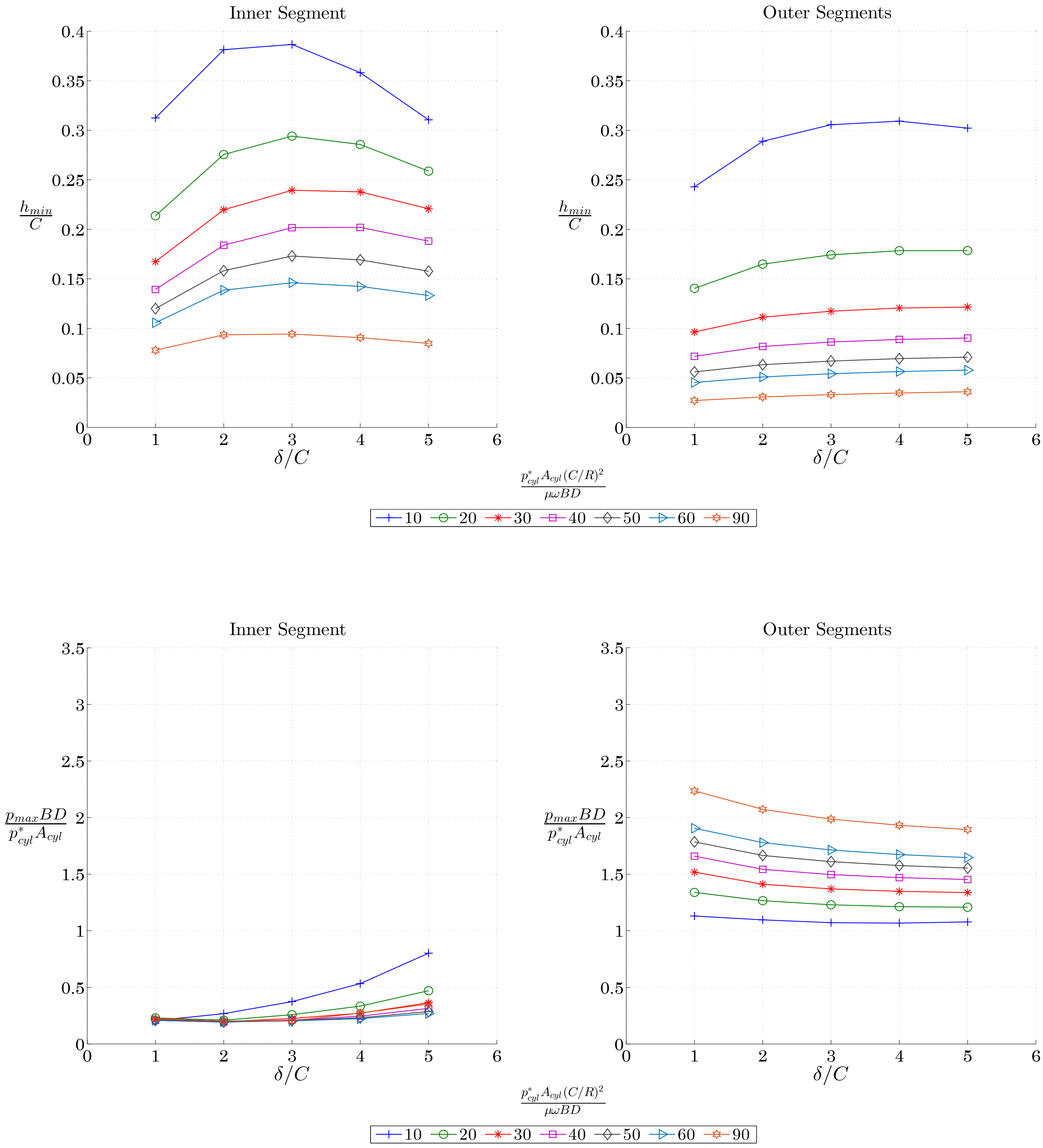

Figure A.25: Full Offset, n=3, $\frac{M_p r\omega^2}{p^*_{cyl}A_{cyl}} = 0.05$; $\frac{r}{L} = 0.2$ (Finite, B/D = 1)

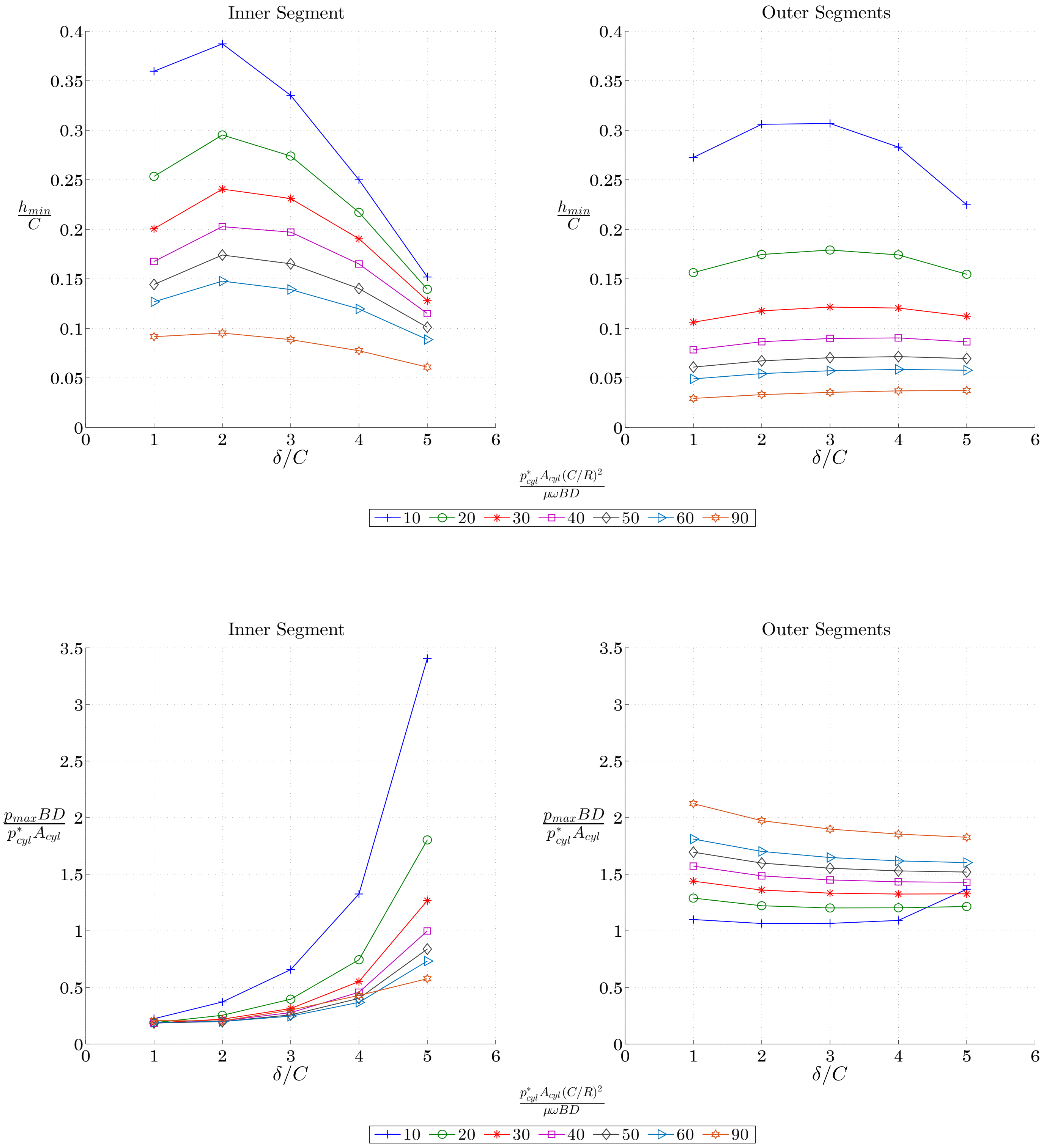

Figure A.26: Full Offset, n=3, $\frac{M_p r\omega^2}{p^*_{cyl}A_{cyl}} = 0.05$; $\frac{r}{L} = 0.3$ (Finite, B/D = 1)

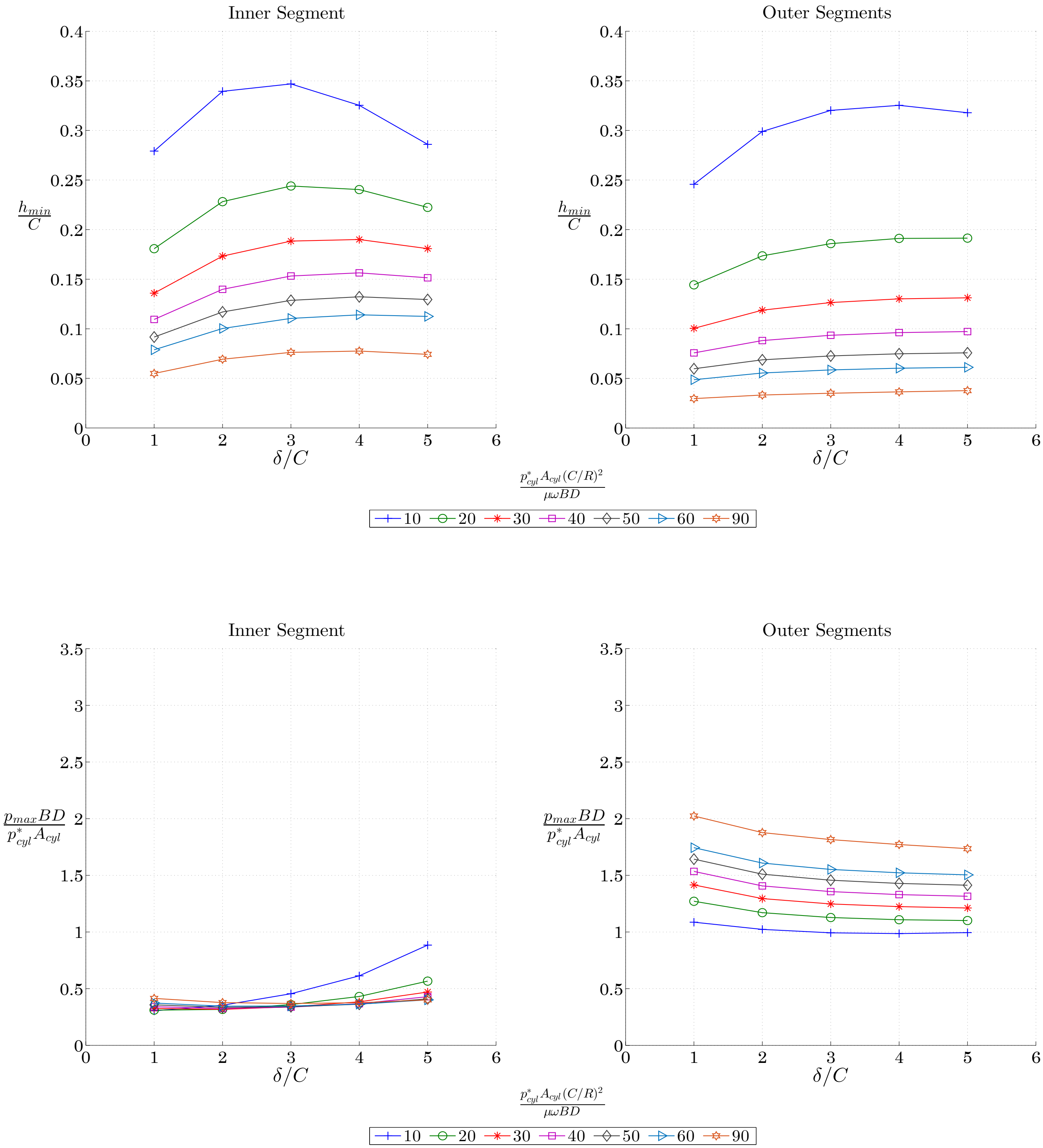

Figure A.27: Full Offset, n=3, $\frac{M_p r\omega^2}{p^*_{cyl}A_{cyl}}$ = 0.1; $\frac{r}{L}$ = 0.2 (Finite, B/D = 1)

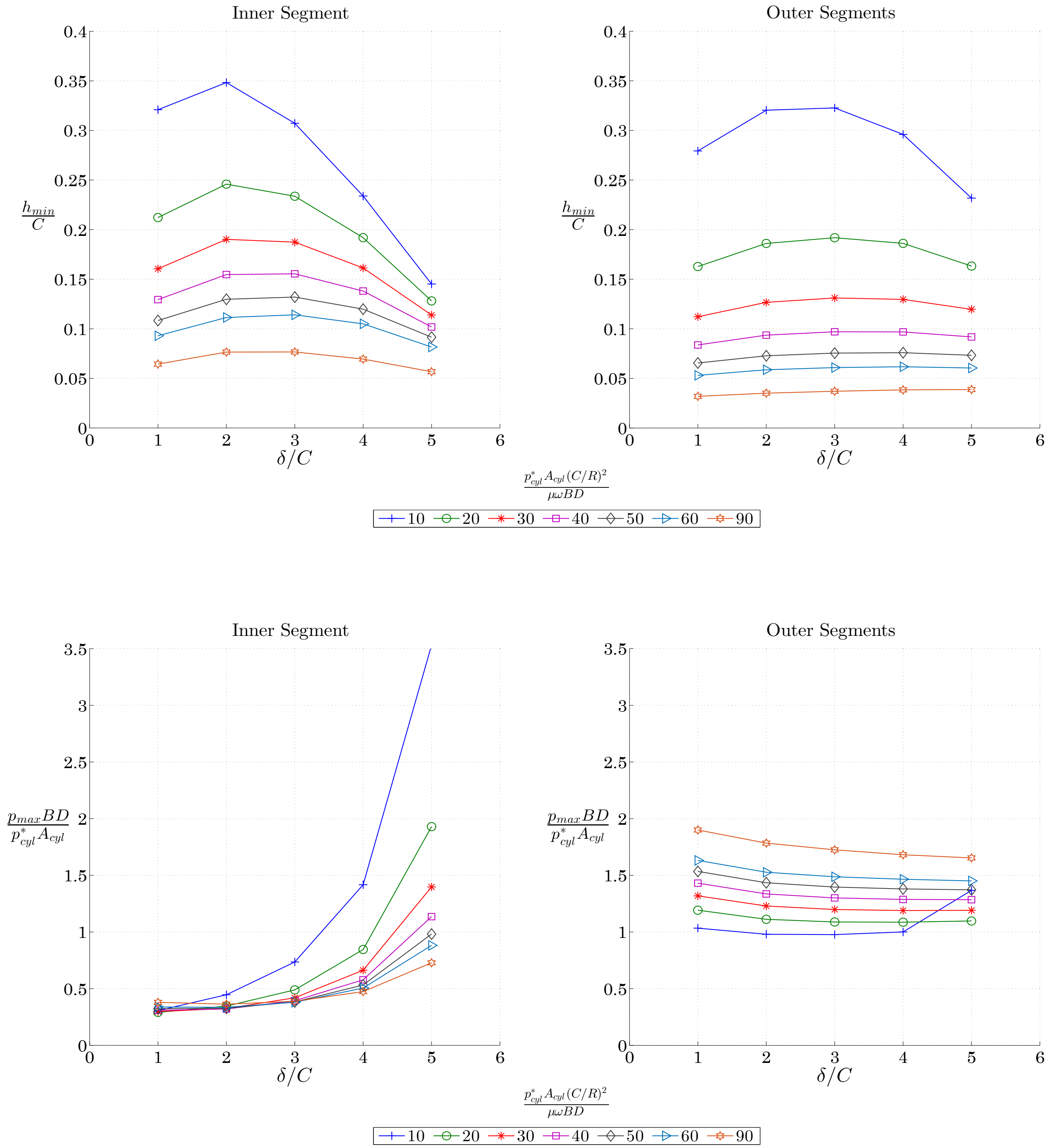

Figure A.28: Full Offset, n=3, $\frac{M_p r\omega^2}{p^*_{cyl}A_{cyl}}$ = 0.1; $\frac{r}{L}$ = 0.3 (Finite, B/D = 1)

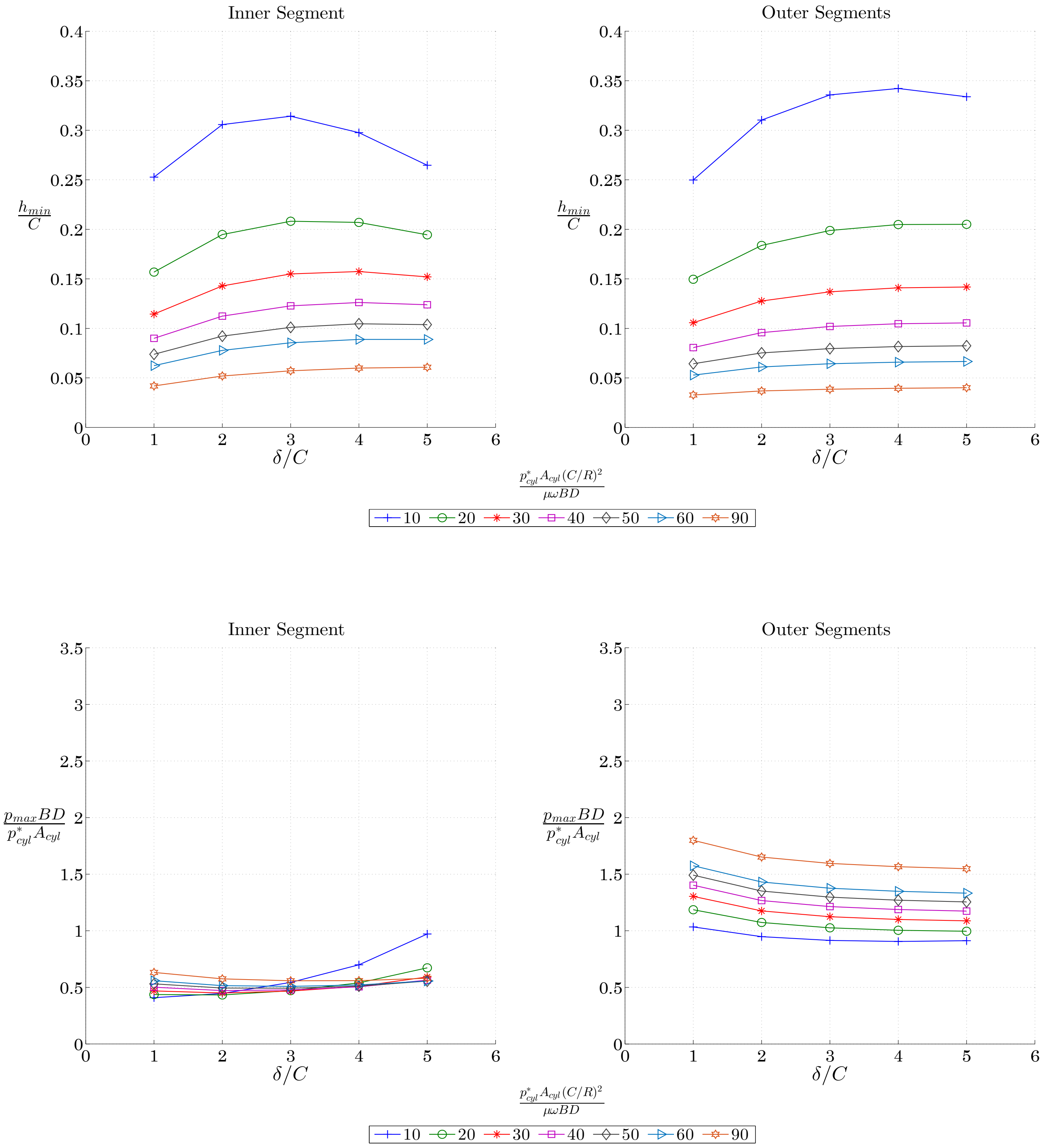

Figure A.29: Full Offset, n=3, $\frac{M_p r\omega^2}{p^*_{cyl}A_{cyl}}$ = 0.15; $\frac{r}{L}$ = 0.2 (Finite, B/D = 1)

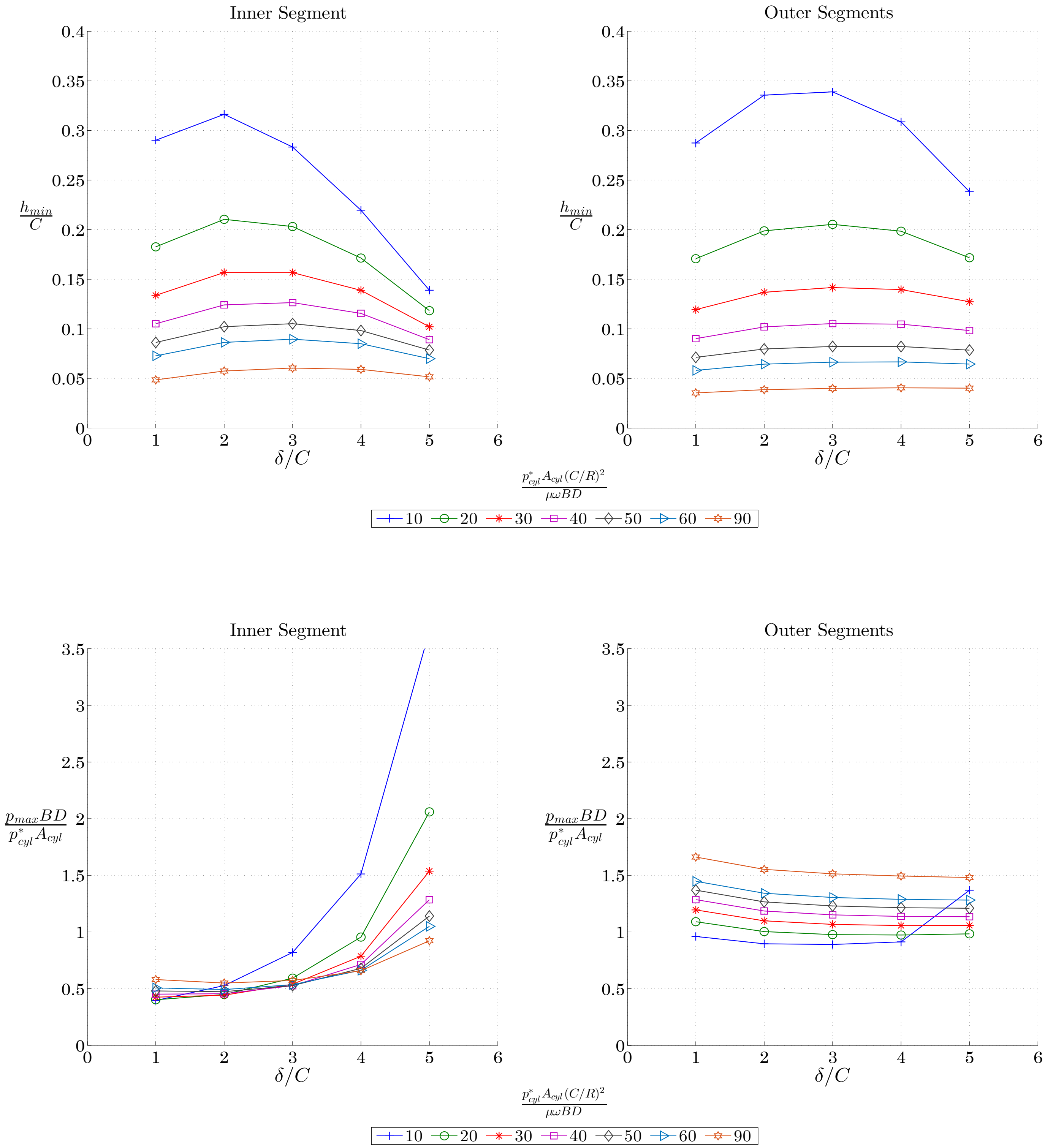

Figure A.30: Full Offset, n=3, $\frac{M_p r\omega^2}{p^*_{cyl}A_{cyl}} = 0.15$; $\frac{r}{L} = 0.3$ (Finite, B/D = 1)

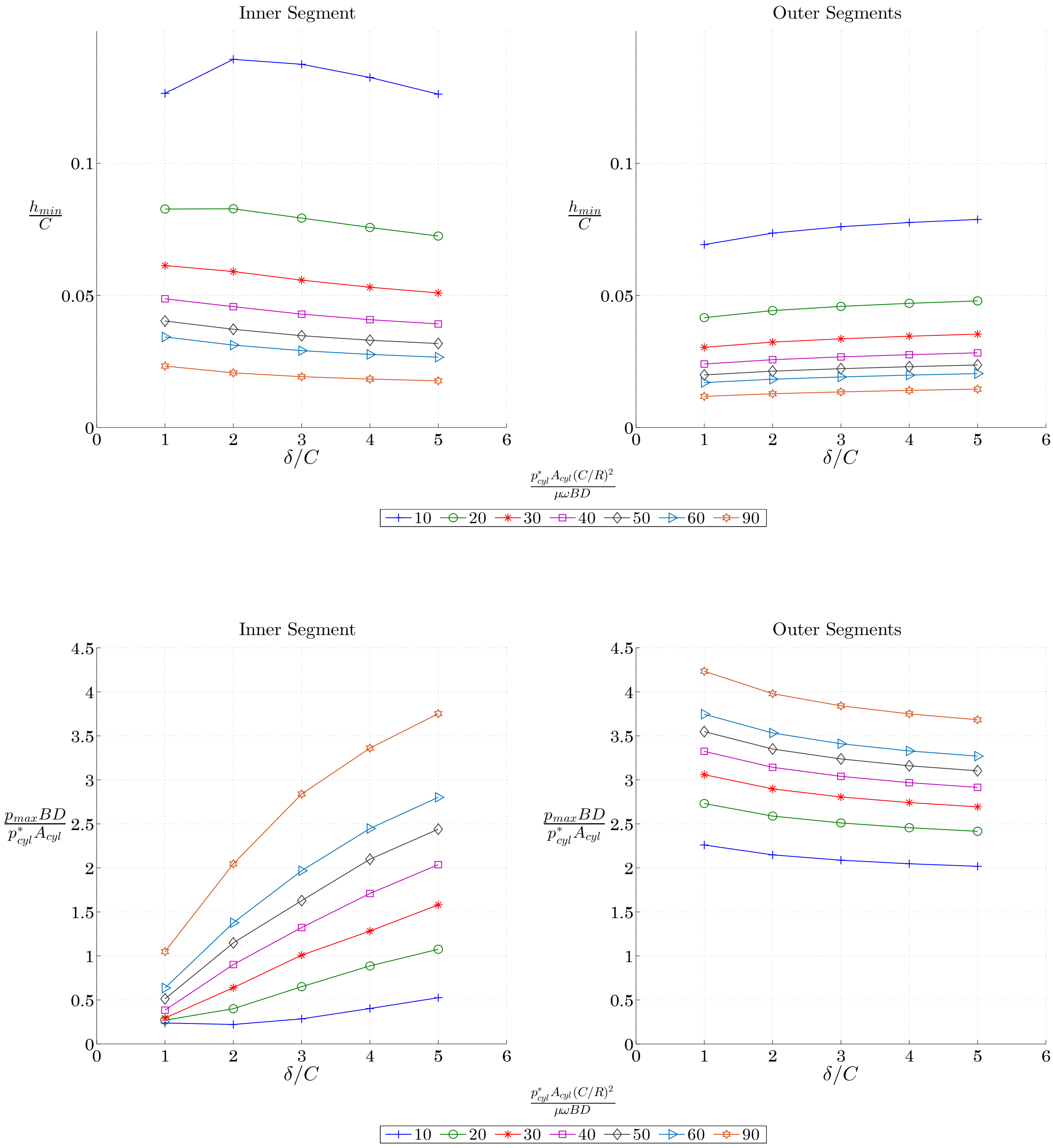

Figure A.31: Full Offset, n=3, $\frac{M_p r\omega^2}{p^*_{cyl}A_{cyl}}$ = 0.05; $\frac{r}{L}$ = 0.2 (Finite, B/D = 1/4)

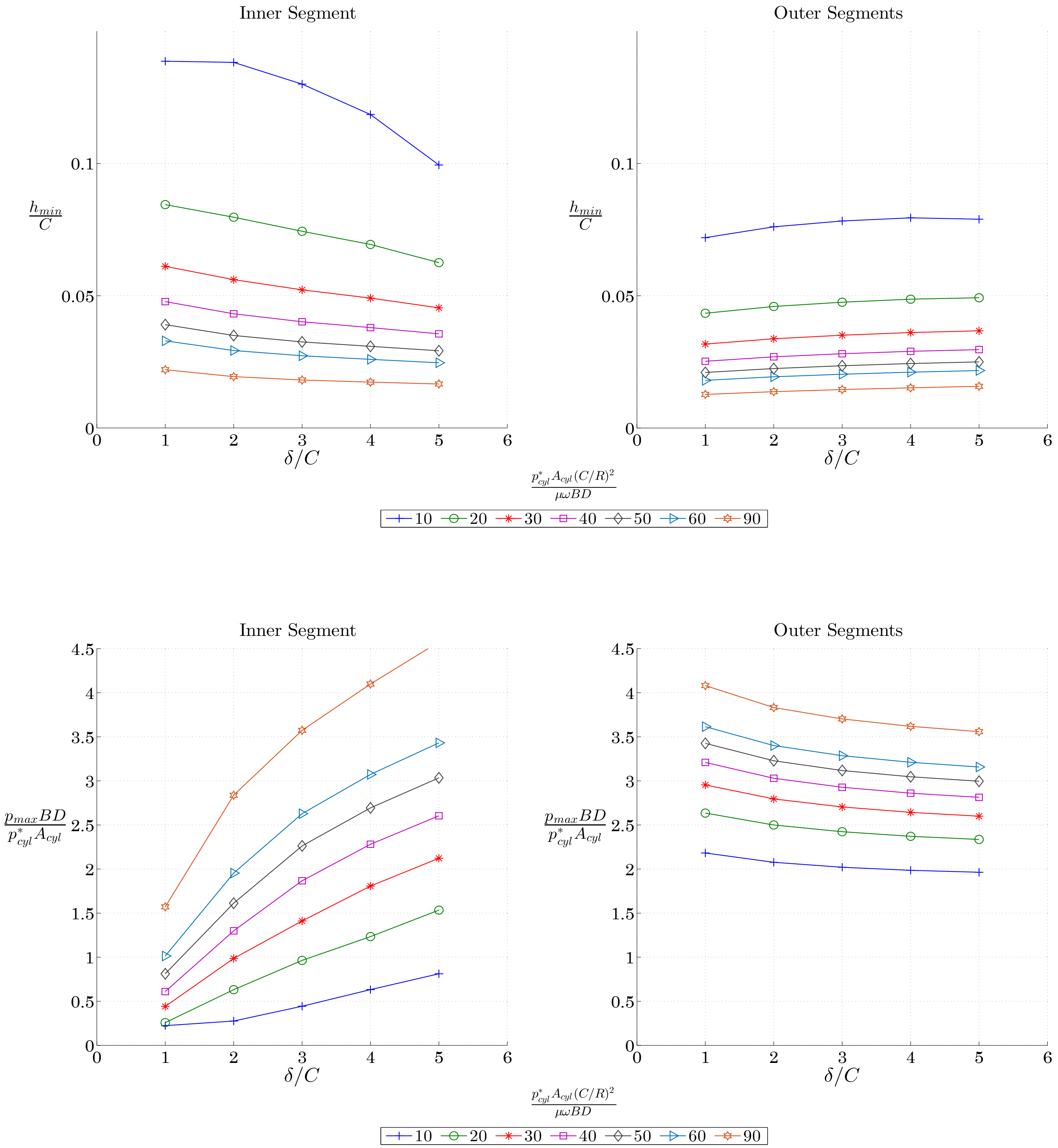

Figure A.32: Full Offset, n=3, $\frac{M_p r\omega^2}{p^*_{cyl}A_{cyl}}$ = 0.05; $\frac{r}{L}$ = 0.3 (Finite, B/D = 1/4)

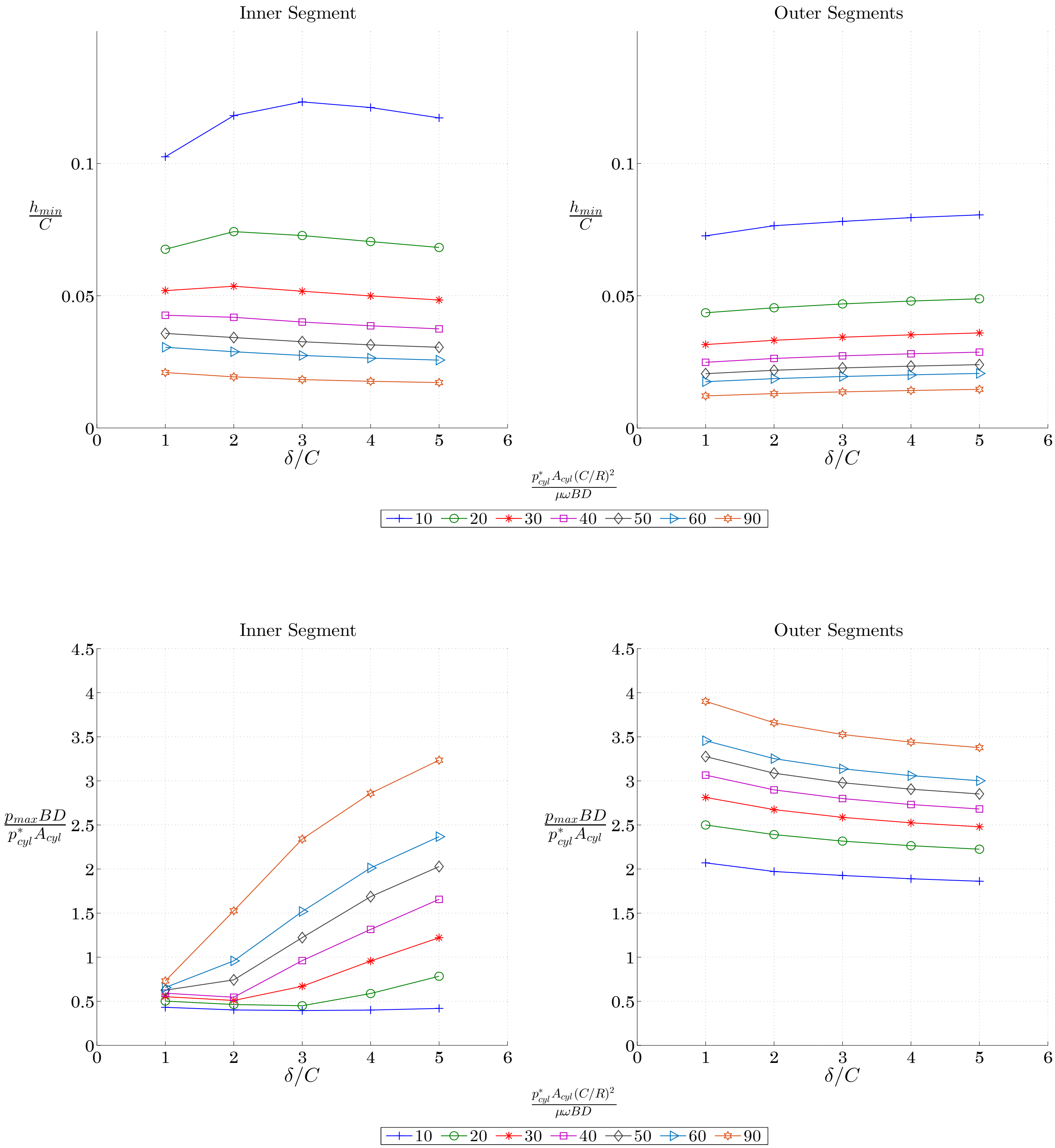

Figure A.33: Full Offset, n=3, $\frac{M_p r\omega^2}{p^*_{cyl}A_{cyl}}$ = 0.1; $\frac{r}{L}$ = 0.2 (Finite, B/D = 1/4)

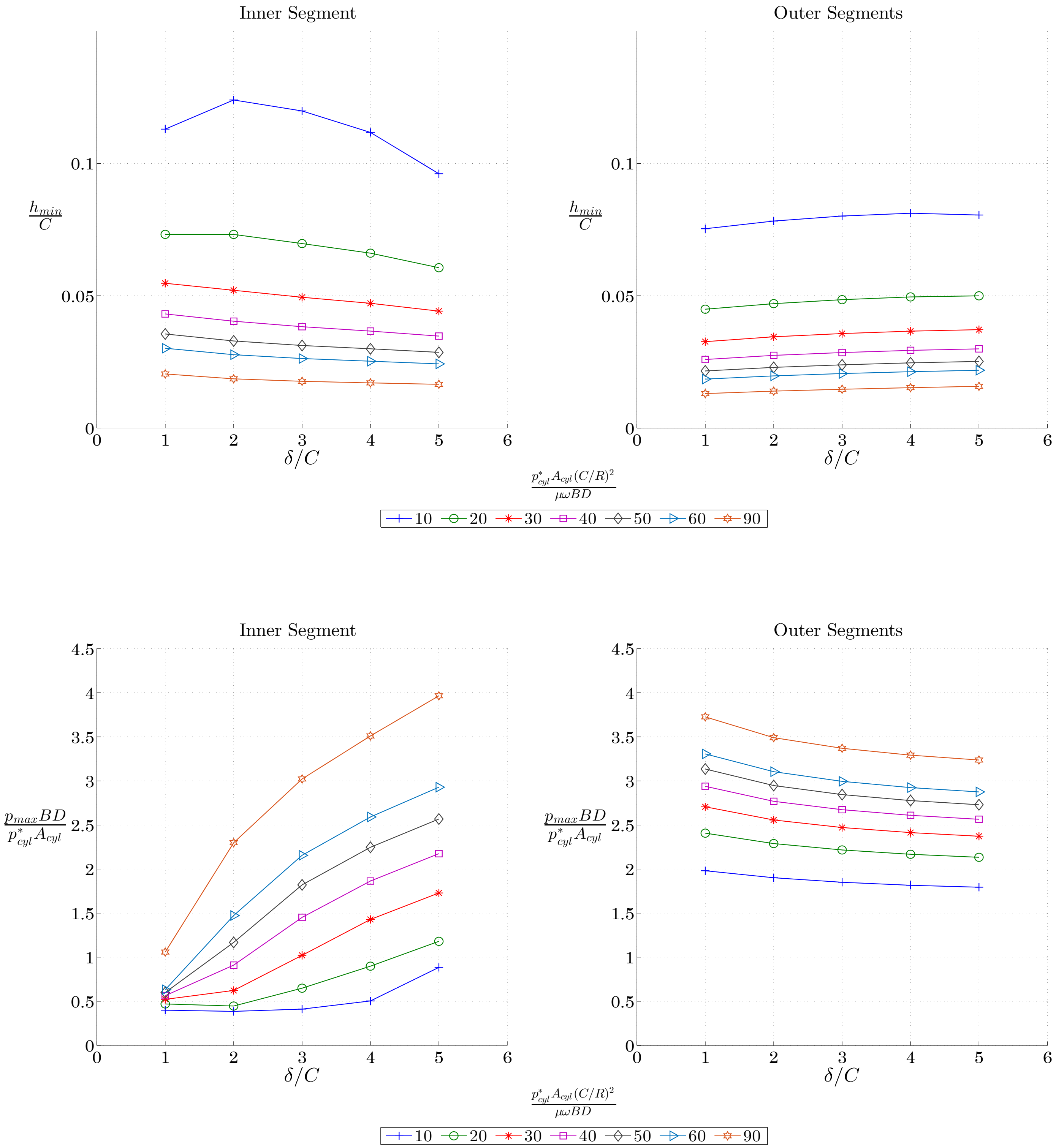

Figure A.34: Full Offset, n=3, $\frac{M_p r\omega^2}{p^*_{cyl}A_{cyl}}$ = 0.1; $\frac{r}{L}$ = 0.3 (Finite, B/D = 1/4)

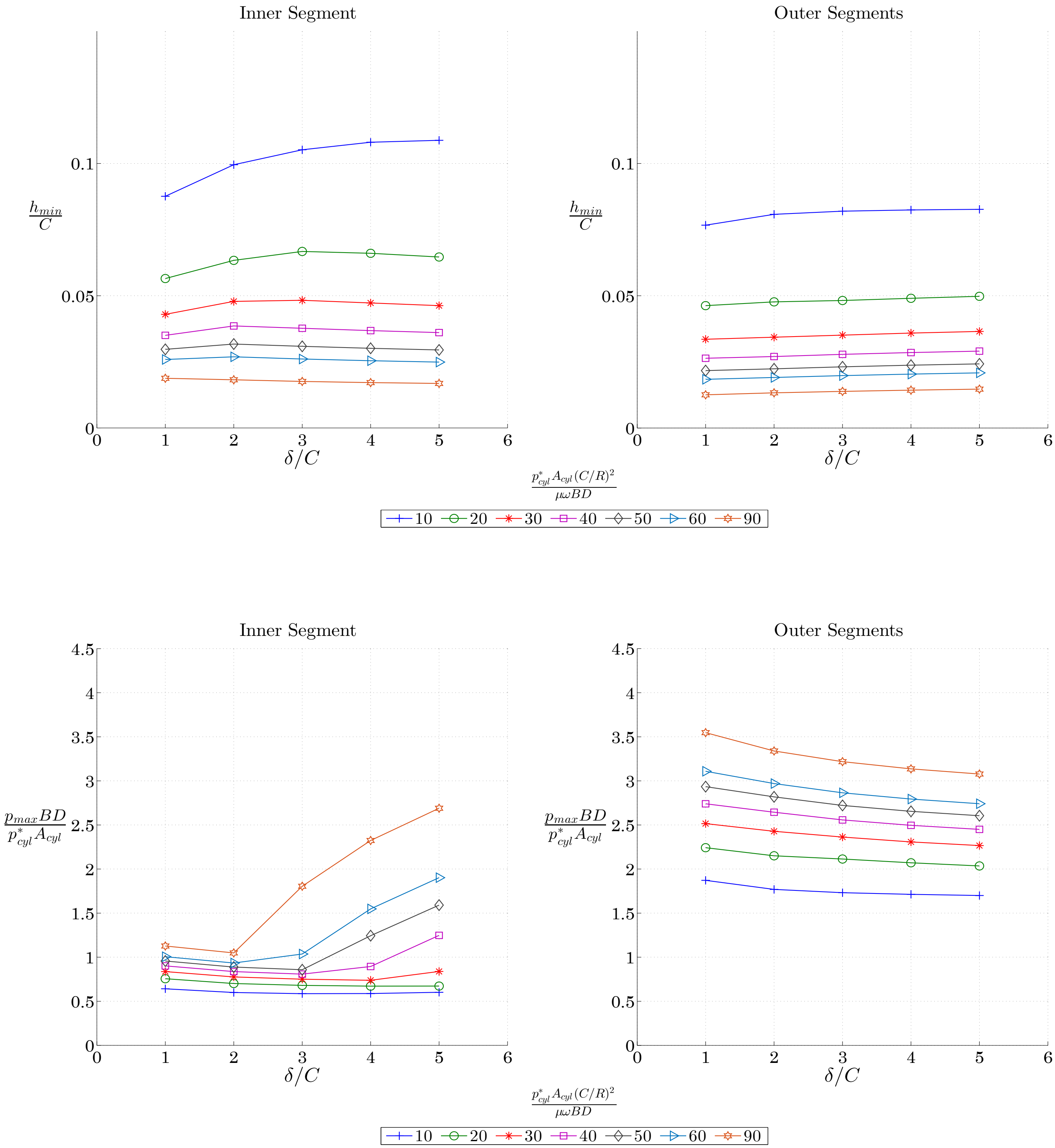

Figure A.35: Full Offset, n=3, $\frac{M_p r\omega^2}{p^*_{cyl}A_{cyl}}$ = 0.15; $\frac{r}{L}$ = 0.2 (Finite, B/D = 1/4)

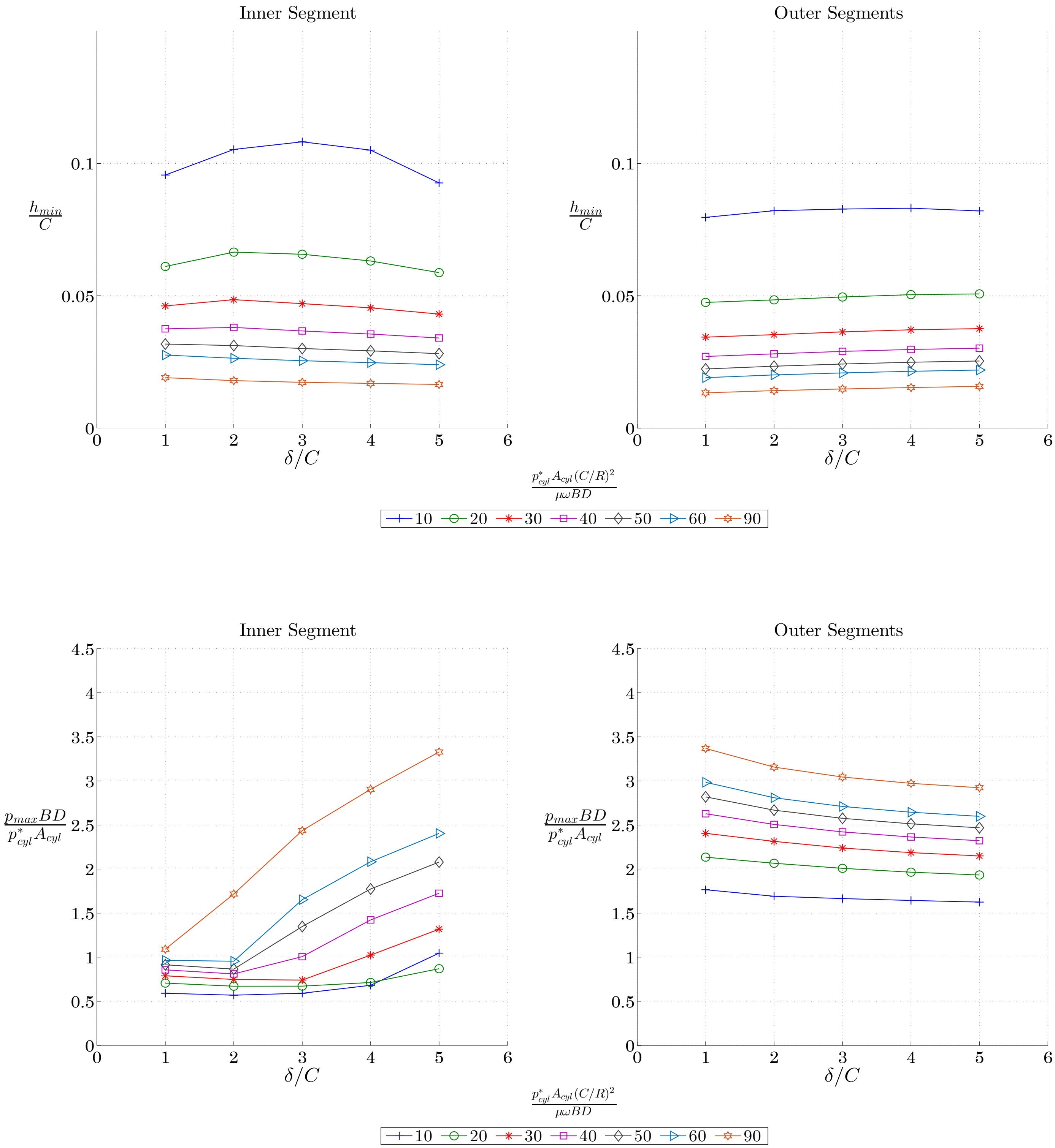

Figure A.36: Full Offset, n=3, $\frac{M_p r\omega^2}{p^*_{cyl}A_{cyl}}$ = 0.15; $\frac{r}{L}$ = 0.3 (Finite, B/D = 1/4)

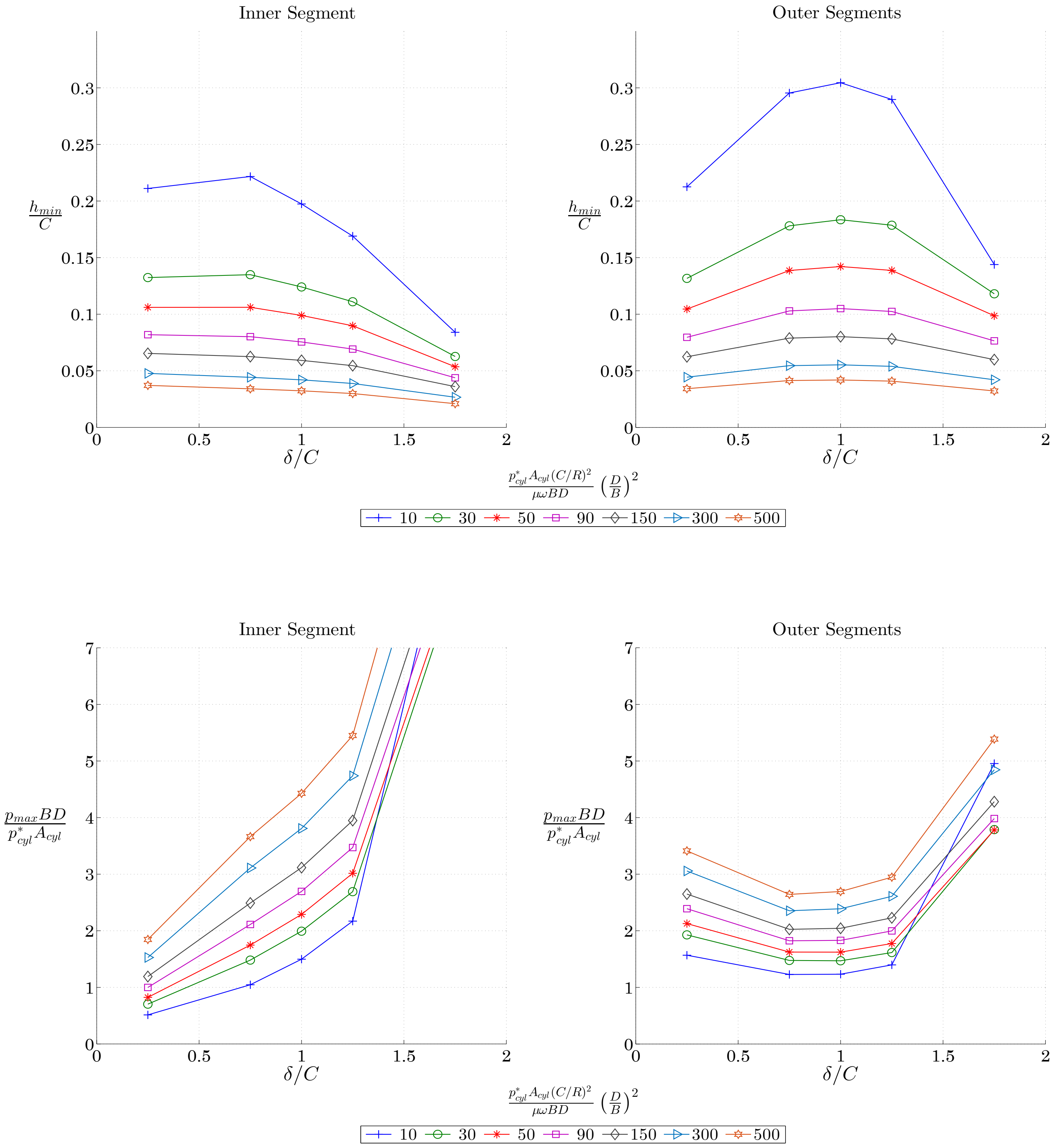

Figure A.37: Wakuri Offset, n=3, $\frac{M_p r\omega^2}{p^*_{cyl}A_{cyl}} = 0.05$; $\frac{r}{L} = 0.2$ (Short)

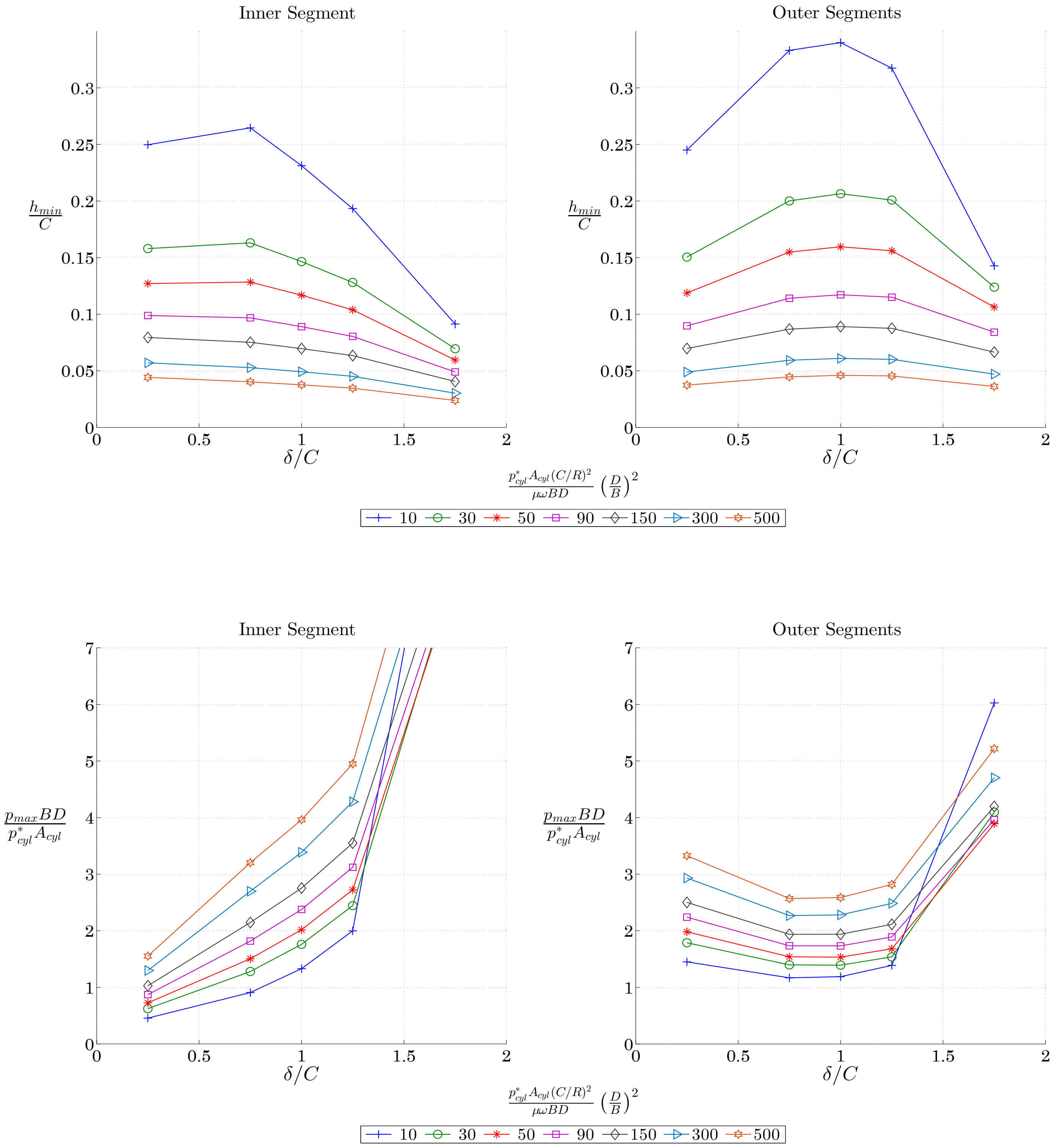

Figure A.38: Wakuri Offset, n=3, $\frac{M_p r\omega^2}{p^*_{cyl}A_{cyl}}$ = 0.05; $\frac{r}{L}$ = 0.3 (Short)

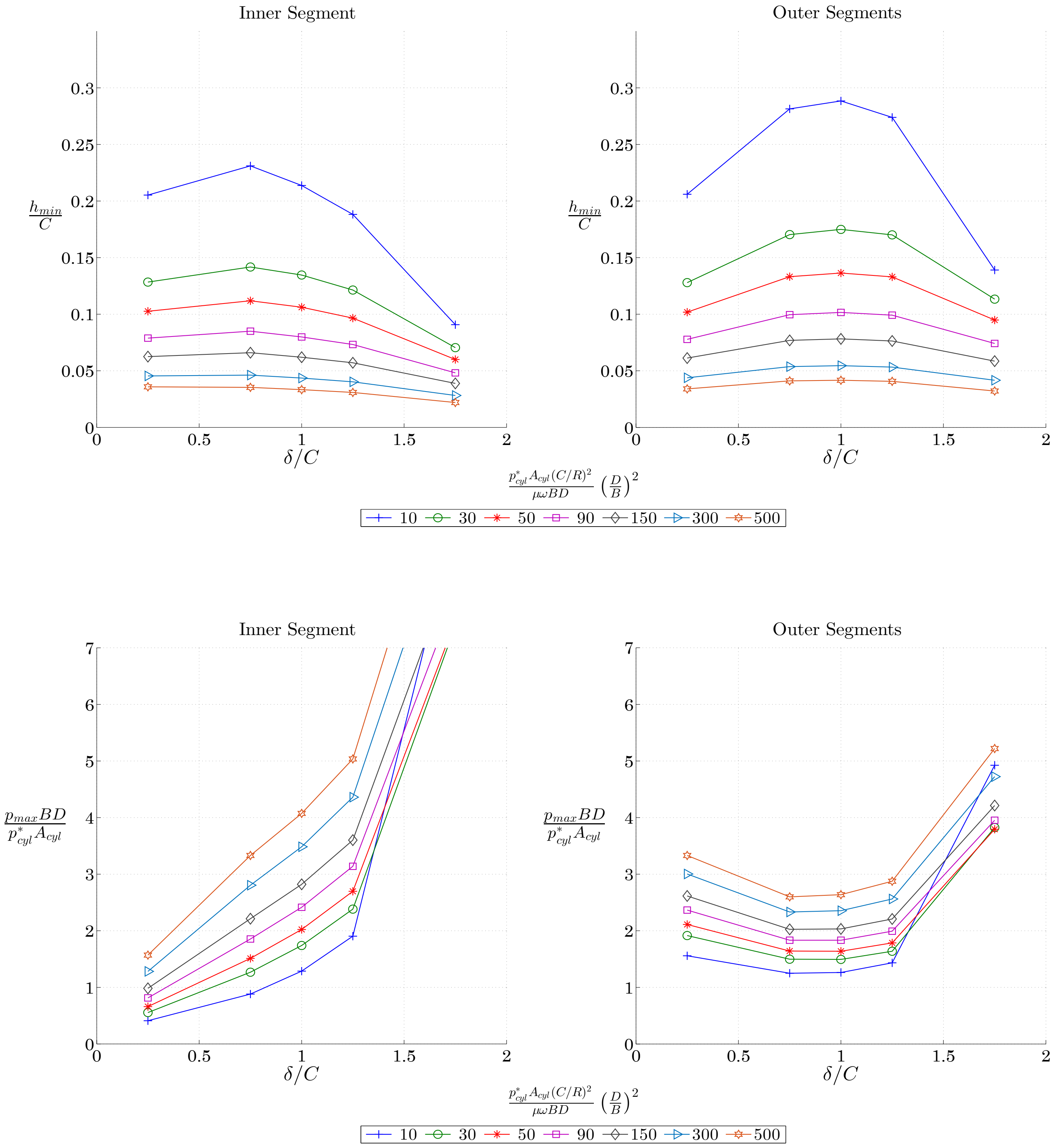

Figure A.39: Wakuri Offset, n=3, $\frac{M_p r\omega^2}{p^*_{cyl}A_{cyl}}$ = 0.1; $\frac{r}{L}$ = 0.2 (Short)

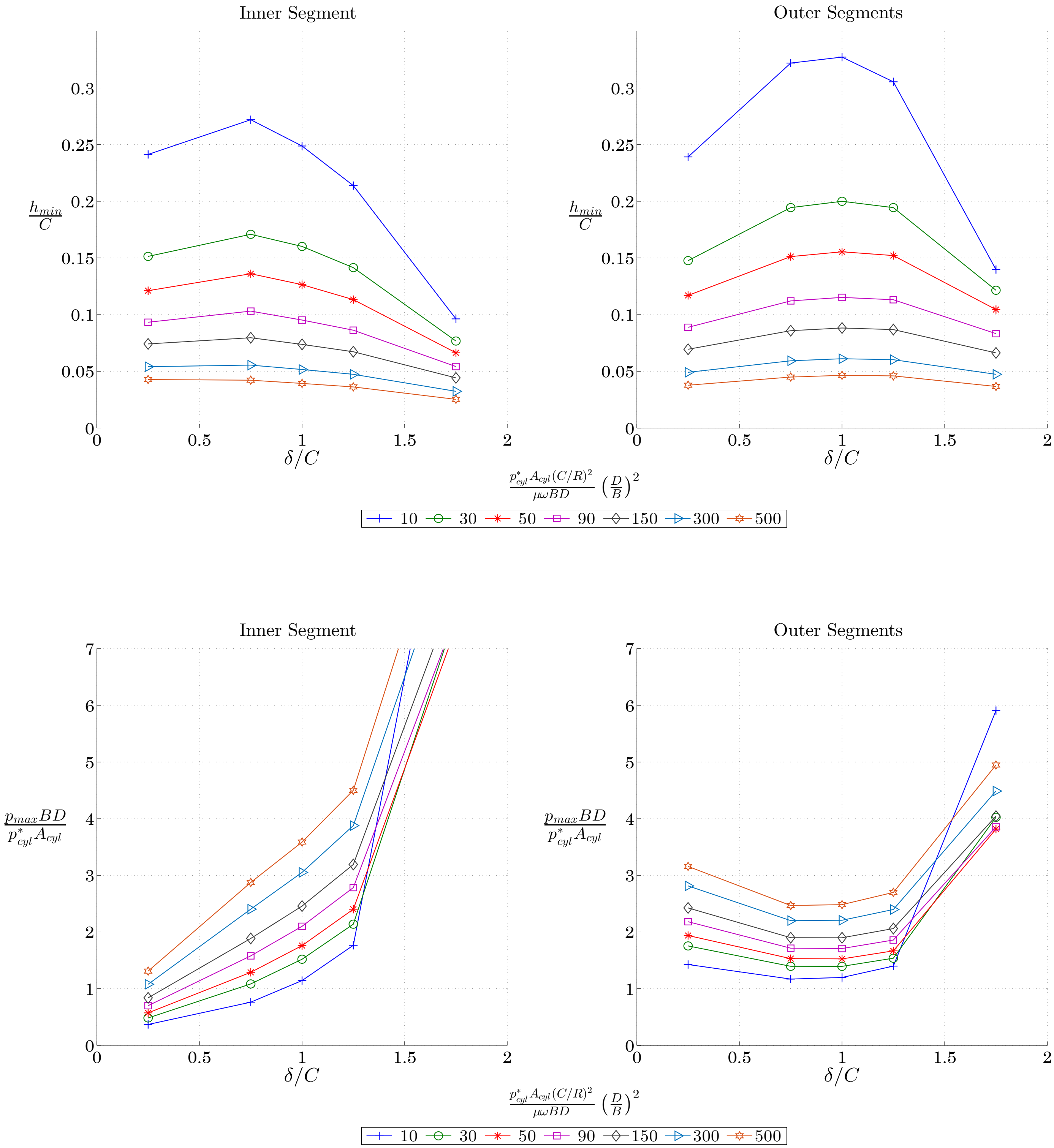

Figure A.40: Wakuri Offset, n=3, $\frac{M_p r\omega^2}{p^*_{cyl}A_{cyl}}$ = 0.1; $\frac{r}{L}$ = 0.3 (Short)

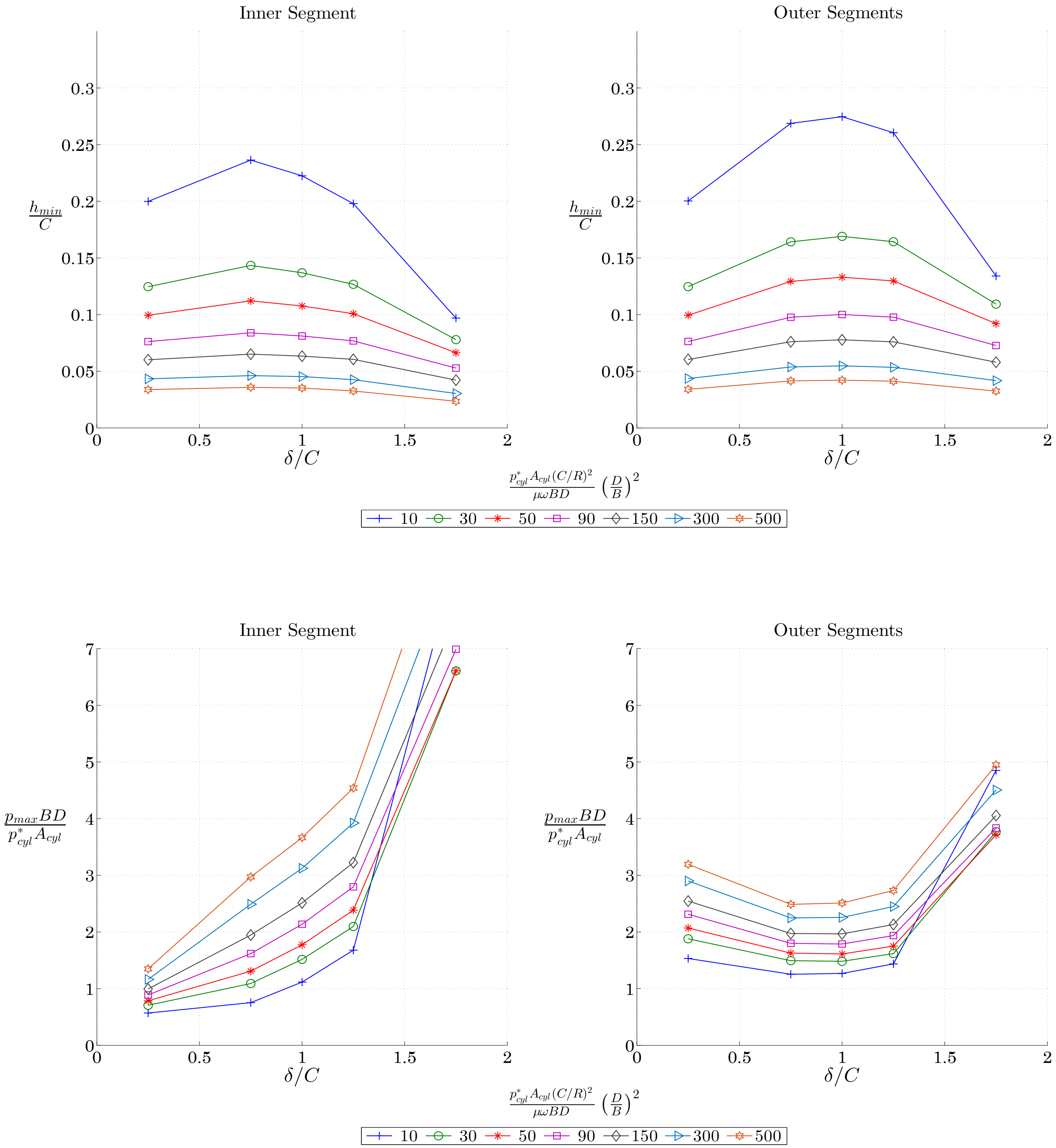

Figure A.41: Wakuri Offset, n=3, $\frac{M_p r\omega^2}{p^*_{cyl}A_{cyl}} = 0.15$; $\frac{r}{L} = 0.2$ (Short)

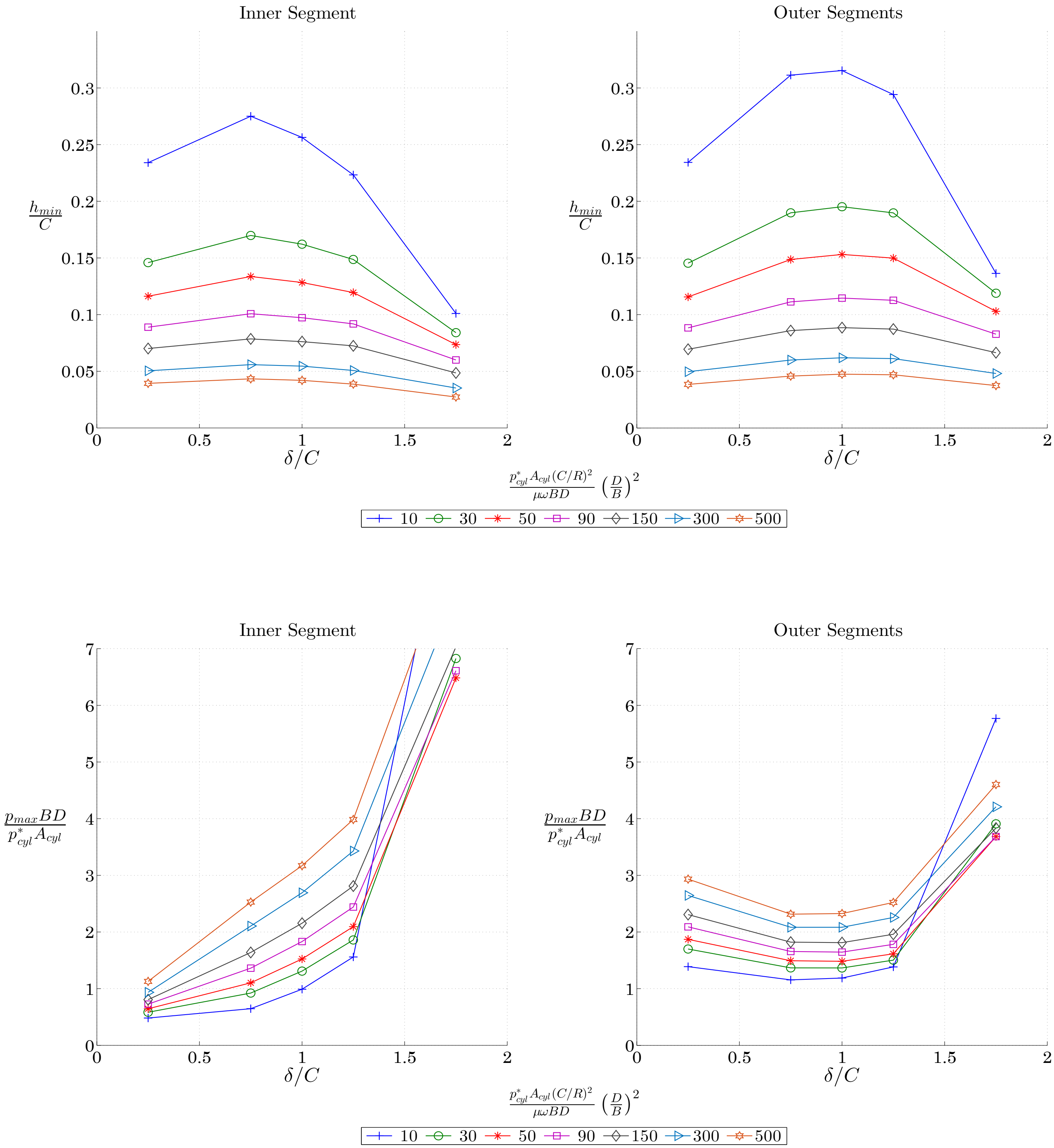

Figure A.42: Wakuri Offset, n=3, $\frac{M_p r\omega^2}{p^*_{cyl}A_{cyl}} = 0.15$; $\frac{r}{L} = 0.3$ (Short)

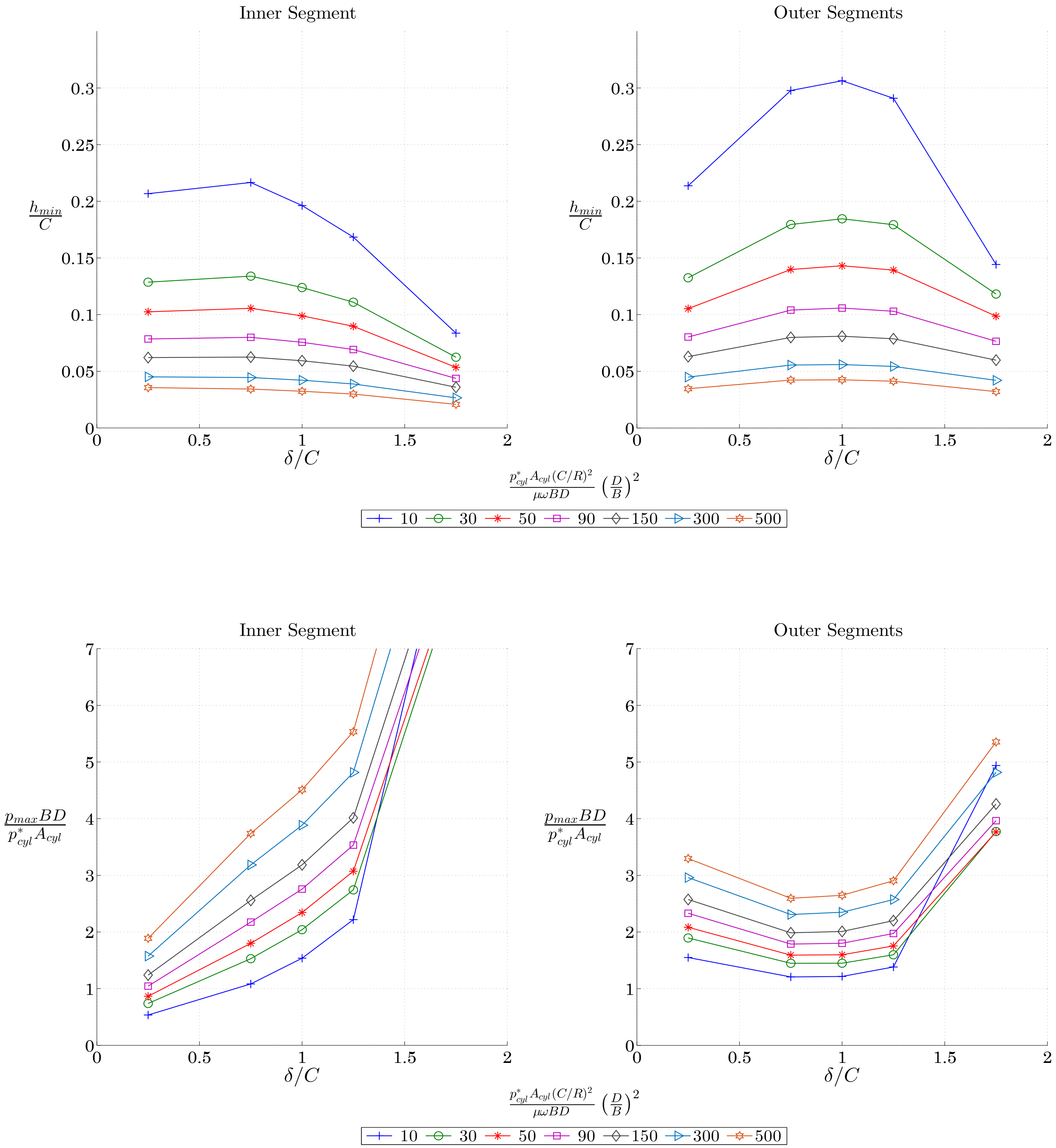

Figure A.43: Camella Offset, n=3, $\frac{M_p r\omega^2}{p^*_{cyl}A_{cyl}}$ = 0.05; $\frac{r}{L}$ = 0.2 (Short)

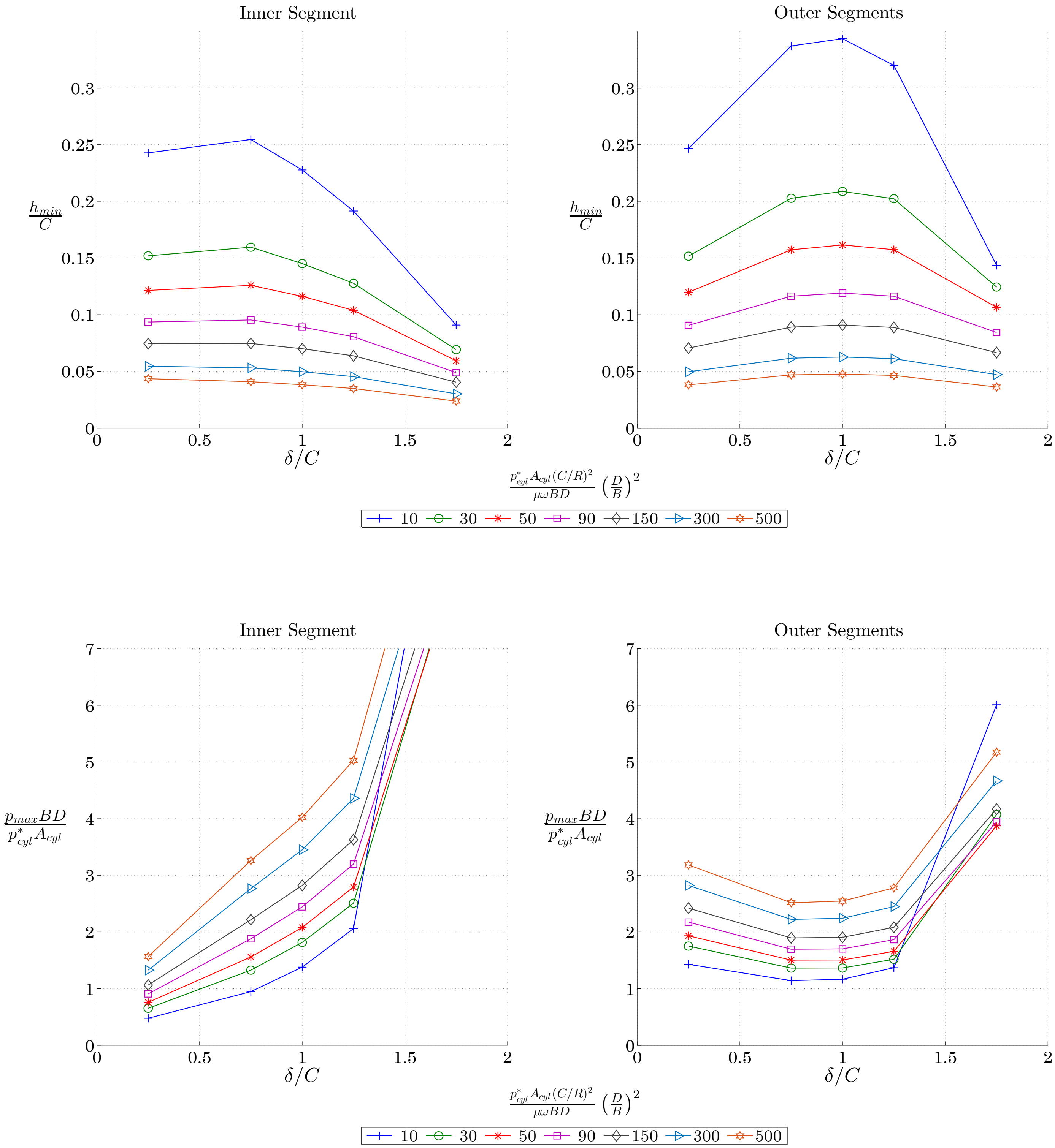

Figure A.44: Camella Offset, n=3, $\frac{M_p r\omega^2}{p^*_{cyl}A_{cyl}} = 0.05$; $\frac{r}{L} = 0.3$ (Short)

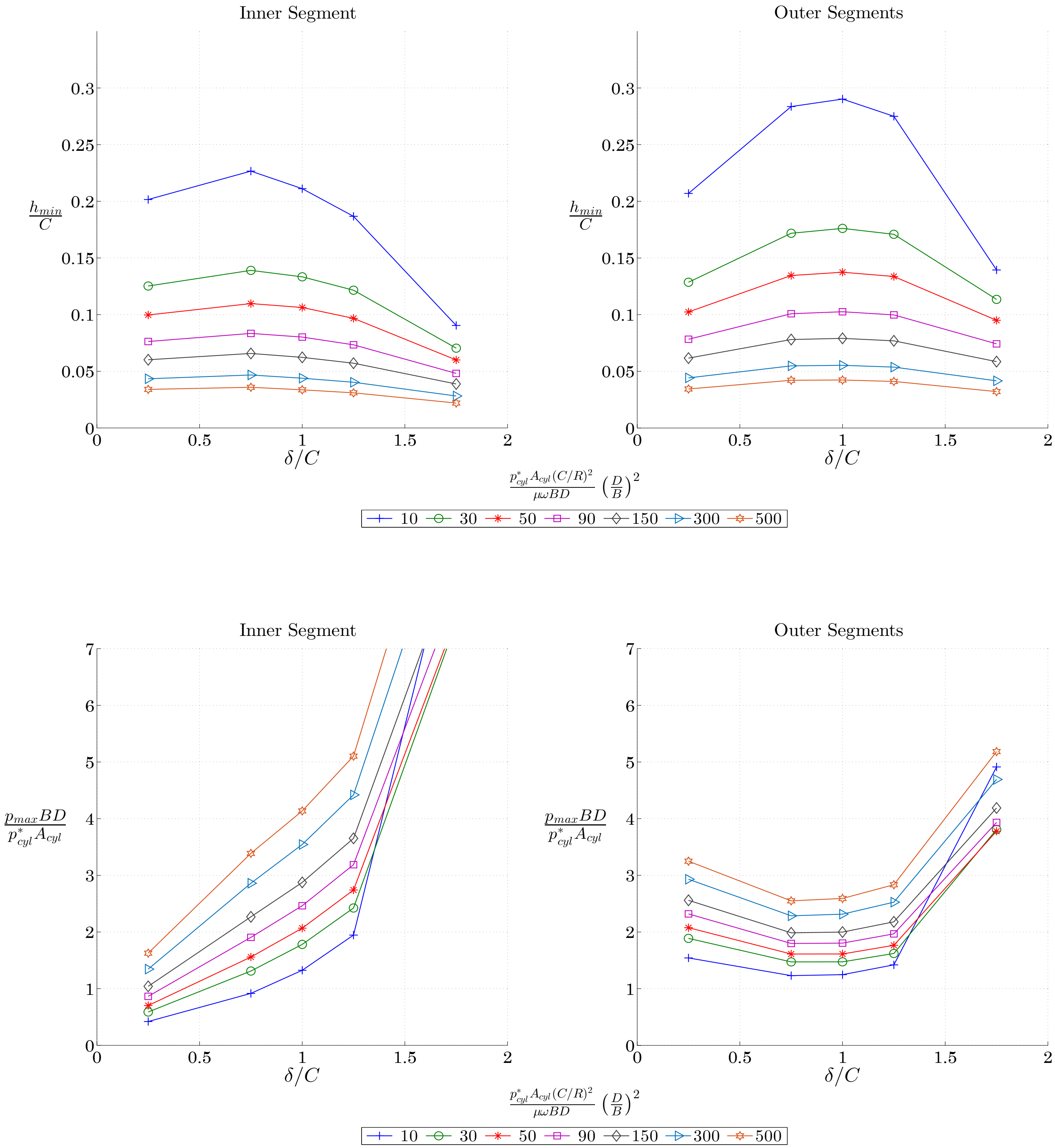

Figure A.45: Camella Offset, n=3, $\frac{M_p r\omega^2}{p^*_{cyl}A_{cyl}} = 0.1$; $\frac{r}{L} = 0.2$ (Short)

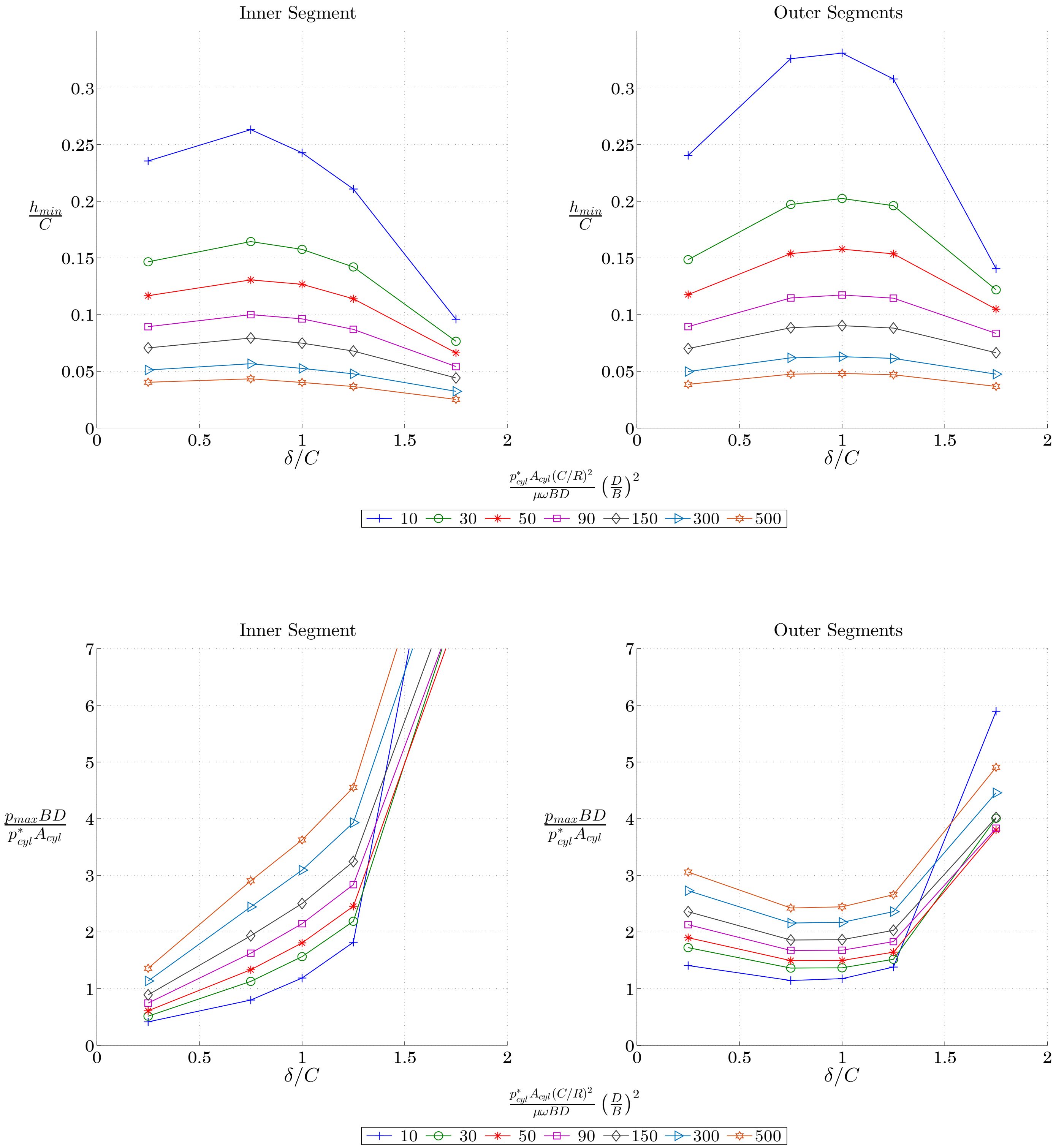

Figure A.46: Camella Offset, n=3, $\frac{M_p r\omega^2}{p^*_{cyl}A_{cyl}} = 0.1$; $\frac{r}{L} = 0.3$ (Short)

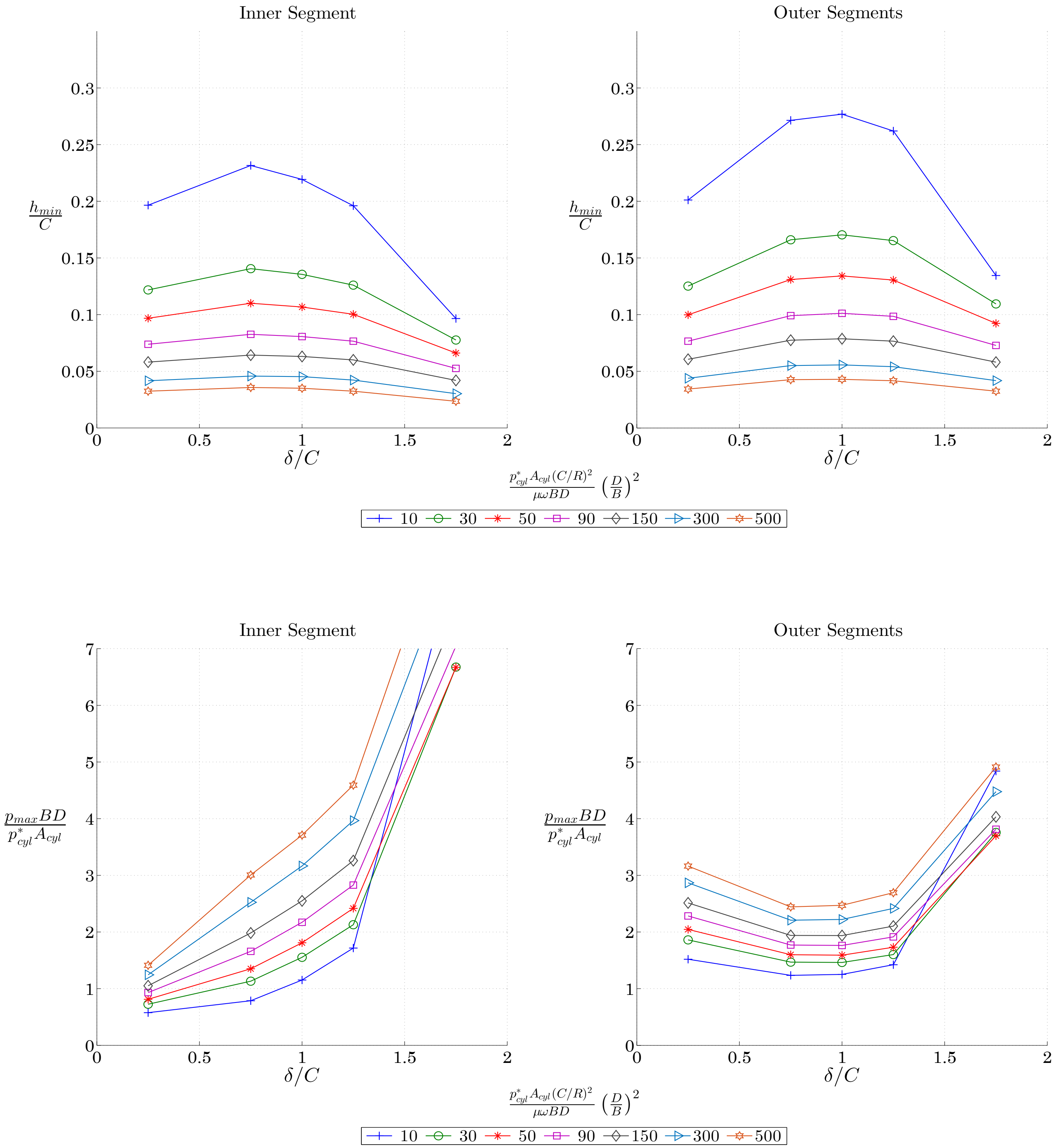

Figure A.47: Camella Offset, n=3, $\frac{M_p r\omega^2}{p^*_{cyl}A_{cyl}} = 0.15$; $\frac{r}{L} = 0.2$ (Short)

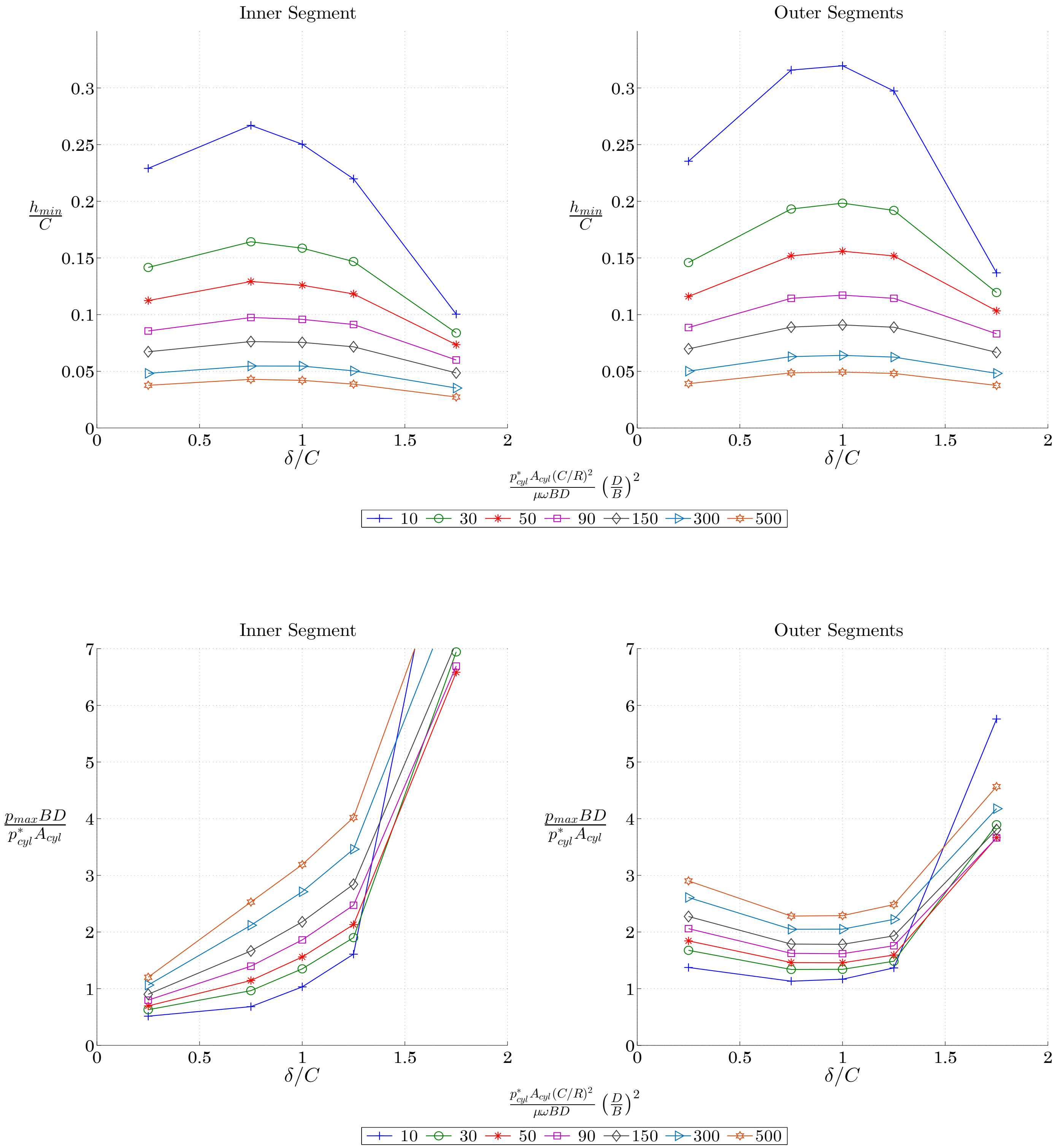

Figure A.48: Camella Offset, n=3, $\frac{M_p r\omega^2}{p^*_{cyl}A_{cyl}} = 0.15$; $\frac{r}{L} = 0.3$ (Short)

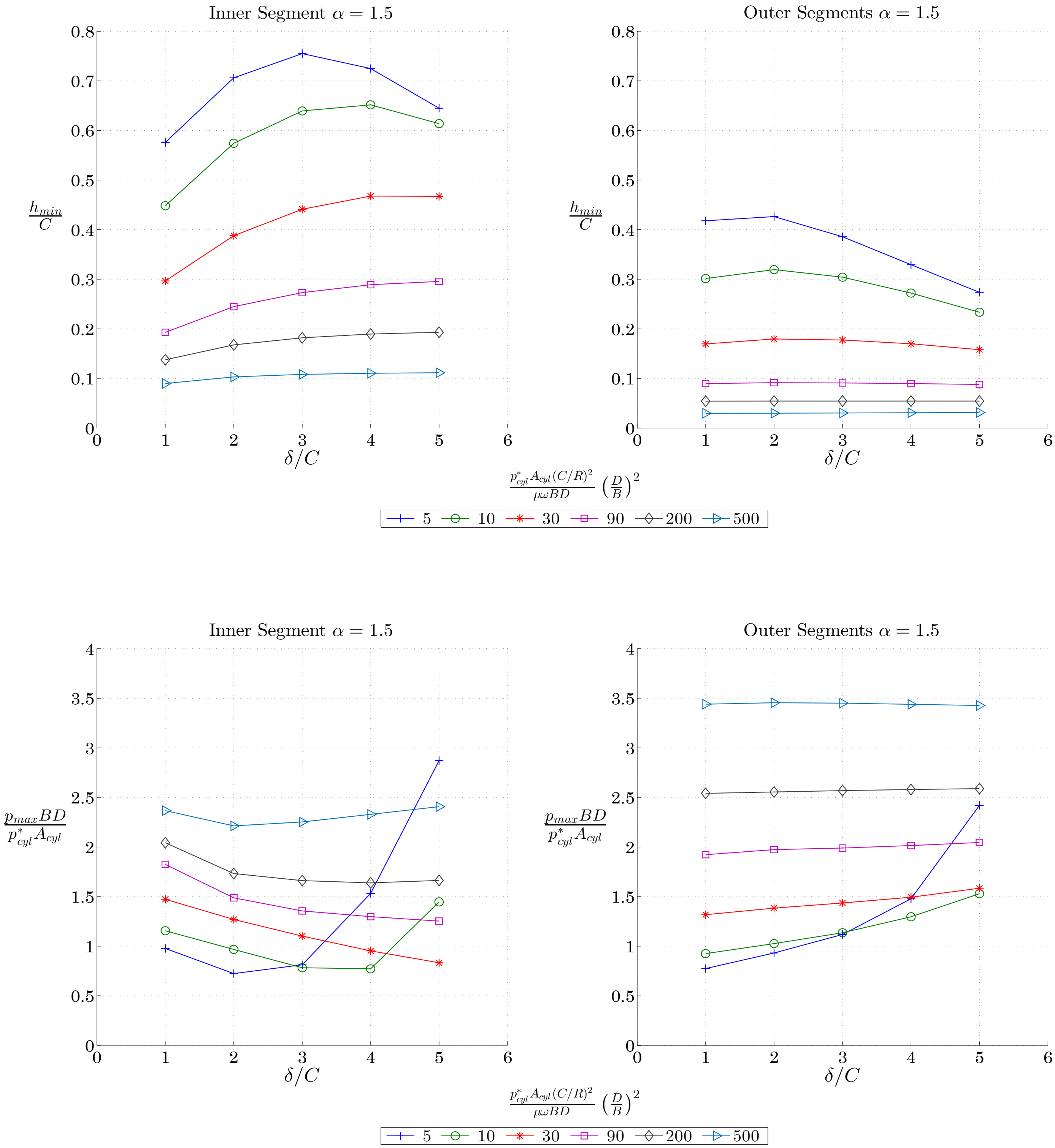

Figure A.49: Full Offset, $\alpha = 1.5$, n=3, $\frac{M_p r\omega^2}{p^*_{cyl}A_{cyl}}$ = 0.05; $\frac{r}{L}$ = 0.2 (Short)

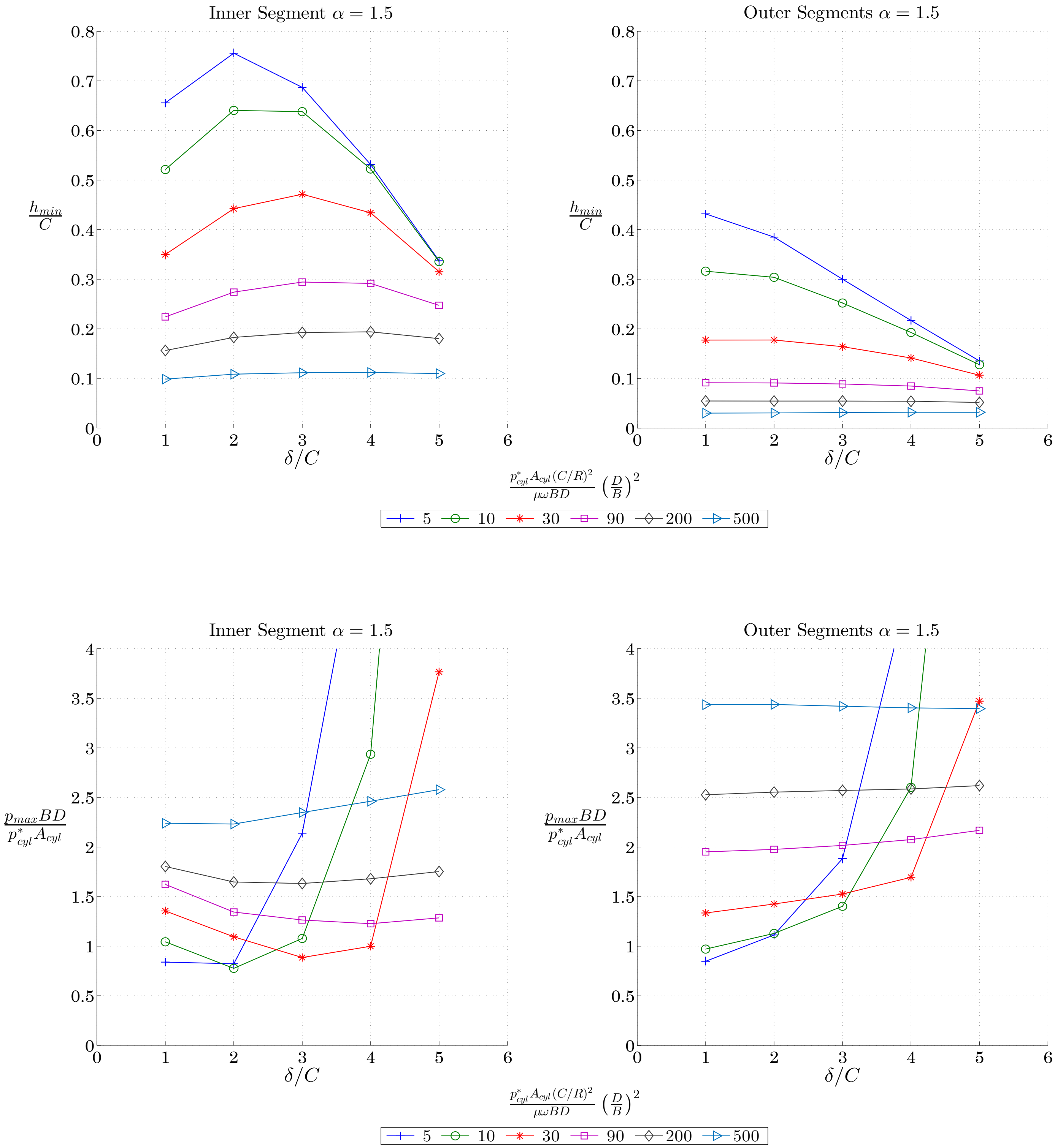

Figure A.50: Full Offset, $\alpha = 1.5$, n=3, $\frac{M_p r\omega^2}{p^*_{cyl}A_{cyl}}$ = 0.05; $\frac{r}{L}$ = 0.3 (Short)

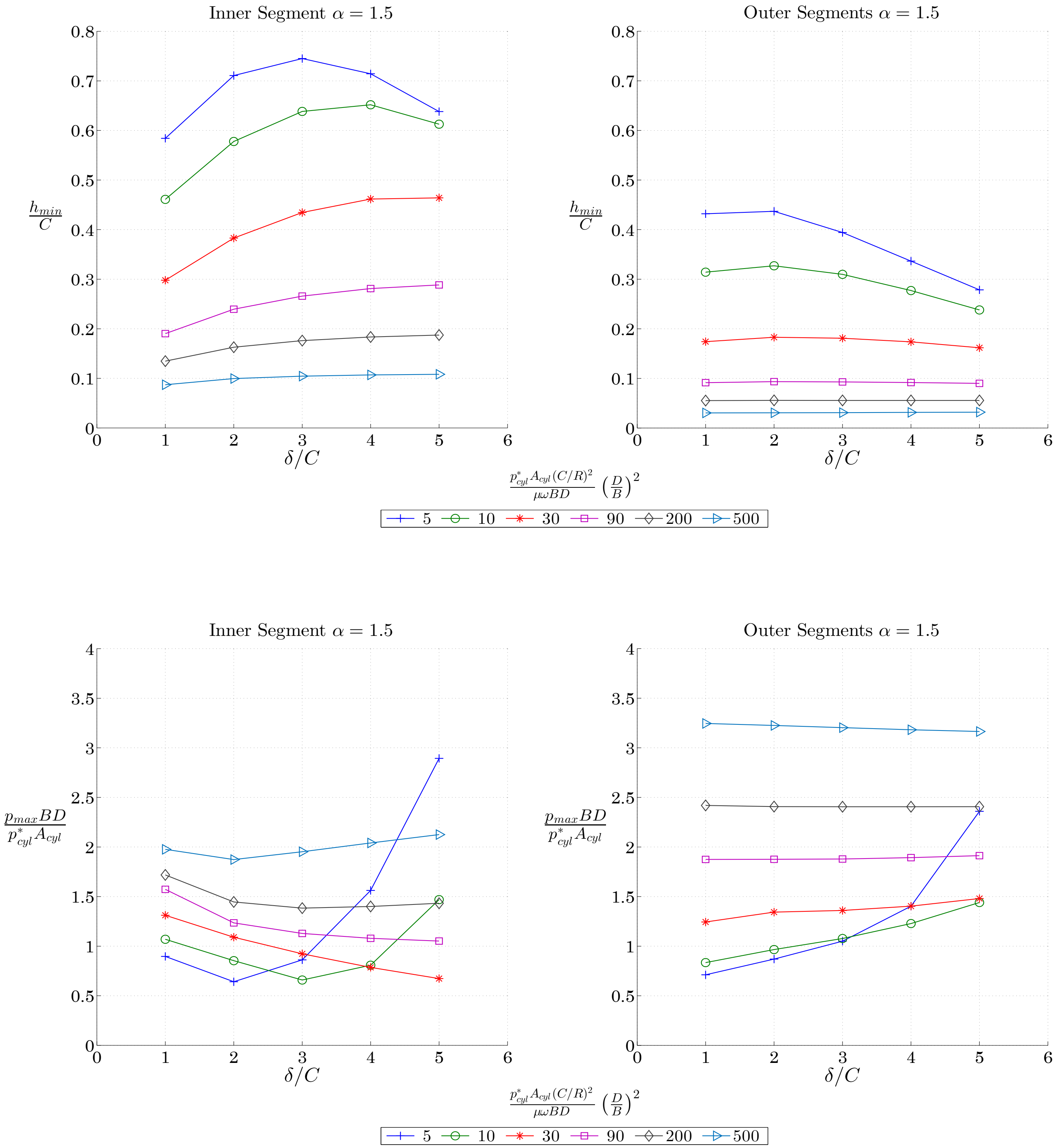

Figure A.51: Full Offset, $\alpha = 1.5$, n=3, $\frac{M_p r\omega^2}{p^*_{cyl}A_{cyl}}$ = 0.1; $\frac{r}{L}$ = 0.2 (Short)

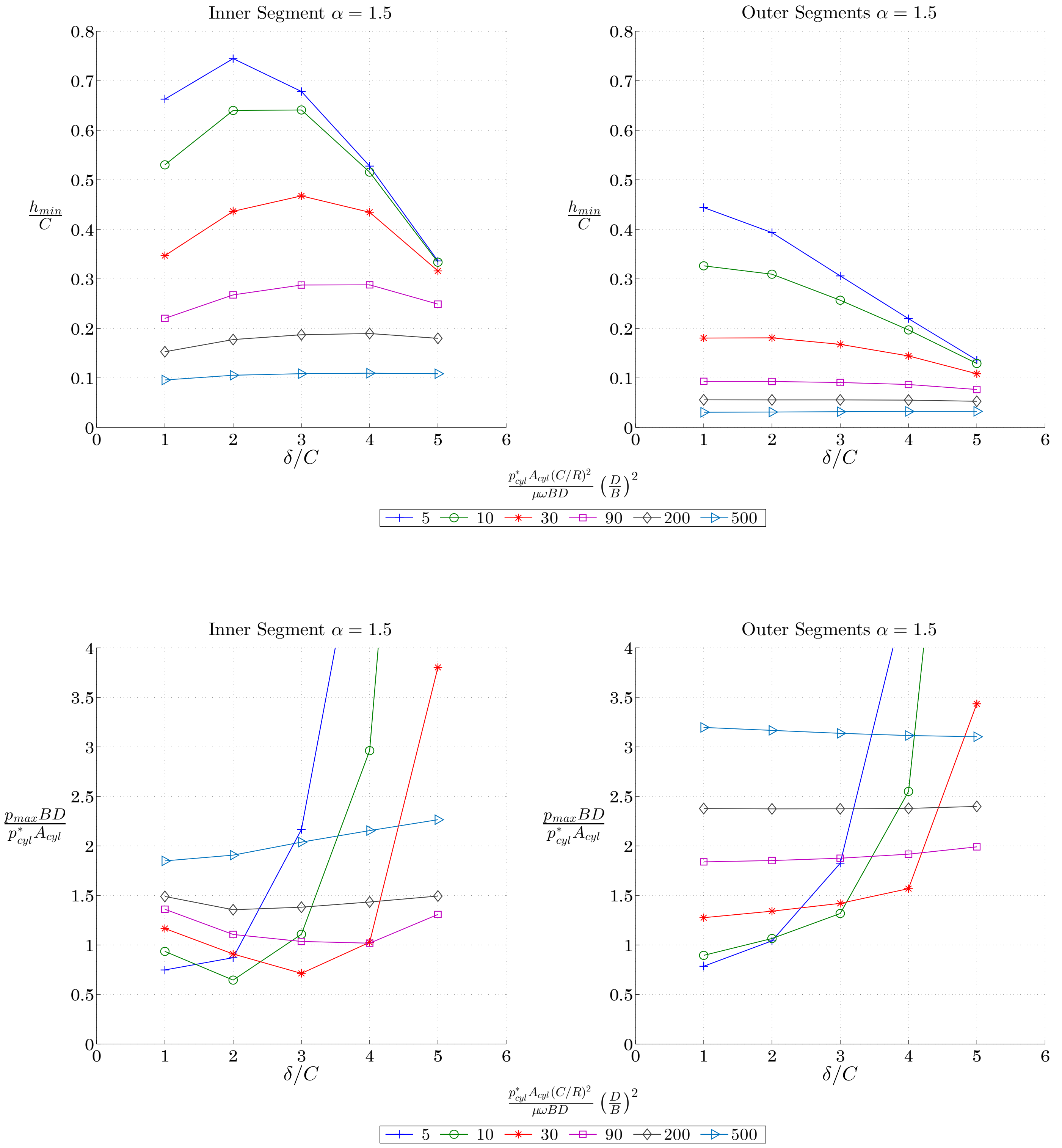

Figure A.52: Full Offset, $\alpha = 1.5$, n=3, $\frac{M_p r\omega^2}{p^*_{cyl}A_{cyl}}$ = 0.1; $\frac{r}{L}$ = 0.3 (Short)

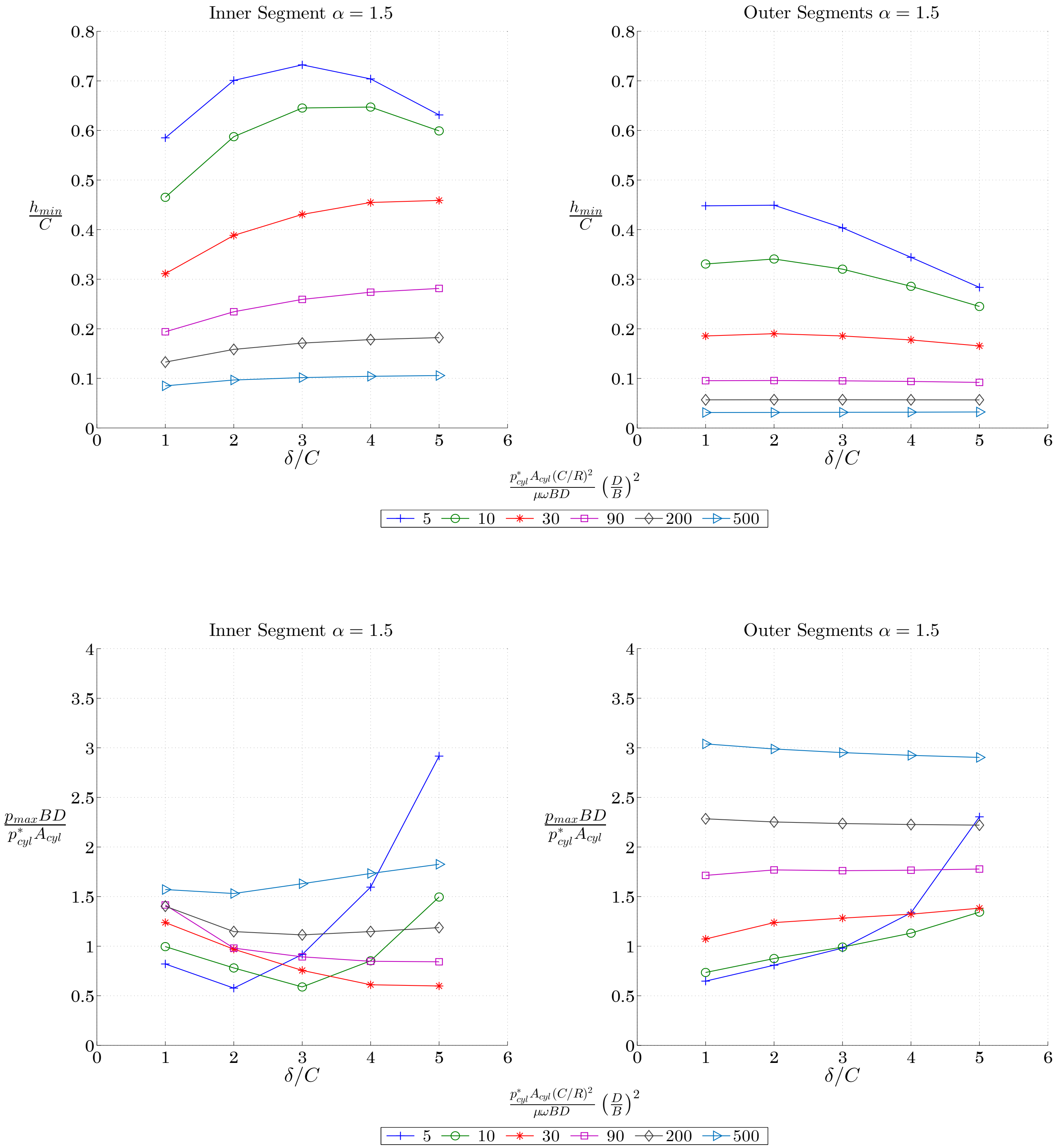

Figure A.53: Full Offset, $\alpha = 1.5$, n=3, $\frac{M_p r\omega^2}{p^*_{cyl}A_{cyl}}$ = 0.15; $\frac{r}{L}$ = 0.2 (Short)

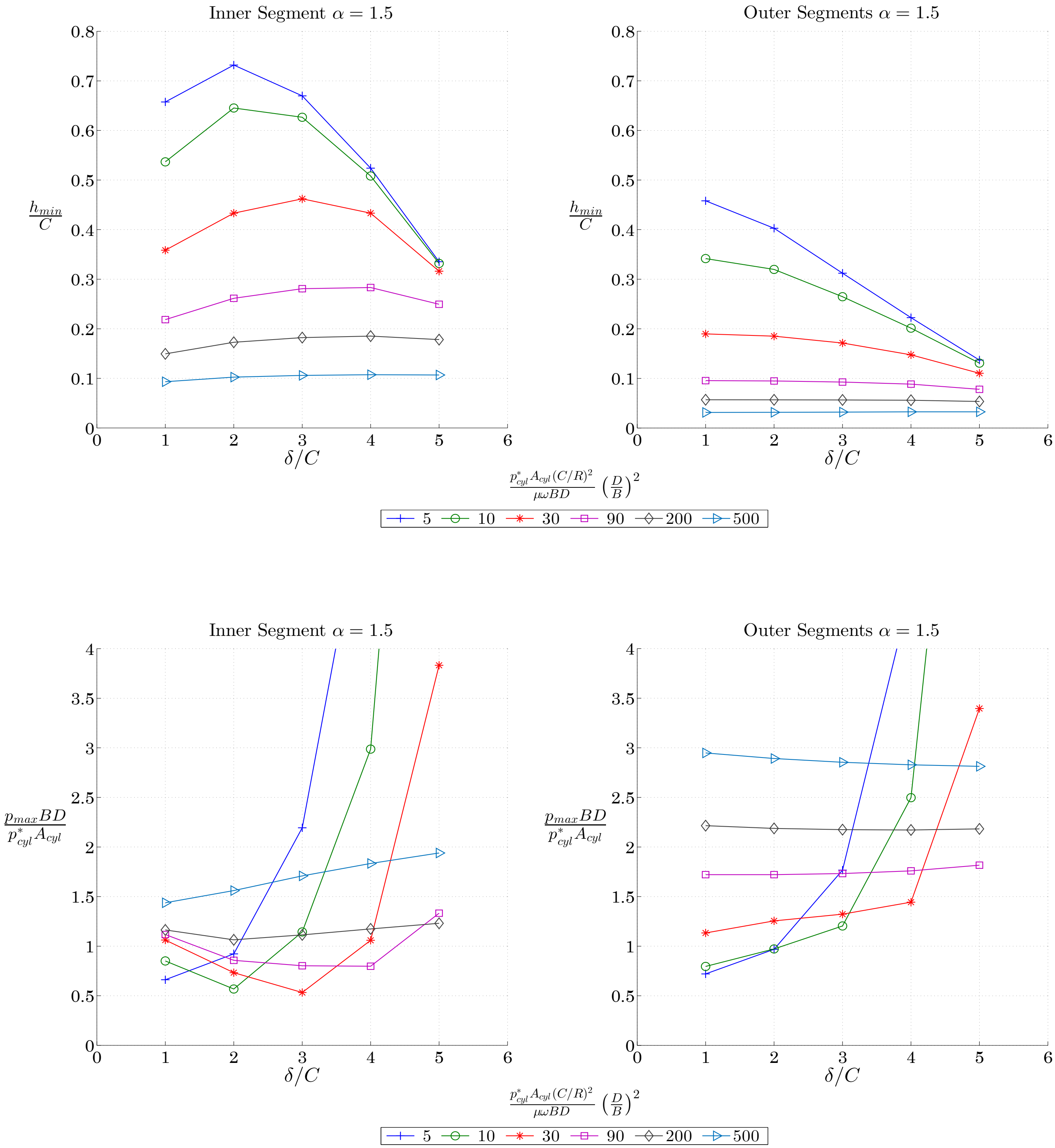

Figure A.54: Full Offset, $\alpha = 1.5$, n=3, $\frac{M_p r\omega^2}{p^*_{cyl}A_{cyl}}$ = 0.15; $\frac{r}{L}$ = 0.3 (Short)

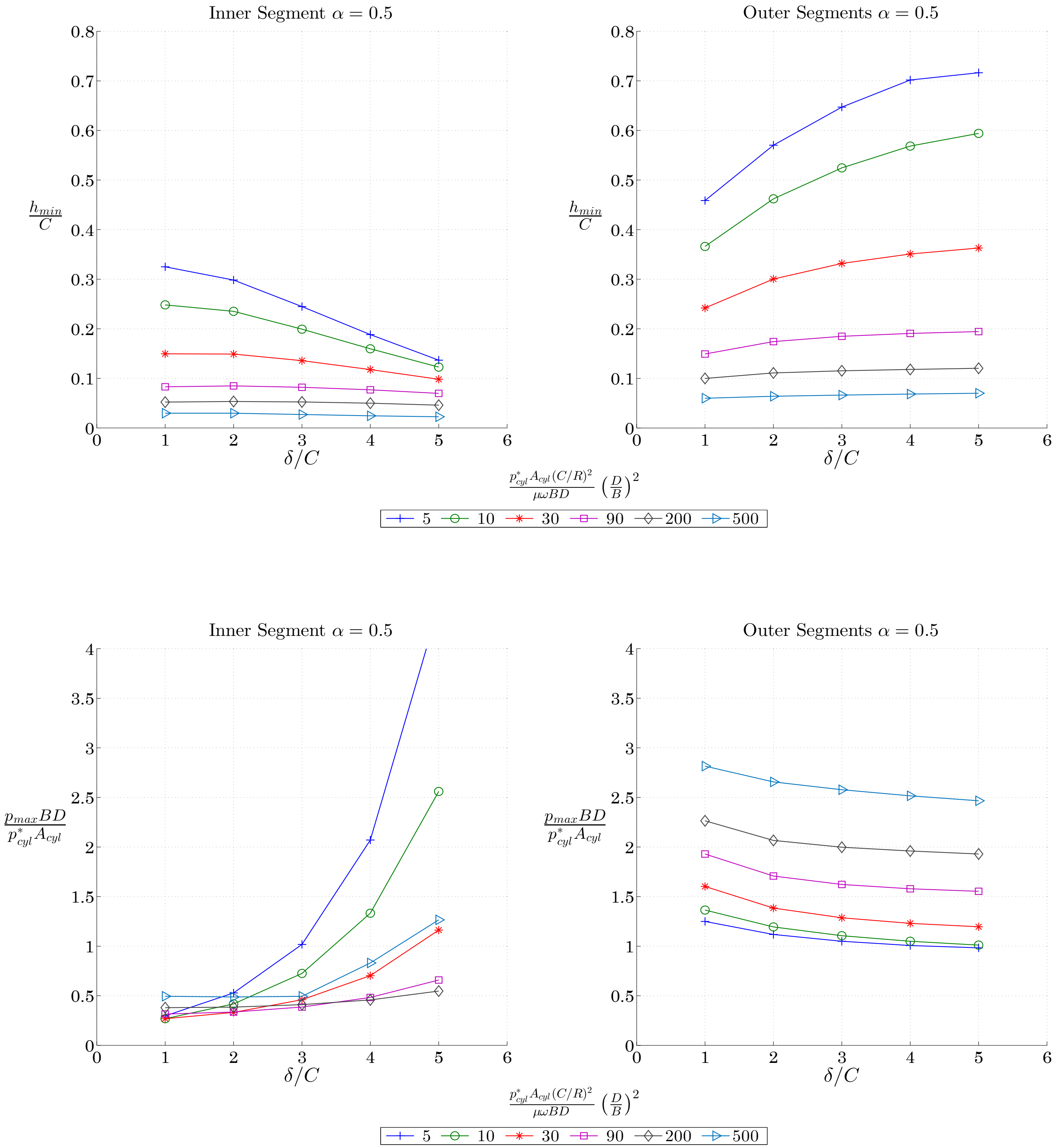

Figure A.55: Full Offset, $\alpha = 0.5$, n=3, $\frac{M_p r\omega^2}{p^*_{cyl} A_{cyl}}$ = 0.05; $\frac{r}{L}$ = 0.2 (Short)

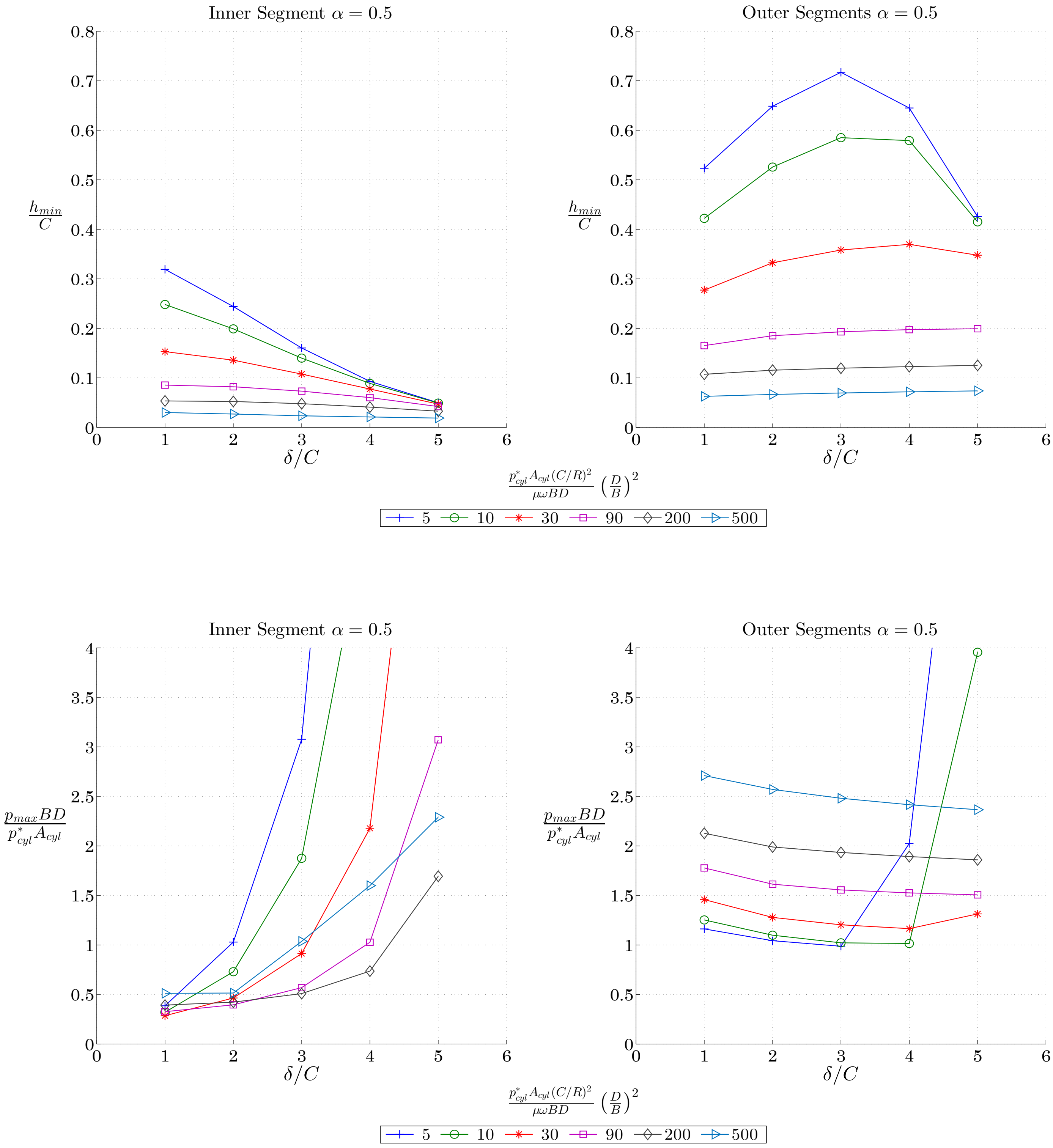

Figure A.56: Full Offset, $\alpha = 0.5$, n=3, $\frac{M_p r\omega^2}{p^*_{cyl}A_{cyl}} = 0.05$; $\frac{r}{L} = 0.3$ (Short)

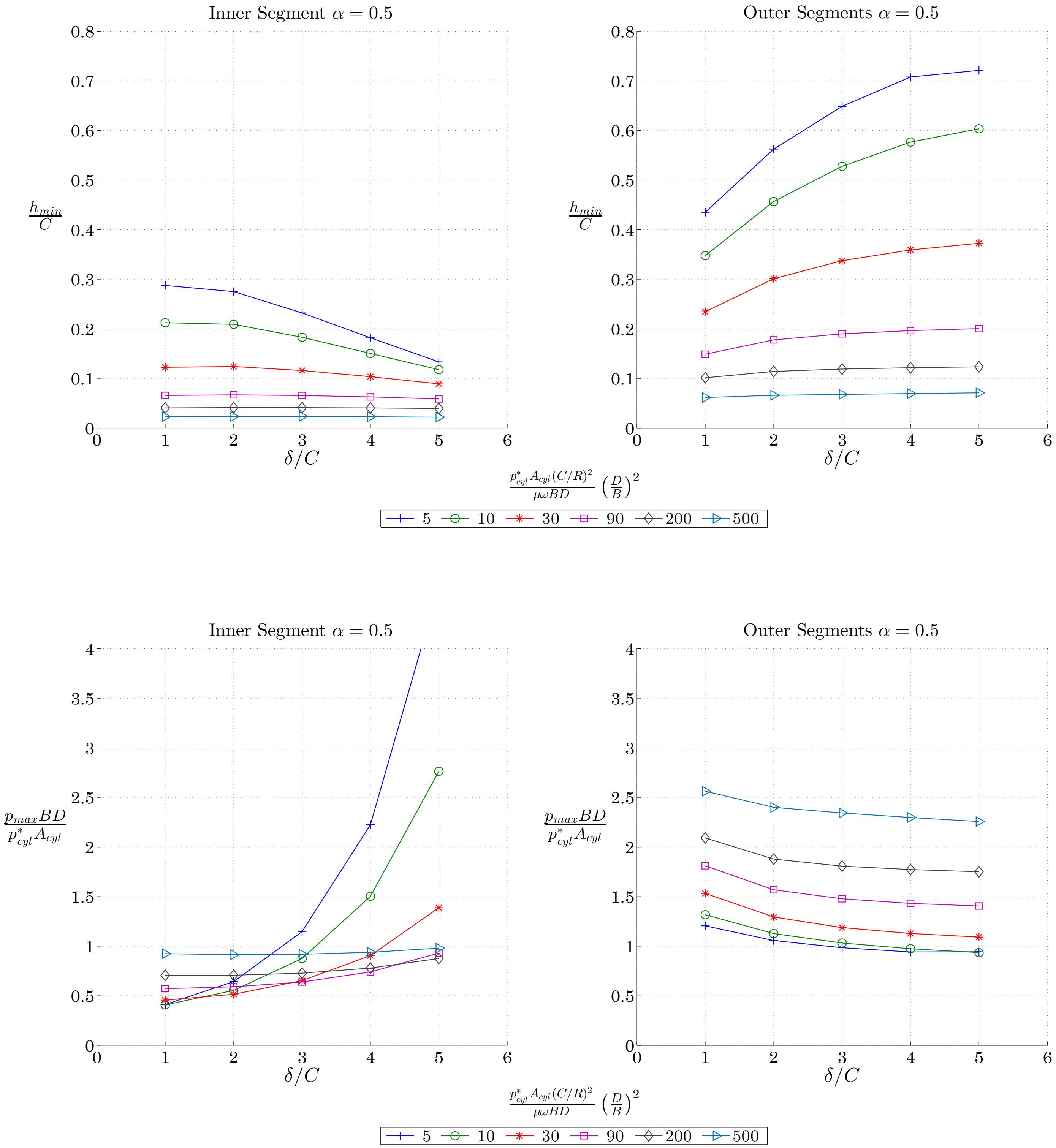

Figure A.57: Full Offset, $\alpha = 0.5$, n=3, $\frac{M_p r\omega^2}{p^*_{cyl}A_{cyl}}$ = 0.1; $\frac{r}{L}$ = 0.2 (Short)

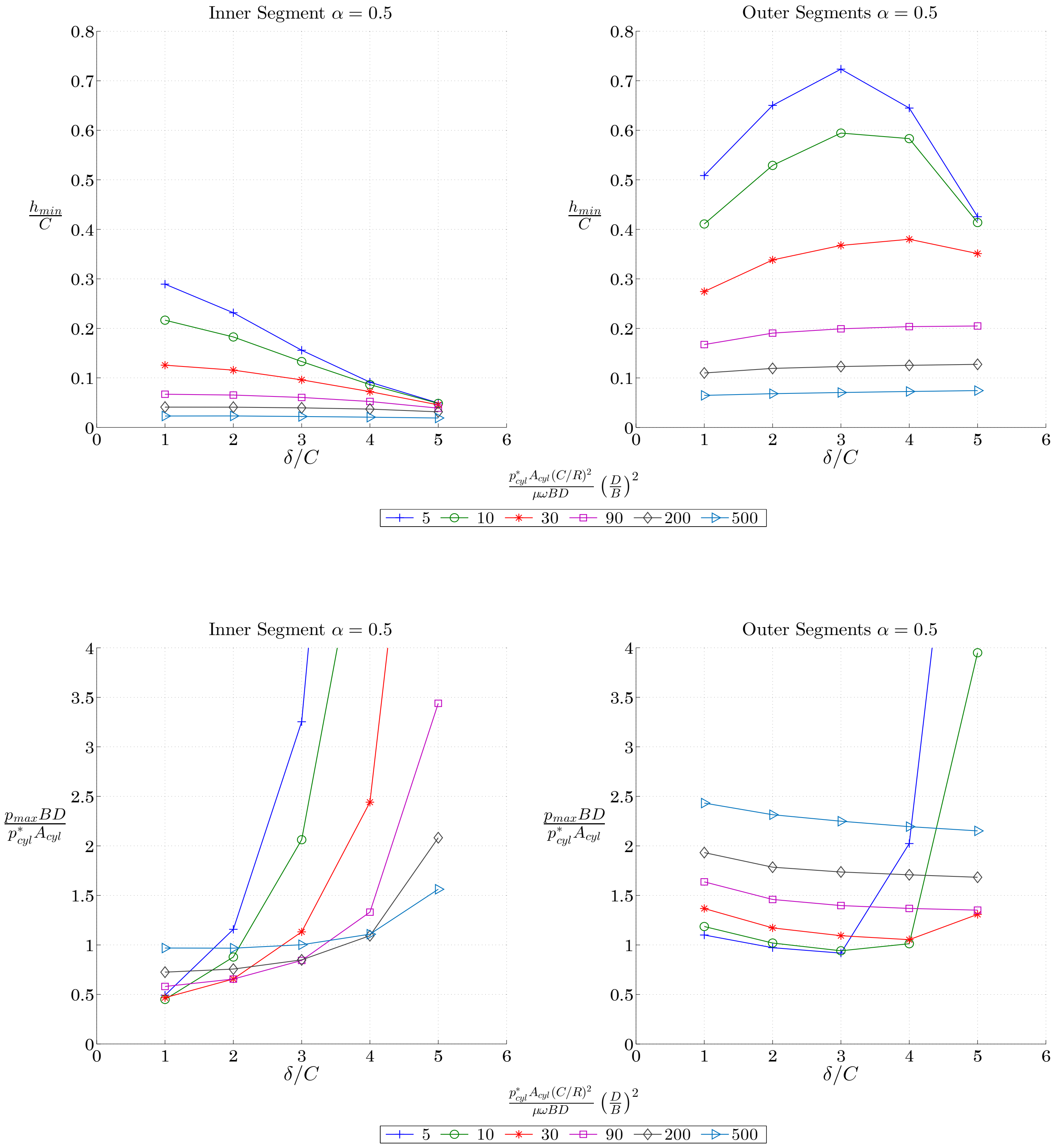

Figure A.58: Full Offset, $\alpha = 0.5$, n=3, $\frac{M_p r\omega^2}{p^*_{cyl}A_{cyl}}$ = 0.1; $\frac{r}{L}$ = 0.3 (Short)

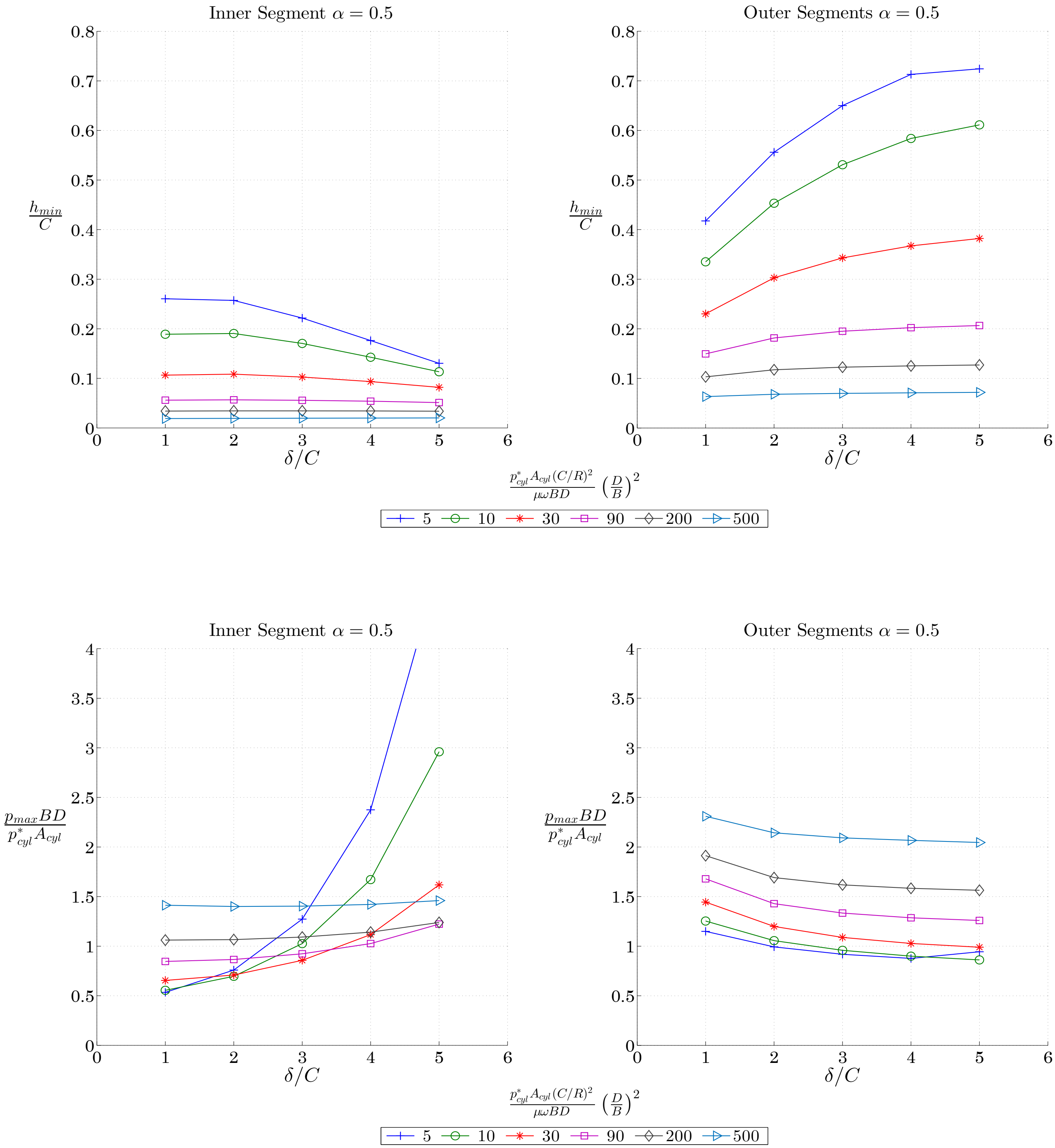

Figure A.59: Full Offset, $\alpha = 0.5$, n=3, $\frac{M_p r \omega^2}{p^*_{cyl} A_{cyl}} = 0.15$; $\frac{r}{L} = 0.2$ (Short)

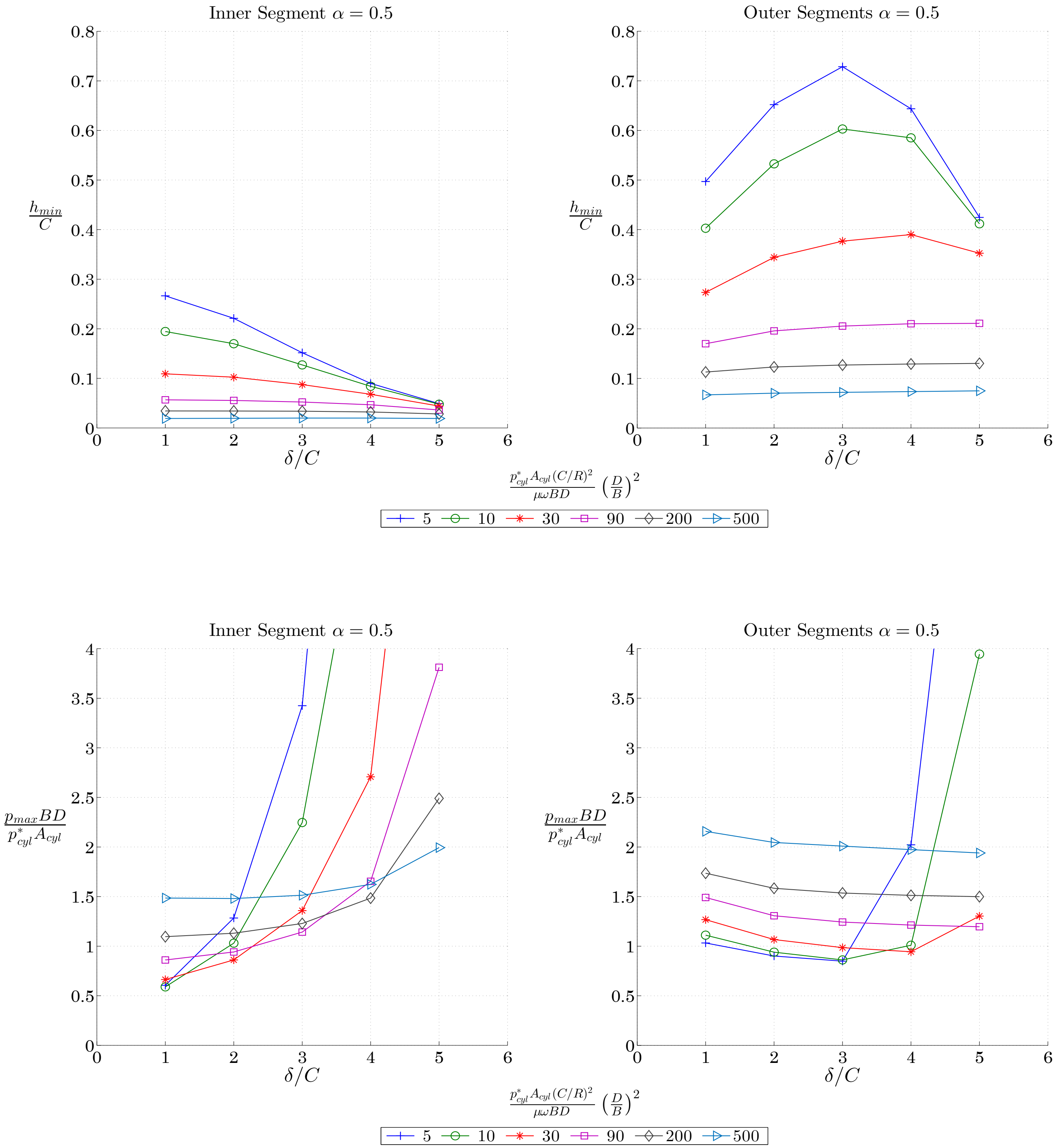

Figure A.60: Full Offset, $\alpha = 0.5$, n=3, $\frac{M_p r\omega^2}{p^*_{cyl}A_{cyl}} = 0.15$; $\frac{r}{L} = 0.3$ (Short)

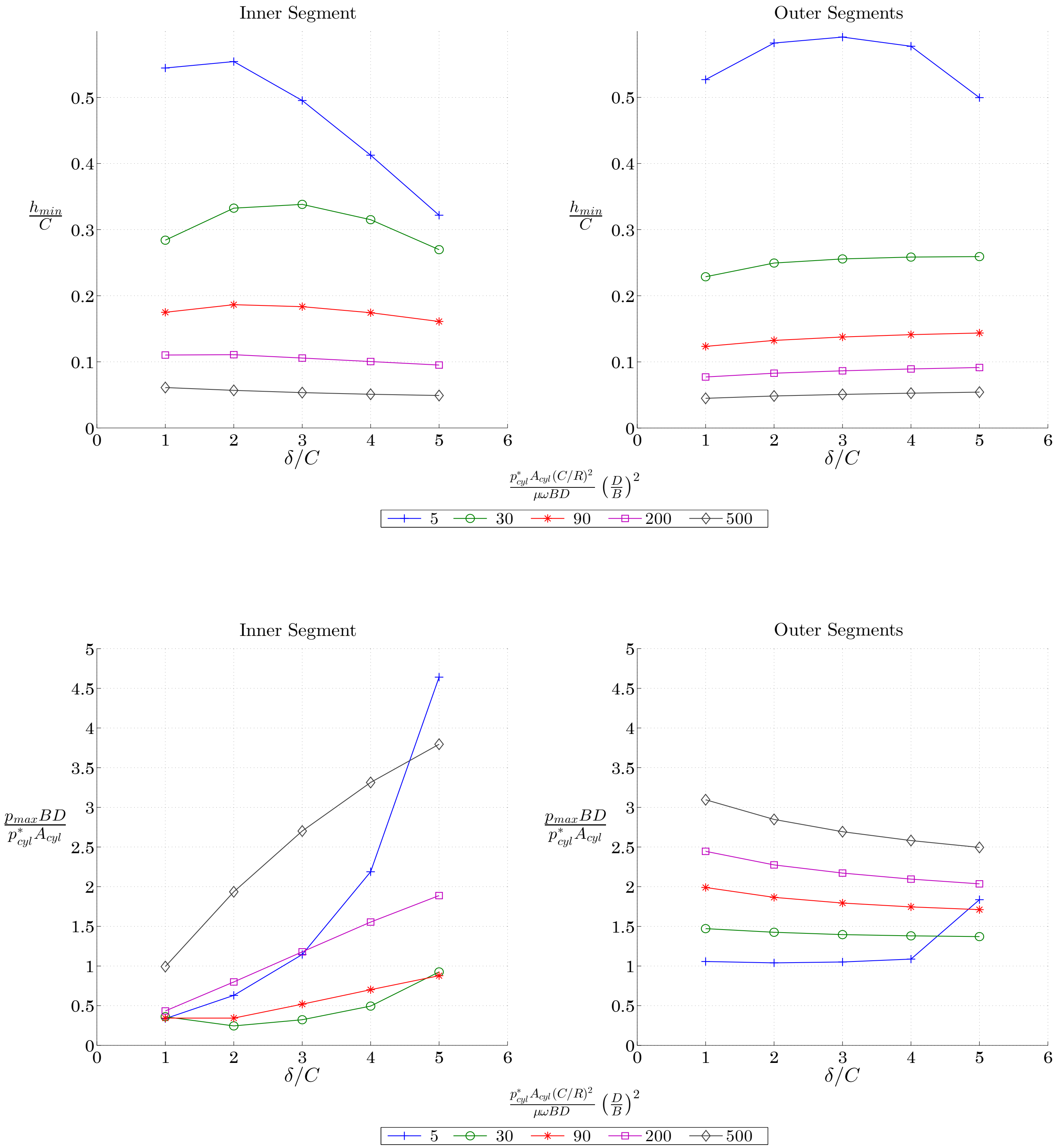

Figure A.61: Full Offset, $\beta = 2°$, n=3, $\frac{M_p r\omega^2}{p^*_{cyl}A_{cyl}}$ = 0.05; $\frac{r}{L}$ = 0.2 (Short)

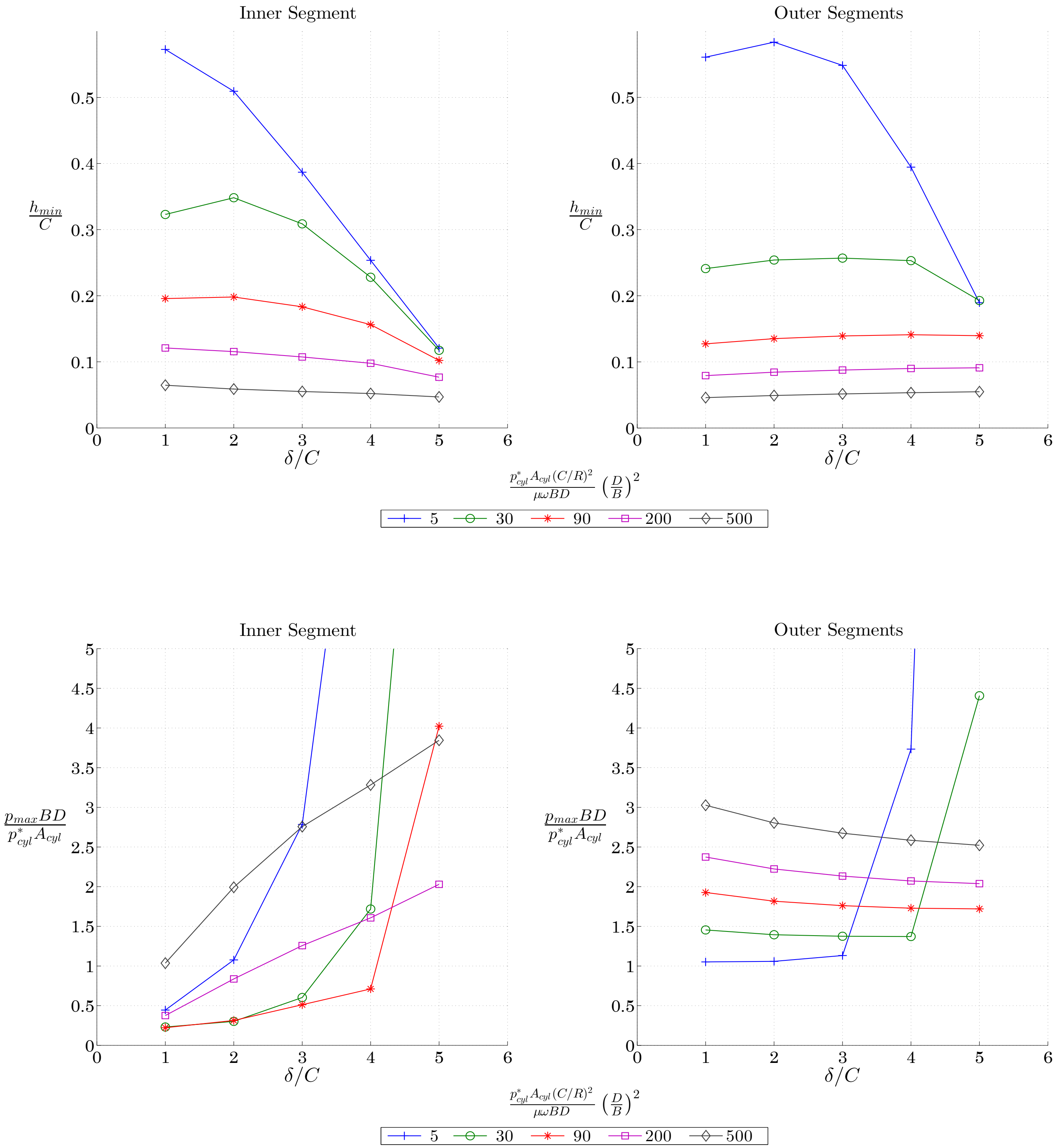

Figure A.62: Full Offset, $\beta = 2°$, n=3, $\frac{M_p r\omega^2}{p^*_{cyl}A_{cyl}}$ = 0.05; $\frac{r}{L}$ = 0.3 (Short)

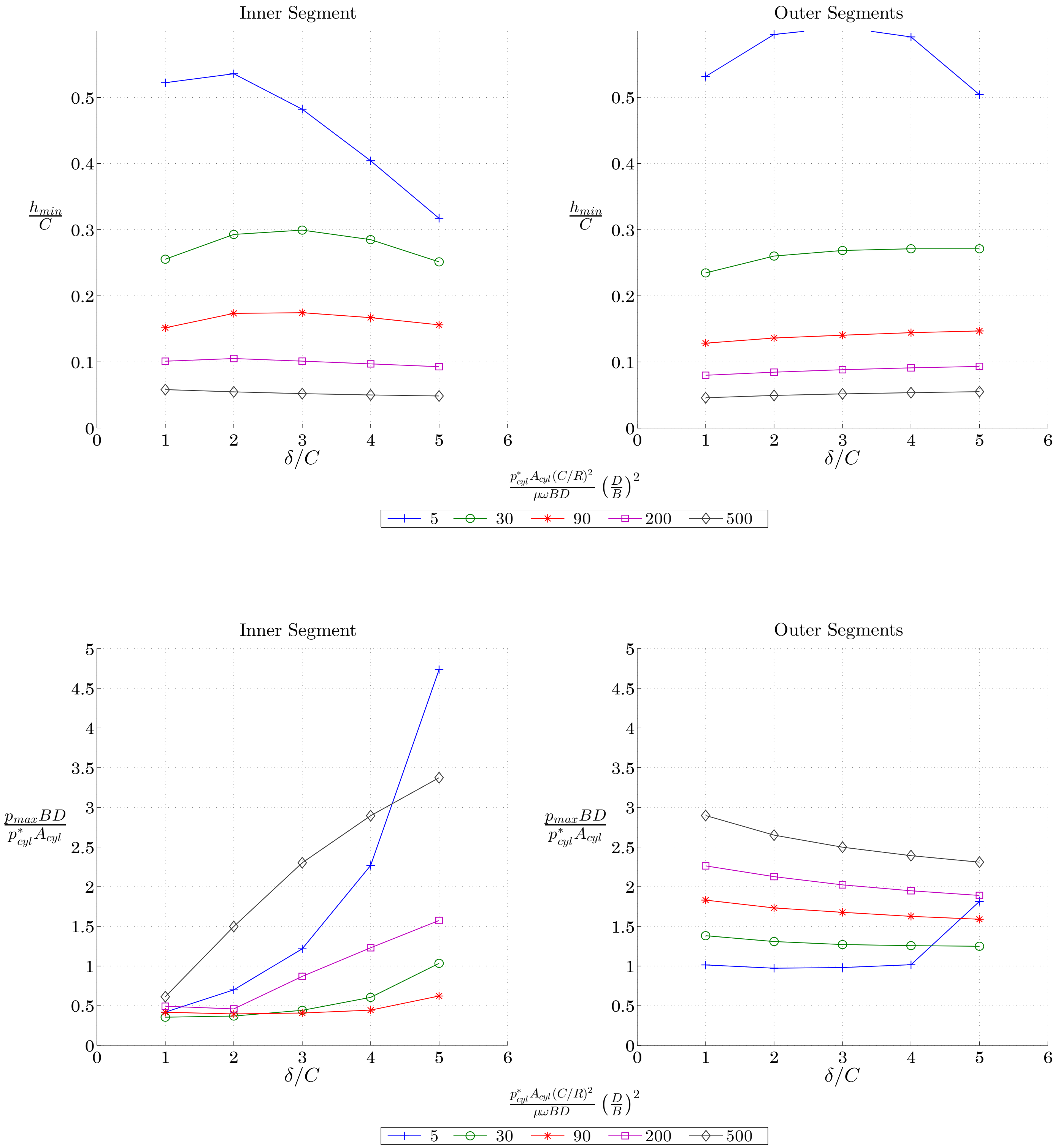

Figure A.63: Full Offset, $\beta = 2°$, n=3, $\frac{M_p r\omega^2}{p^*_{cyl}A_{cyl}}$ = 0.1; $\frac{r}{L}$ = 0.2 (Short)

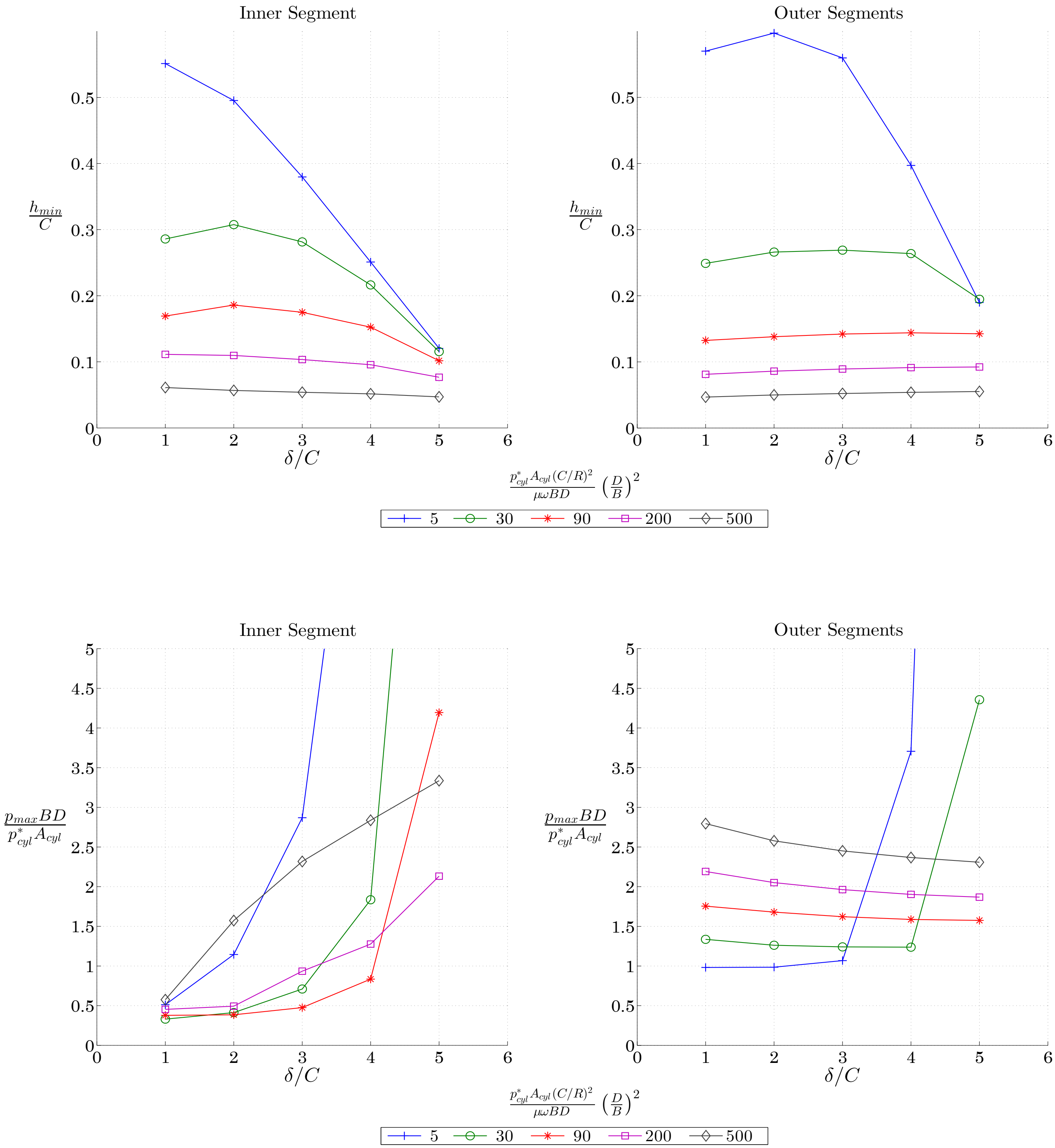

Figure A.64: Full Offset, $\beta = 2°$, n=3, $\frac{M_p r\omega^2}{p^*_{cyl}A_{cyl}}$ = 0.1; $\frac{r}{L}$ = 0.3 (Short)

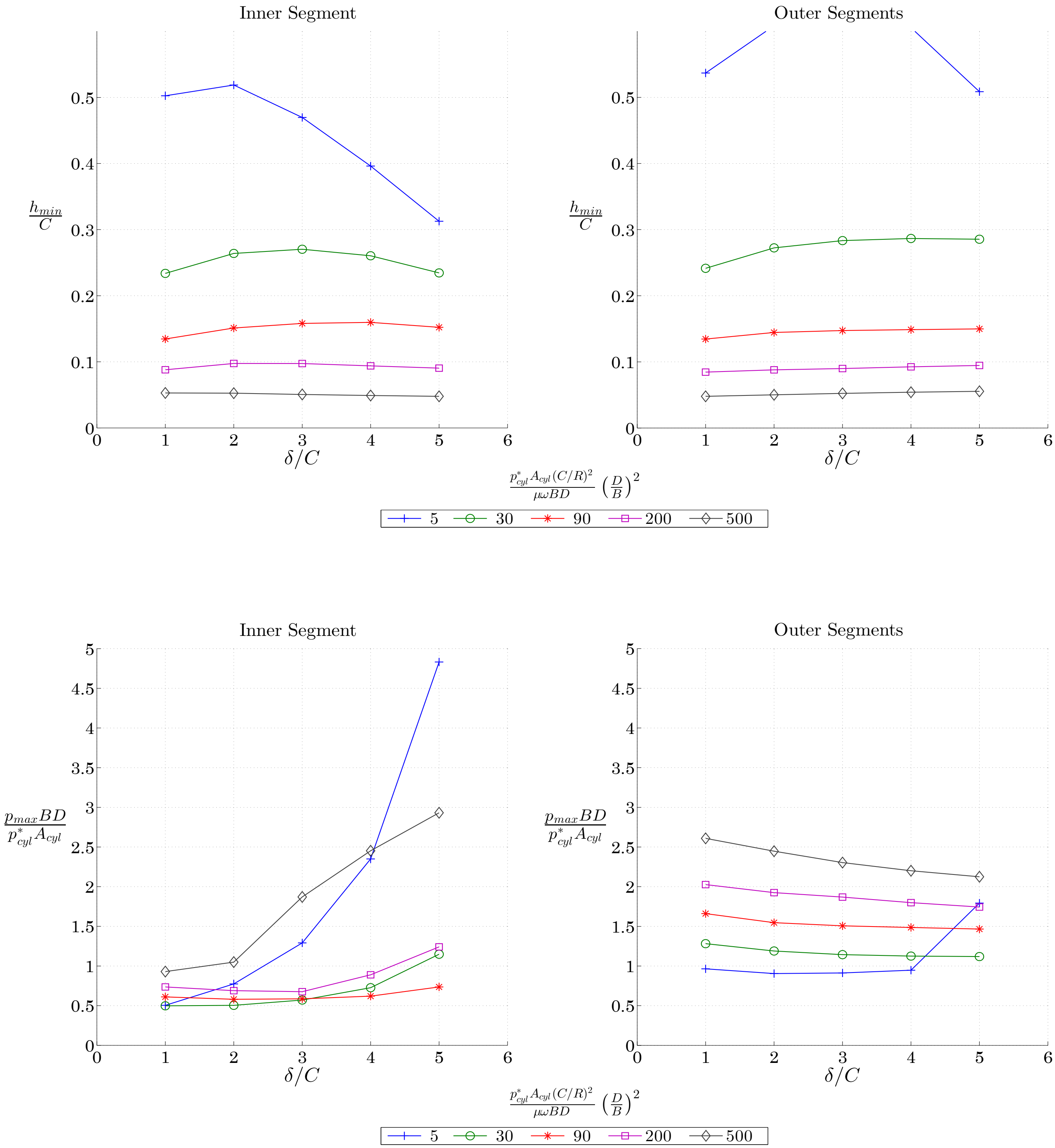

Figure A.65: Full Offset, $\beta = 2°$, n=3, $\frac{M_p r\omega^2}{p^*_{cyl}A_{cyl}}$ = 0.15; $\frac{r}{L}$ = 0.2 (Short)

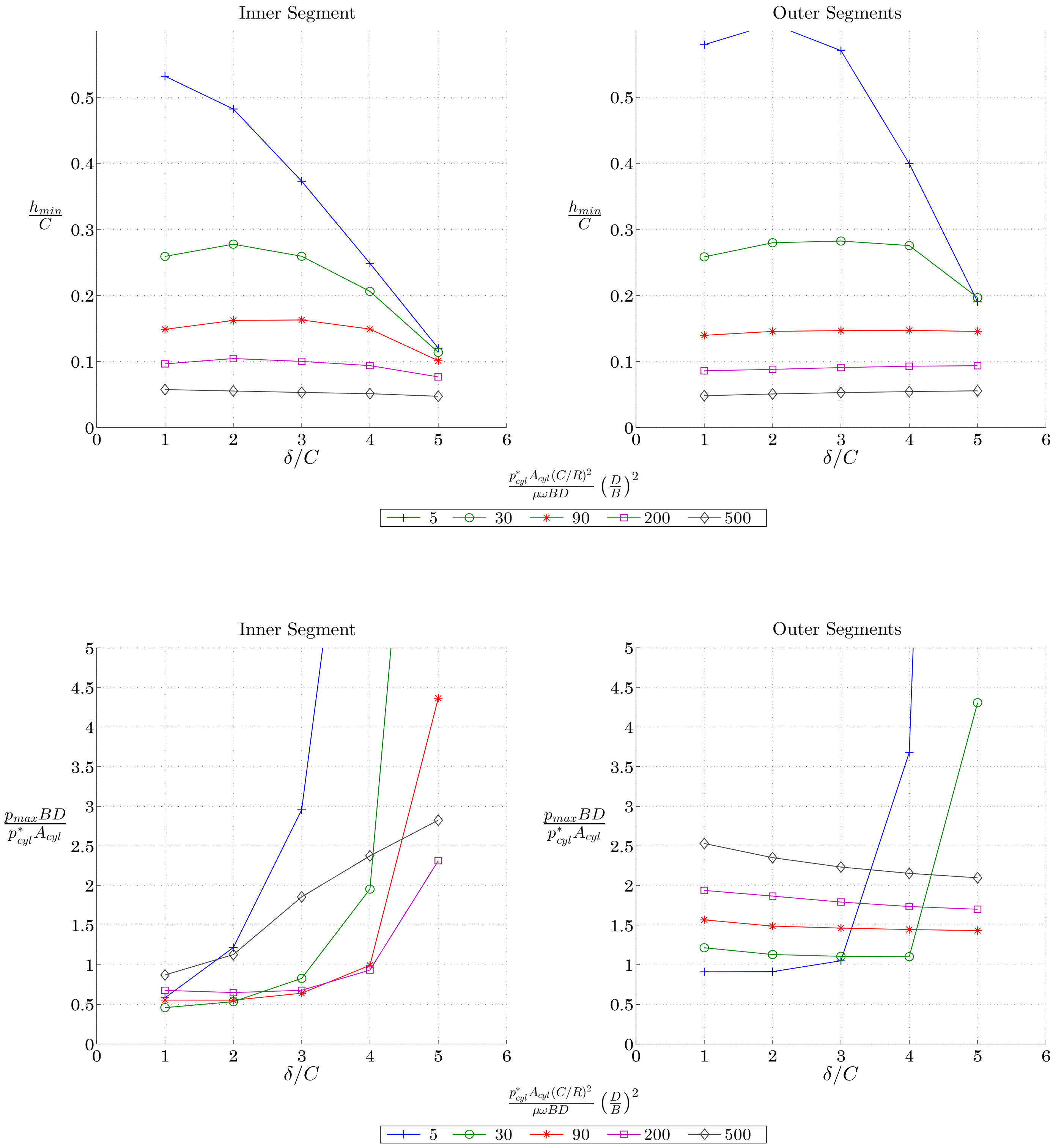

Figure A.66: Full Offset, $\beta = 2°$, n=3, $\frac{M_p r\omega^2}{p^*_{cyl}A_{cyl}}$ = 0.15; $\frac{r}{L}$ = 0.3 (Short)